ADIYAMAN ÜNİVERSİTESİ FEN BİLİMLERİ DERGİSİ
2011

Adıyaman University Journal of Science

Dec. 2024

Volume: 14 Issue: 2

An international peer reviewed journal of science

PHYSIC
BIOLOGY
SCIENCE
CHEMISTRY
MATHEMATICS

ADYU J SCI

ISSN 2147-1630
e-ISSN 2146-586X

An open access, peer-reviewed, international journal of science. Biannual (June & December). ISSN 2147-1630 | e- ISSN 2146-586X. Publisher: Adıyaman University.

Publication Language: English (with Turkish title and abstract)

Issue Published Date: 31.12.2024

Privilege Owner: On Behalf of the Rectorate of Adıyaman University, Prof. Dr. Mehmet KELEŞ (Rector)

Web Site: EN: https://dergipark.org.tr/en/pub/adyujsci
TR: https://dergipark.org.tr/tr/pub/adyujsci

EDITORIAL BOARD

Editor in Chief	: Selcen YÜKSEL PERKTAŞ, Ph.D.
Co-Editor	: Ali Osman AYAŞ, Ph.D.
Editors	
Biology	: Serdar SÖNMEZ, Ph.D.
	: Ertan YOLOĞLU, Ph.D.
Chemistry	: Cumhur KIRILMIŞ, Ph.D.
	: Gökhan ELMACI, Ph.D.
Mathematics	: Serbay DURAN, Ph.D.
	: Merve AVCI ARDIÇ, Ph.D.
Physics	: Salim ÇERÇİ, Ph.D.
	: Özge ERKEN, Ph.D.
Language Editors	: Özlem SAYAR, Ph.D.
	Münevver AKBAŞ
Layout Editor	: Özge ERKEN, Ph.D.

Section Editors

Biology:

Doç. Dr. M. Aydin AKBUDAK
Dr. Öğr. Üyesi Bahadır AKMAN
Dr. Öğr. Üyesi Hasan YILDIZ

Chemistry:

Prof. Dr. Lokman UZUN

Mathematics:

Prof. Dr. James F. PETERS
Prof. Dr. Mehmet GÜLBAHAR
Prof. Dr. Oznur GOLBASİ
Prof. Dr. Aynur KESKİN KAYMAKCI
Prof. Dr. Eylem GUZEL KARPUZ
Prof. Dr. Tahsin ÖNER
Prof. Dr. Mustafa Çağatay KORKMAZ
Prof. Dr. Mehmet Onur FEN
Doç. Dr. Feyza Esra ERDOĞAN

Physics:

Prof. Dr. Ahmet EKİCİBİL
Prof. Dr. Deniz SUNAR ÇERÇİ
Prof. Dr. Faruk KARADAĞ
Prof. Dr. Hakan ÖZTÜRK
Doç. Dr. Mustafa AKYOL
Dr. Levent ATEŞ

Technical Contact: Serdar SÖNMEZ, Ph.D., *ssonmez@adiyaman.edu.tr, sonmezserdar@gmail.com*

The articles published in this journal are licensed under a Creative Commons Attribution- NonCommercial-ShareAlike 4.0 International License.

Table of Contents (İçindekiler)

Volume (Cilt): 14 Number (Sayı): 2 December (Aralık) 2024

BIOLOGY:

C/EBPα Mediated Transcriptional Regulation of Human ADAMTS-3 Gene and Collagen Expression in Osteosarcoma Cells

Osteosarkoma Hücrelerinde İnsan *ADAMTS-3* Geni ve Kollajen Eksresyonunun C/EBPα Aracılı Transkripsiyonel Regülasyonu 1-14

Meltem ALPER, Tuğşen AYDEMİR, Feray KÖÇKAR

Identification and Functional Characterization of Glutamate Decarboxylase (GAD) Genes in Potato (Solanum tuberosum L.) and Analysis of Their Expression under Drought and Salt Stress Conditions

Patateste (*Solanum tuberosum* L.) Glutamat Dekarboksilaz (GAD) Genlerinin Tanımlanması ve Fonksiyonel Karakterizasyonu ile Kuraklık ve Tuz Stresi Koşullarında İfade Analizleri 15-28

M. Aydın AKBUDAK

DPPH Antioxidant Assays, Molecular Docking Studies and ADMET Predictions of Some 4-Chloromethyl Substituted Coumarin Compounds

Bazı 4-klorometil Substitüe Kumarin Bileşiklerinin DPPH Antioksidan Deneyleri, Moleküler Kenetlenme Çalışmaları ve ADMET Tahminleri 29-49

Gamze ÖZGÜL ARTUÇ

Assessment of the Developmental Profiles of ZHY3 and W303 Yeast Strains in Zinc-Modified Media

ZHY3 ve W303 Maya Irklarının Çinko Zenginleştirilmiş Ortamdaki Gelişim Profillerinin Değerlendirilmesi 50-58

Beyza YÜKSEL, M. Aydın AKBUDAK

Investigation of Biological Activities of Some Microalgae Extract Isolated from Kabakli Pond (Diyarbakır) Turkey

Kabaklı Göleti'nden (Diyarbakır) İzole Edilen Bazı Mikroalg Ekstraktlarının Biyolojik Aktivitelerinin Araştırılması 59-77

Feysel ÇAKMAK, Ahmet İsmail ÖZKAN, Nesrin HAŞİMİ, Özlem DEMİRCİ, Melike CİNİVİZ, Lokman VARIŞLİ, Ersin KILINÇ, Veysel TOLAN

Table of Contents (İçindekiler)

Volume (Cilt): 14 Number (Sayı): 2 December (Aralık) 2024

CHEMISTRY:

Synthesis, Characterization, And Thermal Conductivity Properties of Graphene Oxide Doped Chromium-Titanium Oxide Structures

Grafen Oksit Katkılı Krom-Titanyum Oksit Yapılarının Sentezi, Karakterizasyonu ve Termal İletkenlik Özellikleri 78-89

Serhat KOÇYİĞİT

Theoretical Study of Substitution Effects on Reorganization Energy in Indeno [1,2-b] fluorene-6,12-dione-Based Molecular Semiconductors

İndeno[1,2-b]fluoren-6,12-dion Bazlı Moleküler Yarı İletkenlerde Sübstitüsyonun Yeniden Düzenlenme Enerjisi Üzerindeki Etkilerinin Teorik Olarak İncelenmesi 90-102

Resul ÖZDEMİR

MATHEMATICS:

Approximation by a new Schurer type Stancu Operators and Associated GBS Operators

Yeni bir Schurer tipi Stancu Operatörleri ve ilgili GBS Operatörleri ile Yaklaşım 103-122

Nesibe MANAV MUTLU

Congruence of Curves in Weyl-Otsuki Spaces

Weyl-Otsuki Uzaylarında Kongrüans Eğrileri 123-139

Beran PİRİNÇÇİ

Tumor Detection by Classification of Brain MRI Images Using the Vision Transformers

Vision Transformers Kullanılarak Beyin MRI Görüntülerinin Sınıflandırılmasıyla Tümör Tespiti 140-156

Uğur DEMİROĞLU

On Solution of Complex Equations with the Homotopy Perturbation Method

Homotopi Pertürbasyon Metodu ile Kompleks Denklemlerin Çözümü Üzerine 157-167

Murat DÜZ, Şeyda ÇAMLICA

Adıyaman University Journal of Science
https://dergipark.org.tr/en/pub/adyujsci
DergiPark AKADEMİK
ISSN 2147-1630
e-ISSN 2146-586X

C/EBPα Mediated Transcriptional Regulation of Human *ADAMTS-3* Gene and Collagen Expression in Osteosarcoma Cells

Meltem ALPER[1,*], Tuğşen AYDEMİR[2], Feray KÖÇKAR[3]

[1]*Dokuz Eylül University, Institute of Oncology, Department of Translational Oncology, 35340, İzmir, Türkiye*
meltem.alper@deu.edu.tr, ORCID: 0000-0001-6359-9979
[2]*Moffitt Cancer Center and Research Institute,33612, Florida, USA*
tugsen@hotmail.com ORCID: 0000-0003-2803-4782
[3]*Balıkesir University, Faculty of Science and Literature, Department of Molecular Biology and Genetics, 35040, Balıkesir, Türkiye*
fkockar@balikesir.edu.tr, ORCID: 0000-0003-2572-8391

Received: 14.06.2024 **Accepted:** 08.07.2024 **Published:** 31.12.2024

Abstract

ADAM Metallopeptidase with Thrombospondin Type 1, Motif 3 (ADAMTS-3) is a procollagen amino proteinase mainly expressed in type II collagen-rich tissues and its primary function is to maturate amino ends of the type II collagen precursors. This maturation process allows correct fibril formation. ADAMTS-3 also has a tumor-suppressive function by regulating the fibronectin expression in the extracellular matrix (ECM.) CCAAT/enhancer-binding protein (C/EBPα) is a transcription factor playing a pivotal role in the cell cycle regulation. Dysregulations in the C/EBPα expression have been reported in solid tumors. C/EBPα expression has been identified to be associated with the metabolism and prognosis of a malignant bone tumor, osteosarcoma (OS). High heterogeneity, metastasis capability, and recurrence lead to poor prognosis and survival rates in OS. Multiple genetic and epigenetic factors affect OS development. Alterations in the ECM elements are closely related to OS development and

* Corresponding Author DOI: 10.37094/adyujsci.1501420

progression. According to the *in-silico* analyses, the ADAMTS-3 promoter includes multiple C/EBPα binding sites suggesting that C/EBPα could have a regulatory effect on ADAMTS-3 transcriptional regulation. In the present study, over-expression of the C/EBPα decreased ADAMTS-3 mRNA and protein levels in Saos-2 and MG-63 osteosarcoma models. Ectopic expression of the C/EBPα also led to alterations in some fibrillar collagen expression levels. Enhanced C/EBPα levels resulted in an increase in the type I and II collagen expression levels but didn't change the type III collagen expression level in Saos-2 cells. On the contrary, increased C/EBPα levels resulted in a decrease in all collagen expression levels in MG-63 cells Co-transfection analysis revealed that C/EBPα negatively regulates ADAMTS-3 promoter activity in both Saos-2 and MG-63 cells. Further EMSA studies indicated that C/EBPα functionally binds to the proximal region of the *ADAMTS-3* gene. Our findings will contribute to understanding C/EBPα mediated regulation of ADAMTS-3 and collagen composition in osteosarcoma cells.

Keywords: *ADAMTS-3*; C/EBPα; Collagen; Transcriptional regulation; Saos-2; MG-63.

Osteosarkoma Hücrelerinde İnsan *ADAMTS-3* Geni ve Kollajen Eksresyonunun C/EBPα Aracılı Transkripsiyonel Regülasyonu

Öz

ADAMTS-3, temelde tip II kollajen bakımından zengin dokularda eksprese edilen ve primer görevi tip II kollajen öncüllerinin amino uçlarını olgunlaştırmak olan bir prokollajen amino proteinazdır. Bu olgunlaşma süreci fibril oluşumunun düzgün olmasını sağlar. ADAMTS-3, hücrelerarası matriksteki (ECM) fibronektin ekspresyonunu düzenleme yoluyla tümör baskılayıcı bir işleve de sahiptir. C/EBPα, hücre döngüsü düzenlemesinde oldukça önemli rol oynayan bir transkripsiyon faktörüdür. Solid tümörlerde, C/EBPα ekspresyonunda düzensizlikler bildirilmiştir. C/EBPα ekspresyonunun, malign bir kemik tümörü olan osteosarkomanın (OS) metabolizması ve prognozu ile ilişkili olduğu tespit edilmiştir. Yüksek heterojenite, metastaz yeteneği ve rekürrens, OS'de kötü prognoz ve düşük sağkalım oranlarına yol açmaktadır. Osteosarkoma oluşumunda birçok genetik ve epigenetik faktör etkilidir. ECM bileşenlerindeki değişiklikler, OS oluşumu ve progresyonuyla yakından ilişkilidir. *In-silico* analizlere göre, ADAMTS-3 promotoru birçok C/EBPα bağlanma bölgesi içermektedir. Bu durum, C/EBPα'nın *ADAMTS-3* geninin transkripsiyonel regülasyonu üzerinde etkili olabileceğini düşündürmektedir Bu çalışmada, C/EBPα'nın over-ekspresyonu, Saos-2 ve MG-63 osteosarkoma modellerinin her ikisinde de ADAMTS-3 mRNA ve protein seviyelerini azaltmıştır. C/EBPα'nın ektopik

ekspresyonu ayrıca bazı fibriller kollajenlerin ekspresyon seviyelerinde de değişikliklere yol açmıştır. Saos-2 hücrelerinde, artan C/EBPα seviyesi, tip I ve II kollajenlerin ekspresyon seviyelerinde artışla sonuçlanmış ancak tip III kolajen ekspresyon seviyesini değiştirmemiştir.MG-63 hücrelerinde ise tersi şekilde, artan C/EBPα seviyesi tüm kollajen ekspresyon seviyeleri için bir düşüşle sonuçlanmıştır. Ko-transfeksiyon analizi, C/EBPα'nın hem Saos-2 hem de MG-63 hücrelerinde ADAMTS-3 promotör aktivitesini negatif olarak düzenlediğini ortaya koymuştur. EMSA çalışmaları, C/EBPα'nın ADAMTS-3 geninin proksimal bölgesine işlevsel olarak bağlandığını göstermiştir. Bulgularımız, osteosarkoma hücrelerinde ADAMTS-3'ün ve kollajen kompozisyonunun C/EBPα aracılı regülasyonunun anlaşılmasına katkıda bulunacaktır.

Anahtar Kelimeler: ADAMTS-3; C/EBPα; Kollajen; Transkripsiyonel regülasyon; Saos-2; MG-63.

1. Introduction

ADAMTS-3 is a member of ADAMTS (A disintegrin and metalloproteinase with thrombospondin motifs type I) protease family and participates in the procollagen amino proteinase (pNP) subgroup. ADAMTS-3 is mainly expressed in type II procollagen-rich tissues such as cartilage and its primary function is to maturate the amino terminus of the procollagen II [1]. This maturation process is very critical for the conformation of the correct fibril structure. In addition, ADAMTS-3 contributes to lymphatic vessel development by activating Vascular Endothelial Growth Factor (VEGF-C) [2]. Recent studies identified that ADAMTS-3 restricts cancer invasion in early breast cancer models by enhancing fibronectin degradation [3].

The C/EBPs (CCAAT/enhancer-binding protein) are modular proteins including six members sharing structural and functional common features. Members of the family modulate a variety of biological processes [4]. C/EBPα belongs to a basic region leucine zipper (bZIP) transcription factor (TF) family. C/EBPα plays a pivotal role in cell cycle regulation, specifically coordinating the proliferation and differentiation of the myeloid progenitors, adipocytes, and hepatocytes as well as lung and placenta cells [5-8]. In recent studies, the tumor suppressor role of the C/EBPα in acute myeloid leukemia (AML) has been identified. Alterations in the C/EBPα expression have been reported in solid tumors such as liver, breast, or lung cancer [9-11]. C/EBPα has been determined as an immune-related antitumor TF in osteosarcoma [12].

Osteosarcoma (OS) is a malignant bone tumor that commonly affects children and adolescents. High heterogeneity, metastasis capability, and recurrence rates lead to poor prognosis and survival rates in OS. Multiple genetic and epigenetic factors affect OS development. Recent

studies revealed that dysregulations in the ECM elements are also closely related to OS progression and migration and chemotherapy response [13-16].

In the present study, we aimed to elucidate transcriptional regulation of ADAMTS-3-a collagen processing matrix proteinase- by C/EBPα and also fibrillar collagens (type I, II, and III) in osteosarcoma cell lines. *In silico* analysis indicated multiple C/EBPα binding sites at the proximal region of the *ADAMTS-3* gene. So, we hypothesized that C/EBPα would have a regulatory effect on ADAMTS-3 promoter activity and ADAMTS-3 expression. In this context, ADAMTS-3 mRNA and protein levels were determined in C/EBPα over-expressed Saos-2 and MG-63 cells. Because fibrillar collagen types I, II, and III are the substrates of the ADAMTS-3, their mRNA levels were also determined to identify the effect of C/EBPα overexpression on collagen composition. Further, the effect of C/EBPα overexpression on the activity of truncated ADAMTS-3 promoter constructs was evaluated. Functional binding of the C/EBPα on the ADAMTS-3 promoter region was identified by Electrophoretic Mobility Shift Assay (EMSA) experiments.

2. Materials and Methods

2.1. Cell Culture and Plasmids

Saos-2 and MG-63 (human osteosarcoma cell line) cells were grown in DMEM (Dulbecco's modified Eagle's medium, Euroclone) supplemented with 10% FCS (fetal calf serum, Sigma) and 2 mM of L-Glutamine (Sigma). All cells were maintained in a humidified incubator with 5%CO_2 at 37˚C. Four different ADAMTS-3 promoter fragments were cloned into the pMeTLuc reporter vector in our previous studies [17]. The human C/EBPα expression plasmid was kindly gifted from Dr. Dipak P. Ramji, Cardiff School of Biosciences.

2.2. Transient transfection and dual reporter assay

Briefly, the cells were plated into 12-well tissue culture plates (25×10^4) 24 h before the transfection. 1µg of ADAMTS-3 promoter-reporter plasmid was transfected into the cells according to the calcium-phosphate precipitation method. SEAP (0.5 µg) (secreted human alkaline phosphatase, Promega) plasmid used for normalization in transfection assays. In addition, 2 µg of C/EBPα expression plasmid was transfected into the cells for co-transfection assays [18]. The luminescence value was measured from the collected medium after 48 h/72 h of transfection using Ready-To-Glow™ Secreted Luciferase Reporter Systems (Takara) and a Fluoroskan Ascent FL Luminometer. pMetLuc control and empty pMetLuc reporter vectors were used as positive and negative controls [19].

2.3. RNA extraction and quantitative RT-PCR (qRT-PCR)

Total RNA was isolated from control and C/EBPα transfected cell pellets using RNeasy Kit (Thermo Sci.) following the instructions. 1µg of total RNA was reverse-transcribed into cDNA. PCR was performed in 10µl final volume including 1 µL of cDNA template, 5 µL of Light Cycler-FastStart DNA Master SYBR Green I mix (Roche), and 0.5 µL of each pair of primers (10 ng/µL) (Table 1). Cycling conditions were applied as described before. Light Cycler 485 instrument (Roche Diagnostics) was used. Reactions were set up in triplicate for more accurate measurement. hβ-2 (human β-2 microglobulin) was used as an internal control. ΔΔCt method was used to calculate relative changes in *ADAMTS-3* gene expression [20, 21].

2.4. Western blotting

Total protein extraction was performed using RIPA buffer following the previously described instructions. Proteins were loaded on SDS-PAGE with equal concentrations (30-50 µg) for control cells and C/EBPα over-expressed cells. Membranes were treated with polyclonal ADAMTS-3 (3 µg/mL) (Abcam, ab45037), at 4°C for 16 h, or monoclonal β-actin (Santa Cruz Biotech., sc81178) antibody at room temperature for 1 h. Then membranes were washed and treated with HRP-conjugated secondary antibodies at room temperature for 1 h. ECL (Thermo Scientific) was used to visualize the protein bands and the membrane was photographed with Fusion FX Vilber Lourmat. Image J was used for densitometric quantification of protein bands [22, 23].

2.5. Electrophoretic mobility shift assay (EMSA)

EMSA is a core technique used to detect nucleic acid-protein interactions [24]. Here we performed EMSA experiments to identify functional binding of the C/EBPα to the ADAMTS-3 promoter. Nuclear extracts were prepared from control and C/EBPα overexpressing Saos-2 cells as described before [17]. 3' Ends of the Synthetic oligonucleotides (Table 1) were labeled with Biotin-11-UTP and TdT (Terminal Deoxynucleotidyl Transferase) (Thermo Sci.). Nuclear extracts (4 µg) were incubated with biotinylated double-stranded oligonucleotides (20 pmol) in 10% binding buffer and 0.05 µg/mL PolydIdc for 30 min at room temperature. An un-labeled form of the same probe or un-labeled consensus C/EBPα probe (500-fold) was used in competition assays (Table 1). Native polyacrylamide gel (6%) was used to analyze Protein/DNA complexes. [18]. After cross-linking of the complexes to the nylon membrane, biotin signals were detected using a Chemiluminescent Nucleic Acid Detection Module (Thermofisher Sci.) according to the instructions.

2.6. Bioinformatic and statistical analysis

MatInspector (Genomatix Software) was used to determine putative transcription factor-binding sites on the ADAMTS-3 promoter with a threshold of 0.9 [25, 26]. p-values were calculated by using Mini Tab 14 software. $p \leq 0.005$ value accepted as statistically significant. One-way ANOVA analysis was applied between the pairs for statistical significance.

Table 1: Primer sequences used in qRT-PCR and EMSA experiments.

Primer Name	**Sequence**
ADAMTS3 F	5'-TCAGTGGGAGGTCCAAATGCA-3'
ADAMTS3 R	5'-GCAAAGAAGGAAGCAGCAGCC-3'
COL1A1 F	5'-CTAGACATGTTCAGCTTTGTGGACCT-3'
COL1A1 R	5'-GTTGTCGCAGACGCAGATCCG-3'
COL2A1 F	5'-TCGGAGAGTGCTGCCCCATCT-3'
COL2A1 R	5'-GGCAGCAAAGTTTCCACCAAGA-3'
COL3A1 F	5'-AGCTGGCTACTTCTCGCTCTGCT-3'
COL3A1 R	5'-GTTCTGAGGACCAGTAGGGCATGA-3'
β-2Microglobulin F	5'-TTTCTGGCCTGGAGGCTATC-3'
β-2Microglobulin R	5'-CATGTCTCCATCCCACTTAACT-3
C/EBP α consensus F	5'TGCAGATTGCGCAAT3'
C/EBP α consensus R	5'TGCATTGCGCAATCT3'
ADAMTS3[−131/−103] F	5′-GCTCAAATTTCATTTTCATTGAAGCAAAG-3′
ADAMTS3[−131/−103] R	5′-CTTTGCTTCAATGAAAATGAAATTTGAGC-3′
ADAMTS3[−40/12] F	5′-AACTTATTTTGGGCGGGGGGGGTGGGTTTGC-3′
ADAMTS3[−40/12] R	5′-GCAAACCCACCCCCCCCGCCCAAAATAAGTT-3′

3. Results and Discussion

3.1. C/EBPα overexpression leads to decreased ADAMTS-3 mRNA and protein expression in both Saos-2 and MG-63 cells

To evaluate the regulatory effect of C/EBPα on ADAMTS-3 expression in Saos-2 and MG-63 cells, the C/EBPα expression plasmid was transiently transfected into Saos-2 and MG-63 cells. Ectopic C/EBPα expression was confirmed at mRNA and protein levels by qRT-PCR and western-blot assays. C/EBPα mRNA expression level significantly increased in C/EBPα transfected groups up to 2 fold, and protein level up to 2.5 fold after 24 hours of transfection compared to the control groups in Saos-2 cells (Figure 1A and B). Therefore, ADAMTS-3 mRNA and protein levels were analyzed after 24 hours of C/EBPα transfection. C/EBPα reduced

ADAMTS-3 mRNA (5.8 fold) and also protein level (2.6 fold) in a statistically important manner (Figure 1C and 1D). Since the main task of ADAMTS-3 is to process amino ends of the collagens, we also investigated the effect of C/EBPα on the expression of type I, II, and III collagens. C/EBPα overexpression induced mainly collagen types I (2 fold) and II (1.3 fold) and didn't lead to any changes in collagen III expression level (Figure 1E). Next, we assessed alterations in ADAMTS-3 expression in a different osteosarcoma model, MG-63. Although both Saos-2 and MG-63 cells are osteosarcoma models, they differ in origin and gene expression profiles. For instance, while Saos-2 cells have epithelial characteristics, MG-63 cells are fibroblastic. These cells also differ in their collagen compositions ([27, 28]. As can be seen in Figure 2A, C/EBPα expression was significantly increased up to 6.5-fold after 6 h of transfection relative to non-transfected groups. C/EBPα overexpression significantly decreased ADAMTS-3 mRNA (0.024-fold at 6 h and 0.26-fold at 24 h) and protein expression (0.6-fold) levels similar within Saos-2 cells (Figure 2B and 2C) Secondly, the effect of the C/EBPα protein on collagen expression patterns were investigated. Quite different from Saos-2 cells, it was determined that C/EBPα significantly suppressed collagen I, II, and III expressions in MG-63 cells (Figures 2D and 2E). As a main substrate of the ADAMTS-3, the collagen II protein expression level was also confirmed in C/EBPα overexpressing MG-63 cells and a slight decrease was observed (Figure 2F).

Regulation of the ADAMTS family members with CEBP transcription factors is mainly studied in vascular diseases because of the ECM processing activity in the vessel wall. For example, C/EBPβ has been identified as the chief mediator in IL-1β and TNF-α mediated regulation of ADAMTS-1 in vascular cells. Therefore ADAMTS-1 has been suggested as a promising candidate for the development of novel therapeutics for vascular disorders [29]. Abnormalities in the signaling and structural components of the ECM have been known as the leading causes of osteosarcoma formation and progression [14]. Wei and colleagues identified that type I collagen could facilitate malignant OS development and induce the capability of cell proliferation and tumorigenesis [13]. Because of the collagen processing activity of the ADAMTS-3, which are the basic components of the ECM, determining the factors affecting its expression level could be important in terms of OS progression. In our previous studies, we determined that ADAMTS-3 is abundantly found in osteosarcoma cell lines Saos-2 and MG-63 [30]. Previous studies identified that type I collagen levels were higher in Saos-2 cells when compared to type II and III collagen levels. Here we determined that C/EBPα expression resulted in a significant decrease in ADAMTS-3 and an increase in both type I and II collagen levels in Saos-2 cells. Therefore, it can be suggested that the increase in type I collagen level observed as a result of C\EBPα-mediated downregulation of ADAMTS-3 would be critical for OS. Previous

studies identified that MG-63 cells have higher type I and III collagen levels than type II. C\EBPα overexpression in MG-63 cells resulted in a decrease in the expression of all collagens types (type I-II and III). This result may be due to the heterogeneity of the gene expression profiles due to the maturation status of the osteoblastic cell lines.

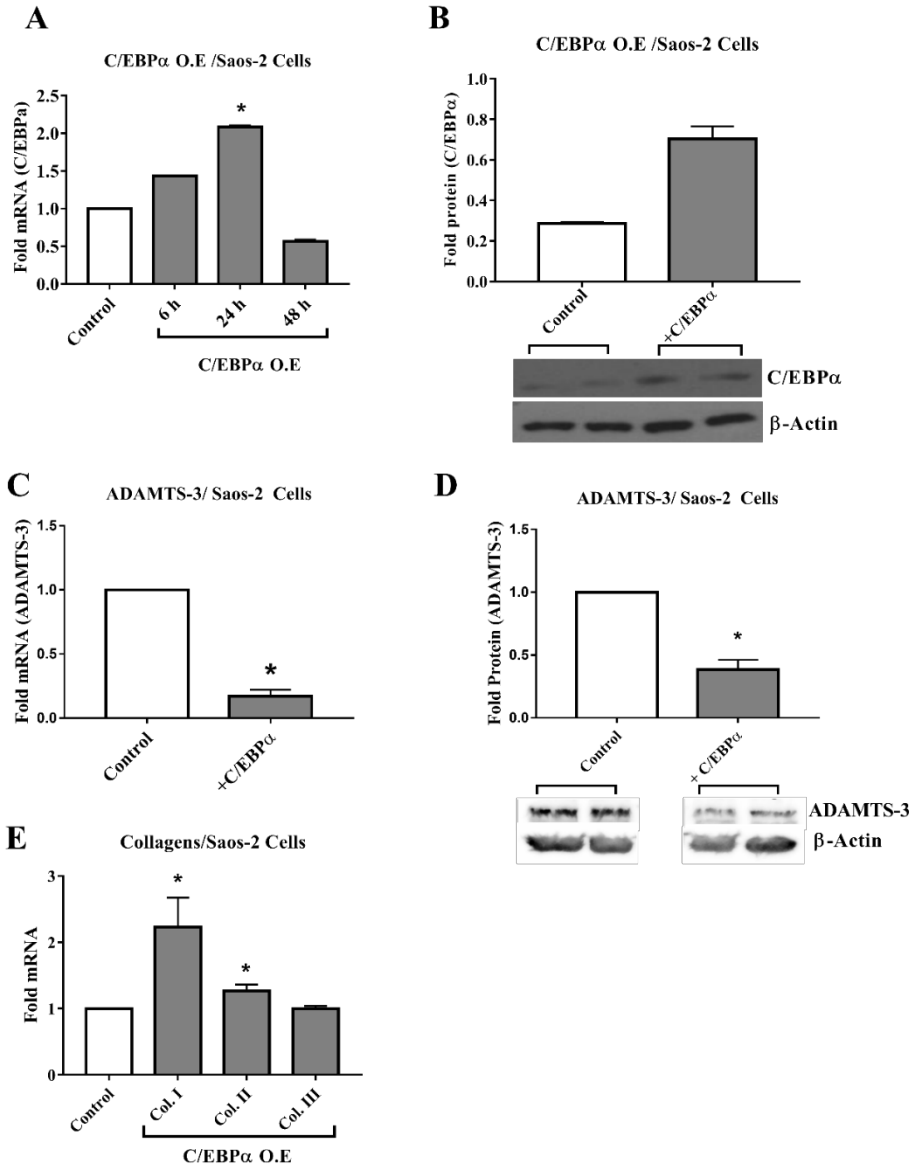

Figure 1: A-B C/EBPα mRNA and protein levels after transfection of C/EBPα expression plasmid. **C-D** ADAMTS-3 mRNA and protein levels in C/EBPα over expressed Saos-2 cells after 24 h of transfection. **E** Fibrillar collagen (type I, II, and III) levels in C/EBPα over expressed Saos-2 cells. Asterisks indicate $p \leq 0.05$.

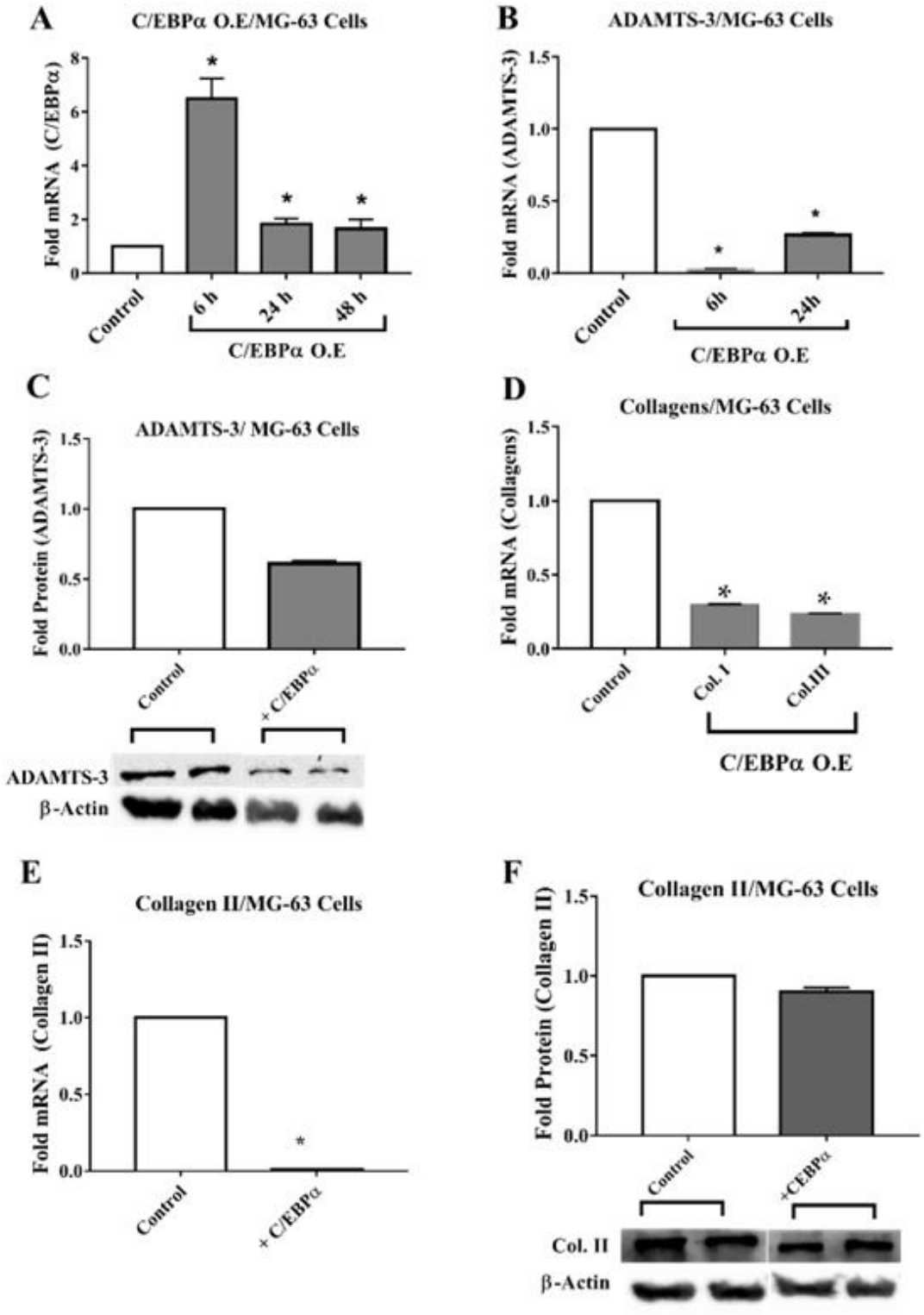

Figure 2: A C/EBPα mRNA levels after transfection of C/EBPα expression plasmid. **B-C** ADAMTS-3 mRNA and protein levels in C/EBPα over expressed MG-63 cells after 6 h of transfection. **D-E** Fibrillar collagen (type I, II, and III) mRNA levels in C/EBPα over expressed MG-63 cells. F. Type II collagen Protein expression level in C/EBPα over expressed MG-63 cells. Asterisks indicate $p \leq 0.05$.

3.2 C/EBPα negatively regulates ADAMTS-3 promoter activity in both Saos-2 and MG-63 cells

C/EBPα has a basic leucine zipper (bZIP) domain and binds the CCAAT sequence in the promoter regions of the target genes [31]. Scanning of 5' upstream of the *ADAMTS-3* gene revealed putative binding sites for the C/EBPα transcription factor and these regions were schematically indicated in Figure 3A. Truncated ADAMTS-3 promoter-reporter constructs were prepared in our previous studies and named pMET_TS-3[–1340/+40], pMET_TS-3[–879/+40], pMET_TS-3 [–576/+40] and pMET_TS-3 [–131/+40] [17]. To determine the regulatory effect of the C/EBPα on the *ADAMTS-3* promoter, luciferase-based *ADAMTS-3* promoter constructs were transiently transfected together with the C/EBPα expression plasmid in Saos-2 and MG-63 cells. Ectopic increase of the C/EBPα, decreased ADAMTS-3 promoter activity up to 0.2-fold for pMET_TS-3[–1340/+40], and approximately 0.4-fold for pMET_TS-3[–899/+40], pMET_TS-3 [–576/+40] and pMET_TS-3 [–131/+40] in Saos-2 cells. The decrease in the activities of the promoter constructs was statistically significant except for the pMET_TS-3[–879/+40]. In MG-63 cells, C/EBPα also downregulated ADAMTS-3 promoter activity with all constructs. Maximum decrease was observed with pMET_TS-3 [–576/+40] (up to 0.2-fold) in a statistically important manner.

When we compared C/EBP binding regions of the ADAMTS-3 promoter constructs, additional binding regions at the -269, -266, and -159 bp positions were determined on the pMET_TS-3 [–576/+40]. The binding of the C/EBPα to these regions was found to make an additional contribution to the reduction of ADAMTS-3 promoter activity in MG-63 cells. Similarly, the C/EBPα binding region at the -1142 bp position on the pMET_TS-3[–1340/+40] promoter fragment was found to make an additional contribution to the reduction of ADAMTS-3 promoter activity in Saos-2 cells.

In the second step, EMSA assays were performed to determine whether C/EBPα functionally binds to the ADAMTS-3 promoter. Probes [-131/-103] and [-40/-12] were designed that specific to ADAMTS-3 promoter. Three DNA-protein complex formations were observed when the biotinylated probes [-131/-103] and [-40/-12] were included in the binding reactions with Saos-2 nuclear extracts (Figure 3D and 3E; lanes 2). Competition assays were performed to determine the specificity of the complexes using the unlabelled (cold) forms of the same oligonucleotides. It was determined that while Complex1 (C1) indicates non-sequence-specific DNA-protein interaction, Complex 2 (C2) and C3 (Complex 3) were sequence-specific since they disappeared in competition assay (Figure 3D and 3E; lanes 3). When the C/EBPα unlabelled

consensus probe was included in the reactions as a competitor, C2 and C3 disappeared indicating functional binding of the C/EBPα to specific regions (Figure 3D and 3E; lanes 4).

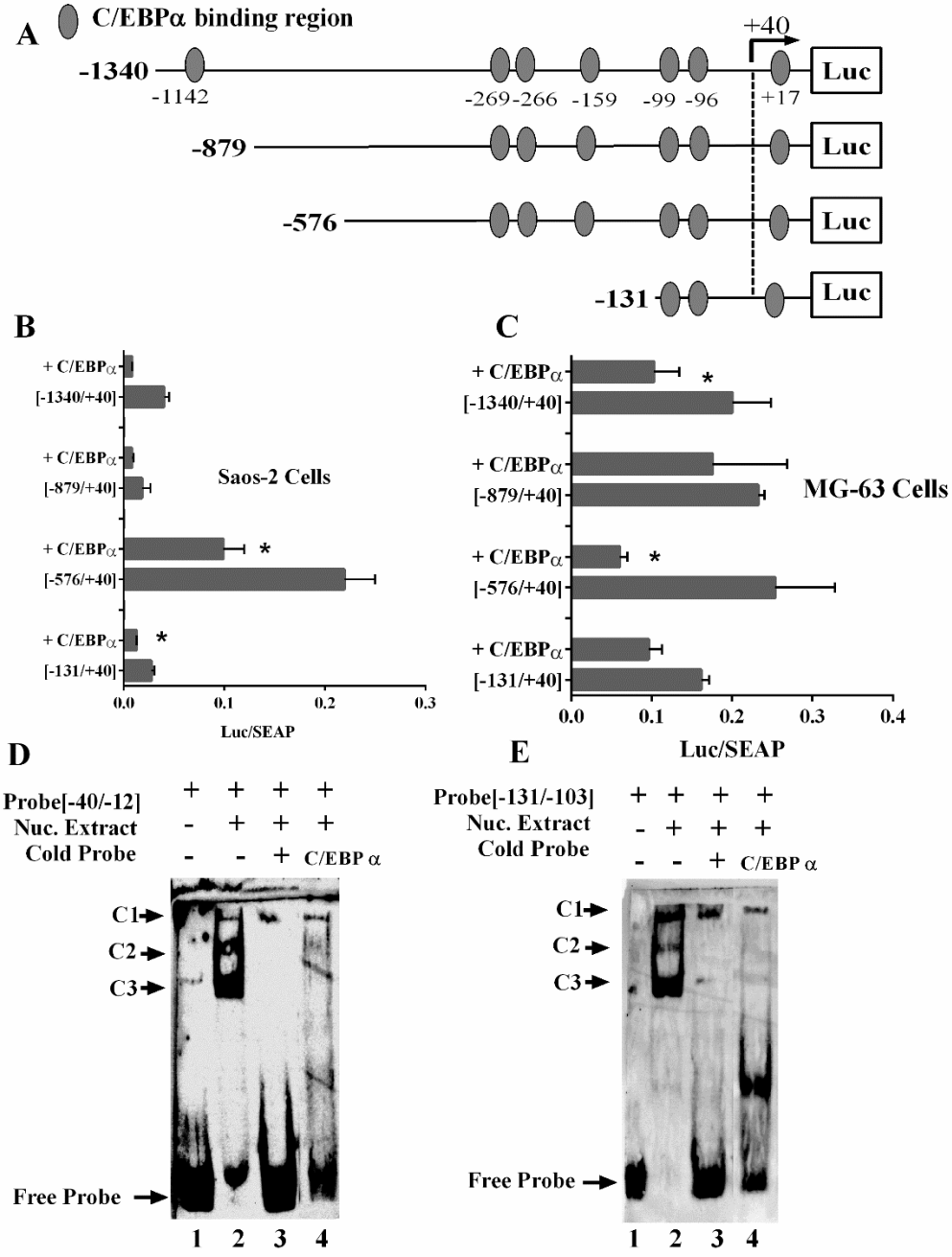

Figure 3: A. Scheme for ADAMTS-3 promoter-reporter constructs used in transfection assays. C\EBPα binding regions were indicated with a circle. **B-C.** Relative Luciferase activities of ADAMTS-3 Promoter reporter constructs in C\EBPα over-expressed Saos-2 and MG-63 cells **D-E**. *In vitro* binding analysis of C\EBPα to ADAMTS-3 promoter region by EMSA. Asterisks indicate p≤0.05.

4. Conclusion

The extracellular matrix (ECM) is an important constituent of the tumor microenvironment. In addition to the structural and biochemical supportive function of its cellular components, the ECM coordinates cellular behaviors. Aberrant changes in the ECM composition enable cells to gain malignant and metastatic characteristics. The contribution of the ECM to osteosarcoma progression and metastasis has been reported. Among the ECM components, collagen I level has been found to increase in OS patients and elevated collagen levels promoted OS progression, invasion, and migration through MMP-2 activation.

Our findings indicated that ADAMTS-3 could be transcriptionally regulated by C/EBPα transcription factor. C/EBPα significantly decreased ADAMTS-3 expression level in osteosarcoma cells. Because ADAMTS-3 can process ECM components, we suggest that changes in the ADAMTS-3 expression levels could be critical for the ECM remodeling in osteosarcoma progression. Further, we determined that decreased ADAMTS-3 levels increased collagen I and II expression levels in Saos-2 cells. So it can be suggested that C/EBPα-mediated down-regulation of ADAMTS-3 could be responsible for decreased collagen I and II expression levels in Saos-2 cells. Saos-2 and MG-63 cells have differently composed ECM [27]. While collagen I and III expression levels are high in Saos-2 cells, collagen II expression levels are quite low. In MG-63 cells, similar to Saos-2 cells, collagen I and III levels were higher than collagen II but generally collagen II and III levels were higher than those in Saos-2 cells. On the contrary, downregulation of the ADAMTS-3 in MG-63 cells resulted in a decrease in both collagen I and III levels. So, it can be concluded that maturation level, heterogeneity, and differences in the ECM composition could be responsible for the different responses of collagen expression levels to ADAMTS-3 decrease in Saos-2 and MG-63 cell models.

Acknowledgments

Saos-2 cells were kindly provided by Dr. Kenneth Wann and human C\EBPα expression plasmid was kindly provided by Dr. Dipak P. RAMJI, (Cardiff, School of Biosciences, Cardiff UK).MG-63 cells were kindly provided by Dr. Berivan ÇEÇEN, (Dokuz Eylül University, İzmir, TÜRKİYE). This work was supported by the Scientific and Technological Research Council of Turkey (TUBITAK), Project number; 114Z025.

References

[1] Porter, S., Clark, I.M., Kevorkian, L., and Edwards, D.R., *The ADAMTS metalloproteinases*, Biochemistry Journal, 386, 15-27, 2005.

[2] Jeltsch, M., Jha, S.K., Tvorogov, D., Anisimov, A., Leppänen, V.M., Holopainen, T., Kivelä, R., Ortega, S., Kärpanen, T., and Alitalo, K., *CCBE1 enhances lymphangiogenesis via A disintegrin and metalloprotease with thrombospondin motifs-3-mediated vascular endothelial growth factor-C activation*, Circulation, 129, 1962-1971, 2014.

[3] Gibson, S.V., Madzharova, E., Tan, A.C., Allen, M.D., Keller, U.A.D., Louise Jones, J., Carter, E.P., and Grose, R.P., *ADAMTS3 restricts cancer invasion in models of early breast cancer progression through enhanced fibronectin degradation*, Matrix Biology, 121, 74-89, 2023.

[4] Wang, W., Xia, X., Mao, L., and Wang, S., *The CCAAT/Enhancer-Binding Protein Family: Its Roles in MDSC Expansion and Function*, Frontiers in Immunology, 10, 1804, 2019.

[5] Lourenço, A.R., Roukens, M.G., Seinstra, D., Frederiks, C.L., Pals, C.E., Vervoort, S.J., Margarido, A.S., van Rheenen, J., and Coffer, P.J., *C/EBPa is crucial determinant of epithelial maintenance by preventing epithelial-to-mesenchymal transition*, Nature Communications, 11, 785, 2020.

[6] Miller, M., Shuman, J.D., Sebastian, T., Dauter, Z., and Johnson, P.F., *Structural basis for DNA recognition by the basic region leucine zipper transcription factor CCAAT/enhancer-binding protein alpha*, Journal of Biological Chemistry, 278, 15178-15184, 2003.

[7] Ramji, D.P., and Foka, P.*, CCAAT/enhancer-binding proteins: structure, function and regulation*, Biochemistry Journal, 365, 561-575, 2002.

[8] Pabst, T., Mueller, B.U., Zhang, P., Radomska, H.S., Narravula, S., Schnittger, S., Behre, G., Hiddemann, W., and Tenen, D.G., *Dominant-negative mutations of CEBPA, encoding CCAAT/enhancer binding protein-alpha (C/EBPalpha), in acute myeloid leukemia*, Nature Genetics, 27, 263-270, 2001.

[9] Leroy, H., Roumier, C., Huyghe, P., Biggio, V., Fenaux, P., and Preudhomme, C., *CEBPA point mutations in hematological malignancies*, Leukemia, 19, 329-334, 2005.

[10] Nerlov, C., *C/EBPalpha mutations in acute myeloid leukaemias*, Nature Reviews Cancer, 4, 394-400, 2004.

[11] Lourenço, A.R., and Coffer, P.J., *A tumor suppressor role for C/EBPα in solid tumors: more than fat and blood*, Oncogene, 36, 5221-5230, 2017.

[12] Liu, W., Xie, X., Qi, Y., and Wu, J., *Exploration of Immune-Related Gene Expression in Osteosarcoma and Association With Outcomes*, JAMA Network Open, 4, e2119132, 2021.

[13] Wei, D., Li, C., Ye, J., Xiang, F., and Liu, J., *Extracellular Collagen Mediates Osteosarcoma Progression Through an Integrin α2β1/JAK/STAT3 Signaling Pathway*, Cancer Management and Research, 12, 12067-12075, 2020.

[14] Cui, J., Dean, D., Hornicek, F.J., Chen, Z., and Duan, Z., *The role of extracelluar matrix in osteosarcoma progression and metastasis*, Journal of Experimental & Clinical Cancer Research, 39, 178, 2020.

[15] Cortini, M., Macchi, F., Reggiani, F., Vitale, E., Lipreri, M.V., Perut, F., Ciarrocchi, A., Baldini, N., and Avnet, S., *Endogenous Extracellular Matrix Regulates the Response of Osteosarcoma 3D Spheroids to Doxorubicin*, Cancers (Basel), 15, 2023.

[16] Hu, J., Lazar, A.J., Ingram, D., Wang, W.-L., Zhang, W., Jia, Z., Ragoonanan, D., Wang, J., Xia, X., Mahadeo, K., et al., *Cell membrane-anchored and tumor-targeted IL-12 T-cell therapy destroys cancer-associated fibroblasts and disrupts extracellular matrix in heterogenous osteosarcoma xenograft models*, Journal for ImmunoTherapy of Cancer, 12, e006991, 2024.

[17] Aydemir, A.T., Alper, M., and Kockar, F., *SP1-mediated downregulation of ADAMTS3 gene expression in osteosarcoma models*, Gene, 659, 1-10, 2018.

[18] Kockar, F.T., Foka, P., Hughes, T.R., Kousteni, S., and Ramji, D.P., *Analysis of the Xenopus laevis CCAAT-enhancer binding protein alpha gene promoter demonstrates species-specific differences in the mechanisms for both auto-activation and regulation by Sp1*, Nucleic Acids Research, 29, 362-372, 2001.

[19] Tokay, E., and Kockar, F., *SP1 is a transcriptional regulator of URG-4/URGCP gene in hepatocytes*, Molecular and Cellular Biochemistry, 423, 75-83, 2016.

[20] Livak, K.J., and Schmittgen, T.D., *Analysis of relative gene expression data using real-time quantitative PCR and the 2(-Delta Delta C(T)) Method*, Methods, 25, 402-408, 2001.

[21] Alper, M., and Kockar, *F., IL-6 upregulates a disintegrin and metalloproteinase with thrombospondin motifs 2 (ADAMTS-2) in human osteosarcoma cells mediated by JNK pathway*, Molecular and Cellular Biochemistry, 393, 165-175, 2014.

[22] Debelec-Butuner, B., Bostancı, A., Ozcan, F., Singin, O., Karamil, S., Aslan, M., Roggenbuck, D., and Korkmaz, K.S., *Oxidative DNA Damage-Mediated Genomic Heterogeneity Is Regulated by NKX3.1 in Prostate Cancer*, Cancer Investigation, 37, 113-126, 2019.

[23] Schneider, C.A., Rasband, W.S., and Eliceiri, K.W., *NIH Image to ImageJ: 25 years of image analysis*, Nature Methods, 9, 671-675, 2012.

[24] Hellman, L.M., and Fried, M.G., *Electrophoretic mobility shift assay (EMSA) for detecting protein–nucleic acid interactions*, Nature Protocols, 2, 1849-1861, 2007.

[25] Quandt, K., Frech, K., Karas, H., Wingender, E., and Werner, T., *MatInd and MatInspector: new fast and versatile tools for detection of consensus matches in nucleotide sequence data*, Nucleic Acids Research, 23, 4878-4884, 1995.

[26] Cartharius, K., Frech, K., Grote, K., Klocke, B., Haltmeier, M., Klingenhoff, A., Frisch, M., Bayerlein, M., and Werner, T., *MatInspector and beyond: promoter analysis based on transcription factor binding sites*, Bioinformatics, 21, 2933-2942, 2005.

[27] Pautke, C., Schieker, M., Tischer, T., Kolk, A., Neth, P., Mutschler, W., and Milz, S., *Characterization of osteosarcoma cell lines MG-63, Saos-2 and U-2 OS in comparison to human osteoblasts*, Anticancer Research, 24, 3743-3748, 2004.

[28] Alper, M., Aydemir, T., and Köçkar, F., *USF1 Suppresses Expression of Fibrillar Type I, II, and III Collagen and pNP Adamts-3 in Osteosarcoma Cells*, Molecular Biology, 55, 634-642, 2021.

[29] Oller, J., Alfranca, A., Méndez-Barbero, N., Villahoz, S., Lozano-Vidal, N., Martín-Alonso, M., Arroyo, A.G., Escolano, A., Armesilla, A.L., Campanero, M.R., et al., *C/EBPβ and Nuclear Factor of Activated T Cells Differentially Regulate Adamts-1 Induction by Stimuli Associated with Vascular Remodeling*, Molecular and Cellular Biology, 35, 3409-3422, 2015.

[30] Alper M, A.A., Köçkar F., *Expression Pattern of ADAMTS-3 (A Disintegrin and Matrix Metalloproteinase Type,1 Motif 3) in Normal and Cancer Cell Lines,* Suleyman Demirel University The Journal of Health Science, 13, 40-47, 2022.

[31] Khanna-Gupta, A., Zibello, T., Sun, H., Gaines, P., and Berliner, N., *Chromatin immunoprecipitation (ChIP) studies indicate a role for CCAAT enhancer binding proteins alpha and epsilon (C/EBP alpha and C/EBP epsilon) and CDP/cut in myeloid maturation-induced lactoferrin gene expression*, Blood, 101, 3460-3468, 2003.

Adıyaman University Journal of Science
https://dergipark.org.tr/en/pub/adyujsci
DergiPark AKADEMİK
ISSN 2147-1630
e-ISSN 2146-586X

Identification and Functional Characterization of Glutamate Decarboxylase (*GAD*) Genes in Potato (*Solanum tuberosum* L.) and Analysis of Their Expression under Drought and Salt Stress Conditions

M. Aydın AKBUDAK[1,*]

[1]Department of Agricultural Biotechnology, Akdeniz University, Antalya, 07070 Türkiye
akbudak@akdeniz.edu.tr, ORCID: 0000-0002-1397-4678

Received: 16.10.2024 **Accepted:** 12.11.2024 **Published:** 31.12.2024

Abstract

Gamma-aminobutyric acid (GABA) plays a critical role in plant stress responses and development by regulating osmotic balance, mitigating oxidative stress, and maintaining cellular homeostasis. Glutamate decarboxylase (GAD) is the first and key enzyme in the GABA biosynthesis pathway. In this study, three distinct *GAD* genes in potato—*StGAD1*, *StGAD2*, and *StGAD3*—were identified, each distributed on separate chromosomes, indicating non-redundant functional roles. Expression profiling revealed that *StGAD1* is the primary stress-responsive gene, with significant upregulation in both roots and leaves under stress, promoting GABA accumulation to enhance water-use efficiency and reduce oxidative damage. Protein-protein interaction analysis highlights functional relationships among the *GAD* proteins, with *StGAD1* and *StGAD2* sharing significant homology. The findings suggest that GABA metabolism, primarily driven by *StGAD1*, plays a more prominent role in drought tolerance than salt stress adaptation, where other regulatory mechanisms such as ion homeostasis may be more critical. This study provides foundational insights into the molecular mechanisms of *GAD*-mediated stress

* Corresponding Author DOI: 10.37094/adyujsci.1568022

responses in potatoes, offering potential avenues for enhancing crop resilience through targeted genetic strategies.

Key Words: Potato; Glutamate decarboxylase (*GAD*); Gamma-aminobutyric acid (GABA); Drought stress; Salt stress.

Patateste (*Solanum tuberosum* L.) Glutamat Dekarboksilaz (GAD) Genlerinin Tanımlanması ve Fonksiyonel Karakterizasyonu ile Kuraklık ve Tuz Stresi Koşullarında İfade Analizleri

Öz

Gamma-aminobutirik asit (GABA), bitkilerin stres tepkileri ve gelişiminde osmotik dengeyi düzenleyerek, oksidatif stresi azaltarak ve hücresel homeostazı koruyarak kritik bir rol oynar. Glutamat dekarboksilaz (GAD), GABA biyosentez yolunda yer alan ilk ve temel enzimdir. Bu çalışmayla üç farklı patates *GAD* geni—*StGAD1*, *StGAD2* ve *StGAD3*—belirlenmiştir. İfade profili analizi, *StGAD1*'in stres yanıtı veren ana gen olduğunu göstermiştir. *StGAD1* hem kök hem de yapraklarda stres altında önemli ölçüde yukarı yönlü düzenlenerek, GABA birikimini artırmakta ve su kullanım verimliliğini iyileştirmekte ve oksidatif hasarı azaltmaktadır. Protein-protein etkileşim analizleri, *GAD* proteinleri arasında işlevsel ilişkiler olduğunu ve *StGAD1* ile *StGAD2* arasında önemli ölçüde benzerlik bulunduğunu ortaya koymaktadır. Bulgular, GABA metabolizmasının, özellikle *StGAD1* tarafından yönlendirilen süreçlerin, kuraklık toleransında daha belirgin bir rol oynadığını, tuz stresi adaptasyonunda ise iyon homeostazı gibi diğer düzenleyici mekanizmaların daha kritik olabileceğini düşündürmektedir. Bu çalışma, *GAD* aracılı stres tepkilerinin moleküler mekanizmalarına ilişkin temel bilgiler sunmakta ve hedeflenmiş genetik stratejilerle bitki dayanıklılığının artırılmasına yönelik potansiyel yollar önermektedir.

Anahtar Kelimeler: Patates, Glutamat dekarboksilaz (*GAD*), Gamma-aminobutirik asit (GABA), Kuraklık stresi, Tuz stresi.

1. Introduction

Gamma-aminobutyric acid (GABA) is widely recognized as a crucial neurotransmitter in the animal nervous system, where it plays a significant role in inhibiting nerve transmission and promoting relaxation [1]. However, GABA's importance extends beyond the animal kingdom, as it is also a vital component in plants, contributing to a myriad of physiological and biochemical

processes [2]. The study of GABA in plants has garnered increasing attention in recent years, revealing its multifaceted roles in plant growth, development, and stress response mechanisms [3].

In plants, GABA is synthesized from the amino acid glutamate through the action of the enzyme glutamate decarboxylase (GAD) [4]. GAD is encoded by a family of GAD genes, which are highly conserved and widely distributed across different plant species [5]. These genes are crucial for the regulation of GABA synthesis, and their expression is tightly controlled by various developmental cues and environmental stimuli [6]. The GAD enzyme catalyzes the irreversible decarboxylation of glutamate to GABA, a key step in the GABA shunt pathway [7]. This pathway serves as an alternative metabolic route that bypasses two steps of the tricarboxylic acid (TCA) cycle, aiding in maintaining the balance of carbon and nitrogen within plant cells and playing a pivotal role in regulating the cytosolic pH [3]. This pH regulation is crucial for various cellular processes, including enzyme activities and metabolic reactions [8]. Glutamate decarboxylase (*GAD*) is an essential enzyme in plants, responsible for catalyzing the conversion of glutamate to γ-aminobutyric acid (GABA), a non-proteinogenic amino acid with key roles in both metabolism and signaling. The GABA shunt, comprising *GAD*, GABA transaminase (*GABA-T*), and succinic semialdehyde dehydrogenase (*SSADH*), links glutamate metabolism to the tricarboxylic acid (TCA) cycle, enabling plants to manage stress and maintain cellular homeostasis [9-10]. The GAD gene family is highly conserved across plant species, with Arabidopsis having five *GAD* isoforms (*GAD1–GAD5*). These isoforms are differentially expressed, with GAD1 playing a crucial role in roots, where it helps maintain GABA levels under normal and stressful conditions. Studies have shown that GAD1 is particularly important during heat stress, where its activation ensures a rapid increase in GABA levels, protecting roots from damage caused by high temperatures [11]. Meanwhile, *GAD2* is more ubiquitously expressed and plays a broader role in responding to stresses in multiple tissues [10-11].

Regulation of GAD enzymes involve calcium/calmodulin (Ca^{2+}/CaM) signaling, a critical pathway that allows plants to sense and respond to environmental stimuli. GAD activity is enhanced in the presence of Ca^{2+}, which binds to the CaM-binding domain in GAD, triggering GABA synthesis in response to stress [12-13]. This regulation is particularly important under salt stress, where increased GABA levels help maintain ion homeostasis and protect against oxidative damage caused by reactive oxygen species (ROS) [14-15].

Drought is one of the most critical environmental stressors affecting plants. GABA accumulation during drought stress helps regulate stomatal closure, reducing water loss through transpiration. In Arabidopsis, *GAD1* and *GAD2* mutants show increased susceptibility to drought

due to their inability to produce sufficient GABA, which is essential for maintaining ion homeostasis and activating antioxidant defense mechanisms [15]. Moreover, exogenous GABA application has been shown to improve drought tolerance in several plant species, enhancing photosynthesis and reducing oxidative damage by increasing the activity of enzymes such as superoxide dismutase (SOD) and catalase (CAT) [13].

GABA also plays a key role in salt stress tolerance. High salinity disrupts cellular ion balance, leading to toxic levels of sodium ions (Na^+) in plant tissues. GABA helps mitigate this by modulating ion transport through aluminum-activated malate transporters (ALMTs), reducing Na^+ uptake and preventing ion toxicity [14-15]. In Arabidopsis, GAD4 is specifically upregulated during salt stress, further underscoring the role of GAD genes in stress adaptation [15]. GABA also contributes to the stabilization of cellular osmotic pressure, which is crucial for plant survival in saline environments [13]. Heat stress induces a rapid accumulation of GABA, particularly in roots, where GAD1 plays a dominant role [11]. GABA production under heat stress helps mitigate the effects of high temperatures by maintaining cellular pH and reducing ROS levels. Additionally, GABA functions as an osmoprotectant, stabilizing proteins and membranes, thus enabling plants to survive prolonged heat exposure [13]. This is evident in crops like rice, where exogenous GABA application enhances heat tolerance by improving leaf turgor, reducing oxidative damage, and activating heat shock proteins [15].

In addition to abiotic stress, GABA is involved in biotic stress resistance. During pathogen infection, such as that caused by *Pseudomonas syringae*, GABA enhances plant immunity by modulating defense-related signaling pathways [16]. In Agrobacterium tumefaciens-mediated gene transformation, GABA inhibits the conjugation of the Ti plasmid, reducing the severity of crown gall disease in plants [13].

GABA also has a significant role in plant development. It regulates pollen tube growth by forming concentration gradients that guide the pollen tube toward the ovule during fertilization [13]. Furthermore, GABA modulates root growth by influencing hormone signaling pathways, including those involving abscisic acid (ABA) and ethylene, which are key regulators of seed germination and root elongation [13-15]. This multifaceted role of GABA in development underscores its importance beyond stress tolerance.

Heavy metal pollution poses a significant threat to plant growth and crop yield. GABA plays a role in mitigating heavy metal toxicity by activating antioxidant enzymes and modulating metal transport. For example, under cadmium (Cd) stress, GABA accumulation helps protect plants by enhancing Cd sequestration and reducing oxidative stress [15]. Studies on soybean and

rice have shown that GABA levels rise in response to zinc (Zn) and copper (Cu) stress, further highlighting its role in heavy metal detoxification [13]. Interestingly, while GABA typically increases under heavy metal stress, its accumulation must be tightly regulated. Excessive GABA levels can sometimes lead to toxicity, as seen in some plants subjected to extreme concentrations of metals like arsenic (As), where high GABA levels may exacerbate stress [13].

The expression of *GAD* genes is regulated by various transcription factors in response to environmental stimuli. For instance, under salt stress, WRKY and MYB transcription factors bind to the promoter regions of *GAD4*, enhancing its expression [15]. Similarly, STOP1 and WRKY40, which are known repressors of *GAD* expression, modulate GABA levels under stress, ensuring that GABA accumulation is appropriately regulated during abiotic stress [15]. This intricate transcriptional regulation allows plants to fine-tune GABA production in response to fluctuating environmental conditions.

Overall, GAD-mediated GABA production is a critical mechanism for stress adaptation in plants. By modulating ion fluxes, scavenging ROS, and maintaining cytosolic pH, GABA plays a multifaceted role in enhancing plant tolerance to abiotic stresses such as drought, salinity, and heat [13-15]. Additionally, GABA is involved in biotic stress responses and developmental processes such as pollen tube guidance and root elongation [13]. As a versatile metabolite and signaling molecule, GABA enables plants to survive and thrive in challenging environments. Continued research into the regulatory networks controlling GABA synthesis and signaling could offer new avenues for improving crop resilience in the face of climate change and environmental stressors [15].

2. Material and Methods

2.1. Chromosomal distribution and phylogenetic analysis

The locations of the *StGAD* genes on each chromosome were obtained from the potato genome database (Ensembl Plants; https://plants.ensembl.org/index.html), and their chromosomal distribution was illustrated using the Mapgene2chrom 2.1 (MG2C v2.1) online tool (http://mg2c.iask.in/mg2c_v2.1/) [17-18]. The protein sequences were obtained from Phytozome (https://phytozome-next.jgi.doe.gov) and analyzed to construct a phylogram using the Clustal Omega web tool (https://www.ebi.ac.uk/jdispatcher/msa/clustalo).

2.2. 3D modeling, subcellular localization prediction and protein–protein interactions

3D modeling of StGAD proteins was conducted using previously identified sequences, with support provided by the UniProt database [19]. Predictions of subcellular localization were generated through the WoLF PSORT database [20]. To investigate both the physical and functional interactions among StGAD proteins, the STRING database was utilized [21].

2.3. Plant materials and stress treatments

In this study, the potato (*Solanum tuberosum*) cultivar 'Agria' was utilized. Plantlets were initially sub-cultured on MS-0 medium, which contained 4.4 g/L MS salts, 3% sucrose, and 0.7% agar, with the pH adjusted to 5.7. The cultures were maintained in a growth chamber set at 22°C with 70% relative humidity, under a 16-hour light / 8-hour dark photoperiod. After five weeks, the plantlets were transferred to hydroponic systems filled with Hoagland's solution (pH 5.8). Following a two-day acclimation period, the nutrient solution was replaced with a fresh Hoagland's solution containing either 25% polyethylene glycol (PEG-6000) to induce drought stress, or 200 mM sodium chloride (NaCl) for salt stress. Control plants received only refreshed Hoagland's solution. After 24 hours of exposure to drought or salt stress, leaves and roots were harvested for RNA extraction.

2.4. RNA isolation and gene expression analysis

RNA was extracted from leaf and root tissues using the RNA Plant Mini Kit (Qiagen, USA) according to the manufacturer's protocol. To eliminate potential genomic DNA contamination, the RNA samples were treated with RQ1 RNase-Free DNase (Promega, USA). The integrity of the RNA and the absence of DNA contamination were confirmed by gel electrophoresis. RNA concentrations were quantified using a Qubit fluorometer (Invitrogen, USA). Subsequent RT-qPCR analyses were conducted on a CFX384 Real-Time PCR System (Bio-Rad, USA). For each sample, 10 ng of RNA was used in the reaction, employing the Luna Universal One-Step RT-qPCR Kit (NEB, USA). Gene sequences of *StGAD* genes were retrieved from the Phytozome database (Phytozome v13, https://phytozome-next.jgi.doe.gov/), and primers were designed using the Primer3 Input web tool (https://primer3.ut.ee/). Gene expression was quantified using specific forward and reverse primers (Table 1). The *StSec3* gene served as the internal reference control for normalization [22].

Table 1: Primers used for RT-qPCR analysis of *StGAD* genes

Genes	Phytozome ID	Forward primer sequences	Reverse primer sequences
StGAD1	PGSC0003DMG400031042	ATGGGATTTCCGTTTGCCT	ATATCACCCAACCGACACCAG
StGAD2	PGSC0003DMG400013331	TAGCGTCGGAAAGTGACATG	CAAGTGGTGCATTAAATAAGT
StGAD3	PGSC0003DMG400022764	CTTCCTCTGAGTCTGATGAT	AAGATCATGCAAGAGTTTG
StSec3	PGSC0003DMG402015451	GCTTGCACACGCCATATCAAT	TGGATTTTACCACCTTCCGCA

3. Results and discussion

3.1. Chromosomal distribution of *StGAD* genes

Queries performed in the Phytozome and Ensembl Plants databases identified three distinct members of GAD gene family in *S. tuberosum*. The chromosomal distribution of GAD genes in the potato genome reveals that each gene is located on a distinct chromosome (Fig. 1). This non-redundant, dispersed distribution suggests that each *GAD* gene is positioned to function independently, potentially reducing overlaps in their roles and regulatory mechanisms.

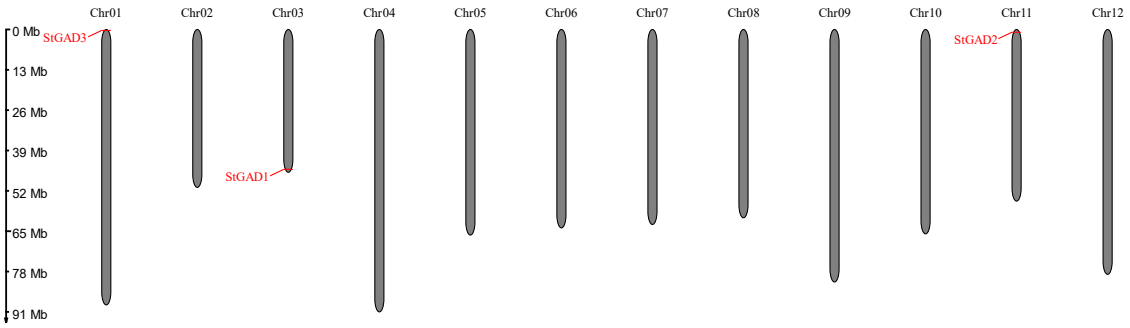

Figure 1: Chromosomal locations of *StGAD* genes in the potato genome, visualized using the MG2C tool. Chromosome numbers are indicated at the top of each chromosome, and the genomic scale in megabases (Mb) is provided on the left.

The GAD genes are strategically placed across the genome. This spatial organization may indicate that each gene contributes uniquely to the plant's physiological processes, particularly in stress-related responses [23-24]. The independent localization of GAD genes across different chromosomes could reflect the plant's adaptive strategy to ensure that multiple regions of the genome are involved in regulating responses to environmental stressors such as drought, salinity, and low temperatures [25-26]. The absence of gene duplication within individual chromosomes further suggests that each GAD gene has a specific role, without functional redundancy within the same chromosomal context. This distribution pattern highlights the importance of a diversified

regulatory mechanism across the genome, providing a genetic framework that allows specialized and flexible responses to environmental challenges [13-27].

3.2. Phylogenetic and protein – protein interaction (PPI) analysis of StGAD proteins

The phylogenetic tree of *StGAD* genes illustrates a likely gene duplication process (Fig. 2). *StGAD2* and *StGAD3* seem to have recently diverged and remain closely related, possibly retaining similar or overlapping functions. *StGAD1*, as the most divergent gene, might have evolved under different evolutionary pressures, taking on specialized or stress-related functions. These evolutionary patterns reflect the complex adaptive strategies employed by plants, where gene duplication allows for functional diversification and enhanced resilience to environmental changes [28-30].

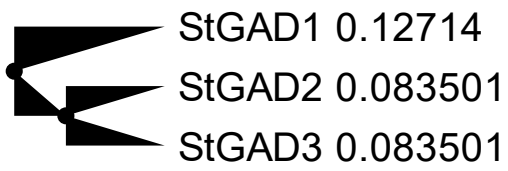

Figure 2: Phylogram of *StGAD* genes illustrating evolutionary divergence with branch lengths indicating genetic distances.

Protein–protein interactions (PPIs) are essential for coordinating numerous biological processes, including cellular regulation, metabolic pathways, and intercellular communication. Alterations or disruptions in these interactions can result in profound physiological and pathological consequences, highlighting their importance in maintaining homeostasis [31]. STRING Analysis showed that all three *StGAD* genes belong to the group II decarboxylase family and function as glutamate decarboxylase. StGAD1 and StGAD2 have 502 aa while StGAD3 has 497 aa. Despite the sequence homology between StGAD2 and StGAD3 (Fig), StGAD1 and StGAD2 genes share more protein homology and co-occurred based on STRING analysis (Fig. 3). This network highlights potential functional relationships and evolutionary conservation among the GAD proteins

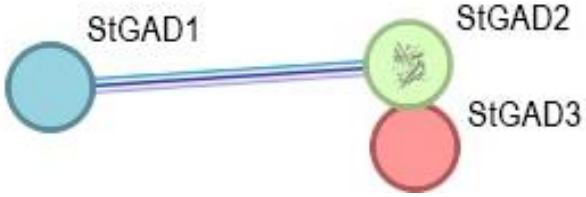

Figure 3: Protein-Protein Interaction (PPI) Network of GAD proteins in *S. tuberosum*: The connections between the nodes represent protein homology, gene co-occurrence, and interactions documented in curated databases.

3.3. 3D modelling and subcellular localization of StGAD proteins

The three StGAD proteins—StGAD1, StGAD2, and StGAD3—share a conserved globular core composed of α-helices, suggesting that all three proteins perform related enzymatic or structural roles. However, their terminal regions exhibit distinct structural differences, influencing their specific subcellular localization and functions (Fig. 4).

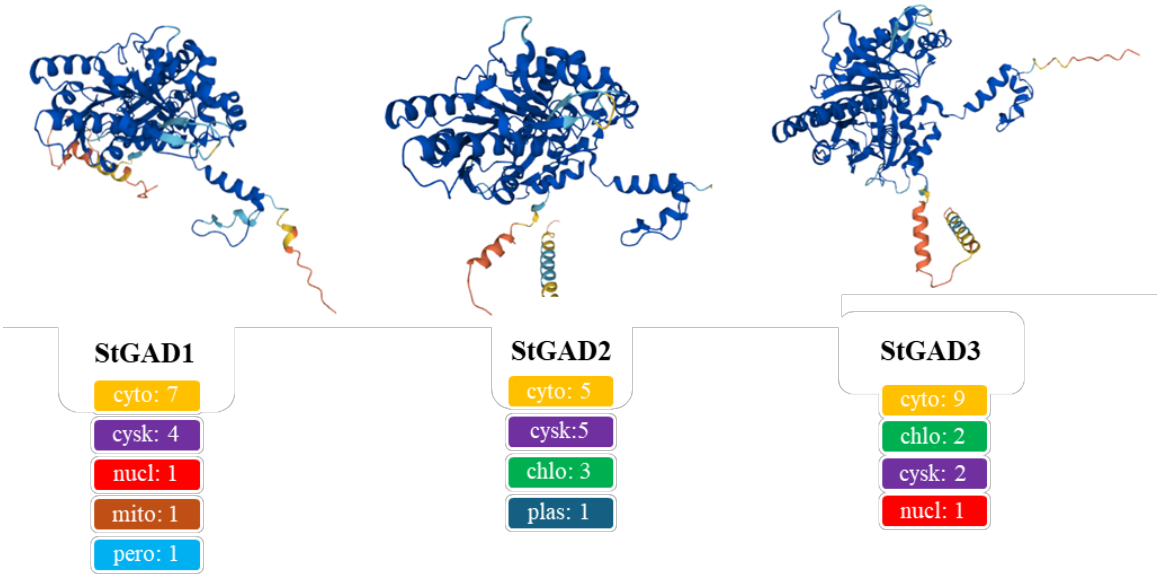

Figure 4: 3D Homology modeling and subcellular localization of StGAD proteins (cyto: Cytoplasm, cysk: Cytoskeleton, nucl: Nucleus, mito: Mitochondria, pero: Peroxisome, chlo: Chloroplast, plas: Plasma Membrane).

StGAD1 is localized to the cytoplasm and cytoskeleton, which aligns with its compact structure and short yellow helix. This design indicates that it functions in metabolic activities or acts as a structural scaffold associated with the cytoskeleton, maintaining stability and requiring minimal conformational flexibility. StGAD2 is predicted to localize to the mitochondria and peroxisome, as indicated by its extended red helix, which suggests a role in membrane interaction. This feature implies that StGAD2 may participate in energy metabolism within mitochondria or help with molecular transport in peroxisomes.

StGAD3 is found in the nucleus and plasma membrane, as highlighted by its flexible long coil and outward-extending red helix. This structural flexibility suggests that StGAD3 is involved in dynamic processes, such as nuclear signaling, gene regulation, or transport across membranes. Its design aligns with the need for proteins that interact with transport receptors or regulate membrane-bound activities.

Overall, StGAD1, StGAD2, and StGAD3 share a conserved core structure that supports related functions, but their variable terminal regions enable them to adapt to specific subcellular

compartments. StGAD1 operates in the cytoplasm and cytoskeleton, StGAD2 localizes to mitochondria and peroxisomes, and StGAD3 functions within the nucleus and plasma membrane. These structural differences empower them to perform specialized roles such as scaffolding, energy metabolism, molecular transport, and signaling, according to the demands of their respective environments.

3.4. Expression Profiles of *StGAD* Genes Under Drought and Salt Stresses

The expression analysis reveals distinct responses of the *StGAD1* and *StGAD2* genes to drought and salt stress in both root and leaf tissues. In root tissues, *StGAD1* was upregulated under drought stress, indicating that it plays an essential role in drought adaptation. This result is consistent with previous studies, which have shown that *GAD* genes contribute to stress tolerance by modulating γ-aminobutyric acid (GABA) accumulation, helping to maintain osmotic balance and mitigate oxidative stress [4]. Under the same drought conditions, *StGAD2* was significantly downregulated, with a negative value of -1.27. This repression suggests that *StGAD2* is not involved in drought response, while *StGAD1* functions as the primary gene regulating the root's metabolic adjustments under drought stress.

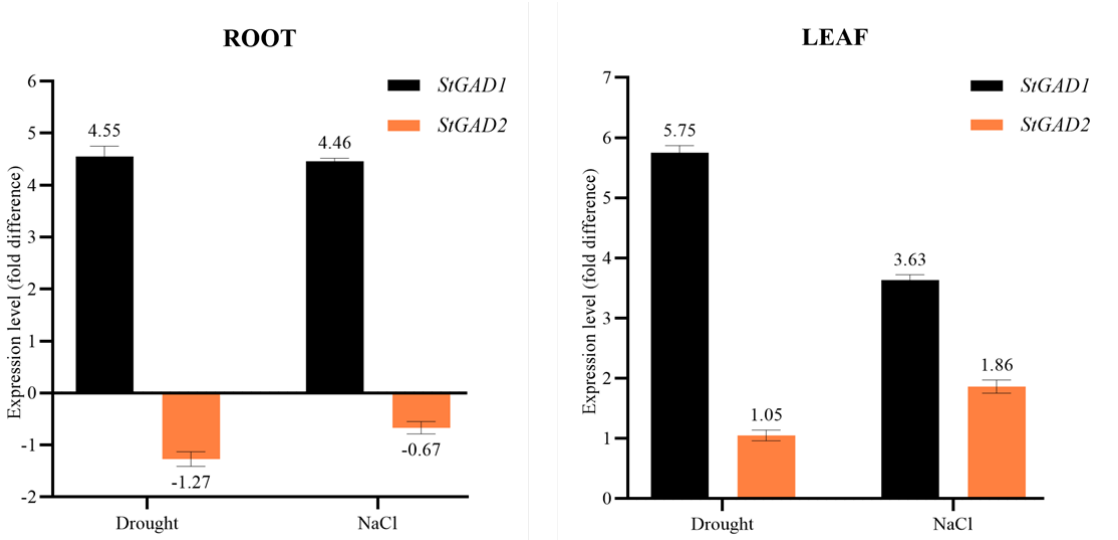

Figure 5: Expression profiles of *StGAD* genes in potato roots and leaves under drought and salt stress, assessed via RT-qPCR. Bars above the x-axis indicate upregulation, while values are presented on a $\log_2$ scale to clearly reflect the extent of both upregulation and downregulation. Error bars represent the standard deviation of the mean (SDOM; n = 3).

In leaf tissues, *StGAD1* expression was strongly upregulated, with a value of 5.75 under drought stress, confirming its prominent role in leaf stress adaptation. This upregulation aligns with reports that enhanced GAD activity promotes GABA accumulation, which serves as a signaling molecule to regulate stomatal closure and maintain water balance [32]. The data in the

present study confirm that *StGAD1* plays a critical role in maintaining cellular homeostasis under drought conditions, likely by preventing oxidative damage and supporting osmotic balance in leaf tissues. However, *StGAD2* did not exhibit a significant increase in expression under either drought or salt stress, indicating that this gene is not actively involved in the leaf's response to these abiotic stresses.

These findings reveal that the expression of *StGAD1* and *StGAD2* is regulated in a tissue-specific manner under drought and salt stress, with *StGAD1* serving as the primary stress-responsive gene in both roots and leaves. *StGAD1*'s upregulation under drought conditions underscores its role in stress adaptation, particularly through the GABA pathway, which supports water-use efficiency and oxidative stress management. In contrast, the downregulation of *StGAD2* in roots suggests that its function is not essential during drought, reflecting a shift in metabolic priorities. Furthermore, the lack of significant expression of *StGAD2* in leaves under stress conditions indicates that its involvement in abiotic stress response is limited compared to *StGAD1*.

The differential expression patterns observed in this study are consistent with previous findings. Li et al. (2016) [32] have reported that GAD genes are involved in regulating GABA signaling under osmotic stress, while Shelp et al. (2012) [4] demonstrated that GABA plays a crucial role in alleviating oxidative stress in plants. The upregulation of *StGAD1* in both roots and leaves during drought suggests a conserved function for this gene in stress adaptation, while the suppression of StGAD2 points to a functional divergence between the two isoforms, with *StGAD1* being the dominant regulator in the glutamate-GABA pathway during abiotic stress.

Notably, no expression of *StGAD3* was detected in either leaves or roots under both drought and salt stress. This absence suggests that *StGAD3* may not play a role in these specific environmental conditions. It is possible that *StGAD3* could be involved in other stress types, developmental stages, or tissues not covered in this study. Alternatively, it could be that the gene is expressed only under specific hormonal signals or environmental triggers, such as biotic stress or nutrient imbalances, which were not evaluated here [1]. This finding underscores the importance of further research to explore the broader functions of *StGAD3* and its role in plant development and stress responses under different conditions.

These findings highlight the distinct roles of *StGAD1* and *StGAD2* in stress response, with *StGAD1* emerging as a key player in drought tolerance, particularly in leaves, where it drives GABA synthesis and modulates cellular responses. *StGAD2* provides complementary support, maintaining basal GABA levels across both drought and salt conditions.

These results emphasize the stress- and tissue-specific regulation of GABA-related genes in plants and suggest that GABA metabolism is more relevant for drought adaptation than salinity tolerance in potatoes. Future studies should investigate the interaction between GABA metabolism and other physiological pathways to better understand the crosstalk between drought and salinity responses. Additionally, the role of *StGAD3* under different conditions or in other tissues should be explored to determine its potential involvement in stress adaptation beyond those examined in this study.

4. Conclusion

This study investigates the identification and functional roles of *GAD* genes in potato in response to drought and salt stress. *StGAD1* plays a key role in drought adaptation by promoting GABA accumulation, which regulates osmotic balance, reduces oxidative stress, and improves water-use efficiency. In contrast, *StGAD2* contributes minimally, maintaining baseline GABA levels but not actively participating under stress. No expression of *StGAD3* was observed, suggesting it may function under different conditions or developmental stages.

The chromosomal distribution shows each *GAD* gene located on distinct chromosomes, suggesting unique functions. Phylogenetic analysis reveals that *StGAD1* has evolved specialized stress-related roles, while *StGAD2* and *StGAD3* share closer evolutionary origins. Subcellular localization predictions indicate that *StGAD1* operates in the cytoplasm and cytoskeleton, *StGAD2* in mitochondria and peroxisomes, and *StGAD3* in the nucleus and plasma membrane. Protein-protein interaction (PPI) analysis shows functional relationships among the *GAD* proteins, particularly between *StGAD1* and *StGAD2*.

This research concludes that GABA metabolism, driven by *StGAD1*, is more relevant for drought adaptation than for salt tolerance, where other pathways like ion regulation take precedence. Future studies are needed to explore the role of *StGAD3* under different conditions and the interactions between GABA and other physiological pathways. These insights are valuable for improving crop resilience to environmental stressors through targeted genetic interventions.

Acknowledgments

MAA gratefully acknowledges the financial support received through the Fulbright Visiting Scholar Grant awarded by the Turkish Fulbright Commission.

References

[1] Bouché, N., Fromm, H., *GABA in plants: Just a metabolite?,* Trends in Plant Science*, 9*(3), 110-115, 2004.

[2] Kinnersley, A. M., Turano, F. J., *Gamma-aminobutyric acid (GABA) and plant responses to stress,* Critical Reviews in Plant Sciences*,* 19(6), 479-509, 2000.

[3] Fait, A., Fromm, H., Walter, D., Galili, G., Fernie, A. R., *Highway or byway: The metabolic role of the GABA shunt in plants,* Trends in Plant Science, 13(1), 14-19, 2008.

[4] Shelp, B. J., Bown, A. W., Zarei, A., *The GABA shunt in plants: A tale of many hats,* Trends in Plant Science, 17(11), 540-548, 2012.

[5] Baum, G., Lev-Yadun, S., Fridmann, Y., Arazi, T., Katsnelson, H., Fromm, H., *Calmodulin binding to glutamate decarboxylase is required for its activation by calcium and its inhibition by autophosphorylation,* The Journal of Biological Chemistry, 271(16), 9226-9231, 1996.

[6] Michaeli, S., Fromm, H., *Closing the loop on the GABA shunt in plants: Are GABA metabolism and signaling entwined?,* Frontiers in Plant Science, 6, 419, 2015.

[7] Bown, A. W., Shelp, B. J., *The metabolism and functions of gamma-aminobutyric acid,* Plant Physiology, 115(1), 1-5, 1997.

[8] Bown, A. W., Macgregor, K. B., Shelp, B. J., *Gamma-aminobutyric acid (GABA) limits the accumulation of reactive oxygen intermediates in plant tissues,* Plant Physiology, 141(3), 915-921, 2006.

[9] D'Mello, J. P. F. (Ed.), *Amino acids in higher plants.* CABI, 2015.

[10] Zik, M., Arazi, T., Snedden, W. A., Fromm, H., *Two isoforms of glutamate decarboxylase in Arabidopsis are regulated by calcium/calmodulin and differ in organ distribution*, Plant molecular biology, 37, 967-975, 1998.

[11] Bouché, N., Fait, A., Zik, M., Fromm, H., *The root-specific glutamate decarboxylase (GAD1) is essential for sustaining GABA levels in Arabidopsis*, Plant Molecular Biology, 55, 315-325, 2004.

[12] Turano, F. J., Fang, T. K., *Characterization of two glutamate decarboxylase cDNA clones from Arabidopsis*, Plant Physiology, 117(4), 1411-1421, 1998.

[13] Li, L., Dou, N., Zhang, H., Wu, C., *The versatile GABA in plants,* Plant Signaling & Behavior, 16(3), 1862565, 2021.

[14] Ramesh, S. A., Tyerman, S. D., Gilliham, M., Xu, B., *γ-Aminobutyric acid (GABA) signalling in plants*, Cellular and Molecular Life Sciences, 74, 1577-1603, 2017.

[15] Zarei, A., Chiu, G. Z., Yu, G., Trobacher, C. P., Shelp, B. J., *Salinity-regulated expression of genes involved in GABA metabolism and signaling,* Botany, 95(6), 621-627, 2017.

[16] Deng, X., Xu, X., Liu, Y., Zhang, Y., Yang, L., Zhang, S., Xu, J., *Induction of γ-aminobutyric acid plays a positive role in Arabidopsis resistance against Pseudomonas syringae,* Journal of Integrative Plant Biology, 62(11), 1797-1812, 2020.

[17] Chao, J. T., Kong, Y. Z., Wang, Q., Sun, Y. H., Gong, D. P., Lv, J., Liu, G. S., *MapGene2Chrom, a tool to draw gene physical map based on Perl and SVG languages,* Yi Chuan = Hereditas, 37(1), 91-97, 2015.

[18] Chao, J., Li, Z., Sun, Y., Aluko, O. O., Wu, X., Wang, Q., Liu, G., *MG2C: A user-friendly online tool for drawing genetic maps,* Molecular Horticulture, 1, 1-4, 2021.

[19] UniProt Consortium, T., *UniProt: The universal protein knowledgebase,* Nucleic Acids Research, 46(5), 2699-2699, 2018.

[20] Horton, P., Park, K. J., Obayashi, T., Fujita, N., Harada, H., Adams-Collier, C. J., Nakai, K., *WoLF PSORT: Protein localization predictor,* Nucleic Acids Research, 35(2), W585-W587, 2007.

[21] Szklarczyk, D., Kirsch, R., Koutrouli, M., Nastou, K., Mehryary, F., Hachilif, R., ... & Von Mering, C., *The STRING database in 2023: Protein–protein association networks and functional enrichment analyses for any sequenced genome of interest,* Nucleic Acids Research, 51(D1), D638-D646, 2023.

[22] Tang, X., Zhang, N., Si, H., Calderón-Urrea, A., *Selection and validation of reference genes for RT-qPCR analysis in potato under abiotic stress,* Plant Methods, 13, 1–8, 2017.

[23] Kabała, K., Janicka, M., *Relationship between the GABA pathway and signaling of other regulatory molecules,* International Journal of Molecular Sciences, 25(19), 10749, 2024.

[24] Guo, Z., Gong, J., Luo, S., Zuo, Y., Shen, Y. *Role of gamma-aminobutyric acid in plant defense response,* Metabolites, 13(6), 741, 2023.

[25] Seifikalhor, M., Aliniaeifard, S., Hassani, B., Niknam, V., Lastochkina, O., *Diverse role of γ-aminobutyric acid in dynamic plant cell responses,* Plant Cell Reports, 38, 847-867, 2019.

[26] Yuan, D., Wu, X., Gong, B., Huo, R., Zhao, L., Li, J., ... & Gao, H., *GABA metabolism, transport and their roles and mechanisms in the regulation of abiotic stress resistance in plants,* Metabolites, 13(3), 347, 2023.

[27] Dabravolski, S. A., Isayenkov, S. V., *The role of the γ-aminobutyric acid (GABA) in plant salt stress tolerance,* Horticulturae*, 9*(2), 230, 2023.

[28] Agrawal, S., *Exploring genome triplication as a driver of plant diversification and adaptive evolution,* International Journal of Statistics and Applied Mathematics, SP-8(6), 594-598, 2023.

[29] Imran, A., Ghosh, A., *Evolutionary expansion, functional diversification, and transcript profiling of plant glutathione peroxidases,* Plant Science, 111991, 2024.

[30] Van de Peer, Y., Mizrachi, E., Marchal, K., *The evolutionary significance of polyploidy,* Nature Reviews Genetics, 18(7), 411-424, 2017.

[31] Chakrabarty, S., Wang, S., Roychowdhury, T., Ginsberg, S. D., Chiosis, G., *Introducing dysfunctional Protein-Protein Interactome (dfPPI)–A platform for systems-level protein-protein interaction (PPI) dysfunction investigation in disease,* Current Opinion in Structural Biology, 88, 102886, 2024.

[32] Li, Z., Yu, J., Peng, Y., Huang, B., *Metabolic pathways regulated by γ-aminobutyric acid contributing to drought tolerance in plants,* Plant Cell Reports, 35(10), 2105-2116, 2016.

Adıyaman University Journal of Science
https://dergipark.org.tr/en/pub/adyujsci
DergiPark AKADEMİK
ISSN 2147-1630
e-ISSN 2146-586X

DPPH Antioxidant Assays, Molecular Docking Studies and ADMET Predictions of Some 4-Chloromethyl Substituted Coumarin Compounds

Gamze ÖZGÜL ARTUÇ [1,*]

[1]*Department of Chemical Engineering, Faculty of Engineering and Natural Science, Istanbul Health and Technology University, İstanbul, Türkiye*
gamze.ozgul@istun.edu.tr, ORCID: 0000-0002-7869-1281

Received: 23.10.2024 **Accepted:** 25.12.2024 **Published:** 31.12.2024

Abstract

Coumarins and their derivatives, which are secondary metobalites of many plants, are heterocyclic bioactive compounds with various biological properties. Due to these properties, the synthesis of various derivatives and the investigation of their properties are of great interest. 4-(chloromethyl)-7-hydroxy-5-methyl coumarin (**1**), 4-(chloromethyl)-7-hydroxy-8-methyl coumarin (**2**), and 4-(chloromethyl)-7-hydroxy coumarin (**3**) synthesized by Pechmann condensation reaction and characterized by FT-IR, NMR spectral data and elemental analysis data. The antioxidant capacities of the compounds were investigated by difhenyl-2-picrylhydrazyl (DPPH) radical scavenger assay using the UV-Vis spectrophotometric method. The interactions of the compounds with ROS-producing cytochrome P-450, xanthine oxidase, lipooxygenase, monoamine oxidase, and nicotinamide adenine dinucleotide phosphate oxidase enzymes were investigated by molecular docking. All compounds interacted well in the active binding site of most of the enzymes (about 6-8 kcal/mol). The pharmacokinetic and toxicokinetic properties of the compounds, indicating their potential as drug candidates, were analyzed by

* Corresponding Author
DOI: 10.37094/adyujsci.1572580

ADMET predictions. All the results obtained showed that the compounds have properties that could be drug candidates.

Keywords: Coumarin; Antioxidant; Molecular docking; ADMET.

Bazı 4-klorometil Substitüe Kumarin Bileşiklerinin DPPH Antioksidan Deneyleri, Moleküler Kenetlenme Çalışmaları ve ADMET Tahminleri

Öz

Birçok bitkinin ikincil metobalitleri olan kumarinler ve türevleri, çeşitli biyolojik özelliklere sahip heterosiklik biyoaktif bileşiklerdir. Bu özelliklerinden dolayı çeşitli türevlerinin sentezi ve özelliklerinin araştırılması oldukça ilgi çekicidir. 4-(klorometil)-7-hidroksi-5-metil kumarin (**1**), 4-(klorometil)-7-histoksi-8-metil kumarin (**2**) ve 4-(klorometil)-7-hidroksi kumarin (**3**) Pechmann kondenzasyon reaksiyonu ile sentezlenmiş ve FT-IR, NMR spektrumları ve elementel analiz ile karakterize edilmiştir. Bileşiklerin antioksidant kapasiteleri UV-Vis spektrofotometrik yöntemi kullanılarak difenil-2-pikrilhidrazil (DPPH) radikal süpürme deneyleri ile araştırılmıştır. Moleküler yerleştirme ile bileşiklerin, ROS üreten enzimler sitokrom P-450, ksantin oksidaz, lipooksijenaz, monoamin oksidaz ve nikotinamid adenin dinükleotit fosfat oksidaz enzimleri ile etkileşimleri incelenmiştir. Tüm bileşikler enzimlerin aktif bölgeleriyle iyi etkileşim göstermiştir (about 6-8 kcal/mol). Bileşiklerin farmakokinetik ve toksikokinetik özellikleri, ilaç adayı olabilme potansiyelleri ADMET tahminleri yapılarak incelenmiştir. Tüm sonuçlar bileşiklerin, ilaç adayı olma potansiyellerine sahip özelliklere sahip bileşikler olduklarını göstermiştir.

Anahtar Kelimeler: Kumarin; Antioksidan; Moleküler yerleştirme; ADMET.

1. Introduction

Coumarins and their derivatives are heterocyclic bioactive compounds that are secondary metabolites of plants [1, 2]. They are among the essential compounds of organic chemistry due to their biological activities. Coumarin and its derivatives have various biological activities such as anticancer, antifungal, antibacterial, antioxidant, anticoagulant, antiviral, anti-inflammatory, etc [3-9]. The coumarin ring can be synthesized by various methods such as Pechmann, Perkin, etc, and its derivatives can be prepared by substituting different groups at multiple positions. New

derivatives with improved biological activity have been obtained by substituting the coumarin ring from various positions with various groups [10-17].

ROS (Reactive oxygen species) play a biological role in cell signaling and defense against structures such as xenobiotics and bacteria. These are unstable and reactive species derived from molecular oxygen. The increase of ROS levels above certain levels in cells causes oxidative stress and damages structures such as lipids, enzymes, and proteins in the body. This causes many diseases, such as cancer, diabetes, etc. Molecules with antioxidant properties prevent the production of ROS by scavenging reactive oxygen species or inhibiting ROS-producing enzymes such as cytochrome P-450, xanthine oxidase, lipooxygenase, cyclooxygenase, monoamine oxidase, nicotinamide adenine dinucleotide phosphate oxidase [18,19].

In this study, three coumarin compounds with chloromethyl group at the C-4 position and hydroxy group at the C-7 position of the coumarin ring were synthesized according to the literature and characterized [20-23]. The antioxidant capacities of the compounds were investigated by DPPH (difhenyl-2-picrylhydrazyl) radical scavenger assay [24]. The synthesized compounds interactions with five enzymes known to produce reactive oxygen species (ROS) in the organism (cytochrome P-450, xanthine oxidase, nicotinamide adenine dinucleotide phosphate oxidase, human myeloperoxidase and lipoxygenase) were investigated by *in silico* molecular docking investigations. Also, the pharmacokinetic and toxicokinetic properties of the synthesized compounds were studied to evaluate their potential as drug candidates.

Antioxidant capacity assays, molecular docking studies, and ADMET predictions of the compounds synthesized in this study were performed and compared for the first time in this study.

2. Materials and methods

2.1. Materials and equipment

4-(chloromethyl)-7-hydroxy-5-methylcoumarin (**1**), 4-(chloromethyl)-7-hydroxy-8-methylcoumarin (**2**) and 4-(chloromethyl)-7-hydroxycoumarin (**3**) were synthesized according to the literature by Pechmann condensation reaction [20, 25, 26].

All chemicals and solvents used were purchased from Sigma-Aldrich. The compounds' purity was checked by TLC (thin layer chromatography) technique. For antioxidant analysis, ultraviolet-visible absorptions of compounds were recorded on Agilent 8453 UV-Vis Spectrophotometer. FT-IR spectra were recorded on Bruker Tensor 27 FTIR Spectrometer. NMR (^{1}H-NMR and ^{13}C-NMR) analysis of all compounds was performed on Bruker NMR 500 MHz

Spectrometer using deutero dimethyl sulfoxide (DMSO) at GUTMAM (Gazi University Basic and Engineering Sciences Central Laboratory Application and Research Center), Ankara, Turkey.

2.2. General synthesis of coumarin compounds

Ethyl 4-chloro-3-oxobutanoate (6.1 mmol) and a resorcinol compound (6 mmol) (5-methylresorcinol for **1**; 2-methylresorcinol for **2** and resorcinol for **3**) were dissolved in 10 mL of concentrated sulfuric acid. The mixture was stirred at 0-5 ^{o}C for 5 hours and then poured into cold water. The crude product was filtered and washed with water until acidity was removed. The solid products obtained were purified by crystallization from organic solvents.

2.2.1. 4-(chloromethyl)-7-hydroxy-5-methylcoumarin (1)

White solid. Yield 91% (1.15 g). MP: 163-166 ^{o}C. FTIR (ATR), (υ_{max}, cm^{-1}): 3102 (-OH); 3006 (ar. CH); 2959-2892 (alip. CH); 1676 (lactone C=O); 1607 (C-O); 1569 (C=C). ^{1}H NMR (DMSO, 500 MHz, ppm): 10.87, brd s, 1H (phenolic OH); 6.59, brd s, 2H (ar. CH); 6.37, s, 1H (lactone C=CH); 5.04, s, 2H (CH_2-Cl); 2.26, s, 3H (CH_3). ^{13}C NMR (DMSO, 500 MHz, ppm): 160.18 (C=O); 156.06-104.73 (C=C); 45.46 (CH_2-Cl); 21.58 (CH_3). Anal. Calc.: C, %58.81 ; H %4.04 Found: C, %58.79 ; H %4.02.

2.2.2. 4-(chloromethyl)-7-hydroxy-8-methylcoumarin (2)

White solid. Yield 89% (1.20 g). MP: 282-284 ^{o}C. FTIR (ATR), (υ_{max}, cm^{-1}): 3263 (-OH); 3066 (ar. CH); 2975-2832 (alip. CH); 1681 (lactone C=O); 1599 (C-O); 1573 (C=C). ^{1}H NMR (DMSO, 500 MHz, ppm): 10.50, brd s, 1H (phenolic OH); 7.49, d, J≈8.7 Hz, 1H (ar. CH); 6.68, d, J≈8.7 Hz, 1H (ar. CH); 6.38, s, 1H (lactone C=CH); 4.90, s, 2H (CH_2-Cl); 2.15, s, 3H (CH_3). ^{13}C NMR (DMSO, 500 MHz, ppm): 160.72 (C=O); 159.68-109.75 (C=C); 41.91 (CH_2-Cl); 8.43 (CH_3). Anal. Calc.: C, %58.81 ; H %4.04 Found: C, %58.80 ; H %4.03.

2.2.3. 4-(chloromethyl)-7-hydroxycoumarin (3)

White solid. Yield 92% (1.24 g). MP: 180-183 ^{o}C. FTIR (ATR), (υ_{max}, cm^{-1}): 3246 (-OH); 3097 (ar. CH); 2943-2821 (alip. CH); 1683 (lactone C=O); 1604 (C-O); 1563 (C=C). ^{1}H NMR (DMSO, 500 MHz, ppm): 10.65, brd s, 1H (phenolic OH); 7.68, d, J≈8.7 Hz, 1H (ar. CH); 6.85, dd, J≈8.7-2.2 Hz, 1H (ar. CH); 6.76, d, J≈2.2 Hz, 1H (ar. CH); 6.42, s, 1H (lactone C=CH); 4.96, s, 2H (CH_2-Cl). ^{13}C NMR (DMSO, 500 MHz, ppm): 161.94 (C=O); 160.61-102.99 (C=C); 40.02 (CH_2-Cl). Anal. Calc.: C, %57.03 ; H %3.35 Found: C, %57.02; H %3.32.

2.3. DPPH antioxidant assay

The antioxidant activity of compounds (**1-3**) was determined with DPPH (difhenyl-2-picrylhydrazyl) radical scavenger assay. Solutions of coumarin compounds at three different concentrations (0.25-0.50-1 mg/mL) and DPPH (25 μg/mL) solution in ethanol were prepared. The compound solution at various concentrations (100 μL) was added to the DPPH solution (3 mL). The solutions were incubated for 30 minutes in the dark at room temperature. A solution containing ethanol instead of the sample was prepared as a control solution. Absorbances of compounds were measured at 517 nm, and DPPH radical percent inhibition was calculated using % Inhibition= $[(Absorbance_{control}-Absorbance_{compound})/Absorbance_{control}]x\ 100$ equation.

2.4. Molecular docking

For molecular docking calculations, Autodock Vina software [27] was used to calculate the binding affinity for coumarin compounds (**1-3**). The X-ray crystal structure of target proteins (human cytochrome P-450 (PDB:1OG5) [28], xanthine oxidase (PDB: 3NRZ) [29], nicotinamide adenine dinucleotide phosphate oxidase (PDB:2CDU) [30], human myeloperoxidase (PDB: 1DNU) [31] and lipoxygenase (PDB: 1N8Q) [32] were obtained from the RCSB (Research Collaboratory for Structural Bioinformatics) Protein Data Bank (http://www.rcsb.org/) [33]. The water molecules in proteins have been removed. The missing polar hydrogens were added. Also, Kollman charges were added. The root of the ligand (synthesized compounds **1-3**) was detected automatically, and torsions were selected. The torsions of the ligands (synthesized compounds **1-3**) were allowed to rotate, and then selected residues were tested. The ligands (synthesized compounds **1-3**) were docked randomly to see where they would preferentially bind. Lamarckian Genetic Algorithm was used as a docking engine and all docking parameters were set as default [34]. The amino acid residues in the active site of target proteins were investigated using the BIOVA Discovery Studio Visualizer 2021 [35].

2.5. ADMET predictions

Absorbtion (A), distribution (D), metabolism (M), excretion (E) and toxicity (T) parameters (ADMET) define the properties that a drug molecule should possess. In drug design, investigating these toxicokinetic and pharmacokinetic properties of potential drug candidate molecules saves time and cost by preventing excessive experimentation and increases the success rate. Two free online databases, the SwissADME [36] and PRoTox-II [37] were used to predict the properties (ADMET) of the synthesized coumarin compounds (**1-3**).

3. Results and Discussion

3.1. Synthesis and Characterization

The coumarin compounds (**1-3**) were prepared by Pechmann condensation (Scheme 1). Reaction according to the literature. Synthesized compound's characterization was performed by spectroscopic methods FTIR, ^{1}H-NMR, ^{13}C-NMR and elemental analysis.

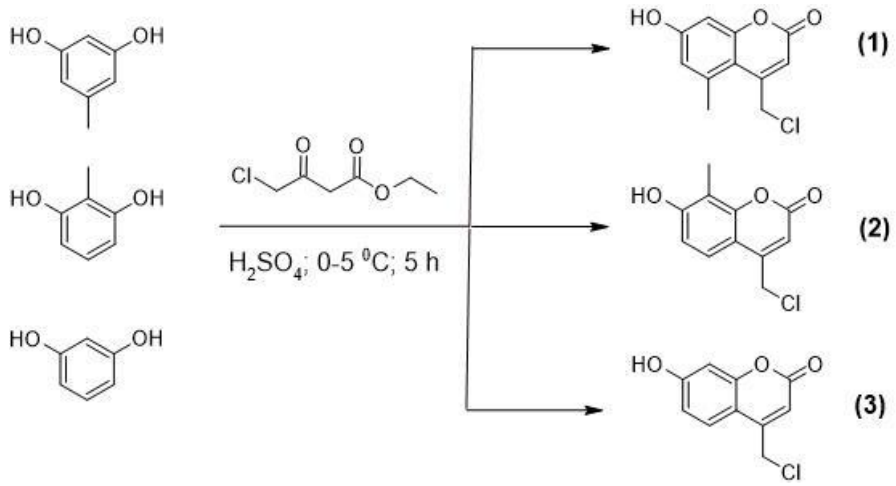

Scheme 1: The synthetic route of coumarin compounds (**1-3**).

In the FTIR spectrum of compounds 1-3, phenolic –OH peaks appeared at 3102, 3263 and 3246 cm^{-1}, respectively. Aromatic –CH peaks appeared at 3006, 3066 and 3097 cm^{-1}; aliphatic peaks appeared at 2959-2892, 2975-2832 and 2943-2821 cm^{-1}; lactone C=O peaks appeared at 1676, 1681 and 1683 cm^{-1}; ester O=C-O peaks appeared at 1607, 1599 and 1604 cm-1; aromatic C=C peaks appeared at 1569, 1573 and 1563 cm^{-1}, respectively. The results of FTIR data of compounds (1-3) support synthesized structures. FTIR spectrum of compounds is given in Figures 1, 2, and 3.

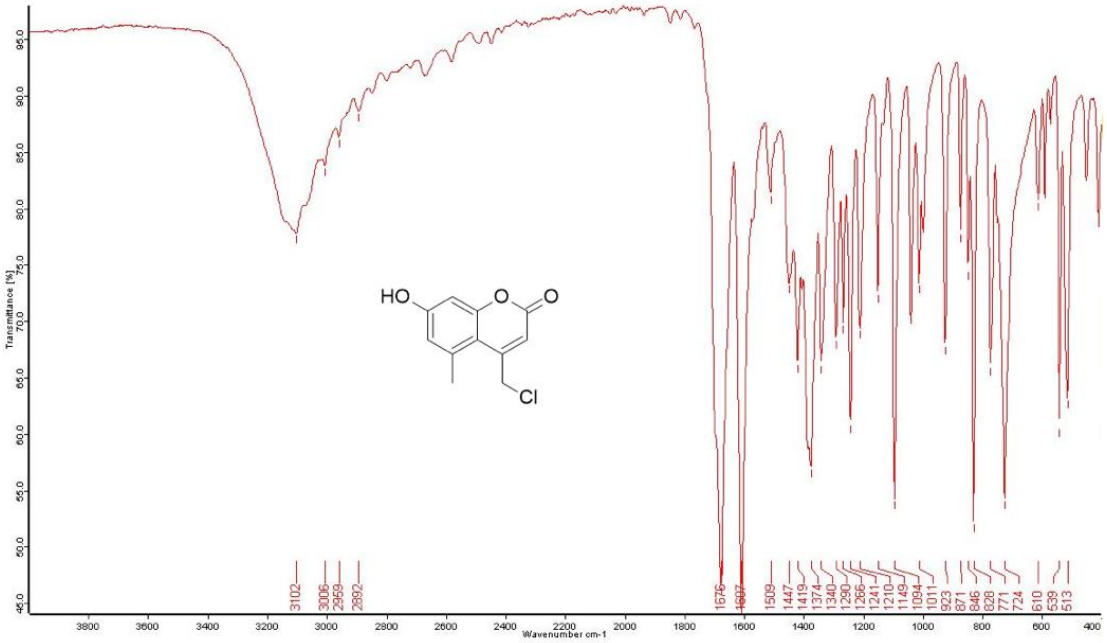

Figure 1: FT-IR spectrum of compound **1.**

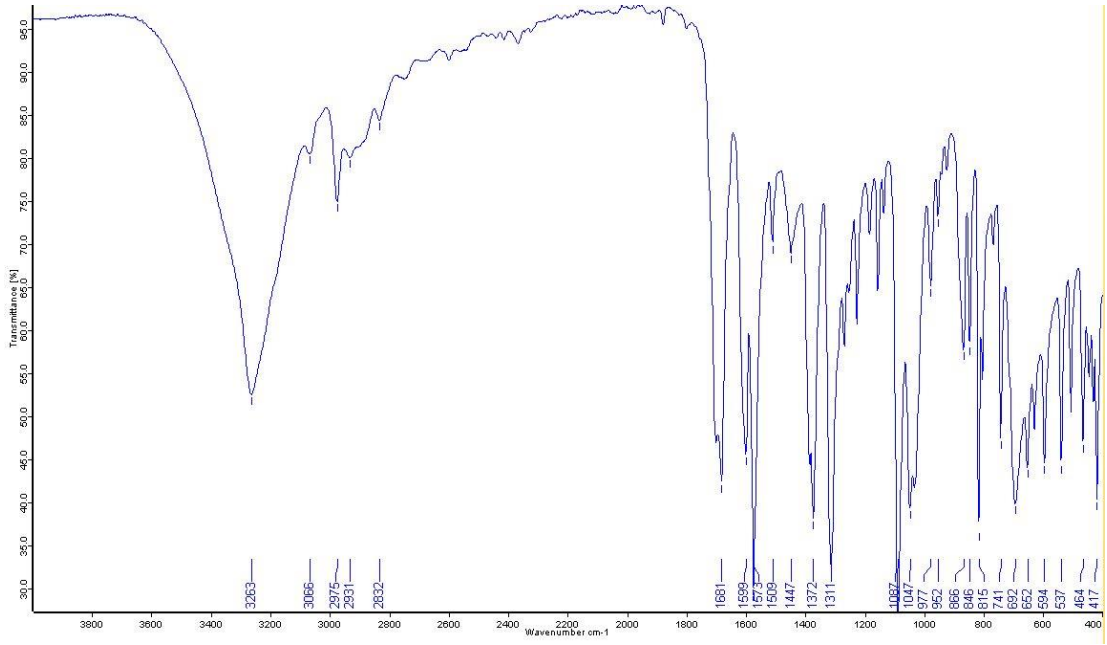

Figure 2: FT-IR spectrum of compound **2.**

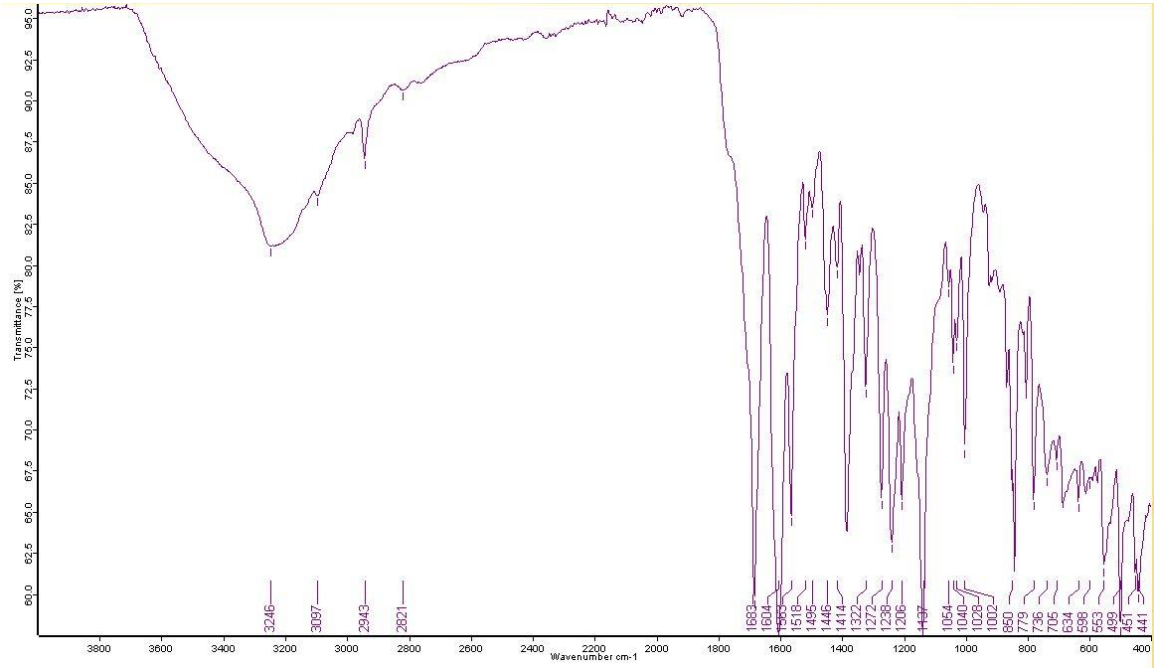

Figure 3: FT-IR spectrum of compound **3.**

In the ^{1}H-NMR spectrum of compounds **1-3** in DMSO, phenolic protons appeared at 10.87, 10.50, and 10.65 ppm as broad singlet peaks, respectively. For compound **1**, aromatic protons appeared as doublet peaks at 6.67 and 6.59 ppm each with 1H integration. C=C-H proton in the lactone ring appeared as a singlet peak at 6.37 ppm with 1H integration, CH_2-Cl protons appeared as a singlet peak at 5.04 ppm with 2H integration, and CH_3 protons appeared as a singlet peak at 2.26 ppm with 3H integration. For compound **2**, aromatic protons appeared as doublet peaks at 7.49 and 6.88 ppm each with 1H integration. C=C-H proton in the lactone ring appeared as a singlet peak at 6.38 ppm with 1H integration, CH_2-Cl protons appeared as a singlet peak at 4.90 ppm with 2H integration, and CH_3 protons appeared as a singlet peak at 2.15 ppm with 3H integration. For compound **3**, aromatic protons appeared as doublet, double doublet, and doublet peaks at 7.68, 6.85, and 6.76 ppm, each with 1H integration. C=C-H proton in the lactone ring appeared as a singlet peak at 6.42 ppm with 1H integration, and CH_2-Cl protons appeared as a singlet peak at 4.96 ppm with 2H integration.

In the ^{13}C-NMR spectrum of **1-3** in DMSO, lactone C=O carbons appeared at 160.18, 160.72 and 161.94 ppm; C=C carbons appeared at between 156.06 and 104.73, 159.68 and 109.75, 160.61 and 102.99; CH_2-Cl carbons appeared at 45.46, 41.91 and 40.02 ppm, respectively. Also, methyl carbon for compound **1** appeared at 21.58, and for compound **2** appeared at 8.43 ppm. NMR spectrums of compounds are given in Figures 4,5 and 6.

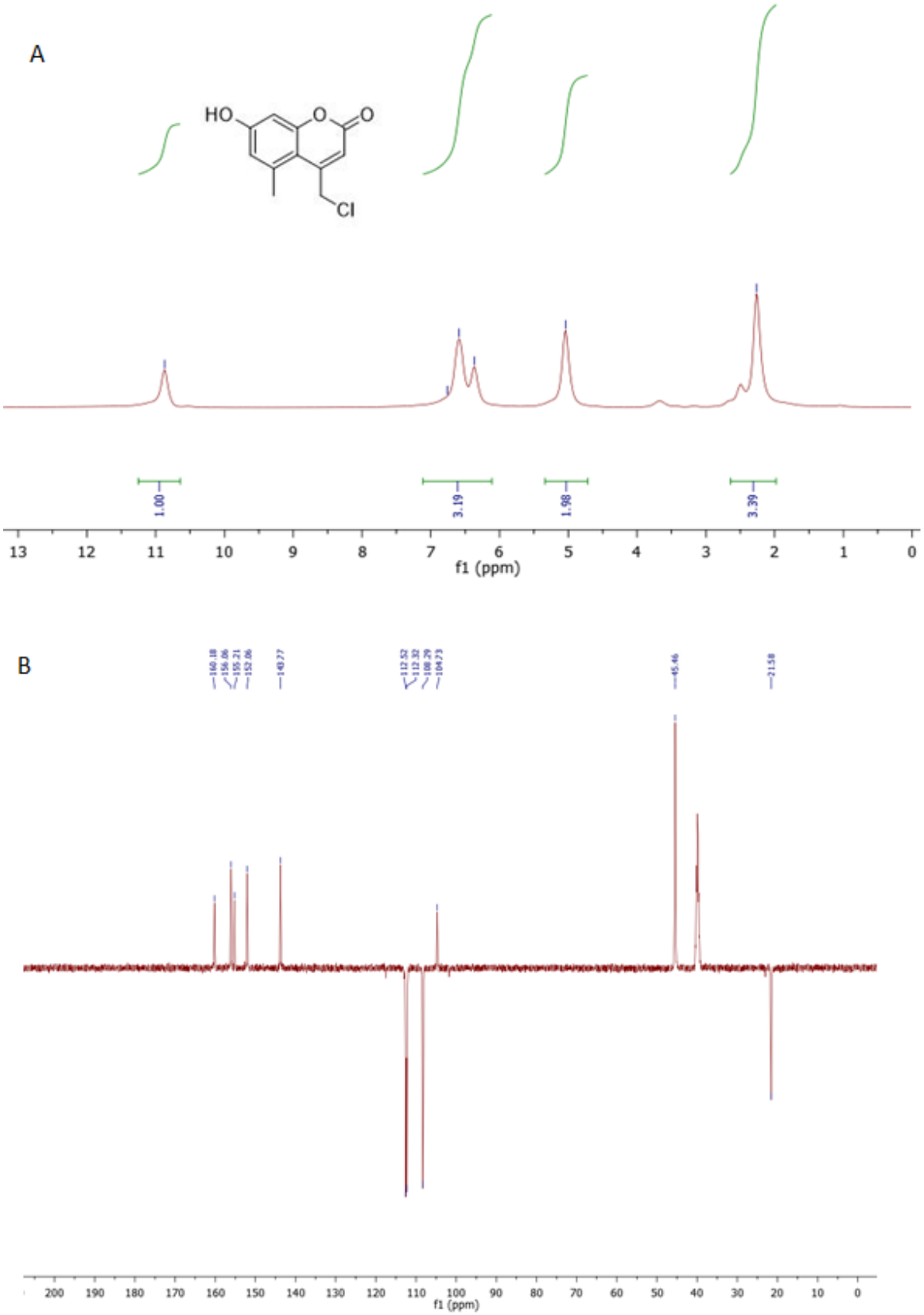

Figure 4: ^{1}H-NMR (A) and ^{13}C-NMR (B) spectrum of compound **1.**

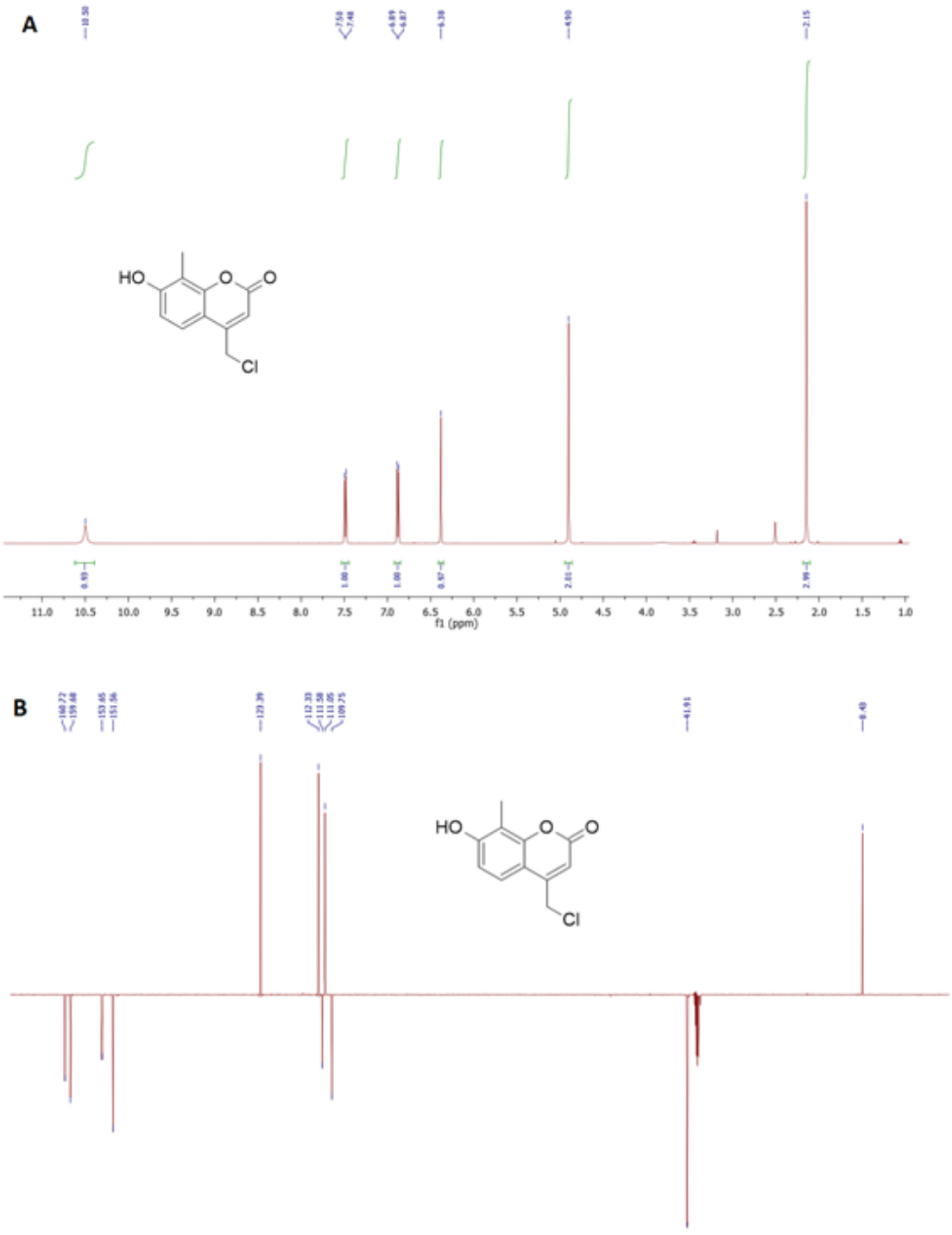

Figure 5: ^{1}H-NMR (A) and ^{13}C-NMR (B) spectrum of compound **2.**

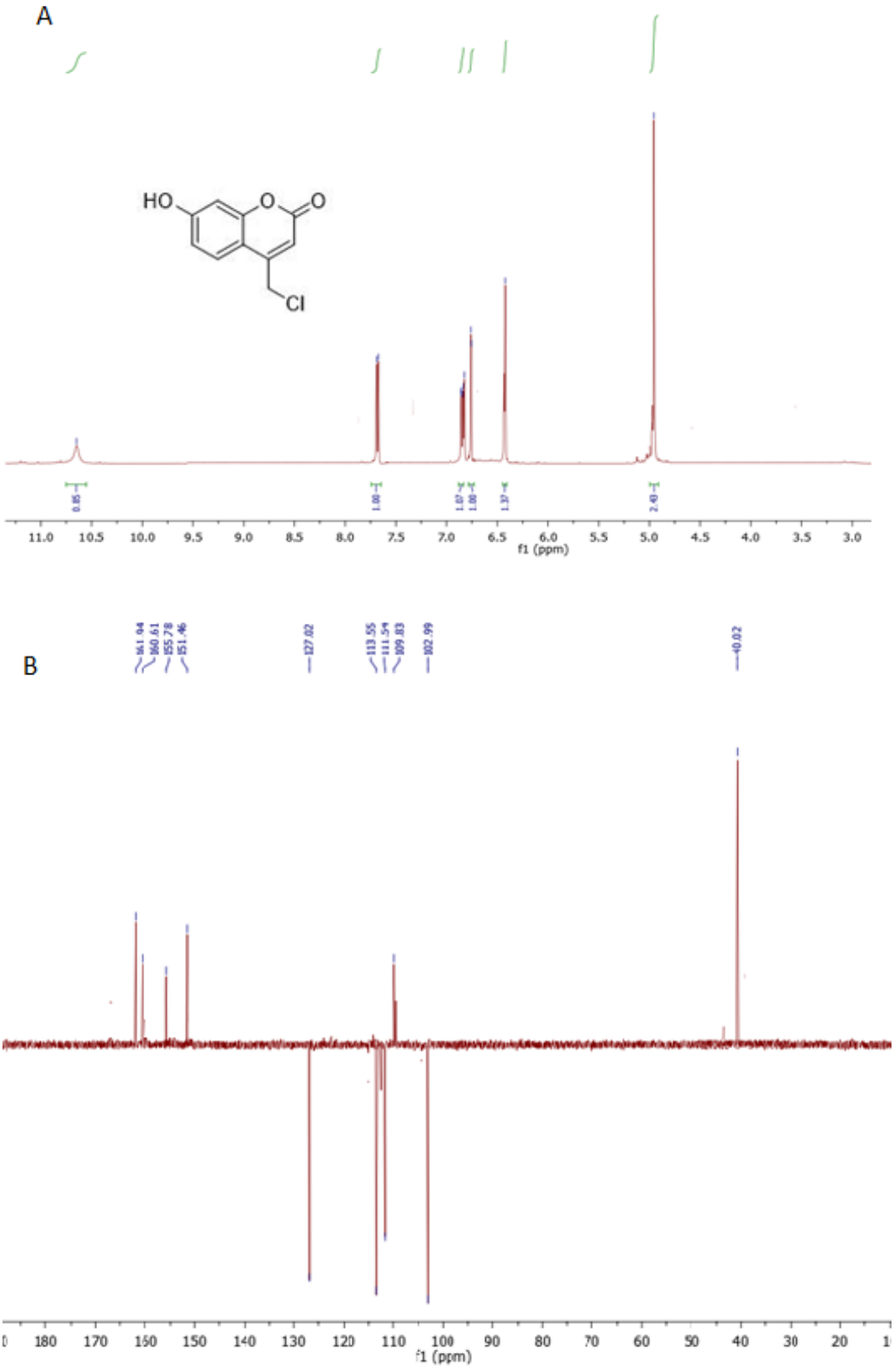

Figure 6: ^{1}H-NMR (A) and ^{13}C-NMR (B) spectrum of compound **3.**

The elemental analysis data results of the synthesized compounds **1-3** were given in the Materials and Methods section. The results of elemental analysis and other spectroscopic data support synthesized coumarin structures.

3.2. Antioxidant activity

DPPH radical scavenging tests were performed to determine the antioxidant activity of the compounds. The percentage of DPPH radical scavenging of the sample solution at three different concentrations for each compound was calculated using the equation given in section 2.3. As a result of DPPH antioxidant assays, it was observed that all three compounds had antioxidant activity at the concentrations studied ($p<0.05$). Furthermore, the results showed that the methyl group substituted at C-5 (compound **1**) and C-8 (compound **2**) positions affected the antioxidant activity. The compound with the highest DPPH radical scavenging activity was determined as compound **1,** containing the methyl group at the C-5 position, and the compound with the lowest activity was determined as compound **2**, containing the methyl group at the C-8 position. The % inhibition values of the compounds are given comparatively in Fig. 7.

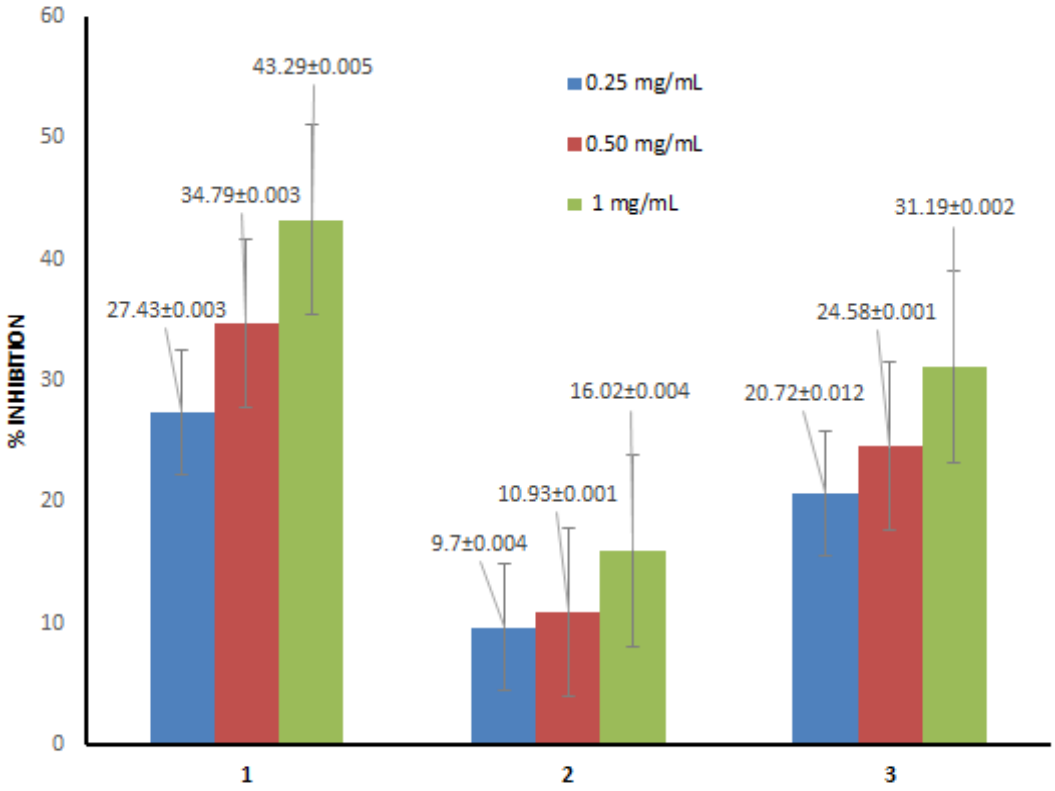

Figure 7: Antioxidant activity results of compounds **1**, **2,** and **3** at three different concentrations (DPPH assay values are mean of triplicate determination (n=3) ± standard deviation; $P<0.005$).

The DPPH radical scavenging ability of the compounds can be attributed to stable radical formation. This ability can be explained by hydrogen transfer from different parts of the compounds to DPPH, as suggested in Scheme 2.

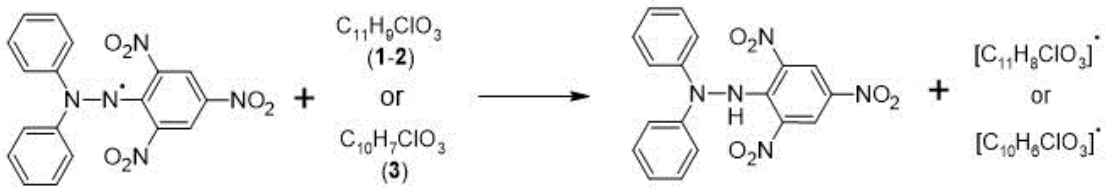

Scheme 2: Proposed mechanism for antioxidant ability of compounds **1**, **2,** and **3.**

There are many studies in the literature to investigate the antioxidant activity of coumarin compounds. In these studies, the change in antioxidant activity was investigated by adding various substituents to the 7-hydroxy coumarin compound. The importance of the substituents attached to the coumarin ring on antioxidant activity is very important [1, 14, 38]. In this study, the antioxidant activities of 7-hydroxy coumarin compounds containing the 4-chloromethyl group were investigated by the DPPH method. In the literature, studies investigating the antioxidant activities of 7-hydroxy-4-methyl coumarin derivative compounds are found [39, 40]. When compared with the results of the DPPH radical scavenging assay in the literature, it was observed that the % inhibition value of 4-(chloromethyl)-7-hydroxycoumarin compound synthesized in this study was higher than the % inhibition value of the 7-hydroxy-4-methyl coumarin given in the literature [39].

3.3. Molecular docking

In silico radical scavenging properties of the synthesized compounds were studied on five potential target enzymes that can produce free radical species in the organism. The enzymes chosen as targets are xanthine oxidase, human cytochrome P-450, nicotinamide adenine dinucleotide phosphate oxidase (NADPH), human myeloperoxidase, and lipoxygenase. The enzymes and the ligands (compounds **1**, **2,** and **3**) whose interactions with the enzymes were studied are prepared for molecular docking as described in section 2.4. The molecular docking results of the compounds are given in Table 1. The compounds were found to interact with four of the five selected enzymes with high molecular docking scores.

When all docking scores were analyzed, it was observed that compound **1** interacted with xanthine oxidase, NADPH oxidase, and myeloperoxidase; compound **2** with myeloperoxidase and xanthine oxidase; compound **3** with myeloperoxidase and xanthine oxidase receptors with high scores. The best-scoring interaction of all three compounds was observed against the myeloperoxidase enzyme.

Table 1: The molecular docking results of the compounds **1**, **2,** and **3.**

Target enyzme	Molecular Docking Scores of Compounds (kcal/mol)		
	1	**2**	**3**
Cytochrome P-450	-6.6	-7.0	-6.3
Xanthine oxidase	-7.5	-7.3	-7.6
NADPH oxidase	-7.1	-7.0	-6.8
Myeloperoxidase	-8.0	-7.5	-7.7
Lipoxygenase	-2.9	-2.6	-4.0

The compounds synthesized in this study were observed to interact with many residues in the active site of enzymes. Interactions of the compounds with some target enzymes are given in the figure 8.

According to the literature and PDB; important active site residues of cytochrome P-450 are ARG97, ILE99, GLY98, ALA103, PHE100, LEU102, ASN217, PHE114VAL113, , LEU366, SER365, THR364, PHE476 and PRO367 [1,28]. Compound **1** made π-π stacking and π-alkyl interactions with PHE114, PHE100, LEU366, PRO367, ILE99, and ALA103. Compound **2** made hydrogen bond interactions with ARG97, π-σ interaction with VAL113, π-alkyl interaction with LEU366. Compound **3** made hydrogen bond interactions with GLY98 and ASN217 residues. Also, compound **3** made π-alkyl interactions with ALA103, LEU366, and PRO367 residues.

Important active site residues of NADPH oxidase are GLY156, ILE243, GLY158, TYR159, GLY244, ASP179, GLY180, LYS213, HIS181, TYR188, VAL214, and ILE160 [19,30]. Compound **1** made hydrogen bond interactions with GLY180 and LYS213, π-σ interaction and π-cation interaction with LYS213, π-alkyl interactions with ILE243 and VAL214. Compound **2** made hydrogen bond interactions with GLY180 and LYS213, π-cation interaction with LYS213, π-alkyl interactions with ILE243 and VAL214, π-σ interaction with HIS181. Compound **3** made hydrogen bond interactions with GLY180 and LYS213, π-cation interaction with LYS213, π-alkyl interactions with ILE243 and VAL214 residues.

Important active site residues of myeloperoxidase are HIS336, GLN91, PHE170, SER174, ASP94, THR168, ASP 172, ASP96, PHE 99, GLU102, PHE407 and HIS95 [31,41]. Compound **1** made hydrogen bond interaction with HIS95, π-σ interaction with GLN91, π-cation interaction with HIS336 residue. Compound **2** made π-cation interactions with HIS336 and HIS95, π-σ interactions with GLN91. Compound **3** made π-alkyl interactions with HIS95 and HIS336, π-π stacking with GLN91.

Important active site residues of xanthine oxidase are GLN1194, ALA1079, MET1038, ARG912, GLU802, ARG880, ALA910, GLY913, PHE914, PHE1005, SER1008, PHE1009, SER1080, THR1010, LEU1014 and PRO1076 [29,42]. Compound **1** made π-sulphur interaction with MET1038, hydrogen bond interaction with SER1082, π-alkyl interaction with ARG912. Compound **2** made π-alkyl interactions with ARG912 and MET1038. Compound **3** made π-π stacking with PHE1009 and PHE914; hydrogen bond interactions with ARG880 and THR1010; π-alkyl interactions with LEU1014 and ALA1079 residues.

3.4. ADMET predictions

The physicochemical, toxicokinetic, and pharmacokinetic properties of compounds were predicted by using the SwissADME [36] and the ProTox-II online [37] data bases. All properties of the studied compounds are given in Table 2. Estimating these properties of drug candidate molecules is very important for the investigation of drug-likeliness of these compounds.

In this study, Lipinski's rule of 5 (Ro5) was studied to determine the drug likeliness of the coumarin compounds. According to the Ro5, the compound can be used as a drug candidate if it has some suitable properties. These properties are suitable molecular weight (MW) (<500 g/mol), hydrogen bond donors (HBD) (<5), hydrogen bond acceptors (HBA) (<10), lipophilicity (Log P) (<5) and rotatable bonds (RB) (<5) [10, 43]. As can be seen in the table, all of the investigated coumarin compounds comply with Lipinski's rule of 5. Also, according to the other rules for the drug likeliness such as Veber's rule (polar surface area TPSA < 140 Å²), Egan's rule (TPSA 0-132 Å² and Log P -1-6), Muegge's rule (MW 200-600 g/mol, Log P -2-5, TPSA 150 < Å², cyclic rings <7, carbon atoms >4, heteroatoms >1, RB <15, HBA<10 and HBD <5) and Ghose rule (MW 160-480 g/mol, Log O -0.4-5.6, MR 40-130 and atoms 20-70) [44] the compounds comply with all rules. These results showed that the studied compounds meet the suggested properties and could be the drug candidate. When the other ADMET parameters in Table 2 are examined, it is seen that gastrointestinal absorption of the compounds is high; all compounds can cross the blood-brain barrier (BBB) and can not be used as a substrate of P-glycoprotein. In addition, the TPSA values shown in the table indicate that the oral bioavailability of the compounds may be good. As can be seen from the results in Table 2, it was observed that all compounds may show an inhibitory effect by interacting with CYP1A2. Toxicity classes of all compounds are 5. 1 means highly toxic, and 6 means non-toxic on the toxicity scale. Compounds are inactive for cytotoxicity, immunotoxicity, hepatotoxicity, mutagenicity, and mitochondrial membrane potential (MMP). But compounds **1** and **3** are active for carcinogenicity. As a result, the studied compounds are molecules with the potential to be used as drug candidates by evaluating their advantages and disadvantages.

Table 2: The pharmacokinetic and toxicokinetic properties of compound **1**, **2** and **3.**

Properties	Compound		
	1	**2**	**3**
MW (g/mol)	224.64	224.64	210.61
Number of atoms	24	24	21
Number of heavy atoms	15	15	14
Number of bonds	25	25	22
Number of RB	1	1	1
Number of HBA	3	3	3
Number of HBD	1	1	1
Molar Refractivity	59.23	59.23	54.27
TPSA (Å²)	50.44	50.44	50.44
Log $P_{o/w}$	2.26	2.31	2.03
GI absorption	High	High	High
BBB permeant	Yes	Yes	Yes
P-gp substrate	No	No	No
CYP1A2 inhibitor	Yes	Yes	Yes
CYP2C19 inhibitor	No	No	No
CYP2C9 inhibitor	No	No	No
CYP2D6 inhibitor	No	No	No
CYP3A4 inhibitor	No	No	No
Skin permeation, Log K_p (cm/s)	-6.35	-6.35	-6.22
Lipinski	Yes, 0 violation	Yes, 0 violation	Yes, 0 violation
Toxicity class*	5	5	5
Predicted LD_{50} (mg/kg)*	3200	3200	3200
Hepatotoxcity*	Inactive	Inactive	Inactive
Carcinogenicity*	Active	Inactive	Active
Immunotoxicity*	Inactive	Inactive	Inactive
Mutagenicity*	Inactive	Inactive	Inactive
Cytotoxicity*	Inactive	Inactive	Inactive
Mitochondrial Membrane Potential (MMP)*	Inactive	Inactive	Inactive

** ProTox-II data. Unlabelled data are SwissADME data.*

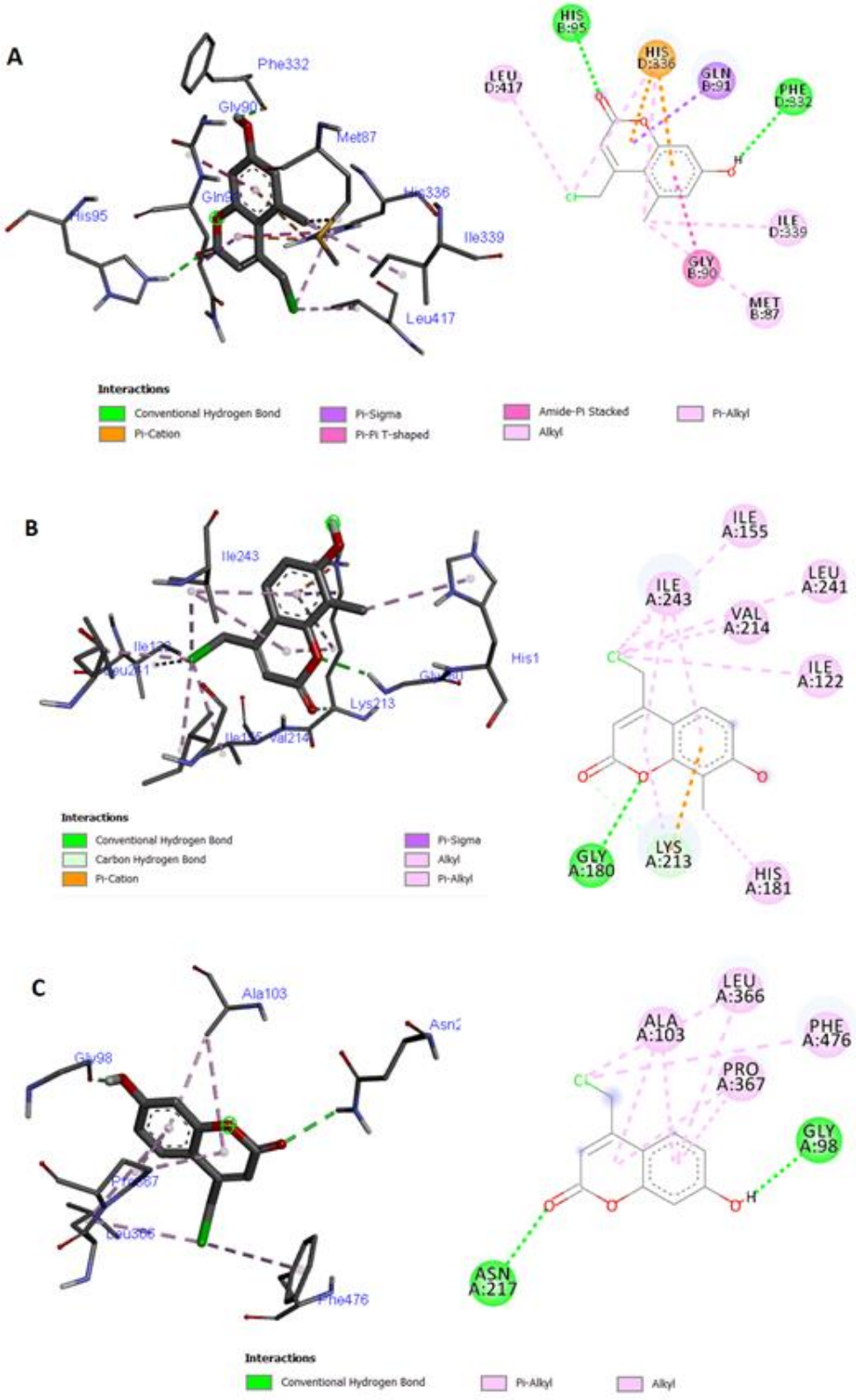

Figure 8: The 2D ligand-enzyme interactions diagrams (**A**: compound **1**-myeloperoxidase; **B**: compound **2**-NADPH oxidase; **C**: compound **3**-cytochrome P-450).

4. Conclusion

In this study, 4-chloromethyl-7-hydroxy substituted coumarin compounds with antioxidant properties were synthesized and characterized. All spectroscopic data and elemental analysis results obtained confirmed the chemical structures of the compounds. The antioxidant capacity determination by the DPPH method showed that all compounds exhibited antioxidant properties at the concentrations studied. The compound with the highest antioxidant activity was determined to be compound **1**. Molecular docking studies showed that the compounds interacted well with four of the five target enzymes studied. ADMET predictions showed that the compounds have the properties to be drug candidates. As a result of all the experimental and theoretical studies, it was concluded that the compounds may be lead compounds for various research due to their antioxidant properties and drug candidate properties.

Declaration of Competing Interest

The author declares that she has no known competing financial interests or personal relationships that could have appeared to influence the work reported in this paper.

Funding Declaration

The study was not funded by any organization or individual.

Data Availability

All data related to the study are given in the manuscript.

References

[1] Kecel-Gunduz, S., Budama-Kilinc, Y., Bicak, B., Gok, B., Belmen, B., Aydogan, F., Yolacan, C., *New coumarin derivative with potential antioxidant activity: Synthesis, DNA binding and in silico studies (Docking, MD, ADMET)*, Arabian Journal of Chemistry, 16(2), 104440, 2023.

[2] Özdemir, M., Taşkın, D., Ceyhan, D., Köksoy, B., Taşkın, T., Bulut, M., Yalçın, B., *7, 8-Dihydroxycoumarin derivatives: In silico molecular docking and in vitro anticholinesterase activity*, Journal of Molecular Structure, 1274, 134535, 2023.

[3] Hadjipavlou-Litina, D., Kontogiorgis, C., Pontiki, E., Dakanali, M., Akoumianaki, A., Katerinopoulos, H. E., *Anti-inflammatory and antioxidant activity of coumarins designed as potential fluorescent zinc sensors*, Journal of Enzyme Inhibition and Medicinal Chemistry, 22(3), 287-292, 2007.

[4] Kostova, I., *Synthetic and natural coumarins as cytotoxic agents*, Current Medicinal Chemistry-Anti-Cancer Agents, 5(1), 29-46, 2005.

[5] Wu, Y., Xu, J., Liu, Y., Zeng, Y., Wu, G., *A review on anti-tumor mechanisms of coumarins,* Frontiers in Oncology, 10, 592853, 2020.

[6] Thakur, A., Singla, R., Jaitak, V., *Coumarins as anticancer agents: A review on synthetic strategies, mechanism of action and SAR studies*, European Journal of Medicinal Chemistry, 101, 476-495, 2015.

[7] Chandra, K. M., Goud, N. S., Arifuddin, M., Alvala, M., Alvala, R., Angeli, A., Supuran, C. T., *Synthesis and biological evaluation of novel 4, 7-disubstituted coumarins as selective tumor-associated carbonic anhydrase IX and XII inhibitors*, Bioorganic & Medicinal Chemistry Letters, 39, 127877, 2021.

[8] Ostrowska, K., *Coumarin-piperazine derivatives as biologically active compounds*, Saudi Pharmaceutical Journal, 28(2), 220-232, 2020.

[9] Batran, R. Z., Kassem, A. F., Abbas, E. M., Elseginy, S. A., Mounier, M. M., *Design, synthesis and molecular modeling of new 4-phenylcoumarin derivatives as tubulin polymerization inhibitors targeting MCF-7 breast cancer cells,* Bioorganic & Medicinal Chemistry, 26(12), 3474-3490, 2018.

[10] Çelik, E., Özdemir, M., Yalçın, B., Koksoy, B., *In silico study and structure-activity relations of glucose-bound coumarin derivatives against the NSP12 protein of SARS-CoV-2*, Journal of Ata-Chem, 1(1), 29-37, 2021.

[11] Sabt, A., Abdelhafez, O. M., El-Haggar, R. S., Madkour, H. M., Eldehna, W. M., El-Khrisy, E. E. D. A., ... & Rashed, L. A., *Novel coumarin-6-sulfonamides as apoptotic anti-proliferative agents: synthesis, in vitro biological evaluation, and QSAR studies*, Journal of Enzyme Inhibition and Medicinal Chemistry, 33(1), 1095-1107, 2018.

[12] Klenkar, J., Molnar, M., *Natural and synthetic coumarins as potential anticancer agents*, Journal of Chemical And Pharmaceutical Research, 7(7), 1223-1238, 2015.

[13] Holiyachi, M., Shastri, S. L., Chougala, B. M., Naik, N. S., Pawar, V., Shastri, L. A., ... & Sunagar, V. A., *Design and synthesis of new series of dipyrromethane-coumarin and porphyrin-coumarin derivatives: Excellent anticancer agents,* Journal of Molecular Structure, 1237, 130424, 2021.

[14] Kecel-Gunduz, S., Budama-Kilinc, Y., Gok, B., Bicak, B., Akman, G., Arvas, B., ... & Yolacan, C., *Computer-aided anticancer drug design: In vitro and in silico studies of new iminocoumarin derivative*, Journal of Molecular Structure, 1239, 130539, 2021.

[15] Song, X. F., Fan, J., Liu, L., Liu, X. F., Gao, F., *Coumarin derivatives with anticancer activities: An update*, Archiv der Pharmazie, 353(8), 2000025, 2020.

[16] Dorababu, A., *Coumarin-heterocycle framework: A privileged approach in promising anticancer drug design*, European Journal of Medicinal Chemistry Reports, 2, 100006, 2021.

[17] Souiei, S., Garah, F. B. E., Belkacem, M. A., Znati, M., Bouajila, J., Jannet, H. B., *New flavonoid glycosides conjugates: synthesis, characterization, and evaluation of their cytotoxic activities*, Turkish Journal of Chemistry, 43(2), 404-414, 2019.

[18] Costa, J. D. S., Ramos, R. D. S., Costa, K. D. S. L., Brasil, D. D. S. B., Silva, C. H. T. D. P. D., Ferreira, E. F. B., ... & Santos, C. B. R. D., *An in silico study of the antioxidant ability for two caffeine analogs using molecular docking and quantum chemical methods*, Molecules, 23(11), 2801, 2018.

[19] Sarı, S., Kılıç, N., Yılmaz, M., *In vitro antioxidant activities and in silico molecular docking studies of N-substituted oxime derivatives*, Structural Chemistry, 34(2), 605-616, 2023.

[20] Ye, X. W., Zheng, Y. C., Duan, Y. C., Wang, M. M., Yu, B., Ren, J. L., ... & Liu, H. M., *Synthesis and biological evaluation of coumarin–1, 2, 3-triazole–dithiocarbamate hybrids as potent LSD1 inhibitors*, Medicinal Chemistry Communications, 5(5), 650-654, 2014.

[21] Reddy, Y. T., Sonar, V. N., Crooks, P. A., Dasari, P. K., Reddy, P. N., Rajitha, B., *Ceric ammonium nitrate (CAN): An efficient catalyst for the coumarin synthesis via Pechmann condensation using conventional heating and microwave irradiation*. Synthetic Communications, 38(13), 2082-2088, 2008.

[22] Jawalekar, A. M., Meeuwenoord, N., Cremers, J. S. G., Overkleeft, H. S., van der Marel, G. A., Rutjes, F. P., Van Delft, F. L., *Conjugation of nucleosides and oligonucleotides by [3+ 2] cycloaddition*, The Journal of organic chemistry, 73(1), 287-290, 2008.

[23] Uroos, M., Javaid, A., Bashir, A., Tariq, J., Khan, I. H., Naz, S., ... & Sultan, M., *Green synthesis of coumarin derivatives using Brønsted acidic pyridinium based ionic liquid [MBSPy][HSO 4] to control an opportunistic human and a devastating plant pathogenic fungus Macrophomina phaseolina*, RSC Advances, 12(37), 23963-23972, 2022.

[24] Fu, W., Chen, J., Cai, Y., Lei, Y., Chen, L., Pei, L., ... & Ruan, J. (2010). *Antioxidant, free radical scavenging, anti-inflammatory and hepatoprotective potential of the extract from Parathelypteris nipponica (Franch. et Sav.),* Ching. Journal of Ethnopharmacology, 130(3), 521-528, 2010.

[25] Xie, L., Guo, H. F., Lu, H., Zhuang, X. M., Zhang, A. M., Wu, G., ... & Jiang, S., *Development and preclinical studies of broad-spectrum anti-HIV agent (3′ R, 4′ R)-3-cyanomethyl-4-methyl-3′, 4′-di-O-(S)-camphanoyl-(+)-cis-khellactone (3-cyanomethyl-4-methyl-DCK)*, Journal of medicinal chemistry, 51(24), 7689-7696, 2008.

[26] Karami, B., Kiani, M., *$ZrOCl_2$. $8H_2O/SiO_2$: An efficient and recyclable catalyst for the preparation of coumarin derivatives by Pechmann condensation reaction*, Catalysis Communications, 14(1), 62-67, 2011.

[27] Trott, O., Olson, A. J., *AutoDock Vina: improving the speed and accuracy of docking with a new scoring function, efficient optimization, and multithreading*, Journal of Computational Chemistry, 31(2), 455-461, 2010.

[28] Williams, P. A., Cosme, J., Ward, A., Angove, H. C., Matak Vinković, D., Jhoti, H., *Crystal structure of human cytochrome P450 2C9 with bound warfarin*, Nature, 424(6947), 464-468, 2003.

[29] Cao, H., Pauff, J. M., Hille, R., *Substrate orientation and catalytic specificity in the action of xanthine oxidase: the sequential hydroxylation of hypoxanthine to uric acid*, Journal of Biological Chemistry, 285(36), 28044-28053, 2010.

[30] Lountos, G. T., Jiang, R., Wellborn, W. B., Thaler, T. L., Bommarius, A. S., Orville, A. M., *The crystal structure of NAD (P) H oxidase from Lactobacillus sanfranciscensis: insights into the conversion of O_2 into two water molecules by the flavoenzyme*, Biochemistry, 45(32), 9648-9659, 2006.

[31] Blair-Johnson, M., Fiedler, T., Fenna, R., *Human myeloperoxidase: structure of a cyanide complex and its interaction with bromide and thiocyanate substrates at 1.9 Å resolution*, Biochemistry, 40(46), 13990-13997, 2001.

[32] Borbulevych, O. Y., Jankun, J., Selman, S. H., Skrzypczak-Jankun, E., *Lipoxygenase interactions with natural flavonoid, quercetin, reveal a complex with protocatechuic acid in its*

X-ray structure at 2.1 Å resolution, Proteins: Structure, Function, and Bioinformatics, 54(1), 13-19, 2004.

[33] Berman, H. M., Westbrook, J., Feng, Z., Gilliland, G., Bhat, T. N., Weissig, H., ... & Bourne, P. E., The protein data bank, *Nucleic Acids Research*, 28(1), 235-242, 2000.

[34] Morris, G. M., Goodsell, D. S., Halliday, R. S., Huey, R., Hart, W. E., Belew, R. K., Olson, A. J., *Automated docking using a Lamarckian genetic algorithm and an empirical binding free energy function*, *Journal of Computational Chemistry*, 19(14), 1639-1662, 1998.

[35] Biovia, D. S., Discovery Studio Visualizer, v21.1.0.20298, Dassault Systèmes, San Diego, CA, USA, 2021.

[36] Daina, A., Michielin, O., Zoete, V., *SwissADME: a free web tool to evaluate pharmacokinetics, drug-likeness and medicinal chemistry friendliness of small molecules*, Scientific Reports, 7(1), 42717, 2017.

[37] Banerjee, P., Eckert, A. O., Schrey, A. K., Preissner, R., *ProTox-II: a webserver for the prediction of toxicity of chemicals*, Nucleic Acids Research, 46(W1), 257-263, 2018.

[38] Al-Majedy, Y. K., Al-Duhaidahawi, D. L., Al-Azawi, K. F., Al-Amiery, A. A., Kadhum, A. A. H., Mohamad, A. B., *Coumarins as potential antioxidant agents complemented with suggested mechanisms and approved by molecular modeling studies*, Molecules, 21(2), 135, 2016.

[39] Onar, H. Ç., Yaşa, H., Sin, O., *Comparison of antioxidant activities of mono-, di-and tri-substituted coumarins*, Journal of the Turkish Chemical Society Section A: Chemistry, 7(1), 87-96, 2019.

[40] Pedersen, J. Z., Oliveira, C., Incerpi, S., Kumar, V., Fiore, A. M., De Vito, P., ... & Saso, L., *Antioxidant activity of 4-methylcoumarins*, Journal of Pharmacy and Pharmacology, 59(12), 1721-1728, 2007.

[41] Solo, P., Prasanna, D., *Designing and docking studies of imidazole-based drugs as potential inhibitors of myeloperoxidase (MPO) mediated inflammation and oxidative stress*, Biocatalysis and Agricultural Biotechnology, 43, 102421, 2022.

[42] Tran, L. T. T., Le, T. N., Ho, D. V., Nguyen, T. H., Pham, V. P. T., Van Pham, K. T., ... & Tran, M. H., *Virtual screening and in vitro evaluation to identify a potential xanthine oxidase inhibitor isolated from Vietnamese Uvaria cordata*, Natural Product Communications, 17(2), 1934578X221080339, 2022.

[43] Öztürkkan, F. E., Özdemir, M., Akbaba, G. B., Sertçelik, M., Yalçın, B., Necefoğlu, H., Hökelek, T., *Synthesis, crystal structure, potential drug properties for Coronavirus of Co (II) and Zn (II) 2-chlorobenzoate with 3-cyanopyridine complexes*, Journal of Molecular Structure, 1250, 131825, 2022.

[44] Nagar, P. R., Gajjar, N. D., Dhameliya, T. M., *In search of SARS CoV-2 replication inhibitors: virtual screening, molecular dynamics simulations and ADMET analysis*, Journal of Molecular Structure, 1246, 131190, 2021.

Adıyaman University Journal of Science
https://dergipark.org.tr/en/pub/adyujsci
DergiPark AKADEMİK
ISSN 2147-1630
e-ISSN 2146-586X

Assessment of the Developmental Profiles of ZHY3 and W303 Yeast Strains in Zinc-Modified Media

Beyza YÜKSEL[1], M. Aydın AKBUDAK[2,*]

[1]*Department of Agricultural Biotechnology, Akdeniz University, Antalya, 07070 Türkiye*
202251054001@ogr.akdeniz.edu.tr, ORCID: 0009-0008-0662-4865
[2]*Department of Agricultural Biotechnology, Akdeniz University, Antalya, 07070 Türkiye*
akbudak@akdeniz.edu.tr, ORCID: 0000-0002-1397-4678

Received: 10.10.2024 **Accepted:** 16.11.2024 **Published:** 31.12.2024

Abstract

All organisms require zinc to sustain their vital functions. In the case of Zn deficiency, plant production, as well as animal and human health, are adversely affected. Baker's yeast (*Saccharomyces cerevisiae*) is a model organism for scientific research and is commonly used in metal deficiency/toxicity studies. This study aims to identify the first stage in the identification of Zn uptake genes, which determines the conditions of Zn-deficient environments that inhibit yeast development. The YNB medium, the basic nutrient medium for yeast cultivation, contains enough Zn conducive to yeast growth. Chelating agents (EGTA or EDTA) have been added to the YNB medium to create conditions of insufficient Zn. The yeast strains ZHY3 (Zn uptake gene mutant) and W303 (wild type – WT) were tested in these environments. The growth profiles of the yeasts were compared in nutrient media containing different concentrations of the chelating agents. The concentrations of EGTA and EDTA that inhibited the growth of the W303 strain were determined to be 25 mM and 1.6 mM, respectively, while the concentrations that inhibited the growth of the ZHY3 strain were determined to be 12.5 mM and 0.01 mM, respectively. These findings are

* Corresponding Author DOI: 10.37094/adyujsci.1565012

significant for understanding the effects of Zn deficiency on different yeast strains and highlighting the importance of Zn uptake genes. It is believed that the identified concentrations and the results obtained will contribute to studies related to Zn uptake and Zn uptake genes.

Keywords: Yeast; Zinc; ZHY3; W303; EDTA; EGTA.

ZHY3 ve W303 Maya Irklarının Çinko Zenginleştirilmiş Ortamdaki Gelişim Profillerinin Değerlendirilmesi

Öz

Tüm organizmalar hayati fonksiyonlarını sürdürebilmek için çinkoya ihtiyaç duymaktadır. Çinko eksikliğinde bitkisel üretim, hayvan ve insan sağlığı olumsuz etkilenmektedir. Ekmek mayası (*Saccharomyces cerevisiae*) bilimsel araştırmalar için model bir organizmadır ve metal eksikliği/toksisitesi çalışmalarında yaygın olarak kullanılmaktadır. Bu çalışmada çinko alım genlerinin tanımlanması çalışmalarında ilk aşama olan, mayanın gelişmesini önleyen yetersiz çinkolu ortam koşullarının belirlenmesi hedeflenmiştir. Mayanın yetiştirildiği temel besin ortamı olan YNB, mayanın büyümesine elverişli yeterli miktarda çinko içermektedir. Yetersiz çinko koşulları oluşturması için şelat ajanları (EGTA ya da EDTA) YNB besin ortamına eklenmiştir. ZHY3 (çinko alım genleri mutant) ve W303 (Yabanıl – WT) maya ırkları bu ortamlarda test edilmiştir. Mayaların büyüme profilleri farklı konsantrasyonlarda şelat ajanı içeren besin ortamlarında karşılaştırılmıştır. W303 ırkının büyümesini engelleyen EGTA ve EDTA konsantrasyonları sırasıyla 25 mM ve 1.6 mM olarak belirlenirken ZHY3 ırkının büyümesini engelleyen EGTA ve EDTA konsantrasyonların sırasıyla 12.5 mM ve 0.01 mM olarak belirlenmiştir. Bu bulgular, çinko eksikliğinin farklı maya ırkları üzerindeki etkilerini anlamak ve çinko alım genlerinin önemini vurgulamak açısından önemlidir. Belirlenen konsantrasyonların ve elde edilen sonuçların çinko alımı ve çinko alım genleri ile ilgili çalışmalara katkıda bulunacağı düşünülmektedir.

Anahtar Kelimeler: Maya; Çinko; ZHY3; W303; EDTA; EGTA.

1. Introduction

Zinc (Zn) is a trace element essential for the survival of living organisms and is the second most abundant trace element in the human body after iron [1]. Zn acts as a cofactor in approximately 300 enzymes and plays roles in various biological processes, including

indoleacetic acid production, photosynthesis, pollen formation, and maintaining cell membrane integrity [2-3]. A healthy adult body contains 1-2.5 grams (g) of Zn, and humans require an average daily intake of 10 milligrams (mg) of Zn. Individuals who receive less than this amount may experience Zn deficiency, leading to conditions such as anemia, vision problems, loss of appetite, immune system issues, delayed wound healing, and severe autoimmune diseases [1]. It is estimated that 17% of the world's population suffers from Zn deficiency [4]. Today, many people use Zn-supplemented medications and commercial products to increase their Zn levels. In plants, Zn deficiency can cause issues such as chlorosis, stunted growth, an increase in reactive oxygen species (ROS), and losses in yield and quality. To prevent these problems, Zn-fortified fertilizers are used, but they do not provide a permanent solution and can result in significant economic losses. Nearly half of the world's soil is deficient in Zn [5]. Moreover, even when sufficient Zn is available in the soil, many plant species cannot efficiently absorb it [2].

Baker's yeast (*Saccharomyces cerevisiae*) is one of the most well-known yeast species. Its simple structure, ease of genetic manipulation, rapid growth, and low cost make it a model organism in biotechnological studies [6]. The W303 yeast strain is a derivative of a yeast strain, S288C. It carries mutations in leu2, *trp1*, *ura3*, *ade2*, and *his3* genes and is known for its high transformation efficiency. It has been used in various studies involving gene expression, protein localization, cell cycle regulation, and DNA repair. YPD (Yeast Extract Peptone Dextrose) is a commonly used non-selective medium for yeast cell growth, while YNB (Yeast Nitrogen Base) is a selective medium for uracil auxotrophic yeast. CSM-ura, which contains amino acids except for uracil, is used in the selection of yeast transformants [7].

ZRT1 and ZRT2 were first identified as Zn transporters in yeast [8]. The *ZRT1* gene encodes a high-affinity Zn transporter, while the *ZRT2* gene encodes a low-affinity transporter. Both genes have eight transmembrane domains and share 67% similarity [8]. The ZRT1 protein has been reported to localize to the plasma membrane [9]. At the onset of Zn deficiency, the expression of the *ZRT2* transporter increases, while during critical levels of Zn deficiency, the expression of the *ZRT1* transporter is upregulated. The ZHY3 yeast strain is derived from the W303 strain. In addition to the mutations carried by W303, ZHY3 also possesses mutations in *ZRT1* and *ZRT2*. Therefore, it cannot take enough Zn from the external environment for growth. ZHY3 is frequently used in complementation tests aimed at determining the function of genes related to Zn uptake/export pathways.

Chelation refers to binding ions and molecules to metal ions [10]. Chelating agents have a reducing effect on the amount of metal ions in the environment. There are two main chelating

agents for Zn: EDTA (ethylenediaminetetraacetic acid) and EGTA (ethylene glycol-bis(β-aminoethyl ether)). EDTA and EGTA are frequently used in growth media to understand the effects of Zn deficiency. EDTA forms a complex by binding divalent free metal ions, and EGTA functions similarly but has a lower affinity for magnesium (Mg^{2+}) ions and a higher affinity for calcium (Ca^{2+}) ions.

In the present study, the pAG426GPD-ccdB yeast expression vector was transformed into two different yeast strains: ZHY3, which has mutations in the Zn uptake genes (*ZRT1* and *ZRT2*), and W303, which does not have these mutations. EGTA and EDTA chelating agents were then added in varying concentrations to the YNB selective medium containing a standard 25 μM $ZnSO_4$ to chelate the Zn. By creating Zn-deficient conditions in the selective medium, the growth profiles of the W303 and ZHY3 strains were determined.

2. Materials and Methods

2.1. Transformation of the pAG426GPD-ccdB Vector into W303 and ZHY3 Yeast Strains

In this study, the pAG426GPD-ccdB yeast expression vector (Addgene, plasmid #14156) was used. Thanks to the *URA3* gene presence in the vector, transformant colonies can survive in a medium lacking uracil by producing the URA3 protein.

The transformation of the pAG426GPD-ccdB vector into the W303 and ZHY3 yeast strains was performed using the transformation protocol reported by Benatuil et al. [11]. The transformed W303 and ZHY3 yeast cells were spread onto a YPD agar medium and incubated at 30°C for approximately three days, after which colony formation was observed. A single colony was selected from the resulting colonies, transferred to a liquid YPD medium, and shaken overnight at 30°C and 225 rpm. The next day, the cell concentration was measured as OD600 = 1.2. The cells were diluted in 50 ml of liquid YPD medium to a concentration of OD600 = 0.2. The cells were then incubated in a shaker at 30°C and 225 rpm until the OD600 reached 1.2. After approximately 5 hours, the cells were centrifuged at 3000 rpm for 3 minutes, and the pellet was obtained. The pellet was washed twice with 50 ml of cold distilled water and once with 50 ml of cold electroporation buffer. The cells were then centrifuged again at 3000 rpm for 3 minutes. The pellet was resuspended in 20 ml of 0.1 M LiAc/10 mM DTT and shaken at 30°C and 225 rpm for 30 minutes. After incubation, the cells were collected again by centrifugation at 3000 rpm, and the supernatant was removed. The pellet was resuspended in 100-200 μL of electroporation buffer, and the final volume was adjusted to 1 ml. The cells were added to electroporation cuvettes

(previously kept on ice), with 400 µL of cells in each cuvette. Then, 1 µg of the pAG426-GPD-ccdB plasmid was added to 400 µL of cells. The electroporation was performed under the conditions of 2.5kV, 25µF, and 3.0 milliseconds. After electroporation, the cells were transferred to tubes containing 8 ml of a 1:1 mixture of 1M sorbitol and YPD medium. The cells were spread (100 µL per plate) onto prepared YPD and YNB-URA selective agar media. The Petri dishes were incubated at 30°C for about three days until colonies were observed.

2.2. Determination of EGTA and EDTA Concentrations Inhibiting the Growth of W303 and ZHY3 Yeast Strains

The growth of ZHY3-pAG426GPD-ccdB and W303-pAG426GPD-ccdB yeast cells was observed in a YNB medium containing various concentrations of EGTA (0 – 25 mM) or EDTA (0 – 3.2 mM) to determine the concentrations that inhibit their growth. For this purpose, the cells were grown overnight in 5 ml of liquid YNB at 30°C and 225 rpm. The next day, the OD600 values of the cells were measured using a spectrophotometer and diluted to 1/10 serial dilutions starting from an OD600 of 0.2. Each cell sample (5 µL) was spotted onto plates containing YNB medium with the predetermined concentrations of EGTA or EDTA. The spotted cells were incubated at 30°C for about three days.

3. Results and Discussion

3.1. Transformation of the pAG426GPD-ccdB Vector into W303 and ZHY3 Yeast Strains

The transformation of the pAG426GPD-ccdB vector into the W303 and ZHY3 yeast strains was successfully performed (Fig.1 and Fig. 2). Colony formation was observed in the transformed cells within approximately three days. Since the W303 and ZHY3 cells without the vector did not produce the URA3 protein, no colony formation was observed on the URA-deficient YNB medium (-URA) for these cells (C, D).

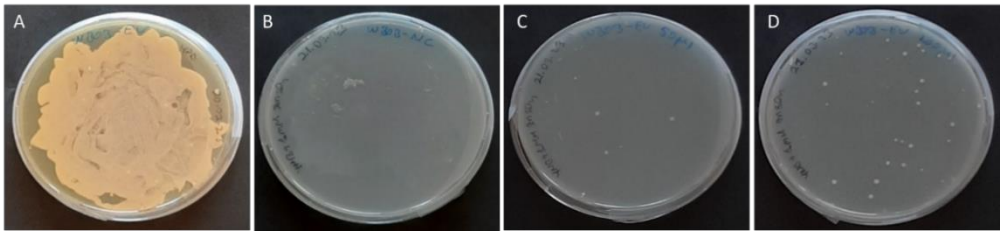

Figure 1: Transformation of the pAG426GPD-ccdB vector into W303 yeast cells. (A) W303 cells with the vector in YPD medium (positive control), (B) W303 cells without the vector in YNB medium (negative control), (C-D) W303 cells with the vector in YNB medium.

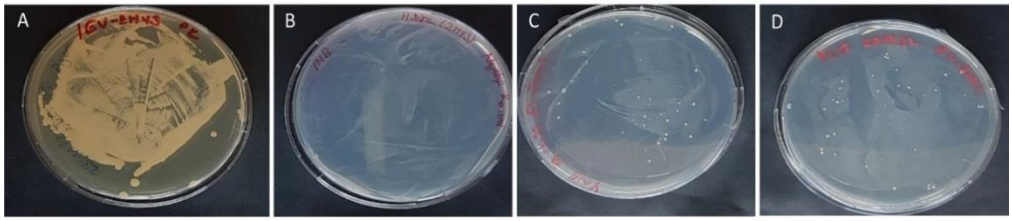

Figure 2: Transformation of the pAG426GPD-ccdB vector into ZHY3 yeast cells. (A) ZHY3 cells with the vector in YPD medium (positive control), (B) ZHY3 cells without the vector in YNB medium (negative control), (C-D) ZHY3 cells with the vector in YNB medium.

The W303 and ZHY3 cells containing the vector were spotted in serial dilutions onto YNB media containing 0, 0.5, 1, 2.5, 5, 7.5, 10, 12.5, 15, 17.5, 20, and 25 mM EGTA (Fig. 3) or YNB media containing 0, 0.0005, 0.001, 0.002, 0.01, 0.025, 0.05, 0.075, 0.1, 0.2, 0.4, 0.8, 1.6, and 3.2 mM EDTA (Fig. 4).

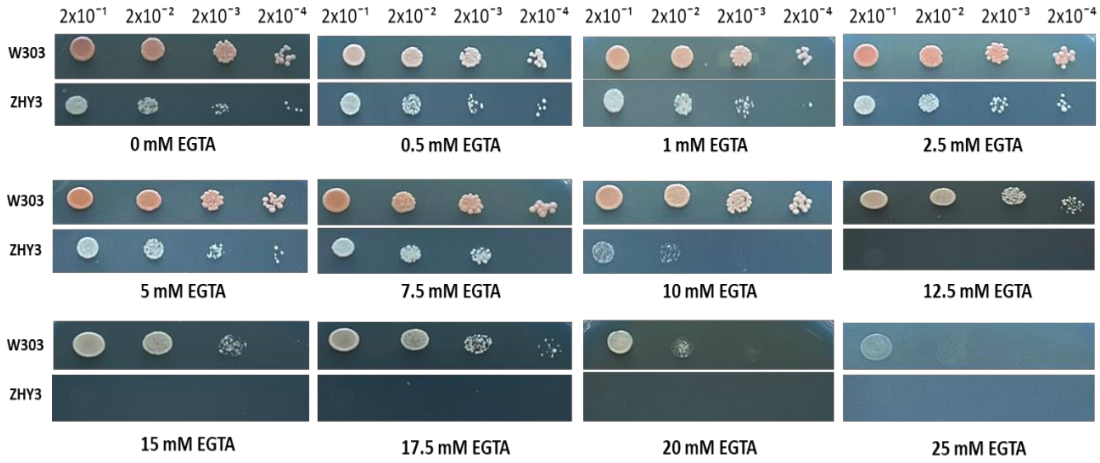

Figure 3: Growth profiles of W303 and ZHY3 yeast strains containing the pAG426GPD-ccdB vector in YNB medium with varying concentrations of EGTA.

The cells of the transformed W303 strain were not critically affected by Zn deficiency, but they did not grow on YNB medium containing 25 mM EGTA. In contrast, the cells of the transformed ZHY3 strain were critically affected by Zn deficiency, and their growth significantly decreased starting from the medium containing 12.5 mM EGTA. In all media, the W303 strain showed more growth than the ZHY3 strain.

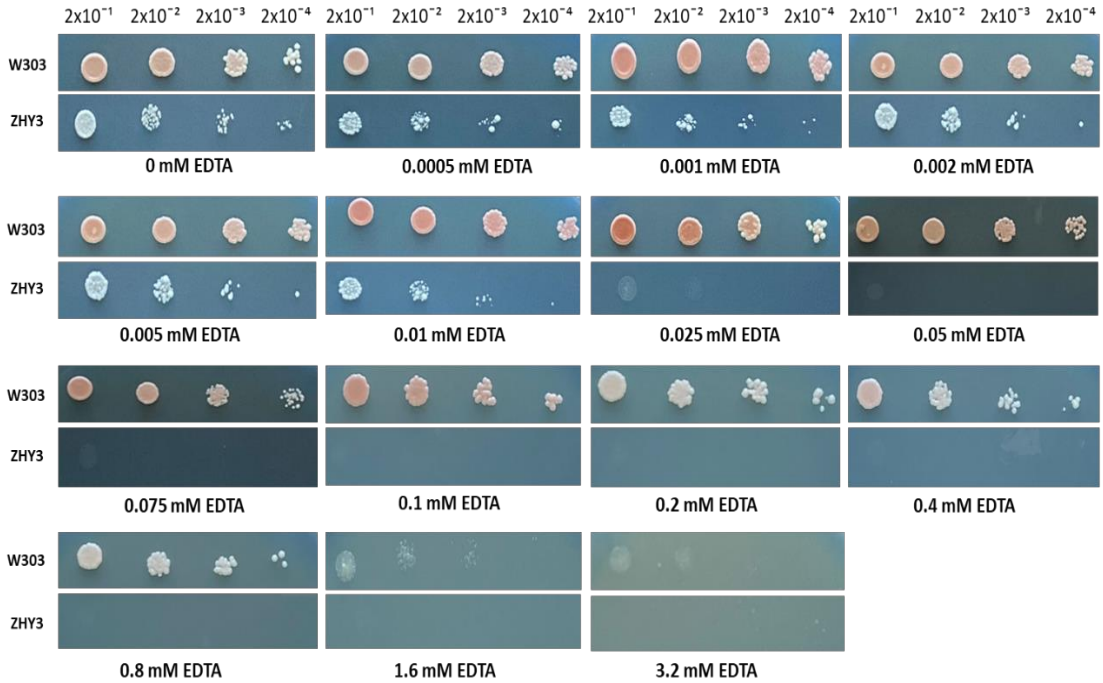

Figure 4: Growth profiles of W303 and ZHY3 yeast strains containing the pAG426GPD-ccdB vector in YNB medium with varying concentrations of EDTA.

The transformed W303 cells continued to grow in the YNB medium containing 0-0.8 mM EDTA, but growth slowed down in the medium containing 1.6 mM EDTA, and it was completely halted in the medium with 3.2 mM EDTA. On the other hand, the transformed ZHY3 cells were critically affected by Zn deficiency and were unable to grow in the medium containing as little as 0.01 mM EDTA. Across all EDTA and EGTA concentrations, the W303 strain exhibited more growth than the ZHY3 strain.

4. Discussion and Conclusion

Zinc deficiency is a widespread issue affecting agricultural productivity and human health. Insufficient zinc levels result in notable reductions in plant yield and quality while also contributing to various health problems in humans. To prevent the negative effects of Zn deficiency in plants, it is crucial to fully understand the mechanisms of plant Zn uptake and to identify the genes associated with Zn absorption. Studies addressing Zinc deficiency have been used the ZHY3 yeast strain, which has mutations in intracellular Zn uptake genes, alongside other wild-type strains. However, the concentration of Zn deficiency that restricts ZHY3's growth varies across studies. For instance, Kozak et al. [12] used the wild-type DY1457 strain and the derived ZHY3 strain in their study. They observed that DY1457 cells could grow in a YNB medium containing 7.5 mM EGTA, whereas ZHY3 cells were unable to grow at both 5 and 7.5 mM EGTA concentrations. Similarly, Li et al. [13] reported that DY1451 cells could grow at 0.4 mM EDTA,

while ZHY3 cells did not show any growth at that concentration. Yang et al. [14] found that wild-type cells could grow in a medium with 5 mM EGTA, but ZHY3 cells were unable to grow in EGTA-containing environments.

In the present study, the growth profiles of the wild-type yeast strain W303 and the ZHY3 strain, derived from W303 but with mutations in Zn uptake genes, were compared in YNB media containing different concentrations of the chelating agents EDTA and EGTA. The impact of the Zn uptake genes *ZRT1* and *ZRT2* was clearly observed in these strains. Zn chelation occurred in YNB media with varying concentrations of EDTA and EGTA, creating progressively increasing Zn-deficient conditions. In YNB media containing EGTA, W303 cells were able to grow up to 25 mM, while ZHY3 cells, due to mutations in Zn uptake genes, were unable to grow starting from 12.5 mM EGTA. Similarly, in YNB media containing EDTA, W303 cells grew up to 0.8 mM, while ZHY3 cells showed no growth starting from as low as 0.01 mM EDTA.

These findings, along with previous studies, demonstrate that slight differences in chelating agent concentrations can affect the growth inhibition of yeast strains depending on the specific strain and the technical conditions of the study. The chelating agent concentrations identified in this study will contribute to gene function analysis and characterization studies related to Zn deficiency.

Acknowledgements

This study was funded by the Akdeniz University Scientific Research Projects Coordination Unit under grant number FYL-2024-6575.

References

[1] Akdeniz, V., Kınık, Ö., Yerlikaya, O., Akan, E., *Importance of zinc in human health and nutrition physiology,* Akademik Gıda*,* 14(3), 307–314, 2016.

[2] Cakmak, I., Marschner, H., *Mechanism of phosphorus-induced Zn deficiency in cotton. I. Zn deficiency-enhanced uptake rate of phosphorus,* Physiologia Plantarum, 68(3), 483-490, 1986.

[3] Ajeesh Krishna, T. P., Maharajan, T., Victor Roch, G., Ignacimuthu, S., Antony Ceasar, S., *Structure, function, regulation and phylogenetic relationship of ZIP family transporters of plants,* Frontiers in Plant Science, 11, 533228, 2020.

[4] Belay, A., Gashu, D., Joy, E. J., Lark, R. M., Chagumaira, C., Likoswe, B. H., Broadley, M. R., *Zinc deficiency is highly prevalent and spatially dependent over short distances in Ethiopia*, Scientific Reports*,* 11(1), 6510, 2021.

[5] Deshpande, J. D., Joshi, M. M., Giri, P. A., *Zinc: The trace element of major importance in human nutrition and health*, International Journal of Medical Science and Public Health, *2*(1), 1-6, 2013.

[6] Karathia, H., Vilaprinyo, E., Sorribas, A., Alves, R., *Saccharomyces cerevisiae as a Model Organism: A Comparative Study,* Plos One, 6(2), e16015, 2011.

[7] Budak, K., Akbudak, M.A., *Yeast functional screen to determine cDNAs of European alkali grass* (*Puccinellia distans) conferring selenium (Se) toxicity*, ISPEC Journal of Agricultural Sciences, 6(4), 698–707, 2022.

[8] Eide, D., Broderius, M., Fett, J., Guerinot, M.L., *A novel iron-regulated metal transporter from plants identified by functional expression in yeast*, Proceedings of the National Academy of Sciences, 93(11), 5624-5628, 1996.

[9] Guerinot, M.L., *The ZIP family of metal transporters*, Biochimica et Biophysica Acta, 1465, 190, 2000.

[10] Evangelou, M. W., Ebel, M., & Schaeffer, A., *Chelate assisted phytoextraction of heavy metals from soil. Effect, mechanism, toxicity, and fate of chelating agents*, Chemosphere, 68(6), 989-1003, 2007.

[11] Benatuil, L., Perez, J.M., Belk, J., Hsieh, C.M., *An improved yeast transformation method for the generation of very large human antibody libraries,* Protein Engineering, Design & Selection, 23(4), 155-159, 2010.

[12] Kozak, K., Papierniak, A., Barabasz, A., Kendziorek, M., Palusińska, M., Williams, L. E., Antosiewicz, D.M., *NtZIP11, a new Zn transporter specifically upregulated in tobacco leaves by toxic Zn level,* Environmental and Experimental Botany, 157, 69–78, 2019.

[13] Li, S., Liu, Z., Guo, L., Li, H., Nie, X., Chai, S., Zheng, W., *Genome-wide identification of wheat ZIP gene family and functional characterization of the TaZIP13-B in plants,* Frontiers in Plant Science, 12, 748146, 2021.

[14] Yang, M., Li, Y., Liu, Z., Tian, J., Liang, L., Qiu, Y., Wang, G., Du, Q., Cheng, D., Cai, H., Shi, L., Xu, F., Lian, X, *A high activity zinc transporter OsZIP9 mediates zinc uptake in rice*, The Plant Journal, 103(5), 1695-1709, 2020.

Adıyaman University Journal of Science
https://dergipark.org.tr/en/pub/adyujsci
DergiPark AKADEMİK
ISSN 2147-1630
e-ISSN 2146-586X

Investigation of Biological Activities of Some Microalgae Extract Isolated from Kabakli Pond (Diyarbakır) Turkey

Feysel ÇAKMAK[1,*], Ahmet İsmail ÖZKAN[2], Nesrin HAŞİMİ[3], Özlem DEMİRCİ[1], Melike CİNİVİZ[4], Lokman VARIŞLİ[5], Ersin KILINÇ[6], Veysel TOLAN[7]

[1]*Dicle University, Faculty of Science, Department of Biology, 21280, Diyarbakır, Türkiye*
feyselcakmak@gmail.com, ORCID: 0000-0002-4827-150X
[2]*Artvin Çoruh University, Medicinal-Aromatic Plants Application and Research Center, Artvin, Türkiye*
aiozkan@artvin.edu.tr, ORCID: 0000-0002-4511-2386
[3]*Batman University, Faculty of Science, Department of Biology, Batman, Türkiye*
nesrinhasimi@hotmail.com, ORCID: 0000-0003-1367-5624
[1]*Dicle University, Faculty of Science, Department of Biology, 21280, Diyarbakır, Türkiye*
ozdem22@gmail.com, ORCID: 0000-0001-9511-2010
[4]*Bursa Uludağ University, Department of Food Engineering, Bursa, Türkiye*
melike.ciniviz.mc@gmail.com, ORCID: 0000-0001-6089-1659
[5]*Dicle University, Faculty of Science, Department of Molecular Biology and Genetics, 21280, Diyarbakır, Türkiye*
lokman.varisli@dicle.edu.tr, ORCID: 0000-0002-4337-9327
[6]*Dicle University, Department of Chemistry and Chemical Processing Technologies, Vocational School of Technical Sciences, Diyarbakır, Türkiye*
kilincersin@gmail.com, ORCID: 0000-0001-5223-9919
[7]*Dicle University, Faculty of Science, Department of Molecular Biology and Genetics, 21280, Diyarbakır, Türkiye*
vetolan@dicle.edu.tr, ORCID: 0000-0003-0172-6957

Received: 14.10.2024 **Accepted:** 16.11.2024 **Published:** 31.12.2024

Abstract

The antimicrobial, antioxidant and mutagenic activities of methanolic extracts of microalgae species isolated from Kabakli Pond (37° 55' 23N, 40°17' 40E, Diyarbakır) and identified as *Chlorella vulgaris* Beyerinck and *Chroococcus limneticus* Lemmermann were

* Corresponding Author DOI: 10.37094/adyujsci.1566859

investigated. The highest antioxidant activity was observed in the ABTS•+ assay of *C. vulgaris* (36.63%) and *C. limneticus* (28.48%) at a concentration of 100 µg/ml concentration. The DPPH and CUPRAC assays showed weak activity. The antioxidant activity did not appear to be significant for either species when compared with the positive controls. *C. vulgaris* showed high antimicrobial activity with inhibition zone and MIC value against S. aureus. There seemed to be no mutagenic activities; however, *C. limneticus* showed an effect on the colony structure of S. *typhimurium strain TA98. C. vulgaris* has a good antimicrobial potential, whereas *C. limneticus* has relatively weak potential. *C. limneticus* a relatively has a higher antioxidant activity compared to *C. vulgaris,* but the activities of both extracts are weak compared to the controls. None of the tested extracts showed mutagenic activity against *S. typhimurium* TA98 at any of the concentrations. These organisms via different solvents or extraction systems since they may affect various biological systems.

Keywords: Microalgae; Mutagenicity; Biological activity; Antioxidant; Antimicrobial**.**

Kabaklı Göleti'nden (Diyarbakır) İzole Edilen Bazı Mikroalg Ekstraktlarının Biyolojik Aktivitelerinin Araştırılması

Öz

Kabaklı Göleti'nden (37° 55' 23K, 40°17' 40D, Diyarbakır) izole edilen ve *Chlorella vulgaris* Beyerinck ve *Chroococcus limneticus* Lemmermann olarak tanımlanan mikroalg türlerinin metanol ekstraktlarının antimikrobiyal, antioksidan ve mutajenik aktiviteleri araştırıldı. En yüksek antioksidan aktivite, 100 µg/ml konsantrasyonunda *C. vulgaris* (%36,63) ve *C. limneticus* (%28,48) için ABTS•+ analizinde gözlendi. DPPH ve CUPRAC analizleri zayıf aktivite gösterdi. Antioksidan aktivite, pozitif kontrollerle karşılaştırıldığında her iki tür için de önemli görülmedi. *C. vulgaris* metanol ekstraktlarının *S. aureus*'a karşı inhibisyon zonu ve MİK değeri ile yüksek antimikrobiyal aktivite gösterdi. *C. limneticus* metanol ekstraktlarının *S. typhimurium* TA98 üzerinde herhangi bir mutajenik aktivitesi gözlenmedi. *C. vulgaris* metanol ekstraktı iyi bir antimikrobiyal potansiyele sahipken, *C. limneticus* ektraktı nispeten zayıf bir potansiyele sahiptir. *C. limneticus* metanol ekstraktı*, C. vulgaris* metanol ekstraktına kıyasla nispeten daha yüksek bir antioksidan aktiviteye sahip ancak her iki özütün aktiviteleri kontrollerle karşılaştırıldığında zayıf olarak gözlendi. Test edilen özütlerin hiçbiri, herhangi bir konsantrasyonda *S. typhimurium* TA98'e karşı mutajenik aktivite göstermedi. Bu organizmalar

farklı çözücüler veya ekstraksiyon sistemleri aracılığıyla çeşitli biyolojik sistemleri etkileyebilirler.

Anahtar Kelimeler: Mikroalg; Mutajenite; Biyolojik aktivite; Antioksidan, Antimikrobiyal.

1. Introduction

Algae, which are multicellular or single-celled organisms, are classified as macro- or microalgae depending on their size [1]. Microalgae are the most important members of aquatic ecosystems because they accumulate important metabolites in their cells. They also play a key role at the top of the food pyramid as photosynthetic eukaryotes, which are among the oldest life forms on the planet. Microalgae have long attracted attention, both as a food source and for their use in many fields such as cosmetics, and this interest has increased in recent years [2, 3].

Although microalgae range from prokaryotic cyanobacteria to eukaryotic microalgae, this diversity is not yet fully understood. Recent research shows that although more than 50,000 different species of microalgae are found in oceans and fresh water (lakes, ponds and rivers), only 30,000 of these species have been studied [4–7].

Microalgae are unicellular and fast-growing organisms that produce various bioactive compounds through photosynthesis and are more productive than terrestrial plants [8, 9]. In addition, the high adaptability of microalgae to changing environmental conditions, such as ambient temperature, pH, humidity and salinity, makes them good candidates for drug discovery [3, 10–13]. In fact, microalgae have been shown to produce different and higher levels of metabolites under stress and laboratory conditions than they can produce in their natural environment [14].

Plants have been used as medicines for many years because these natural products have therapeutic potential and have led to the development of new medicines [15, 16]. Microalgae have also been used for the same purpose for a long time. The biologically active metabolites present in microalgae can be derived from a multitude of molecular structures, including various fatty acids; peptides, carbohydrates, lipopeptides, polyketides, lactones, amides, alkaloids, amino acid derivatives, aromatic substances, terpenoids, and terpenes. On the other hand, although most metabolites accumulate in the cells, some can be released into the environment, examples of the biological activity of extracellular metabolites can be attributed to five antibacterial diterpenoids derived from *Nostoc commune* [17], a brominated indole alkaloid of *Anabaena constricta* that possesses antimicrobial activity [18], the antifungal peptides produced by *Tolypotrix byssoidea*

[17], *Fischerella ambigua* excretes a broad-spectrum antibacterial and antifungal substance called "parsiguine," which was also gathered from paddy fields [19]. Moreover, it has been demonstrated that isolates of cyanobacteria from Brazil are capable of producing antimicrobial non-ribosomal peptides [20], and lipophilic extracts of *Synechocystis* sp. have antimicrobial fatty acids and volatiles [21].

Kabaklı pond is a natural pond located at the provincial borders of Diyarbakır in Türkiye (37° 55' 23N, 40°17' 40E), and 94 algae taxa have been recorded in Kabaklı pond in previous studies. The pond is exposed to a significant amount of organic pollution because of sewage waste and animal husbandry in the surrounding area; therefore, the number of algae in the water reaches millions per liter. The pond is exposed to a significant amount of organic pollution because of sewage waste and animal husbandry in the surrounding area; therefore, the number of algae in the water reaches millions per litter [22].

In this study, the antioxidant, antimicrobial, and mutagenic activities of methanol extracts of *Chlorella vulgaris* Beyerinck [Beijerinck] (*C. vulgaris*) and *Chroococcus limneticus* Lemmermann (*C. limneticus*) were investigated.

2. Materials and Methods

2.1. Sample preparation

Two freshwater species of microalgae, *C. vulgaris* and *C. limneticus*, were collected from Kabaklı Pond (37° 55' 23N, 40° 17' 40E, Diyarbakır, southeastern Türkiye) and isolated using subculture BG-11 agar medium. Colonies were photographed using a Nikon 80i microscope with a 100x objective and an attached digital camera. The samples were then identified according to Prescott [23].

2.2. Extraction procedure

The microalgae species were harvested by centrifugation (4500 rpm for 5 min) in the stationary phase, and the supernatants were discarded. The wet pellets (about 1 g) were re-suspended in 18 ml of methanol: water (5:1) and the cells were disrupted by sonication using a Soniprep 150 sonicator. Sonication was performed on ice for a total of 5 min (5 pulses of 30 s each at 30-second intervals to keep it out from any temperature rise). The cells were then incubated on ice for 2 h by shaking at 120 rpm and centrifuged at 4800 rpm for 15 min to remove cell debris. Subsequently, the supernatants were collected and evaporated using a rotary vacuum evaporator at 40°C [24].

2.3. GC-MS analysis of essential oils

The sample was analyzed using an Agilent Technologies 6890N Network GC System, Agilent Technologies 5973 Inert Mass Selective Detector, and Columns: 19091N-136 HP-INNOWAX Length (meters) =60; I.D. (mm)=0.250; Film (micrometer) = 0.25. Temperature Limits: From 40°C to 260°C. 1- The detector was set to 250 °C. The stepped temperature program was held at 60 °C for 10 minutes initial, followed between 60-250 °C by 50 minutes at a rate of 5 °C/min. The GC-MS interface temperature was 250 °C. The injection volume was 2 µL and the solvent delay was 2 minutes. The total run time was 98 minutes. Compounds identification were obtained by mass spectra of references in Mass Spectral Library.

2.4. Antioxidant activity of ethanol extract

2.4.1. DPPH radical scavenging assay

DPPH (2,2´-diphenyl-1-picrylhydrazyl) radical scavenging activity was determined according to the Blois [25].

The percentage of DPPH scavenging activity is calculated using the following formula: [Ac–As/Ac] × 100.

In this context, "AC" represents the absorbance value of the control sample, while "AS" denotes the absorbance value of a solution added as a test sample. Microsoft Excel was used to calculate these values. The tests were performed in triplicates. The values indicated are as the mean ± SD of three independent measurements.

2.4.2. ABTS assay

2,2'-Azinobis-[3-ethylbenzthiazoline-6-sulfonic acid] (ABTS) was dissolved in water (7mM) then ABTS solution was combined with the $K_2S_2O_8$ solution and allowed to stand for 12-16 hours at room temperature in the absence of light. Subsequently, the ABTS solution was diluted to an absorbance of 0.70 at 734 nm. BHA and BHT were used as positive controls. 160 µL of ABTS•+ solution and 40 µL of different concentrations of samples (10, 25, 50, and 100 µg/ml) were added to 96 well plates. Following a 30-minute incubation period at room temperature, the absorbance was determined at 734 nm using a spectrophotometer [26].

$$I\% = (Acontrol - Asample / Acontrol) \times 100 \quad (1)$$

2.4.3. Copper (II) reductive antioxidant activity (CUPRAC) assay

The Cupric ion-reducing antioxidant capacity (CUPRAC) was determined using the method described by Apak et al. [27]. In summary, 61 µL $CuCl_2.2H_2O$, 61 µL neocuproine, and 61 µL ammonium acetate buffer were added to 67 µL of extract samples prepared at different concentrations (10, 25, 50,100 µg/mL). Following incubation for 1 h measurements were performed at 450 nm using a plate reader, and the half-maximal inhibitory concentration (IC50) values were calculated.

2.4.4. Antimicrobial activity

Antimicrobial activity of the extract samples prepared at different concentrations (200, 300, and 400 µg/mL) against Gram positive (*Staphylococcus aureus* ATCC 25923, *Streptococcus pyogenes* ATCC 19615), Gram negative (*Escherichia coli* ATCC 25922, *Pseudomonas aeruginosa* ATCC 27853) bacteria and yeast (*Candida albicans* ATCC 10231) were determined using the disc diffusion method [28].

100 µL of each microorganism equal to 0.5 McFarland turbidity was seeded onto Mueller-Hinton agar plates. The 15 µL volume samples, which were prepared at different concentrations of all extracts, were impregnated on sterile paper discs placed in plates. Following incubation at 37°C for 24 h (bacteria) and 30°C for 48 h (yeast), the inhibition zone diameters were measured in millimetres, and the extracts were processed to determine the MIC value. Serial dilutions (100 µL) of extracts, 90 µL of nutrient broth, and 10 µL of microorganism overnight cultures (turbidity equal to 0.5, McFarland) were pipetted into 96 well sterile plates. Following incubation at 37°C for 24 h, the evaluations were performed. The concentration without visible growth was determined as the MIC value. All tests were performed in triplicate. As positive controls for bacteria and yeast, respectively, ampicillin and fluconazole were used.

2.4.5. Mutagenic activity

The *Salmonella typhimurium* TA98 strains were purchased from the Salmonella Genetic Stock Centre (University of Calgary, Canada), and their genetic backgrounds were controlled as previously described [29, 30].

Our experiment was performed using the TA98 strain of *S. typhimurium*. Positive and negative controls were used for each test. Compounds were considered mutagenic (reduction in the number of returning colonies). The data were ranked as follows.

Test compounds were considered mutagens if there was a two-fold increase in the number of returned colonies or a dose-dependent increase in the number of spontaneously returned colonies. Microalgae extracts were dissolved in dimethyl sulfoxide (DMSO). The sample concentrations were prepared as 12.5, 25, 50, 100, 200, 400 and 800 µg/plate. Daunomycin (in distilled water- 6 µg/ml) was used as the positive control and DMSO as the negative control.

2.5. Statistical analysis

The antimicrobial and antioxidant activity results are expressed as the mean ± standard deviation (SD) of three experiments. Analysis of variance (ANOVA) followed by Dunnett's test was used to compare the treated groups with the control group. P-values less than or equal to 0.05 were considered to indicate statistical significance.

3. Results

Both qualitative and quantitative GC-MS analysis results of *C. vulgaris* and *C. limneticus* ethanol extracts are shown in Tables 1 and 2. Methanol extracts of algae have been found to contain bioactive components. The chemical components of the algae used in this study for *C. limneticus* were oleic acid and hexadecanoic acid (Table 2, Fig. 2), and 9,12-Octadecadienoic acid was the major fatty acid for *C. vulgaris*.

Table 1: GC/MS Analysis of the Methanol Extract of *C. vulgaris*.

PK	RT	Area%	ID	Qual
1	29.702	0.10	Decanoic Acid	49
3	32.752	0.03	Heptanoic Acid	78
4	36.969	0.15	Octanoic Acid	90
5	43.309	0.07	Nonanoic Acid	95
6	50.570	0.03	Alpha-(Aminomethylene)glutaconic anhydride	49
7	51.360	0.04	(9E)-9-Octadecenoic Acid	58
8	55.938	-0.03	Undecanoic Acid	38
10	67.393	14.47	n-Hexadecanoic Acid	96
15	70.958	3.28	Heptaethylene glycol monododecyl ether	62
16	71.318	18.22	9-Octadecenoic acid, (E)	99
19	74.288	2.69	15-Crown-5	78
21	75.324	1.74	Octaethylene glycol	86
22	75.936	5.97	1,4,7,10,13,16-Hexaoxacyclooctadecane	90
32	83.975	1.94	2-[2-[2-[2-[2-[2-[2-[2-[2-(2-Hydroxyethoxy)ethoxy]ethoxy]ethoxy]ethoxy]ethoxy]ethoxy]ethoxy]ethanol	86
37	91.545	2.68	18,18'-Bi-1,4,7,10,13,16-hexaoxacy clononadecane	86

PK: Peak; RT: Reiteration Time. Area% gives the percentage of that item from the peak area.

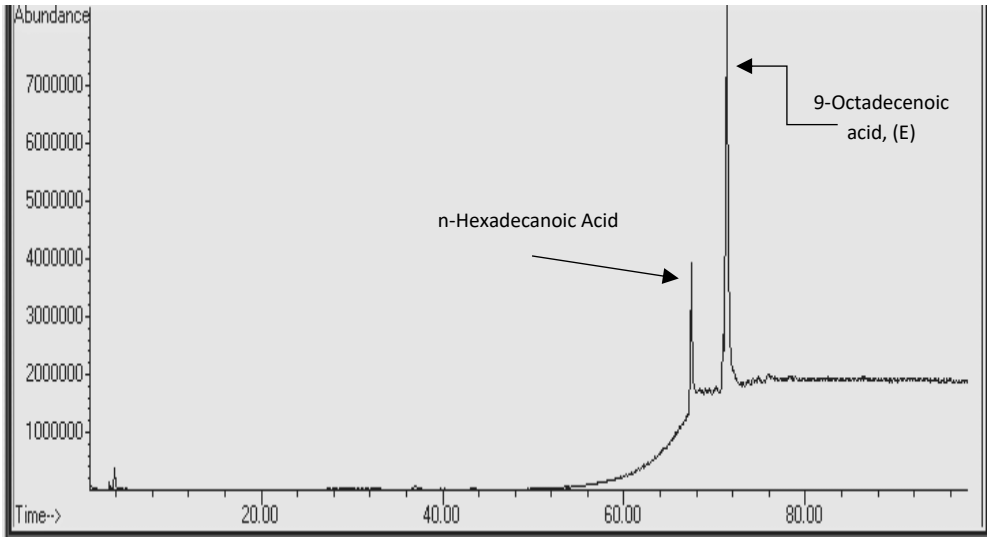

Figure 1: GC-MS analysis of methanol extract of *C. vulgaris*.

Table 2:GC/MS Analysis of the Methanol Extract of *C. limneticus*.

PK	RT	Area %	ID	Qual
1	28.804	0.25	Methyl d-glycero-beta-d-gulo-heptoside	59
2	31.499	0.09	Heptanoic acid	59
4	35.281	0.20	Octanoic acid	93
6	42.273	0.10	Nonanoic acid	91
8	51.165	0.06	Decanoic Acid	81
9	55.840	-0.01	Undecanoic Acid	83
11	58.438	0.06	(9Z)-1-(2,3-Dimethoxypropoxy)-9-OC Tadecene	72
12	67.393	15.25	n-Hexadecenoic acid	97
13	69.407	3.11	Octaethylene glycol monododecyl ether	83
15	71.324	29.60	Oleic Acid	94
16	73.115	1.70	18,18'-Bi-1,4,7,10,13,16-hexaoxacy clononadecane	86
20	75.913	5.72	Octaethylene glycol monododecyl ether	81
21	77.366	1.50	Octaethylene glycol	86
25	81.692	1.79	1,4,7,10,13,16-Hexaoxacyclooctadecane	90
31	89.279	0.79	2-[2-[2-[2-[2-[2-[2-[2-[2-(2-Hydroxyethoxy)ethoxy]ethoxy]ethoxy]ethoxy]ethoxy]ethoxy]ethoxy]ethanol	86
33	91.488	2.25	Heptaethylene glycol monododecyl ether	80

PK: Peak; RT: Reiteration Time. Area% gives the percentage of that item from the peak area.

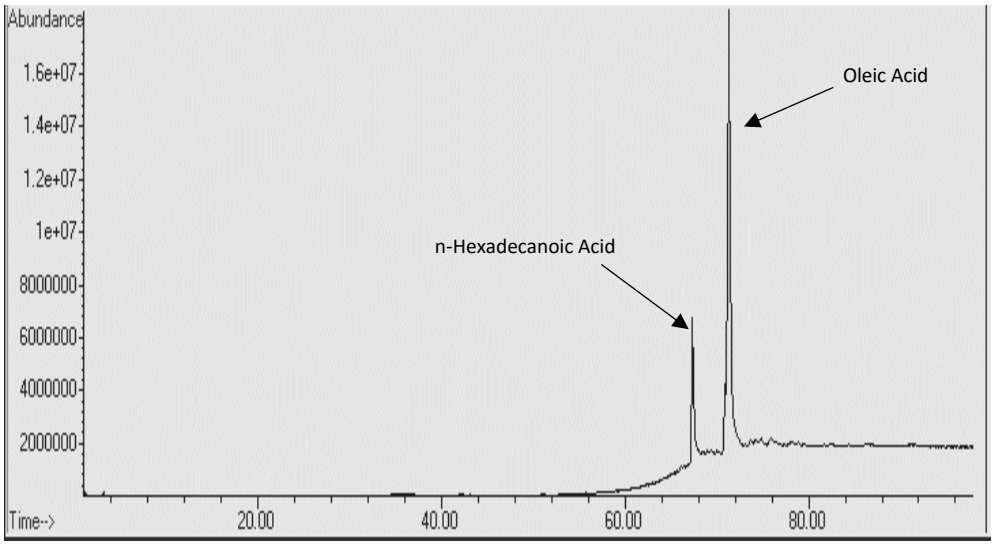

Figure 2: GC-MS analysis of methanol extract of *C. limneticus.*

3.1. Antioxidant activity

3.1.1. DPPH radical scavenging assay

The antioxidant activities of microalgae extracts were determined as percent inhibition according to the DPPH method at 10, 25, 50, and 100 µg/ml concentrations, and IC50 values are shown in Table 3 and Fig. 3, respectively. DPPH free radical scanning activities increased as concentrations increased, regardless of the non-significant antioxidant activity of the two microalgae extracts compared to that of the positive controls. An IC50 value of 325.89 µg/ml for *C. vulgaris* and an IC50 value of 471.26 µg/ml for *C. limneticus* was calculated (Fig. 3). *C. limneticus* showed stable antioxidant activity at concentrations below 50 µg/ml, whereas there was a significant increase from 50 µg/ml to 100 µg/ml. Taghavi et al. [31] demonstrated a 42.96% inhibition of ethanol extract at a concentration of 200 µg/ml in the DPPH assay.

Table 3: DPPH free radical-scavenging activities of *C. vulgaris* and *C. limneticus* methanol extracts. The results show the I% values. BHA and BHT were used as positive controls.

Concentrations (µg/ml)	***C. vulgaris***	***C. limneticus***	**BHA**	**BHT**
10	3.84±0.02	1.86±0.00	70.28±0.00	21.49±0.04
25	4.06±0.01	2.59±0.00	87.03±0.00	25.37±0.03
50	7.57±0.01	4.67±0.08	94.69±0.05	44.7±0.02
100	15.48±0.02	41.02±0.02	95.77±0.00	58.25±0.00

The results are presented as the mean ± standard deviation.

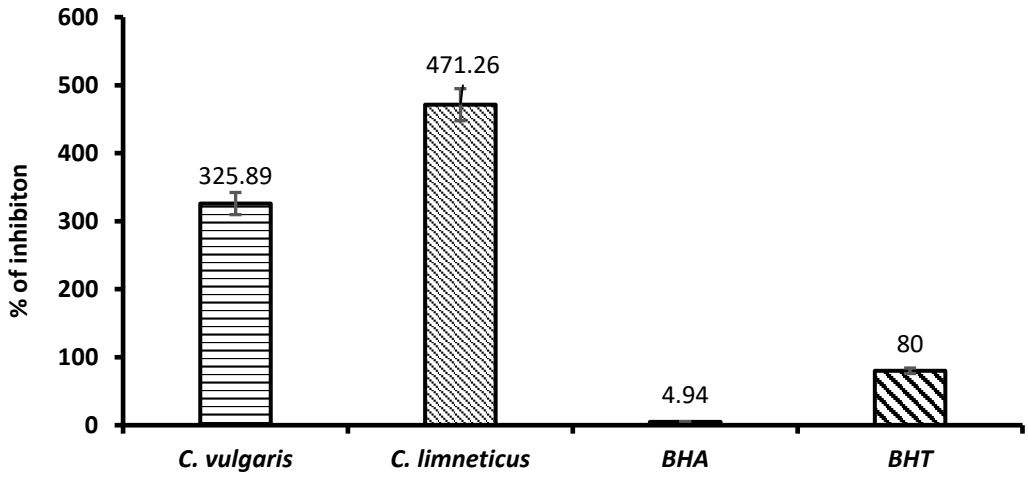

Figure 3: DPPH free radical-scavenging activities of *C. vulgaris* and *C. limneticus* methanol extracts. The results showed IC50 values (µg/ml) of I%. BHA and BHT were used as positive controls.

3.1.2. ABTS assay

The ABTS assay results of the extracts at concentrations of 10, 25, 50, and 100 µg/ml are shown in Table 4, and IC50 values are shown in Fig. 4. In this method, higher activity was obtained than in the DPPH method. However, no significant antioxidant activity was observed when the extracts were compared with the positive controls. The IC50 value of 137.32 µg/ml for *C. vulgaris* and an IC50 value of 172.83 µg/ml and *C. limneticus* was calculated (Fig. 4). In contrast, BHA and BHT possess values of 2.57 and 52.14 µg/ml IC50 respectively. The *C. vulgaris* extract showed better antioxidant activity than *C. limneticus* in both DPPH and ABTS assays, with no significant difference.

Table 4: ABTS cation radical-scavenging activity of *C. vulgaris* and *C. limneticus* methanol extracts. The results show the I% values. BHA and BHT were used as positive controls.

Concentrations (µg/ml)	***C. vulgaris***	***C. limneticus***	**BHA**	**BHT**
10	5.21±0.00	2.1±0.00	88.23±0.00	56.89±0.03
25	9.66±0.00	5.71±0.01	89.41±0.00	86.89±0.00
50	19.83±0.00	16.55±0.02	89.57±0.00	80.33±0.00
100	36.63±0.00	28.48±0.06	89.74±0.00	69.74±0.00

The results are presented as the mean ± standard deviation.

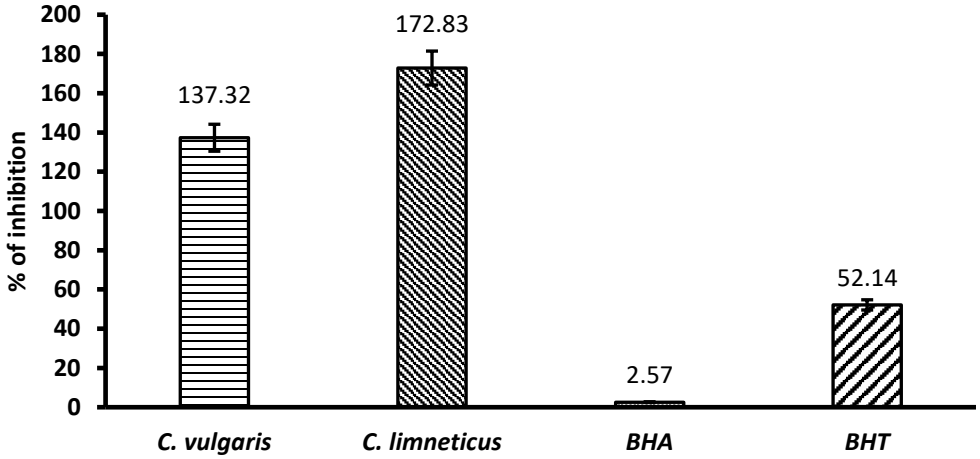

Figure 4: ABTS radical-scavenging activity of *C. vulgaris* and *C. limneticus* methanol extracts. The results showed IC50 values (µg/ml) of I%. BHA and BHT were used as positive controls.

3.1.3. Copper (II) reductive antioxidant activity (CUPRAC) assay

The copper (II) ion reduction capacities of the extracts and the positive control samples are presented in Table 5 and Fig. 5. In this method, the results are given as the absorbance value that increased absorbance value expressed increased activity. The extracts showed increased concentration-dependent activity, whatever there were no significant activities compared with the positive controls. As shown at Fig. 5, an A0.5 value of 198.22 µg/ml for *C. vulgaris* and an A0.5 value of 360 µg/ml for *C. limneticus* was calculated.

Table 5: CUPRAC-copper (II) ion-reduction capacities of *C. vulgaris* and *C. limneticus* methanol extracts. The results show the I% values. BHA and BHT were used as positive controls.

Concentrations (µg/ml)	***C. vulgaris***	***C. limneticus***	**BHA**	**BHT**
10	0.16±0,03	0.15±0.01	1.59±0.71	0.93±0.21
25	0.17±0,00	0.19±0.04	2.4±0.3	1.63±0.24
50	0.23±0,01	0.19±0.03	>4	3.67±0.1
100	0.32±0,00	0.24±0.05	>4	>4

The results are presented as the mean ± standard deviation.

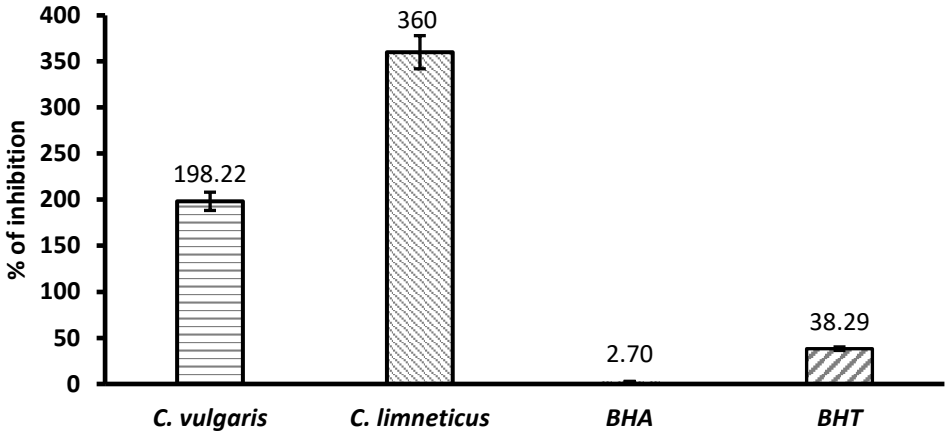

Figure 5. Copper (II) ion-reduction capacities of *C. vulgaris* and *C. limneticus* methanol extracts. The results showed IC50 values (µg/ml) of I%. BHA and BHT were used as positive controls.

3.1.4. Antimicrobial assay

Table 6 indicates the antimicrobial activity of the microalgae. The tested samples exhibited varying levels of antimicrobial activity. *C. vulgaris* was exhibited high activity with inhibition zone diameter greater than 22 mm and the MIC values range from 75 to 85 µg/ml. *C. limneticus* was exhibited weak activity with an inhibition zone diameter less than 12 mm and the MIC values range from 200 to 240 µg/ml. The major effectiveness (inhibition zone diameter 28±0.8 and MIC value 75 µg/ml) was recorded for *C. vulgaris* against *S. aureus*.

Table 6: Antimicrobial activities of *C. vulgaris* and *C. limneticus* methanol extracts.

Doses (µg/ml)		*E. coli*		*P. aeruginosa*		*S. aureus*		*S. pyogenes*		*C. albicans*	
		DD	MIC	DD	MIC	DD	MIC	DD	MIC	DD	MIC
C. vulgaris	400	24±0.3		22±0.8		28±0.8		23±0.8		22±1.0	
	300	20±0.9	85±1.0	16±0.5	75±0.3	24±1	75±0.9	19±1.0	85±0.8	18±0.8	85±0.8
	200	10±0.7		16±1.0		13±0.3		11±0.9		9±0.7	
C. limneticus	400	10±0.6		9±0.7		11±0.6		10±0.8		9±0.3	
	300	8±0.8	200±1.0	7±0.8	240±0.7	9±0.8	240±0.2	8±0.8	240±0.6	8±1.0	240±0.3
	200	7±0.8		NA		NA		7±0.8		NA	
PC		20±0.6	7.8±0.4	NA	NA	35±0.0	95±0.3	19±0.1	7.8±0.1	30±0.0	3.1±0.2

PC: positive controls that are ampicillin for bacteria and fluconazole for yeast, DD: disc diameter in mm, MIC as µg/ml, NA: not active. The results are presented as the mean ± standard deviation.

3.1.5. Mutagenic assay

Table 7: Plaque incorporation test results of *C. vulgaris* and *C. limneticus* methanol extracts on the *S. typhimurium* TA98 strain.

Concentrations (µg/Plate)	*Revertant colony number*	
	C. vulgaris	***C. limneticus***
Control	30.3±4.5	17±0.3
DMSO	32.1±2.2	15±0.1
Daunomycin	608±37.5	767±44.0
12.5	32.5±6.5	28.8±3.4
25	34.6±6.6	33.1±4.8
50	33.1±5.5	32.7±6.6
100	30.3±4.0	33.2±4.7
500	31.6±3.7	-30.9±6.4
1000	34.8±4.6	-32.3±2.8

Negative control: DMSO, Positive control: Daunomycin, Mean statistically significant at $p<0.05$ (Dunnett's t-test). The results are presented as the mean ± standard deviation.

The mutagenic activities of microalgae extracts are presented in Table 7. There were no mutagenic activities at all concentrations when comparing colony numbers of Control, DMSO, and Positive Control plates. Regardless of *C. limneticus* at any concentration, colony numbers could not be counted and the effect on the colony structure of *S. typhimurium* TA98.

4. Discussion and Conclusion

Microalgae are unicellular organisms that can survive extreme conditions. On the other hand, these cells are well-known sources of various secondary metabolites that are highly valuable in the pharmaceutical and cosmetic industries. These activities might have been due to the presence of biologically important phytoconstituents in the different algal extracts. In this study, we investigated the antimicrobial, antioxidant, and mutagenic activities of methanol extracts of two microalgae, *C. vulgaris* and *C. limneticus*, which were collected from Kabaklı pond in Diyarbakir-Türkiye. In the relevant literature, there are not enough studies reporting the activities of *C. limneticus* extracts. However, the *Chroococcus* genus has been relatively well studied, and its antimicrobial and antioxidant activities have been studied [32, 33]. *Chroococcus disperses* [19], and *Chroococcus minutus* [34].

GC-MS analysis of the ethanol extracts of these algae revealed the presence of several phytochemicals widely known for their biological activities (Table 1,2). These extracts are rich

in various bioactive compounds such as oleic acid, 9-Octadecenoic acid, (E), n-hexadecanoic acid, 1,4,7,10,13,16-Hexaoxacyclooctadecane, Heptaethylene glycol monododecyl ether, 15-Crown-5, 18,18'-Bi-1,4,7,10,13,16-hexaoxacy clononadecane, and octaethylene glycol monododecyl ether.

As shown in Table 3 and Fig. 3, DPPH free radical scanning activities increased in a dose-dependent manner, regardless of the non-significant antioxidant activity of the two microalgae extracts compared to the positive controls. Although *C. vulgaris* showed a dose-dependent increase in activity, *C. limneticus* showed stable antioxidant activity at concentrations of 50 µg/ml, whereas it significantly increased from 50 µg/ml to 100 µg/ml.

The ABTS radical scavenging assay results showed higher activity than the DPPH assay results for both *C. vulgaris* and *C. limneticus* extracts (Table 4). However, no significant antioxidant activity was observed when comparing the extracts with the positive controls. *C. vulgaris* extract showed better antioxidant activity than *C. limneticus* in both DPPH and ABTS assays, but the difference was not significant (Fig. 4). Copper (II) ion reduction capacity of algae extracts has increased concentration-dependent activity, although there were no significant activities compared with positive controls (Table 5 and Fig. 5). *C. vulgaris* showed antioxidant activity in similar studies, but it showed weak antioxidant activity compared to positive controls in our study [35]. The antioxidant and antimicrobial activities of ethanol extracts of microalgae are potentially attributable to the presence of specific chemical structures comprising hydroxyl groups and unsaturated carbon-carbon bonds. In both food systems and the human body, antioxidants play a critical role in reducing oxidative processes and the harmful effects of reactive oxygen species (ROS).

The antimicrobial activity of *C. vulgaris* and *C. limneticus* showed different levels of antimicrobial activity (Table 6) While *C. vulgaris* exhibited high microbial activity, *C. limneticus* exhibited weak activity. The major effectiveness (inhibition zone diameter 28±0.8 and MIC value 75 µg/ml) was recorded for *C. vulgaris* against *S. aureus*. As shown in Table 6 and Fig. 6, *C. vulgaris* showed high antimicrobial activity against *S. aureus* with 28 mm diameter and 75 MIC value and high activity against *E. coli* compared to the positive control. Similar studies have confirmed that *C. vulgaris* has the potential to become an antimicrobial agent [36, 37]. This is extremely important, as bacteria become resistant to a wide range of antibiotics used to treat bacterial diseases in humans.

The Salmonella microsome mutagenicity test (Ames test) is a test system used to understand both the mutagenic and antimutagenic effects of various chemicals and provides over

90% correlation in predicting genotoxicity [38]. In the Ames test, S. typhimurium strains with a mutation in the his-operon are used to detect the mutagenicity of substances [30]. Prokaryotic bioassays provide information about primary DNA damage and gene mutations induced by any agent [39]. In this study, the mutagenic activity of algae was determined using the Ames test, and the results showed that algae did not induce mutations in TA98 at all doses. Mutagenic activities of microalgae extracts (Table 7) were not shown any mutagenic activities at all concentrations. *C. vulgaris* and *C. limneticus* extracts affected on colony structure of *S. typhimurium* strain TA98. Because of water pollution, algal blooms occur when cyanobacteria produce toxins that are harmful to biological organisms. The mutagenic activity of *C. vulgaris* was not observed in the *S. typhimurium strain* TA98. A similar study with *C. vulgaris* has revealed that there is no mutagenic activity in *S. typhimurium* and working with rats [40, 41]

The chemical contents of microalgae used in our study oleic acid, hexadecanoic acid and 9,12-Octadecadienoic acid (Fig. 1,2) were the major fatty acid compounds in both *C. vulgaris* and *C. limneticus*. Wei et al. [42] reported that oleic acid exerted excellent antioxidative stress activity in vivo. Hexadecanoic acid is a saturated fatty acid (14:47%). Meanwhile, 9,12-Octadecadienoic acid is a polyunsaturated fatty acid (18:22%). Sawant and Mane [43] and Elshobary et al. [44] reported the antimicrobial activities of these fatty acids in *Chlorella emersonii*. In addition, several researchers have correlated the effects of fatty acids with different pathological conditions, such as positive effects against cardiovascular diseases and anticarcinogenic, anti-inflammatory, and antimicrobial activities [45].

The non-toxic and non-harmful natural antioxidants present an appealing alternative to synthetic chemical oxidants. Due to their non-toxic, non-carcinogenic and biodegradable nature, microalgae are regarded as a promising substitute for chemical antioxidants [46, 47].

A class of bioactive substances derived from microalgae, including polysaccharides, carotenoids, and phenolic compounds, is being increasingly recognised as a potent and durable source of natural antioxidants. The use of natural antimicrobials and antioxidants is a more attractive proposition than the use of synthetic chemical oxidants due to the non-toxic, non-harmful and biodegradable properties of the former. Hence, microalgae-derived bioactive compounds are an extremely valuable source of biologically active fractions that play a major role in the search for new drug candidates.

The results observed in this study demonstrated that although *C. vulgaris* has good antimicrobial potential, its activity is relatively weak. However, despite the relatively higher antioxidant activity of *C. limneticus* than that of *C. vulgaris*, the activities of both extracts were

weaker than those of the controls. Furthermore, the results showed that the extracts did not have mutagenic activity at any concentration tested.

Consequently, the results presented here show that *C. vulgaris* and *C. limneticus* may contain metabolites that affect various biological mechanisms. Therefore, this study may be considered as a starting point for investigating the biological activities of these microorganisms. Finally, we suggest further investigation of the biological activities of these organisms via different solvents or extraction systems since they may affect various biological systems.

Acknowledgments

This Project was supported by the Dicle University, Coordinatorship of Scientific Research Projects (DUBAP) Fen.17.020.

References

[1] El-Asmy, A.A., Al-Abdeen, A.Z., El-Maaty, W.M.A., Mostafa, M.M., *Synthesis and spectroscopic studies of 2,5-hexanedione bis(isonicotinylhydrazone) and its first raw transition metal complexes,* Spectrochimica Acta, Part A: Molecular and Biomolecular Spectroscopy, 75, 1516–1522, 2010.

[2] Sisman-Aydin, G., *Microalgae Technology and Environmental* Uses, Harran Üniversitesi Mühendislik Dergisi, 4, 81–92, 2019.

[3] Falkowski, P.G., Katz, M.E., Knoll, A.H, Quigg, A., Raven, J.A., Schofield, O. et al., *The evolution of modern eukaryotic phytoplankton*, Science, 305, 354–360, 2004.

[4] Massana, R., Terrado, R., Forn, I., Lovejoy, C., Pedros-Alio, C., *Distribution and abundance of uncultured heterotrophic flagellates in the world oceans*, Environmental Microbiology, 8, 1515–1522, 2006.

[5] Fehling, J., Stoecker, D., Baldauf, S.L., *Photosynthesis and the Eukaryote Tree of Life. Evolution of Primary Producers in the Sea*, in: Falkowski, P.G. et al., Evolution of primary producers in the sea, 75-107, 2007.

[6] Stern, R.F., Horak, A., Andrew, R.L., Coffroth, M.A., Andersen, R.A., Küpper, F.C., et al., *Environmental Barcoding Reveals Massive Dinoflagellate Diversity in Marine Environments*, PLoS One, 5, 2010.

[7] Richmond, A., Handbook of Microalgal Culture. Oxford, UK: Blackwell Publishing Ltd., 1st ed., 566p, 2003.

[8] Prarthana, J., Maruthi, K.R., *Fresh Water Algae as a Potential Source of Bioactive Compounds for Aquaculture and Significance of Solvent System in Extraction of Antimicrobials*, Asian Journal of Scientific Research, 12, 18–28, 2018.

[9] Sathasivam, R., Radhakrishnan, R., Hashem, A., Abd_Allah, E.F., *Microalgae metabolites: A rich source for food and medicine,* Saudi Journal of Biological Sciences, 26, 709–722, 2019.

[10] Landsberg, J.H., *The effects of harmful algal blooms on aquatic organisms*, Reviews in Fisheries Science, 10, 113–390, 2002.

[11] Irigoien, X., Hulsman, J., Harris, R.P., *Global biodiversity patterns of marine phytoplankton and zooplankton*, Nature, 429, 863–867, 2004.

[12] Caldwell, G.S., *The influence of bioactive oxylipins from marine diatoms on invertebrate reproduction and development*, Marine Drugs, 7, 367–400, 2009.

[13] Alwathnani, H., Johansen, J.R., *Cyanobacteria in Soils from a Mojave Desert Ecosystem*, Monographs of the Western North American Naturalist, 5, 71–89, 2011.

[14] Khan, M.I., Shin, J.H., Kim, J.D., The promising future of microalgae: *Current status, challenges, and optimization of a sustainable and renewable industry for biofuels, feed, and other products*, Microbial Cell Factories,17:1, 2018.

[15] Huang, S.S., Huang, G.J., Ho, Y.L., Lin, Y.H., Hung, H.J., Chang, T.N., et al. *Antioxidant and antiproliferative activities of the four Hydrocotyle species from Taiwan*, Botanical Studies, 49, 311–322, 2008.

[16] Luna-Castro, S., Samaniego-Barrón, L., Serrano-Rubio, L.E, Ceballos-Olveral I., Avalos-Gómez, C., De La Garza, M., *Lactoferrin: A Powerful Antimicrobial Protein Present in Milk.* Advances in Dairy Research, 5:4, 2017.

[17] Jaki, B., Orjala, J., Heilmann, J., Linden, A., Vogler, B., Sticher, O., *Novel extracellular diterpenoids with biological activity from the cyanobacterium Nostoc commune,* Journal of Natural Products, 63, 339–343, 2000.

[18] Volk, R.B., Girreser, U., Al-Refai, M., Laatsch, H., *Bromoanaindolone, a novel antimicrobial exometabolite from the cyanobacterium Anabaena constricta*, Journal of Natural Products Research, 23, 607–612, 2009.

[19] Ghasemi, Y., Moradian, A., Mohagheghzadeh, A., Shokravi, S., Morowvat, M.H., *Antifungal and Antibacterial Activity of the Microalgae Collected from Paddy Fields of Iran: Characterization of Antimicrobial Activity of Chroococcus disperses,* Journal of Biological Sciences, 6, 904-910, 2007.

[20] Silva-Stenico, M.E., Silva, C.S.P., Lorenzi, A.S., Shishido, T.K., Etchegaray A., Lira S.P., et al. *Non-ribosomal peptides produced by Brazilian cyanobacterial isolates with antimicrobial activity,* Microbiological Research, 166, 161–175, 2011.

[21] Plaza, M., Santoyo, S., Jaime, L., García-Blairsy Reina, G., Herrero, M., Señoráns F.J., et al. *Screening for bioactive compounds from algae,* Journal of Pharmaceutical and Biomedical Analysis, 51, 450–455, 2010.

[22] Çakmak F., *Kabaklı Göleti'nin Bacillariophyta Dışı Planktonik Algleri Üzerine Bir Araştırma*. Master Thesis, Dicle University Institute of Natural and Applied Sciences, 2013.

[23] Prescott, G.W., Algae of the Western Great Lakes Area Hardcover. 1. Ed. Iowa: WM. C. Brown Company, 1973.

[24] Corona, E., Fernandez-Acero, J. and Bartual, A., *Screening study for antibacterial activity from Marine and freshwater microalgae,* International Journal of Pharma and Bio Science, 8(1), 189-194, 2017.

[25] Blois, M.S., *Antioxidant determinations by the use of a stable free radical*. Nature, 181,1199–1200, 1958.

[26] Miller, N.J., Rice-Evans, C., Davies, M.J., Gopinathan, V., Milner, A., *A Novel Method for Measuring Antioxidant Capacity and its Application to Monitoring the Antioxidant Status in Premature Neonates*, Clinical Science, 84, 407–412, 1993.

[27] Apak, R., Güçlü, K., Özyürek, M., Karademir, S.E., *Novel total antioxidant capacity index for dietary polyphenols and vitamins C and E, using their cupric ion reducing capability*

in the presence of neocuproine: CUPRAC method, Journal of Agricultural and Food Chemistry, 52, 7970–7981, 2004.

[28] National Committee for Clinical Laboratory Standards. Performance standards for antimicrobial disk susceptibility tests : approved standard : NCCLS document M2-A6. 6th ed. Wayne Penn.: NCCLS; 1997.

[29] Levin, D.E., Yamasaki, E., Ames, B.N., *A new Salmonella tester strain, TA97, for the detection of frameshift mutagens: A run of cytosines as a mutational hot-spot,* Mutation Research/Fundamental and Molecular Mechanisms of Mutagenesis, 94, 315–330, 1982.

[30] Maron, D.M., Ames, B.N., *Revised methods for the Salmonella mutagenicity test,* Mutation Research/Environmental Mutagenesis and Related Subjects, 113, 173–215, 1983.

[31] Taghavi Takyar, M.B., Haghighat Khajavi, S., Safari, R., *Evaluation of antioxidant properties of Chlorella vulgaris and Spirulina platensis and their application in order to extend the shelf life of rainbow trout (Oncorhynchus mykiss) fillets during refrigerated storage*, LWT-Food Science and Technology, 100, 244–249, 2019.

[32] Hidhayati, N., Agustini, N.W.S., Widyagustina, D., *Antimicrobial activity of ethanol fraction from cyanobacteria Chroococcus turgidus,* IOP Conference Series: Earth and Environmental Science, 439 012046, 2020.

[33] Bharanidharan, M., Sivasubramanian, V., Rama Raja, S., Nayagam, V., *Evaluation of antioxidant and antimicrobial potential of cyanobacteria, Chroococcus turgidus (Kützing) Nägeli,.* International Journal of Current Microbiology and Applied Sciences, 2, 300–305, 2013.

[34] Arguelles, E., *Total Phenolic Content and in Vitro Analysis of Antioxidant, Antibacterial, and Alpha-Glucosidase Inhibition Properties of Chroococcus Minitus (Kützing) Nageli (Chroococcales, Cyanobacteria),* Journal of Faculty of Pharmacy of Ankara University, 46, 170–181, 2022.

[35] Hamdy, O., Karim, A., Farouk Gheda, S., Ismail, G.A., Abo-Shady, A.M., *Assistant of Phycology T. Phytochemical Screening and antioxidant activity of Chlorella vulgaris*, Delta Journal of Science, 41, 81–91, 2020.

[36] Hussein, H.J., Naji, S.S., Al-Khafaji, N.M.S., *Antibacterial properties of the Chlorella vulgaris isolated from polluted water in Iraq*, Journal of Pharmaceutical Sciences & Resesarc, 10(10), 2457–2460, 2018.

[37] Zielinski, D., Fraczyk, J., Debowski, M., Zielinski, M., Kaminski, Z.J., Kregiel D., et al. *Biological Activity of Hydrophilic Extract of Chlorella vulgaris Grown on Post-Fermentation Leachate from a Biogas Plant Supplied with Stillage and Maize Silage*, Molecules, 25(8),1790, 2020.

[38] Weisburger, J.H., *Antimutagenesis and anticarcinogenesis, from the past to the future*, Mutation Research/Fundamental and Molecular Mechanisms of Mutagenesis, 480–481, 23–35, 2001.

[39] Leme, D.M., Marin-Morales, M.A., *Allium cepa test in environmental monitoring: A review on its application,* Mutation Research/Reviews in Mutation Research, 682, 71–81, 2009.

[40] Himuro, S., Ueno, S., Noguchi, N., Uchikawa, T., Watanabe, K., *Safety evaluation of mutagenecity, acute and subacute toxicity study of Chlorella vulgaris CK-22 in rats,* Fundamental Toxicology, Science, 1, 151–159, 2014.

[41] Zainul Azlan, N., Abd Ghafar, N., Mohd Yusof, Y.A., Makpol, S., *Toxicity study of Chlorella vulgaris water extract on female Sprague Dawley rats by using the Organization for Economic Cooperation and Development (OECD) Guideline 420,* Journal Applied Phycology, 32, 3063–3075, 2020.

[42] Wei, C.C., Yen, P.L., Chang, S.T., Cheng, P.L., Lo, Y.C., Liao, V.H.C., *Antioxidative Activities of Both Oleic Acid and Camellia tenuifolia Seed Oil Are Regulated by the Transcription Factor DAF-16/FOXO in Caenorhabditis elegans,* PLoS One, 11(6), e0157195, 2016.

[43] Sawant, S.S., Mane, V.K., *Nutritional profile, antioxidant, antimicrobial potential, and bioactives profile of chlorella emersonii KJ725233*, Asian Journal of Pharmaceutical and Clinical Research, 11, 220–225, 2018.

[44] Elshobary, M.E., El-Shenody, R.A., Ashour, M., Zabed, H.M., Qi, X., *Antimicrobial and antioxidant characterization of bioactive components from Chlorococcum minutum*, Food Bioscience, 35(4), 100567, 2020.

[45] Flickinger, B.D., Huth, P.J., *Dietary fats and oils: Technologies for improving cardiovascular health.* Current Atherosclerosis Reports, 6, 468–476, 2004.

[46] Yang, N., Zhang, Q., Chen, J., Wu, S., Chen, R., Yao, L., et al. *Study on bioactive compounds of microalgae as antioxidants in a bibliometric analysis and visualization perspective,* Frontiers in Plant Science, 14, 2023.

[47] El-Fayoumy, E.A., Shanab, S.M.M., Gaballa, H.S., Tantawy, M.A., Shalaby E.A., *Evaluation of antioxidant and anticancer activity of crude extract and different fractions of Chlorella vulgaris axenic culture grown under various concentrations of copper ions,* BMC Complementary Medicine and Therapies, 21, 51, 2021.

Adıyaman University Journal of Science
https://dergipark.org.tr/en/pub/adyujsci
DergiPark AKADEMİK
ISSN 2147-1630
e-ISSN 2146-586X

Synthesis, Characterization, And Thermal Conductivity Properties of Graphene Oxide Doped Chromium-Titanium Oxide Structures

Serhat KOÇYİĞİT[1,*]

[1]*Bingol University, Central Laboratory Application and Research Centre, 12000, Bingol, Turkiye*
skocyigit@bingol.edu.tr, ORCID: 0000-0003-0172-6180

Received: 10.10.2024 **Accepted:** 28.11.2024 **Published:** 31.12.2024

Abstract

This study investigates synthesis and characterization of graphene oxide (GO) undoped and doped chromium-titanium oxide structures, along with their thermal conductivity properties in detail. The importance of low or high thermal conductivity varies depending on the intended application, and it is known that thermal conductivity, which determines which determines a material's ability to conduct heat, plays a crucial role in energy, electronics, and thermoelectric applications. Materials with low thermal conductivity are widely used in various industrial fields due to their effective heat insulation capabilities. For experimental studies, GO-undoped(T1), 1%-GO-doped(T2), and 3%-GO-doped(T3) samples were produced via the sol-gel method, followed by calcination, pelletization, and sintering processes. Characterization of these pellets was performed using X-ray Diffraction (XRD), Scanning Electron Microscopy (SEM), and Fourier Transform-Infrared Spectroscopy (FTIR). Thermal conductivity was measured using Physical Properties Measurement System (PPMS). No structural or peak changes were detected in the XRD and FTIR results, but differences in peak intensities were observed. SEM images revealed reductions in structural dimensions with GO doping, which corresponded to changes in thermal conductivity data. The thermal conductivity values of the T1, T2, and T3 samples were measured

* Corresponding Author DOI: 10.37094/adyujsci.1564392

as 6.49, 3.45, and 1.50 W/K·m, respectively. These findings indicate that GO-doping reduces thermal conductivity and that differences in the material structure are significant. Additionally, it was observed that reducing the structure to the nanoscale also led to a decrease in thermal conductivity. These materials could play an important role in developing next-generation material designs.

Keywords: Chrome oxide; Graphene oxide; Sol-gel; Thermal conductivity; Titanium oxide.

Grafen Oksit Katkılı Krom-Titanyum Oksit Yapılarının Sentezi, Karakterizasyonu ve Termal İletkenlik Özellikleri

Öz

Bu çalışmada, grafen oksit katkılı ve katkısız krom titanyum oksit yapılarının sentez ve karakterizasyonları ile birlikte termal iletkenlik özellikleri detaylı bir şekilde incelenmiştir. Termal iletkenlik değerlerinin düşük veya yüksek olması hedeflenen malzeme türüne göre önem arz etmekte ve malzemelerin ısıyı iletme yeteneğini belirleyen termal iletkenliğin enerji, elektronik ve termoelektrik uygulamalarda önemli rol oynadığı bilinmektedir. Düşük termal iletkenliğe sahip malzemeler, ısıyı etkin bir şekilde izole edebilme yetenekleri sayesinde çeşitli endüstriyel alanlarda yaygın olarak kullanılmaktadır. Deneysel çalışmalar sonucunda, GO-undoped (T1), 1% GO-doped (T2) ve 3% GO-doped (T3) örnekleri sol-jel yöntemi ile üretilmiş olup örneklerin ilk olarak kalsinasyonu ardından peletleme sonrası sinterleme işlemi yapılmıştır. Bu sinterlenen peletlerin karakterizasyonu X-ışınları Kırınımı (XRD), Taramalı Elektron Mikroskobu (SEM) ve Fourier Dönüşümlü Kızılötesi Spektroskopi (FTIR) ile yapılmıştır. Termal iletkenlik ölçümleri ise Fiziksel Özellikler Ölçüm Sistemi (PPMS) ile yapılmıştır. Karakterizasyonlarda XRD ve FTIR sonuçlarında herhangi yapı ve pik değişikliği saptanmamış, ancak pik şiddetlerinde farklılıklar görülmüştür. SEM görüntülerinde GO katkılaması ile yapı boyutlarında azalmalar meydana geldiği anlaşılmış ve termal iletkenlik verilerindeki değişimle bu durum açıklanmıştır. T1, T2, ve T3 örneklerinin termal iletkenlik değerleri sırasıyla 6.49, 3.45 ve 1.50 W/K·m olarak ölçülmüştür. Bu bulgular, grafen oksit katkısının termal iletkenliği azalttığını ve malzeme yapısındaki değişikliklerin bu süreçte etkili olduğunu göstermektedir. Ayrıca yapının nanoboyuta indirgenmesiyle termal iletkenlik verilerinin de düştüğü gözlemlenmiştir. Enerji verimliliğini artırma potansiyeli açısından bu malzemelerin yeni nesil malzeme tasarımlarının geliştirilmesinde önemli rol oynayabilecektir.

Anahtar Kelimeler: Krom oksit; Grafen oksit; Sol-jel; Termal iletkenlik; Titanyum oksit.

1. Introduction

Thermal conductivity is a crucial property that determines the heat transfer ability of materials, significantly impacting energy, electronic, and thermoelectric applications [1]. While high thermal conductivity is advantageous in some contexts, low thermal conductivity is beneficial in others. Materials with low thermal conductivity are used in various industrial applications due to their effective heat isolation capabilities. Specifically, metal oxide materials with low thermal conductivity are preferred for use as thermal insulation materials in the construction sector, for controlling heat distribution in electronic circuit systems, for increasing energy efficiency in solar panels, for achieving more precise measurements in heat sensors, and for retaining heat generated from temperature differences in thermoelectric materials [2-4].

The synthesis of nanostructured materials is of great importance due to their higher surface area, higher sinterability, and improved optical, electronic, and magnetic properties [5-7]. Additionally, the increased potential for thermoelectric power generation and the wide thermal management of nanoparticles through phonon transport provide significant advantages in using these structures [8-10].

Chromium oxide nanoparticles are a preferred material due to their ease of synthesis [11]. They offer advantages in doping and possess properties such as durability in high-temperature and high-pressure applications, high wear and corrosion resistance, and catalytic capabilities [12].

Titanium oxide structures can provide thermal insulation due to their low thermal conductivity. Particularly in TiOx structures, it has been observed that the thermal conductivity values decrease as the x value decreases from 2 to 1, with accompanying changes in crystal structures. It is known that even when the x value is between 2 and 1.66, the compound exhibits n-type semiconductor properties, behaves as a p-type semiconductor at room temperature between 1.66 and 1.25, and shows n-type characteristics at room temperature and p-type at higher temperatures when the x value is between 1 and 1.25 [13]. This property allows titanium oxide structures to yield significant results when used in a controlled manner in thermal conductivity data.

Graphene exhibits high thermal conductivity when utilized in its pure, single-layer form, complemented by its exceptional mechanical properties and lightweight nature. While graphene oxide does not match graphene's thermal conductivity levels, the low thermal conductivity of graphene oxide is primarily due to increased phonon-boundary scattering caused by surface functional groups. Since graphene oxide is dispersible in water and organic solvents, it can be used for specific applications [14,15]. Additionally, the structural properties and atomic

interactions with the materials to which it is added can lead to significant reductions in thermal conductivity values [16,17]. Furthermore, the high surface area and nanostructure of graphene oxide significantly influence its thermal conductivity [2]. For instance, graphene and graphene oxide doping have been shown to reduce the potential barrier and grain boundary resistivity by creating high-density oxygen vacancies in SrTiO3 significantly reducing the average grain size, increasing phonon scattering, and thus reducing thermal conductivity [18,19].

This study focuses on the synthesis and characterization of graphene oxide (GO) doped chromium-titanium oxide structures and the effects of varying GO concentrations on thermal conductivity. The findings reveal significant decreases in thermal conductivity with GO doping, providing new insights into the structural changes that affect heat transfer properties at the nanometer scale.

The motivation for this research stems from the increasing demand for materials with specialized thermal properties for applications in energy efficiency, electronics, and thermoelectric systems. As industries increasingly seek materials that can effectively manage heat transfer, it becomes important to understand how additives such as graphene oxide can influence thermal conductivity. This study aims to contribute to the development of next-generation materials that improve energy efficiency and thermal management by addressing both environmental sustainability and technological advancement.

2. Materials and Methods

2.1. Material

In the formation of chromium-titanium oxide, organic salts of these metals were preferred. Chromium (III) acetylacetonate and titanyl acetylacetonate salts were supplied by Sigma-Aldrich. Glacial acetic acid, supplied by Merck, was used to support the solutions of these salts. Graphene oxide, which is >99% pure and in powder form, was supplied by Graphene Supermarket. Polyvinyl alcohol (PVA) (Mw: 85,000 - 124,000) was chosen as the polymer source and was supplied by Sigma-Aldrich.

2.2. Sample preparation

The preparation of chromium-titanium oxide structures began by dissolving the acetate salts of these metals in a water and acetic acid mixture for 6 hours at room temperature using a magnetic stirrer at 250 rpm. 10% (w/v) PVA solution was then dissolved by maintaining a constant temperature of 80 °C for 2 hours, and this solution was left to cool to room temperature [20]. In preparing the graphene oxide dispersion, graphene oxide powder was added to the metal

acetate solution and kept in an ultrasonic bath for 24 hours until the dispersion was ready. The PVA solution was added to the graphene oxide-doped metal acetate mixture and stirred with a magnetic stirrer for 3 hours. Thus, graphene oxide-doped and undoped metal acetate/PVA solutions were prepared. In these mixtures, the graphene oxide undoped was named T1, the 1% graphene oxide-doped was named T2, and the 3% graphene oxide-doped was named T3. To ensure gelation in the prepared T1, T2, and T3 sol-gel mixtures, these mixtures were transferred to porcelain crucibles and dried in an oven at 100 °C. The dried mixtures were then heated in the oven at 650 °C for 4 hours, undergoing a calcination process to remove organic structures. After calcination, the nanomaterials obtained were pulverized in an agate mortar. These powders were then pressed into pellets with a diameter of 8 mm and a thickness of 3 mm under 6 tons of pressure and sent back to the tubular oven, where they were sintered at 850 °C for 4 hours to ensure the fusion of nanoparticles in the material.

2.3. Characterization

The sintered pellet structures were first characterized using XRD, SEM and FTIR, and their thermal conductivities depending on temperature were calculated using a PPMS device. XRD characterization was performed with a PANalytical Empyrean device to create the diffraction pattern of the crystal structures of the sintered pellets. A Zeiss Supra 40VP SEM device was used to reveal the morphological properties of the pellets. The bond structures were analyzed using a PerkinElmer Spectrum 100 Series FTIR spectrometer, which revealed the various vibrational structures of the molecules. A Quantum Design PPMS instrument was used to determine the thermal properties of the samples as a function of temperature. The analyses with the XRD, SEM, and FTIR devices were conducted at Bilecik Şeyh Edebali University, while the PPMS analyses were conducted at Malatya Inönü University.

3. Results and Discussion

3.1. XRD Results

The diffraction patterns of the peak intensities corresponding to the 2θ (two theta) angles of the T1 (black), T2 (red), and T3 (blue) samples, obtained from X-ray diffraction (XRD) analysis, are presented in Fig. 1. Upon examining the XRD diffraction patterns, it was observed that all samples contained two crystal structures and exhibited the same peak values. Analysis of these peak values indicated that they corresponded to the peaks of the Cr_2O_3 compound, which has a rhombohedral crystal structure, as referenced by the Joint Committee on Powder Diffraction Standards (JCPDS) # 00-038-1479 [21]. It was determined that the 2θ values of the rhombohedral Cr_2O_3 peaks were at 36.71°, 42.60°, and 61.83°, with orientations of (111), (002), and (022),

respectively. Additionally, it was found that the peaks also belonged to the Ti_1O_1 compound, which has a cubic crystal structure, as referenced by JCPDS # 98-005-6612 [22]. The cubic crystal structure Ti_1O_1 peaks were identified at 24.52°, 33.63°, 34.27°, 41.53°, 50.33°, 54.95°, and 63.58°, with orientations of (012), (104), (110), (113), (024), (116), and (214), respectively. Due to the low concentrations of graphene oxide doping, at 1% and 3%, these peaks were not observed in the XRD diffraction patterns. No structural change was deteted as a result of graphene oxide doping; only differences in peak intensities were noted. This indicates that no degradation occurred in the structure due to graphene oxide doping. The results in the diffraction pattern also confirm the compound structure.

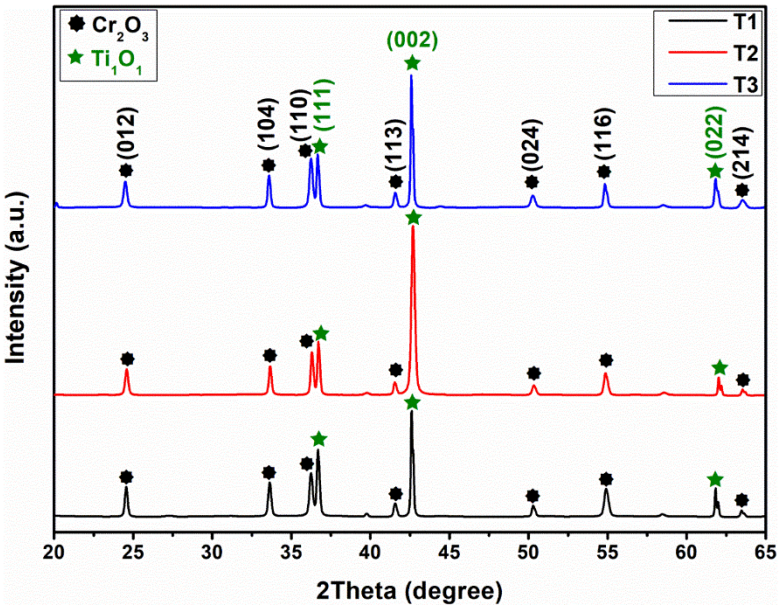

Figure 1: X-ray diffraction pattern of T1 (black), T2 (red), and T3 (blue) samples.

3.2. SEM Results

SEM images of the T1, T2, and T3 samples are presented in Figure 2. These images were captured at a voltage of 15 kV and magnification of 100,000x. Upon examining the SEM images, a comparison of the T1 and T2 samples reveals that they exhibit similar structures. However, it is evident that the gap ratio between the structures in the T2 sample is greater than that in the T1 sample, and the clusters are denser. While the T1 and T2 samples exhibit similar clustering, the T3 sample shows that the nanostructures are detached from the clustered formations, resulting in a reduction of the average diameter of the structures. Measurements indicated that the diameters of the clustered structures in the T1 sample ranged from 60 to 80 nm, while those in the T2 sample varied between 60 and 110 nm. In contrast, the diameters of the separated structures in the T3 sample were found to range from 20 to 40 nm.

Goncalves et al. stated that higher-density oxygen functional groups support the dispersion of nanoparticles along the graphene oxide surface and suggested that oxygen groups on the GO surface affect the size growth of nanoparticles [23]. Thus, it was observed that there were openings between the particles and the particles grew due to the effect of oxygen groups in the T1 and T2 samples. While there was a particle cluster where the particles merged in the T1 and T2 samples, it is estimated that in the T3 sample, due to this feature of GO, the particle cluster opened and the particles inside were separated. It was understood that the particle size decreased due to the size of the opened particles.

Given that it is established that thermal conductivity decreases with reduced phonon participation in nanotechnological processes and increased gaps between structures, it can be concluded that the temperature-dependent thermal conductivity data presented in Fig. 4 is consistent with the SEM images.

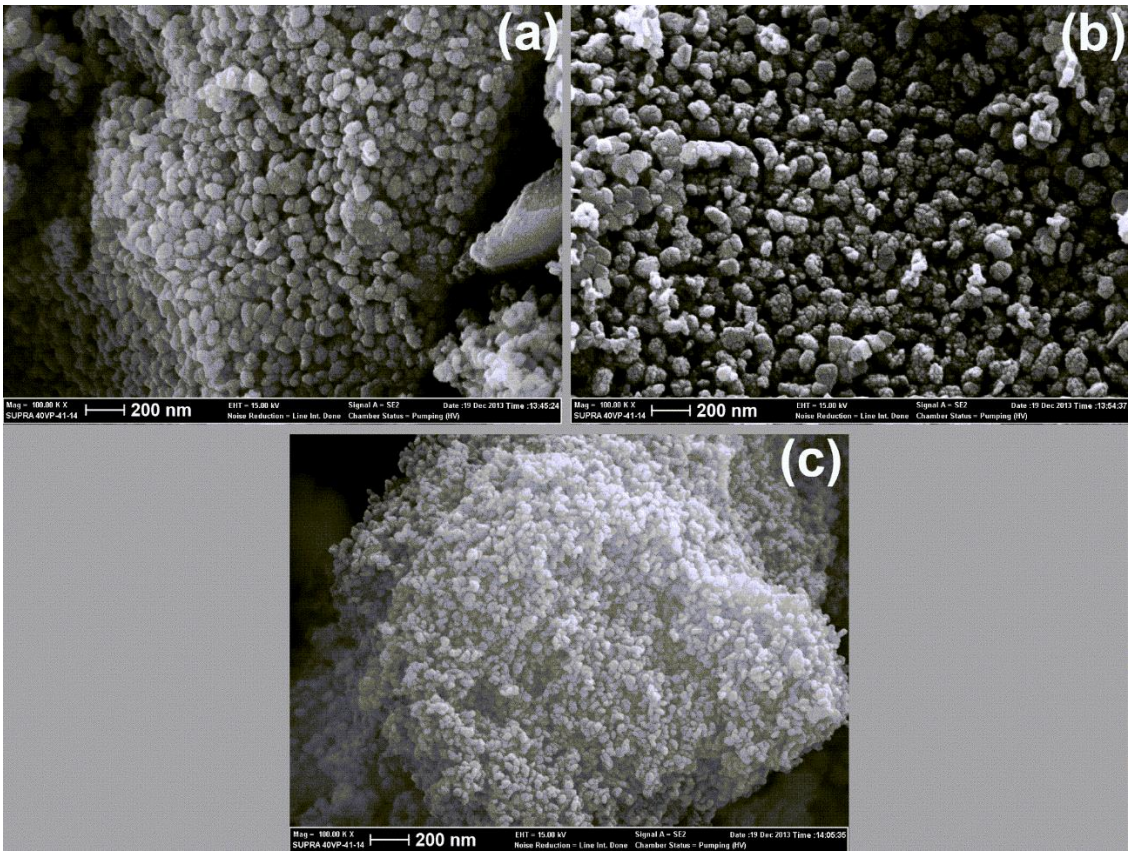

Figure 2: SEM images of T1 (a), T2 (b), and T3 (c) samples (15 kV, 100000x).

3.3. FTIR Results

The FTIR spectra for the T1, T2, and T3 calcined powder samples are illustrated in Figure 3. Analyzing this graph reveals that all samples display identical peak structures, suggesting that

their molecular compositions are also the same. Specifically, the peaks observed at 2162 cm^{-1}, 1971 cm^{-1}, and 1625 cm^{-1} are recognized as corresponding to Cr2O3, as supported by previous studies [24,25]. Furthermore, the peaks located at 907 cm^{-1}, 872 cm^{-1}, and 763 cm^{-1} align with the Ti-O-Ti structural configuration, indicating the presence of titanium oxide in the samples [26]. The peaks at 606 cm^{-1} and 479 cm^{-1} have been identified as compatible with Cr-O bonds, further confirming the presence of chromium oxide in the structures. Additionally, the peak at 424 cm^{-1} is found to overlap with titania structures, reinforcing the structural integrity of the materials [27]. Due to the low concentrations of graphene oxide doping, at 1% and 3%, these peaks were not observed in the FTIR spectra. These findings suggest that the presence of both Ti-O and Cr-O structures in the FTIR spectra aligns with the results obtained from the XRD diffraction patterns. This correlation between the two characterization techniques provides strong evidence that they validate each other, enhancing the reliability of the analysis conducted on these samples.

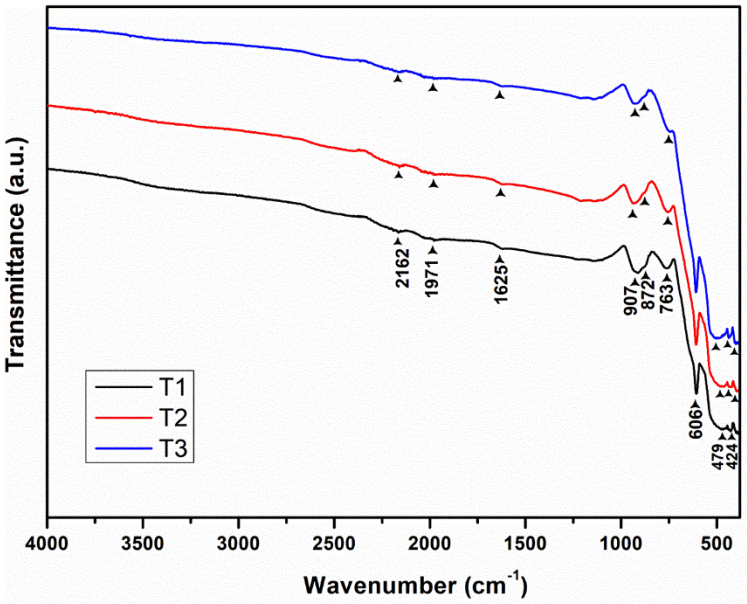

Figure 3: FTIR spectra of T1 (black), T2 (red), and T3 (blue) samples.

3.4. Thermal Conductivity Results

When examining the thermal conductivity versus temperature values of the T1, T2, and T3 samples, it was determined that the thermal conductivity value ranking for each temperature is T1 > T2 > T3, as shown in Figure 4. This ranking is related to the structural properties of the materials and the effects of dopants. Notably, when the graphene oxide content is 1%, a slight decrease in thermal conductivity is observed. Increasing the graphene oxide content to 3% further reduces the thermal conductivity value.

Upon examining the SEM images, it was observed that in the graphene oxide undoped sample, the nanostructures are clustered. In the 1% graphene oxide doped sample, similar clustering was detected; however, in this case, the clustered structures were observed to be separated from each other. This formation of voids has contributed to the decrease in thermal conductivity. In the T3 sample, it was found that the clustered structures in the T1 and T2 samples were completely separated. In this sample, the structure demonstrates more pronounced nanoproperties, and this observation is further supported by the particle size data derived from the SEM images.

The thermal conductivity values for the T1, T2, and T3 samples, measured at room temperature (298 K), were found to be 6.49, 3.45, and 1.50 W/K·m, respectively. In this context, the effect of graphene oxide as a dopant in reducing thermal conductivity is related to changes in the material structure, indicating that phonon activity plays a significant role in the thermal management of nanostructured materials [9,28,29].

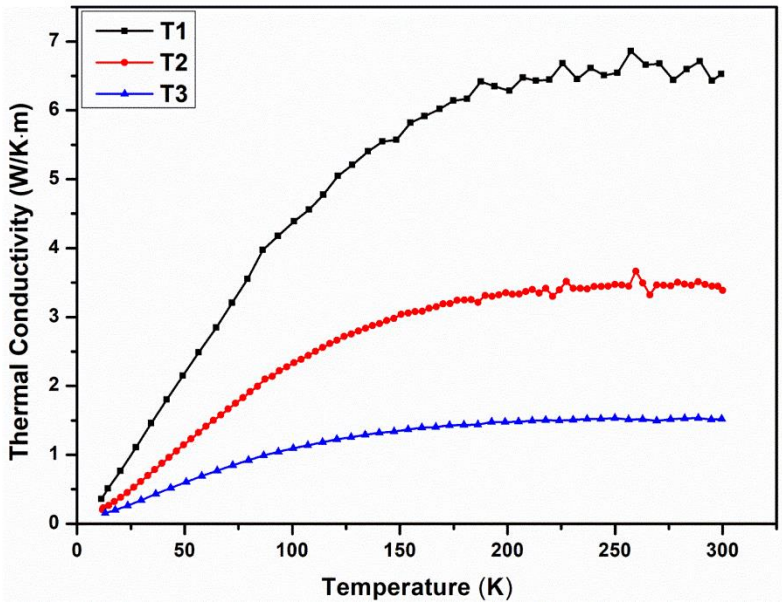

Figure 4: Thermal conductivity vs temperature graphs of T1 (black), T2 (red), and T3 (blue) samples.

This study aims to provide innovative solutions to increase energy efficiency and control heat through the combination of materials used. This approach could serve as an important foundation for the development of next-generation material designs and the improvement of existing applications, with positive effects on energy savings, heat management, and environmental sustainability**.**

4. Conclusion

In this study, the synthesis, characterization, and thermal conductivity properties of graphene oxide-doped and undoped chromium-titanium oxide structures were investigated in detail. The findings show that graphene oxide doping significantly reduces thermal conductivity. Thermal conductivity values of the T1, T2, and T3 samples were measured as 6.49, 3.45, and 1.50 W/K·m at room temperature, respectively. These results reveal the effects of graphene oxide on thermal conductivity along with the changes it induces in the material structure.

X-ray diffraction (XRD) and Fourier transform infrared spectroscopy (FTIR) analyses confirmed that all samples have similar molecular structures, and no structural changes were observed. Scanning electron microscope (SEM) images showed that graphene oxide doping causes expansion in the structure with the increase in the presence of oxygen in structural dimensions, which is related to thermal conductivity data.

In conclusion, graphene oxide-doped chromium-titanium oxide structures can play an important role in the development of new-generation material designs due to their potential to increase energy efficiency. The effects of these materials on thermal management applications and environmental sustainability provide an inspiring basis for future research.

References

[1] Tritt, T.M., *Thermal conductivity: Theory, properties, and applications:* Springer Science & Business Media, 2005.

[2] Eivari, H.A., Sohbatzadeh, Z., Mele, P., Assadi, M.H.N., *Low thermal conductivity: Fundamentals and theoretical aspects in thermoelectric applications*, Materials Today Energy, 21, 100744, 2021.

[3] Binici, H., Aksogan, O., Demirhan, C., *Mechanical, thermal and acoustical characterizations of an insulation composite made of bio-based materials*, Sustainable Cities and Society, 20, 17-26, 2016.

[4] Tsilingiris, P.T., *Heat transfer analysis of low thermal conductivity solar energy absorbers*, Applied Thermal Engineering, 20, 1297-1314, 2000.

[5] Chavan, S.V., Sastry, P.U.M., Tyagi, A.K., *Combustion synthesis of nanocrystalline Nd-doped ceria and Nd_2O_3 and their fractal behavior as studied by small angle X-ray scattering*, Journal of Alloys and Compounds, 456, 51–56, 2008.

[6] Gleiter, H., *Nanocrystalline solids*, Journal of Applied Crystallography, 24, 79-90, 1991.

[7] Weller, H., *Colloidal semiconductor q-particles-chemistry in the transition region between solid-state and molecules*, Angewandte Chemie International Edition in English, 32, 41–53, 1993.

[8] Narayanamurti, V., *Phonon optics and phonon propagation in semiconductors*, Science, 213, 717-723, 1981.

[9] Maldovan, M., *Phonon wave interference and thermal bandgap materials*, Nature Materials, 14, 667-674, 2015.

[10] Xie, G., Ding, D., Zhang, G., *Phonon coherence and its effect on thermal conductivity of nanostructures*, Advances in Physics: X, 3, 720-755, 2018.

[11] Liu, G., Liu, Z., Wang, L., Zhang, K., Xie, X., *A combined chrome oxide and titanium oxide based electron-transport layer for high-performance perovskite solar cells*, Chemical Physics Letters, 771, 138496, 2021.

[12] Pei, Z., Zheng, X., Li, Z., *Progress on synthesis and applications of Cr_2O_3 nanoparticles*, Journal of Nanoscience and Nanotechnology, 16, 4655-4671, 2016.

[13] He, Q., Hao, Q., Chen, G., Poudel, B., Wang, X., Wang, D., Ren, Z., *Thermoelectric property studies on bulk TiO_x with x from 1 to 2*, Applied Physics Letters, 91, 052505, 2007.

[14] Pei, Q.X., Sha, Z.D., Zhang, Y.W., *A theoretical analysis of the thermal conductivity of hydrogenated graphene*, Carbon, 49, 4752-4759, 2011.

[15] Chen, J., Li, L., *Thermal conductivity of graphene oxide: a molecular dynamics study*, JETP Letters, 112, 117-121, 2020.

[16] Chen, J., Li, L., *Thermal conductivity of graphene oxide: A molecular dynamics study*, JETP Letters, 112, 117-121, 2020.

[17] Sevinçli, H., Sevik, C., Çağın, T., Cuniberti, G., *A bottom-up route to enhance thermoelectric figures of merit in graphene nanoribbons,* Scientific Reports, 3, 1228, 2013.

[18] Huang, J., Yan, P., Liu, Y., Xing, J., Gu, H., Fan, Y., Jiang, W., *Simultaneously breaking the double Schottky barrier and phonon transport in $SrTiO_3$-based thermoelectric ceramics via two-step reduction*, ACS Applied Materials & Interfaces, 12, 52721-52730, 2020.

[19] Liu, X., Li, S., Yu, J., Zhu, Y., Lin, K., Wang, B., Rongsheng, C., Dursun, E., David L., Ian, A.K., Michael J.R., Freer, R., *Enhancing the thermoelectric properties of TiO_2-based ceramics through addition of carbon black and graphene oxide*, Carbon, 216, 118509, 2024.

[20] Koçyiğit, S., Aytimur, A., & Uslu, I., *Graphene-doped $Ca_{0.9}Er_{0.1}Mn_{1.5}O_\alpha$ thermoelectric nanocomposite materials: Temperature-dependent thermal and Seebeck properties*, Ceramics International, 46, 6377-6382, 2020.

[21] Yue, H.R., Xue, X.X., Zhang, W.J., *Diffusion Characteristics of Intermediate in Cr_2O_3/CaO System and Its Formation Mechanism*, Metallurgical and Materials Transactions B, 52, 3477-3489, 2021.

[22] Filiberto, M., Daniele, B., Franco, B., Antonio, S., Adriano, P., Giovanna, I., Raimondo, Q., *Histological and histomorphometric comparison of innovative dental implants laser obtained: Animal pilot study*, Materials, 14, 1830, 2021.

[23] Goncalves, G., Marques, P.A., Granadeiro, C.M., Nogueira, H.I., Singh, M.K., Gracio, J., *Surface modification of graphene nanosheets with gold nanoparticles: the role of oxygen moieties at graphene surface on gold nucleation and growth*, Chemistry of Materials, 21, 4796-4802, 2009.

[24] Hallam, H.E., *Infrared and Raman spectra of inorganic compounds*, Royal Institute of Chemistry, Reviews, 1, 39-61, 1968.

[25] Scarano, D., Zecchina, A., Bordiga, S., Ricchiardi, G., Spoto, G., *Interaction of CO with α-Cr_2O_3 surface: A FTIR and HRTEM study*, Chemical Physics, 177, 547-560, 1993.

[26] Nakamura, R., Nakato, Y., *Primary intermediates of oxygen photoevolution reaction on TiO_2 (rutile) particles, revealed by in situ FTIR absorption and photoluminescence measurements*, Journal of the American Chemical Society, 126, 1290-1298, 2004.

[27] Kumar, P.M., Badrinarayanan, S., Sastry, M., *Nanocrystalline TiO_2 studied by optical, FTIR and X-ray photoelectron spectroscopy: correlation to presence of surface states*, Thin solid films, 358, 122-130, 2000.

[28] Mahanta, N.K., Abramson, A.R., *Thermal conductivity of graphene and graphene oxide nanoplatelets,* 13th InterSociety Conference on Thermal and Thermomechanical Phenomena in Electronic Systems, 1-6, 2012.

[29] Okhay, O., Tkach, A*., Impact of graphene or reduced graphene oxide on performance of thermoelectric composites,* Journal of Carbon Research, 7, 37, 2021.

Adıyaman University Journal of Science
https://dergipark.org.tr/en/pub/adyujsci
DergiPark AKADEMİK
ISSN 2147-1630
e-ISSN 2146-586X

Theoretical Study of Substitution Effects on Reorganization Energy in Indeno[1,2-b]fluorene-6,12-dione-Based Molecular Semiconductors

Resul ÖZDEMİR[1,*]

[1]*Eskişehir Osmangazi University, Eskişehir Vocational School, Department of Electronics and Automation, 26110 Eskişehir, Türkiye*
resul.ozdemir@ogu.edu.tr, ORCID: 0000-0002-7957-110X

Received: 09.10.2024 **Accepted:** 28.11.2024 **Published:** 31.12.2024

Abstract

The reorganization energy of an organic semiconductor can be modulated through molecular design. Density functional theory (DFT) calculations enable researchers to strategically design organic molecular semiconductors with low reorganization energy through chemical substitution. Herein, hole and electron reorganization energies of unsubstituted indeno[1,2-b]fluorene-6,12-dione (IFDK), and its 5,11- and 2,8-disubstituted derivatives were computed. Substituents positioned along the molecular long axes and short axes were employed to enhance understanding of how substitution position influences the molecular reorganization energy. Additionally, substituents with varying electron-withdrawing and electron-donating properties were also investigated to reveal the structure-property relationship in IFDKs. Based on DFT calculations, triphenylamine (TPA) substitution at the 5,11 and 2,8 positions exhibited the largest decreases in hole reorganization energy compared to the parent IFDK, reducing it from 240 meV to 80 meV and 110 meV, respectively. This suggests that more effective charge transfer is expected with TPA substitution in IFDKs due to lower reorganization energy. This work reveals the significant substitution effect on reorganization energy through the specific position and

* Corresponding Author DOI: 10.37094/adyujsci.1564147

electronic characters (EWG vs EDG), providing a foundation for the future design of IFDK-based molecules with high charge transfer efficiency.

Keywords: Organic semiconductors; Small molecules; Reorganization energy.

İndeno[1,2-b]fluoren-6,12-dion Bazlı Moleküler Yarı İletkenlerde Sübstitüsyonun Yeniden Düzenlenme Enerjisi Üzerindeki Etkilerinin Teorik Olarak İncelenmesi

Öz

Organik bir yarı iletkenin yeniden düzenleme enerjisi moleküler tasarım yoluyla modüle edilebilir. Yoğunluk fonksiyonel teorisi (DFT) hesaplamaları araştırmacıların kimyasal sübstitüsyon yoluyla düşük yeniden düzenleme enerjisine sahip organik moleküler yarı iletkenleri stratejik olarak tasarlamalarına olanak tanır. Burada, sübstitüye olmamış indeno[1,2-b]fluoren-6,12-dion (IFDK) ve onun 5,11- ve 2,8-disübstitüe türevlerinin boşluk ve elektron yeniden düzenleme enerjileri hesaplandı. Moleküler uzun eksen ve kısa eksen boyunca konumlandırılan sübstitüye gruplar, sübstitüsyon konumunun moleküler yeniden düzenleme enerjisini nasıl etkilediğinin anlaşılmasını için kullanıldı. Ek olarak, değişen elektron çekme ve elektron itme özelliklerine sahip sübstitüentler IFDK'lardaki yapı-özellik ilişkisini ortaya çıkarmak için kullanıldı. DFT hesaplamalarına göre, 5,11 ve 2,8 pozisyonlarındaki trifenilamin (TPA) sübstitüsyonu, ana IFDK molekülü ile karşılaştırıldığında boşluk yeniden düzenleme enerjisinde en büyük azalmayı gösterdi ve bunu sırasıyla 240 meV'den 80 meV'ye ve 110 meV'ye düşürdü. Bu, daha düşük yeniden düzenleme enerjisi nedeniyle IFDK'lerde TPA sübstitüsyonu daha etkili yük transferinin beklendiğini göstermektedir. Bu çalışma, belirli pozisyon ve elektronik karakterler (EWG ve EDG) aracılığıyla yeniden düzenleme enerjisi üzerindeki önemli sübstitüsyon etkisini ortaya koyarak, yüksek yük transfer verimliliğine sahip IFDK tabanlı moleküllerin gelecekteki tasarımı için bir temel sağlamaktadır.

Anahtar Kelimeler: Organik yarıiletkenler; Küçük moleküller; Yeniden düzenlenme enerjisi.

1. Introduction

Organic semiconductors have garnered considerable attention from both industry and academia due to their superior properties, including lightweight, low cost, large area coverage, and compatibility with plastic substrates compared to inorganic counterparts. In addition to traditional applications such as Organic Field-Effect Transistors (OFETs) [1,2], Organic Light-

Emitting Diodes [3,4] (OLEDs), and Organic Photovoltaics (OPVs) [5] organic semiconductors are also utilized in Electrochemical Transistors (OECTs) [6], bio(chemical) sensors [7], thermoelectrics (OTEs) [8] and photodetectors [9]. Compared to polymeric semiconductors, small molecules offer advantages such as facile synthesis with good reproducibility, well-defined chemical structure and molecular weight, good solubility in common organic solvents and high purity due to their suitability for chromatographic purification. Over the past few decades, there has been significant interest in developing novel molecular semiconductors to enhance the efficiency of organic semiconductors in above-mentioned applications. However, the advancement of *n*-type molecular organic semiconductors has lagged behind that of their p-type analogues in terms of material diversity and device performance [10].

Among the electron deficient π-conjugated building blocks developed to date, indeno[1,2-b]fluorene-6,12-dione (IFDK) stands out due to its highly coplanar π-backbone, excellent physicochemical and thermal stability, and structural versatility resulting from various functionalization and substitution positions [11]. In recent years, numerous reports have emerged on the experimental studies of IFDK-based OFET applications, including our previous work on TIPS-IFDK [12] and 2OD-TTIFDK [13] molecules. However, the literature reveals a limited number of theoretical studies examining the structure-property relationships of IFDKs. For instance, Martinez *et al.* investigated the effects of electron-donating and electron-withdrawing groups on the electronic structure of 6,12-disubstituted IFDK derivatives. Their findings indicated that NH_2, NO_2, and CN functional groups could serve as effective light harvesters and sensitizers in solar cells [14]. Additionally, Ma *et al.* explored the influence of 2,8-butyl, 2,8-butylthio and 2,8-dibutylamino substitution on the electronic and optical properties of IFDK-based molecules [15]. They examined the reorganization energies, intermolecular electronic couplings and charge-injection barriers, concluding that the incorporation of sulfur atom into the side chains decreased the hole reorganization energies. In contrast, the dibutylamino functional group reduced the electronic coupling between π-cores due to increased steric interactions among the side chains. Thus, a comprehensive theoretical investigation is necessary to deepen our understanding of the structure-property relationships in IFDKs and to guide the future design of new organic semiconductors aimed at achieving high device performance with this material class. A detailed theoretical study is needed that explores a greater variety of substituents with different electronic characteristics, as well as the effects of substitution positions by using the same substituents in different locations on the IFDK molecule.

Charge transport ability plays a crucial role in the device performance of organic semiconductors. It is well known that organic materials exhibit two charge transport patterns at

the molecular scale: the band regime for delocalized electrons and the hopping regime for localized electrons. The majority of organic molecules typically transport charge via a thermally activated hopping process [16]. The charge hopping rate in organic molecules is typically described accurately by Marcus–Hush theory. As shown in Eq. 1, this theory quantifies the hopping rate for holes (or electrons) in the absence of an external electric field and assumes that the trap states are degenerate.

$$W = \frac{V^2}{\hbar} \left(\frac{\pi}{\lambda k_B T}\right)^{\frac{1}{2}} \exp\left(-\frac{\lambda}{4k_B T}\right) \quad (1)$$

Here, V represents the coupling matrix element, λ denotes the reorganization energy, k_B is the Boltzmann constant, $\hbar$ is the Planck constant, and T is the temperature in Kelvin. As shown, the electronic coupling matrix element and reorganization energy are the two critical parameters that influence the charge hopping rate which determines the charge mobility. Electronic coupling matrix elements (or transfer integrals), which is largely dictated by orbital overlap, heavily depends on the relative position and orientation of adjacent molecules. Therefore, optimizing V requires molecular reorientation in the solid state, which can be achieved through various techniques, including annealing, adjusting thin-film fabrication parameters, and employing solvent vapor annealing processes to enhance charge mobility. Without single crystal structures, it is not possible to calculate the transfer integrals*(V)*. On the other hand, reorganization energy (λ) is a geometric relaxation in a molecule upon charge transfer, can be calculated with Density Functional Theory (DFT) [17,18] prior to synthesis.

The reorganization energy of an organic semiconductor can be modulated through molecular design. Molecular engineering via chemical substitution, employed in the early stages of molecular design, is an effective method for achieving low reorganization energy. This approach typically enhances intermolecular interactions, increases solubility, and improves the quality of thin films, leading to lower synthesis costs and time savings. In addition to revealing the consistency between experimental results and theoretical calculations [19-22], DFT enables researchers to strategically design organic molecular semiconductors with low reorganization energy through chemical substitution.

In this study, the hole and electron reorganization energies of unsubstituted IFDK, as well as its 5,11- and 2,8-disubstituted derivatives, were computed using quantum mechanical calculations. Substituents positioned along the molecular long axes and short axes were employed to enhance understanding of how substitution position influences the molecular reorganization energy. Additionally, substituents with varying electron-withdrawing and electron-donating properties were also investigated to reveal the structure-property relationship in IFDKs. The

chemical structures of parent IFDK and its derivatives obtained through substitution at molecular short (5,11-position) and long axis (2,8-position) are depicted in Fig. 1.

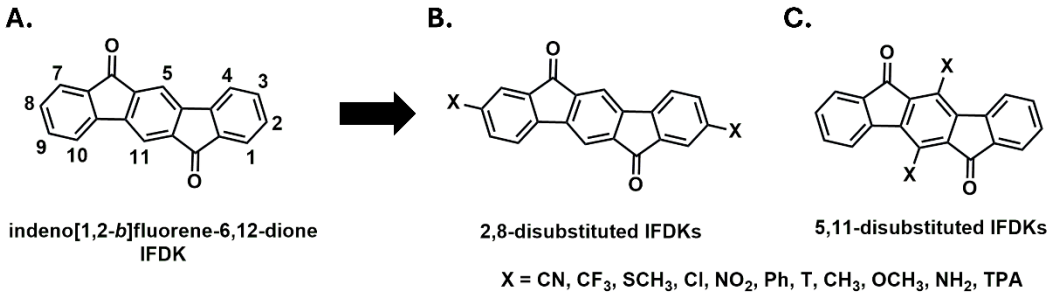

Figure 1: Chemical structures of indeno[1,2-b]fluorene-6,12-dione (IFDK) are shown, highlighting the number of carbon atoms (A), and its derivatives with substitution at the long molecular axis (2,8-positions) (B) and the short molecular axes (5,11-positions) (C), which are used for intramolecular hole and electron reorganization energy calculations in this study.

2. Computational Methodology

In this work, the total reorganization energy was calculated using potential energy surface method. The molecular geometry optimizations and single point energy calculations for the neutral and charged states were carried out in Gaussian 03W using density functional theory (DFT) at the B3LYP/6-31G** level.[23] The hole and electron reorganization energies in the 5,11- and 2,8-substituted IFDK derivatives were determined using a standard procedure outlined in the literature.[24]

A total of 23 molecules were studied for hole reorganization energy calculations in both neutral and cationic states, including 11 2,8-disubstituted derivatives, 11 5,11-disubstituted derivatives, and a parent IFDK molecule. Similarly, a total of 23 molecules were analyzed for electron reorganization energy calculations in both their neutral and anionic forms. This included 11 derivatives with substitutions at the 2,8 positions, 11 derivatives with substitutions at the 5,11 positions, and one parent IFDK molecule.

As illustrated in Figure 2, M, M^- and M^+ denote the neutral, anionic and cationic states. E_1, E_3, and E_6 represent the energy of neutral, anionic and cationic states in their lowest energy geometries, respectively. E_4 and E_7 represent the energy of neutral state at the geometry of the anion and cation, respectively. E_2 and E_5 represent the anionic and cationic states at the geometry of neutral molecule, respectively.

Here, $\lambda^{(3)}$ and $\lambda^{(4)}$ stand for the energies of geometric relaxation for the neutral and cationic states, respectively. The hole reorganization energy ($\lambda_h^{(+)}$) is the sum of the geometric relaxation

energies involved in transitioning from the neutral state geometry to the cationic state geometry, and vice versa. It is defined as:

$$\lambda_h^{(+)} = \lambda^{(3)} + \lambda^{(4)} \quad (2)$$

where $\lambda^{(3)} = E_7 - E_1$ and $\lambda^{(4)} = E_5 - E_6$

In Figure 2, $\lambda^{(1)}$ and $\lambda^{(2)}$ represent the energies of geometric relaxation for the neutral and anionic states, respectively. The reorganization energy for electron transfer ($\lambda_e^{(-)}$) consists of $\lambda^{(1)}$ and $\lambda^{(2)}$, which correspond to the energies of geometric relaxation for the neutral and anionic states, respectively. It is evaluated as follows:

$$\lambda_e^{(-)} = \lambda^{(1)} + \lambda^{(2)} \quad (3)$$

where $\lambda^{(1)} = E_4 - E_1$ and $\lambda^{(2)} = E_2 - E_3$

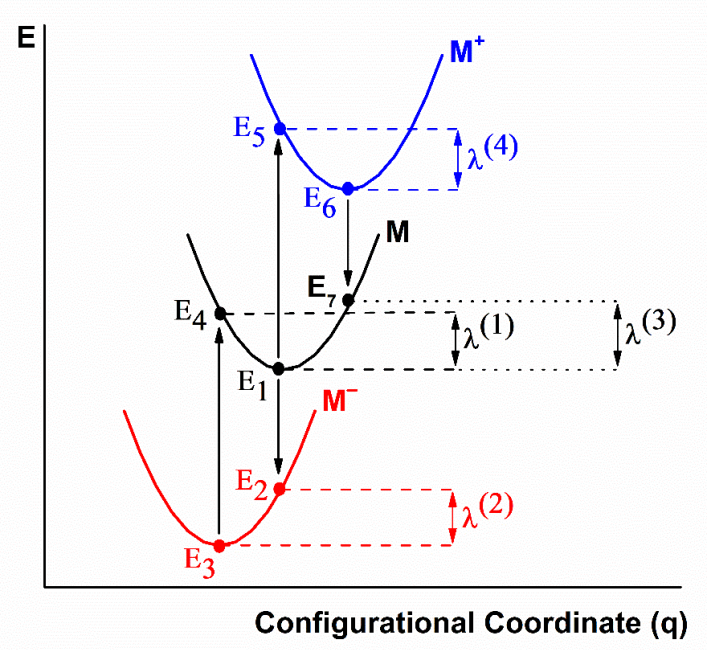

Figure 2: Sketch of Potential Energy Surfaces (PES) for anionic (M^-), neutral (M) and cationic (M^+) states.

3. Results and Discussion

First, the hole and electron reorganization energies, along with frontier molecular orbital energies and topographies of the parent molecule were calculated. Next, the effects of chemical substitution on the parent IFDK were examined to determine how these alterations impacted the initial results.

Figure 3 displays the results for the hole and electron reorganization energies of the parent IFDK and its derivatives, with substitutions along the short molecular axes (5,11-positions) and long molecular axes (2,8-positions), using the equations 2 and 3.

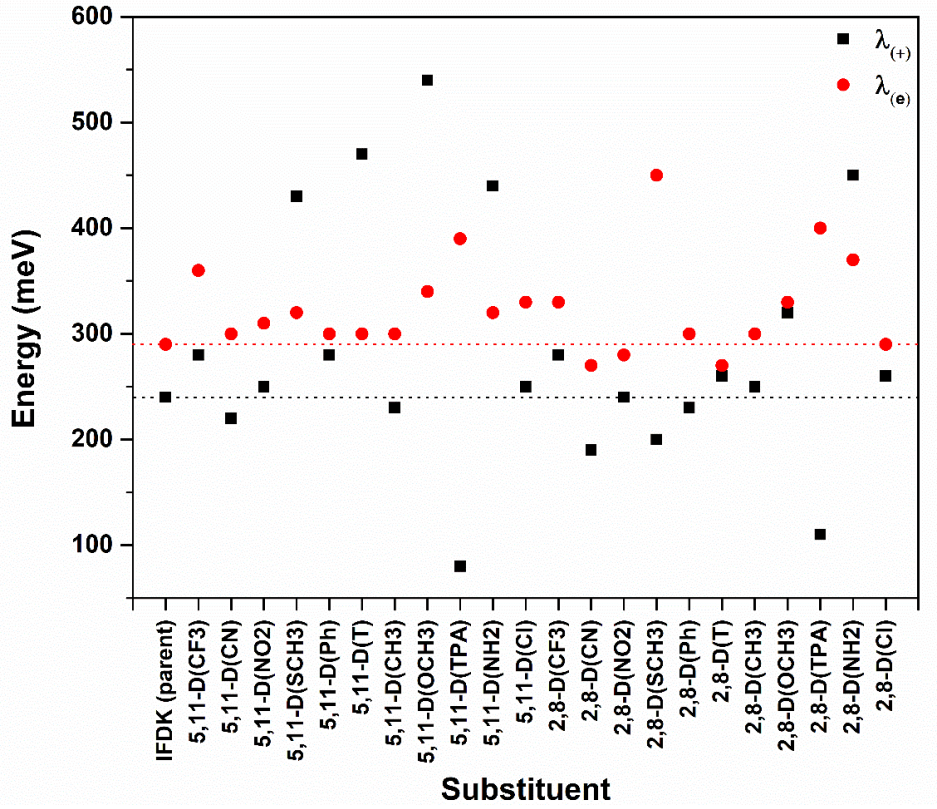

Figure 3: Results for the hole ($\lambda_h^{(+)}$) and electron ($\lambda_e^{(-)}$) reorganization energy of the parent IFDK molecule and its derivatives along the short molecular axes (5,11-positions) and long molecular axis (2,8-positions).

The numerical results have been displayed in Table 1. Notably, some of the substituents reduce the reorganization energy to some extent while some enhance it. Among all the substituents the methoxy (-OCH_3) group in 5,11-position leads to the highest increase in the hole reorganization energy, while the methylthio (-SCH_3) group at the 2,8-position results in the greatest increase in the electron reorganization energy. Other substituents at 5,11-position including -CF_3, -NO_2, -SCH_3, -Ph, -T, -NH_2 and -Cl also increased the hole reorganization energy. Additionally, all substituents at this position increased the electron reorganization energy. These results showed that most of the substituents used here increased the reorganization energy compared to parent molecule regardless of the position of the substituents.

The HOMO/LUMO topographies and energy levels of all substituents are shown in Fig. 4. Parent IFDK molecule, without any substitution, has HOMO energy level of -6.06 eV and a

LUMO energy level of -2.89 eV (Fig. 4), with reorganization energies of 240 meV for holes and 290 meV for electrons (Table 1).

The largest decrease in the hole reorganization energy, about threefold (80 meV), was observed with triphenylamine (TPA) substitution at the 5,11 positions, attributed to the localization of HOMO electrons on the TPA units. This behavior may stem from the strong electron-donating nature of TPAs. Additionally, cyano (-CN) and methyl (-CH_3) substitutions at the this position resulted in decreases of 20 meV and 10 meV in the hole reorganization energy, respectively. This cannot be explained solely by the nature of the substituents, as cyano is a strong electron-withdrawing group (EWG) while alkyl group is a weak electron-donating group (EDG).

The HOMO energy levels in TPA and CH_3-substituted IFDKs were upshifted by 1.08 eV and 0.11 eV, respectively, while CN-substitution resulted in a decrease of 0.66 eV. Thus, there is no clear relationship between the HOMO energy level and the hole reorganization energy.

Based on the frontier orbital topographies, the localization of HOMO electrons on substituents favors a reduction in the hole reorganization energy, whereas the delocalization of HOMO electrons throughout the entire molecule increases it. Therefore, substitution along the short molecular axes appears promising for designing *p*-type IFDK-based molecular semiconductors.

On the other hand, no decrease in the electron reorganization energy was observed in 5,11-substituted IFDKs compared to the parent molecule. There was also no significant change in wavefunction distribution of LUMO electrons upon substitution at 5,11-position. As shown in Figure 4, regardless of the electronic character of substituents, there is no relationship between the LUMO energy level and the electron reorganization energy. Additionally, correlation between the LUMO coefficients on the 5 and 11 carbons, and the reorganization energy could not be established.

Table 1: The hole and electron reorganization energies of 5,11- and 2,8-disubstituted IFDKs calculated at B3LYP/6-31G** theory level.

Molecule		E_1 (eV)	E_2 (eV)	E_3 (eV)	E_4 (eV)	E_5 (eV)	E_6 (eV)	E_7 (eV)	$\lambda^{(4)}$ (eV)	$\lambda^{(3)}$ (eV)	$\lambda_h^{(+)}$ (meV)	$\lambda^{(1)}$ (eV)	$\lambda^{(2)}$ (eV)	$\lambda_e^{(-)}$ (meV)
IFDK (parent)		-24997.49	-24998.93	-24999.07	-24997.34	-24990.00	-24990.12	-24997.37	0.12	0.12	240	0.15	0.14	290
5,11-IFDK	CF_3	-43339.01	-43340.83	-43341.01	-43338.83	-43331.15	-43331.29	-43338.87	0.14	0.14	280	0.18	0.18	360
	CN	-30017.14	-30019.31	-30019.46	-30016.99	-30009.06	-30009.17	-30017.03	0.11	0.11	220	0.15	0.15	300
	NO_2	-36125.89	-36128.09	-36128.24	-36125.73	-36117.72	-36117.84	-36125.76	0.12	0.13	250	0.16	0.15	310
	SCH_3	-48807.29	-48808.91	-48809.07	-48807.13	-48800.04	-48800.26	-48807.08	0.22	0.21	430	0.16	0.16	320
	Ph	-37572.17	-37573.60	-37573.75	-37572.02	-37564.94	-37565.08	-37572.03	0.14	0.14	280	0.15	0.15	300
	T	-55028.34	-55029.86	-55030.01	-55028.19	-55021.04	-55021.24	-55028.07	0.20	0.27	470	0.15	0.15	300
	CH_3	-27137.37	-27138.77	-27138.92	-27137.22	-27130.03	-27130.14	-27137.25	0.11	0.12	230	0.15	0.15	300

	OCH_3	-31230.00	-31231.51	-31231.68	-31229.83	-31222.78	-31223.10	-31229.78	0.32	0.22	540	0.17	0.17	340
	TPA	-65733.99	-65735.50	-65735.69	-65733.79	-65728.10	-65728.14	-65733.95	0.04	0.04	80	0.2	0.19	390
	NH_2	-28010.63	-28012.04	-28012.20	-28010.47	-28003.90	-28004.16	-28010.45	0.26	0.18	440	0.16	0.16	320
	Cl	-50009.49	-50011.24	-50011.40	-50009.32	-50001.77	-50001.89	-50009.36	0.12	0.13	250	0.17	0.16	330
	CF_3	-43339.84	-43341.78	-43341.94	-43339.67	-43331.85	-43331.99	-43339.70	0.14	0.14	280	0.17	0.16	330
	CN	-30017.39	-30019.65	-30019.79	-30017.26	-30009.29	-30009.39	-30017.30	0.10	0.09	190	0.13	0.14	270
	NO_2	-36126.78	-36129.21	-36129.35	-36126.64	-36118.41	-36118.53	-36126.66	0.12	0.12	240	0.14	0.14	280
	SCH_3	-48807.66	-48809.20	-48809.41	-48807.42	-48800.93	-48801.03	-48807.56	0.10	0.1	200	0.24	0.21	450
	Ph	-37572.63	-37574.20	-37574.35	-37572.48	-37565.73	-37565.85	-37572.52	0.12	0.11	230	0.15	0.15	300
2,8-IFDK	T	-55028.88	-55030.54	-55030.67	-55028.74	-55022.18	-55022.32	-55028.76	0.14	0.12	260	0.14	0.13	270
	CH_3	-27137.44	-27138.81	-27138.96	-27137.29	-27130.23	-27130.36	-27137.32	0.13	0.12	250	0.15	0.15	300
	OCH_3	-31230.29	-31231.65	-31231.81	-31230.12	-31223.47	-31223.62	-31230.12	0.15	0.17	320	0.17	0.16	330
	TPA	-65734.46	-65736.01	-65736.21	-65734.26	-65728.67	-65728.72	-65734.40	0.05	0.06	110	0.2	0.2	400
	NH_2	-28010.30	-28011.46	-28011.65	-28010.12	-28003.85	-28004.11	-28010.11	0.26	0.19	450	0.18	0.19	370
	Cl	-50009.81	-50011.63	-50011.77	-50009.66	-50002.22	-50002.35	-50009.68	0.13	0.13	260	0.15	0.14	290

Among the 11 substituents, cyano (-CN), methylthio (-SCH_3), phenyl (-Ph) and TPA at the 2,8- position showed reductions in the hole reorganization energy of 50 meV, 40 meV, 10 meV and 130 meV, respectively, compared to the parent IFDK. Similar to the 5,11-substitution, the 2,8- substitution with TPA results in the largest decrease in the hole reorganization energy, with a downshift of 2.2 times. In this case, the 2,8-substitution with TPA leads to full localization of HOMO electrons on the substituent groups, which exhibit a strong electron-donating character. However, the relationship between the HOMO energy level and the hole reorganization energy at this position remains unclear. Additionally, cyano (-CN), nitro (-NO_2) and thiophene (-T) substitutions at this position resulted in smaller decrease in the electron reorganization energy of 20 meV, 10 meV, and 20 meV, respectively. While the strong EWG character of the -CN and -NO_2 groups appears to play a role in reducing the electron reorganization energy, thiophene, which is weak EDG, has a similar impact. This suggests that there is no clear relationship between the electronic character of substituents and the reduction in the electron reorganization energy. Compared to parent IFDK LUMO energy level, all these substituents have lower (stabilized) LUMO energy levels, Similar to the 5,11-substitution, the relationship between the wavefunction distribution of LUMO electrons and the LUMO coefficients at the 2,8 carbons, and electron reorganization energy has not been clearly established in this position.

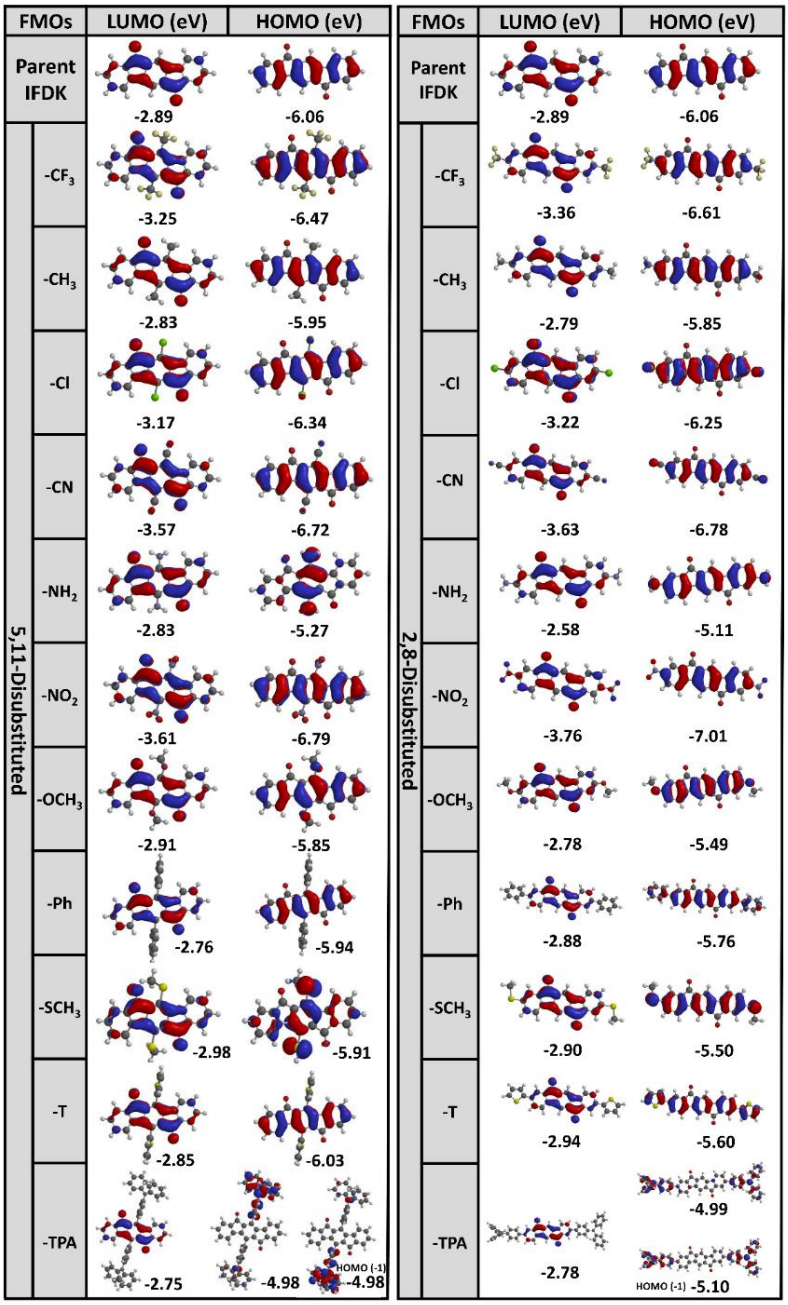

Figure 4: Computed HOMO and LUMO energy levels, and topographical representations of IFDK derivatives with DFT and B3LYP/6-31G** basis set.

4. Conclusion

In conclusion, the hole and electron reorganization energies of 23 IFDK-based small molecules were calculated using DFT for the first time, systematically investigating the impact of substituent nature and position on the reorganization energy. Owing to its strong electron-donating ability, 5,11-ditriphenylamine substituted IFDK molecule exhibited a much lower hole reorganization energy than its unsubstituted counterpart, with a significant difference of 160 meV

observed, alongside the localization of HOMO electrons on the TPA groups. This behavior became less pronounced when moving from the 5,11-position to the 2,8-position with the same substituent, where a downshift of 130 meV was noted in the hole reorganization energy. The same substituent group showed varying reorganization energy based on the specific substitution position, highlighting the significant impact of substitution on the reorganization energy. More effective charge transfer is expected upon TPA substitution in IFDKs, due to lower reorganization energy.

In contrast to general observation for other substituent that typically resulted in an absolute increase, -CN and -CH_3 substitutions at 5,11-position, as well as -CN, -SCH_3, and -Ph substitutions at 2,8-position, displayed similar downshift in the hole reorganization energy, albeit to a lesser extent compared to TPA substitution. The same substituent groups including -TPA and -CN resulted in different hole reorganization energies based on the precise position of the substitution. To the best of my knowledge, this is the first study in literature comparing the reorganization energy of the same substituent at different positions around the IFDK π-core.

It was found that introducing any of the substituents used in study into the IFDK molecule at the 5,11-position increased the electron reorganization energy. Meanwhile, substitutions at the 2,8-position with -CN, -NO_2, and -T groups resulted in a slight decrease in the electron reorganization energy. These results clearly indicate the importance of substitution position around the IFDK molecule. Substitution at the 2,8-position appears to be more favorable for designing n-type molecular semiconductors within this family. Additionally, the downshift in the hole reorganization energies upon substitution at the same position suggests that achieving ambipolar semiconductivity with 2,8-substituted IFDKs is highly feasible. Moreover, 5,11-substitution of IFDK appears promising for designing *p*-type semiconductors, as the electron reorganization energy increased for all substituents, while the hole reorganization energy decreased upon -CN and -CH_3 substitution.

With these new results, the crucial structure–property relationships for IFDKs are better established now/have been better established, paving the way for future material designs in this family by identifying the optimal positions and substituents for improving charge transport properties through the reduction of the reorganization energy. The findings here demonstrate that 5,11- and 2,8-disubstituted IFDKs with lower hole and electron reorganization energies are promising candidates for *p*-type and *n*-type semiconducting materials.

Acknowledgements

I would like to thank Prof. Hakan Usta for his helpful discussions.

References

[1] Shen, T., Jiang, Z., Wang, Y., Liu, Y., *Rational molecular design of diketopyrrolopyrrole-based n-type and ambipolar polymer semiconductors*, Chemistry–A European Journal, 30, e202401812, 2024.

[2] Ozcan, E., Ozdemir, M., Ho, D., Zorlu, Y., Ozdemir, R., Kim, C. Usta, H., Cosut, B., *A solution-processable meso-phenyl bodipy-based n-channel semiconductor with enhanced fluorescence emission*, ChemPlusChem, 84, 1423-1431, 2019.

[3] Kim, T., Shin, G., Park, T., Kim, M., *Molecular design leveraging non-covalent interactions for efficient light-emitting organic small molecules*, Advanced Functional Materials, 2412267, 2024.

[4] Ozdemir, M., Genc, S., Ozdemir, R., Altintas, Y., Citir, M., Sen, U., Mutlugun, E., Usta, H., *Trans-cis isomerization assisted synthesis of yellow fluorescent maleic anhydride derivatives for white-light generation,* Synthetic Metals, 210, 192–200, 2015.

[5] Langa, F., de la Cruz, P., Sharma, G. D., *Organic solar cells based on non-fullerene low molecular weight organic semiconductor molecules,* ChemSusChem, e202400361, 2024.

[6] Wang, Y., Wustoni, S., Surgailis, J., Zhong, Y., Koklu, A., Inal. S., *Designing organic mixed conductors for electrochemical transistor applications*, Nature Reviews Materials, 9, 249–265, 2024.

[7] Li, S., Duan, Y., Zhu, W., Cheng, S., Hu, W., *Sensing interfaces engineering for organic thin film transistors-based biosensors: opportunities and challenges*, Advanced Materials, 2412379.

[8] Ji, Z. Li, Z., Liu, L., Zou, Y., Di, C., Zhu, D., *Organic thermoelectric devices for energy harvesting and sensing applications,* Advanced Materials Technologies, 2302128, 2024.

[9] Solari, W. Liu, R., Erkızan, S.N., Osypiw, A.R.C., Smowton, P.M., Hou, B*., Image sensors and photodetectors based on low-carbon footprint solution-processed semiconductors,* Advanced Sensor Research, 2400059, 2024.

[10] Chen, J., Zhang, W., Wang, L., Yu, G., *Recent research progress of organic small-molecule semiconductors with high electron mobilities*, Advanced Materials, 35, 2210772, 2023.

[11] Can, A., Facchetti, A., Usta, H., *Indenofluorenes for organic optoelectronics: the dance of fused five- and six-membered rings enabling structural versatility*, Journal of Materials Chemistry C, 10, 8496–8535, 2022.

[12] Ozdemir, Park, R. S., Deneme, İ., Park, Y., Zorlu, Y., Alidagi, H. A., Harmandar, K., Kim C., Usta, H., *Triisopropylsilylethynyl-substituted indenofluorenes: carbonyl: versus dicyanovinylene functionalization in one-dimensional molecular crystals and solution-processed n-channel ofets*, Organic Chemistry Frontiers, 5, 2912–2924, 2018.

[13] Ozdemir, R. Choi, D., Ozdemir, M., Kwon, G., Kim, H., Sen, U., Kim, C., Usta, H., *Ultralow bandgap molecular semiconductors for ambient-stable and solution-processable ambipolar organic field-effect transistors and inverters*, Journal of Materials Chemistry C, 5, 2368–2379, 2017.

[14] Martinez, I., Zarate, X., Schott, E., Morales-Verdejo, C., Castillo, F., Manríquez, J. M., Chávez, I., *A theoretical study of substituted indeno[1,2-b]fluorene compounds and their possible applications in solar cells*, Chemical Physics Letters, 636, 31–34, 2015.

[15] Huang, J.-D., Zhao, J., Yu, K., Huang, X., Cheng, S.-B., Ma, H., *Theoretical study of charge-transport and optical properties of indeno[1,2- b]fluorene-6,12-dione-based*

semiconducting materials, Acta Crystallographica Section B Structural Science, Crystal Engineering and Materials, 74, 705–711, 2018.

[16] Coropceanu, V., Cornil, J., da Silva Filho, D. A., Olivier, Y., Silbey, R., Brédas, J.-L., *Charge transport in organic semiconductors*, Chemical Reviews, 107, 926–952, 2007.

[17] Oliveira, E. F., Lavarda, F. C., *Reorganization energy for hole and electron transfer of poly(3-hexylthiophene) derivatives*, Polymer, 99, 105–111, 2016.

[18] Lee, C., Sohlberg, K., *The effect of substitution on reorganization energy and charge mobility in metal free phthalocyanine*, Chemical Physics, 367, 7–19, 2010.

[19] Ozdemir, R., Ahn, K., Deneme, I., Zorlu, Y., Kim, D., Kim, MG., Usta, H., *Engineering functionalized low LUMO [1]benzothieno[3, 2-b][1]benzothiophenes (BTBTs): unusual molecular and charge transport properties,* Journal of Materials Chemistry C, 8, 15253–15267, 2020.

[20] Elmacı, G., Aktan, E., Seferoğlu, N., Hökelek, T., Seferoğlu, Z., *Synthesis, molecular structure and computational study of (z)-2-((e)-4-nitrobenzylidene)hydrazone)-1,2-diphenylethan-1-one,* Journal of Molecular Structure, 1099, 83–91, 2015.

[21] Elmacı, G., Duyar, H., Aydıner B., Seferoğlu, N., Naziri, MA., Şahin, E., Seferoğlu, Z., *The syntheses, molecular structure analyses and DFT studies on new benzil monohydrazone based Schiff bases,* Journal of Molecular Structure, 1162, 37–44, 2018.

[22] Elmacı, G., Duyar, H., Aydıner B., Yahaya, I., Seferoğlu, N., Şahin, E., Çelik, S. P., Sçık. L., Seferoğlu, Z., *Novel benzildihydrazone based Schiff bases: Syntheses, characterization, thermal properties, theoretical DFT calculations and biological activity studies,* Journal of Molecular Structure, 1184, 271–280, 2019.

[23] Frisch, M.J., Trucks, G.W., Schlegel, H.B., Scuseria, G.E., Robb, M.A., Cheeseman, J.R., Montgomery Jr, J.A., Vreven, T., Kudin, K.N., Burant, J.C., Millam, J.M., Iyengar, S.S., Tomasi, J., Barone, V., Mennucci, B., Cossi, M., Scalmani, G., Rega, N., Petersson, G.A., Nakatsuji, H., Hada, M., Ehara, Toyota, M., K., Fukuda, R., Hasegawa, J., Ishida, M., Nakajima, T., Honda, Y., Kitao, O., Nakai, H., Klene, M., Li, X., Knox, J.E., Hratchian, H.P., Cross, J.B., Adamo, C., Jaramillo, J., Gomperts, R., Stratmann, R.E.,Yazyev, O., Austin, A.J., Cammi, R., Pomelli, C., Ochterski, J.W., Ayala, P.Y., Morokuma, K., Voth, G.A., Salvador, P., Dannenberg, J.J., Zakrzewski, V.G., Dapprich, S., Daniels, A.D., Strain, M.C., Farkas, O., Malick, D.K., Rabuck, A.D., Raghavachari, K., Foresman, J.B., Ortiz, J.V., Cui, Q., Baboul, Clifford, A.G., S., Cioslowski, J., Stefanov, B.B., Liu, G., Liashenko, A., Piskorz, P., Komaromi, I., Martin, R.L., Fox, D.J., Keith, T., Al-Laham, M.A., Peng, C.Y., Nanayakkara, A., Challacombe, M., Gill, P.M.W., Johnson, B., Chen, W., Wong, M.W., Gonzalez, C., Pople, J.A., Gaussian 03, Gaussian, Inc., Pittsburgh, PA, 2003.

[24] Brédas, J.-L., Beljonne, D., Coropceanu, V., Cornil, J., *Charge-transfer and energy-transfer processes in π-conjugated oligomers and polymers: a molecular picture*, Chemical Reviews, 104, 4971–5004, 2004.

Adıyaman University Journal of Science
https://dergipark.org.tr/en/pub/adyujsci
DergiPark AKADEMİK
ISSN 2147-1630
e-ISSN 2146-586X

Approximation by a new Schurer type Stancu Operators and Associated GBS Operators

Nesibe MANAV MUTLU[1,*]

[1]*İstanbul Nişantaşı University, Faculty of Economics, Administrative and Social Sciences, İstanbul, Turkey*
nesibe.manavm@gmail.com, ORCID: 0000-0002-7853-6337

Received: 15.05.2024 **Accepted:** 21.09.2024 **Published:** 31.12.2024

Abstract

This study presents a novel extension of the Schurer type Stancu operators and investigates their properties in terms of approximation. The uniform convergence of these operators is provided using the Korovkin Theorem, and the rates of convergence are expressed in terms of the modulus of continuity. Subsequently, the theorem known as Grüss-Voronovskaja is proven. In addition, the related generalized Boolean sum (GBS) operators are defined, and the rates of approximation for these operators are obtained using the mixed modulus of smoothness and functions from the Lipshitz class. Then, numerical examples and graphical results for both operators are presented.

Keywords: Schurer-Stancu operators; Modulus of continuity; Grüss-Voronovskaja type theorem; GBS operators.

* Corresponding Author
DOI: 10.37094/adyujsci.1484906

Yeni bir Schurer tipi Stancu Operatörleri ve ilgili GBS Operatörleri ile Yaklaşım

Öz

Bu çalışma, Schurer tipi Stancu operatörlerinin yeni bir genelleştirmesini sunmakta ve bu operatörlerin yaklaşım özelliklerini incelemektedir. Bu operatörlerin düzgün yakınsaklığı Korovkin Teoremi yardımıyla verilmiş ve yakınsama hızları süreklilik modülü cinsinden ifade edilmiştir. Daha sonra Grüss-Voronovskaja olarak bilinen teorem ispatlanmıştır. Ayrıca, ilgili genelleştirilmiş Boolean toplamı (GBS) operatörleri tanımlanmış ve bu operatörlerin yaklaşım hızları karma düzgünlük modülü ile Lipshitz sınıfından fonksiyonlar kullanılarak elde edilmiştir. Sonrasında, her iki operatör için sayısal örnekler ve grafiksel sonuçlar sunulmuştur.

Anahtar Kelimeler: Schurer-Stancu operatörleri; Süreklilik modülü; Grüss-Voronovskaja tipi teorem; GBS operatörleri.

1. Introduction

Polynomials are considered the fundamental functions that computers can directly compute. The Weierstrass approximation theorem in mathematical analysis states that any continuous function defined on a closed interval may be represented by a polynomial function. The Weierstrass approximation theorem is highly useful in both practical and theoretical contexts, particularly in the domain of polynomial interpolation, due to this characteristic of the property. An exemplary demonstration of this theorem is S.N. Bernstein got it by defining the subsequent polynomials in reference [1]. The Bernstein polynomials are expressed by the following equation:

$$\mathrm{B}_{\eta}(\phi,\tau)=\sum_{\rho=0}^{\eta}\mathbf{p}_{\eta,\rho}(\tau)\phi\left(\frac{\rho}{\eta}\right),\eta\in\mathrm{N},$$

for each function ϕ in the space $C[0,1]$, which includes all real-valued continuous functions defined on the closed interval $[0,1]$ and $\mathbf{p}_{\eta,\rho}(\tau)$ is a Bernstein basis function equal to $\binom{\eta}{\rho}\tau^{\rho}(1-\tau)^{\eta-\rho}$.

F. Schurer, [2], introduced and investigated the features of the linear positive operators known as Bernstein-Schurer polynomials,

$$B_{\eta,\gamma}(\phi,\tau)=\sum_{\rho=0}^{\eta+\gamma}\boldsymbol{p}_{\eta+\gamma,\rho}(\tau)\phi\left(\frac{\rho}{\eta}\right),\eta\in N,$$

for ϕ be an element of $C[0,1+\gamma]$, which is a set of all real-valued continuous functions defined on the expanded closed interval $[0,1+\gamma]$.

Then, D. Bărbosu as an extension of Bernstein operators, created the linear positive Schurer-Stancu operators, in [3], $\widetilde{S_{\eta,\gamma}^{\alpha,\beta}}: C[0,1+\gamma]\rightarrow C[0,1]$ as

$$\widetilde{S_{\eta,\gamma}^{\alpha,\beta}}(\phi,\tau)=\sum_{\rho=0}^{\eta+\gamma}\boldsymbol{p}_{\eta+\gamma,\rho}(\tau)\phi\left(\frac{\rho+\alpha}{\eta+\beta}\right),$$

where γ be a given integer from the set of natural numbers, and α and β be provided parameters from the set of real numbers. These parameters must satisfy the requirements $0\leq\alpha\leq\beta$. Note that for $\alpha=\beta=0$ these polynomials become Schurer operators, for $\gamma=0$ the operators are the Stancu operators, for $\alpha=\beta=0$ and $\gamma=0$ the operators are the Bernstein operators. Bărbosu's work has inspired many studies in literature. Some of them are as [4-6].

Stancu introduced a new type of linear positive operators named Stancu operators in the literature, as follows,

$$L_{\eta,\mu}(\phi,\tau)=\sum_{\rho=0}^{\eta}w_{\eta,\rho,\mu}(\tau)\phi\left(\frac{\rho}{\eta}\right),\quad \tau\in[0,1] \tag{1}$$

for $\phi\in C[0,1]$, a non-negative integer parameter $\mu,\eta\in N$ such that $\eta>2\mu$, where

$$w_{\eta,\rho,\mu}(\tau)=\begin{cases}(1-\tau)\boldsymbol{p}_{\eta-\mu,\rho}(\tau); & 0\leq\rho<\mu\\ (1-\tau)\boldsymbol{p}_{\eta-\mu,\rho}(\tau)+\tau\boldsymbol{p}_{\eta-\mu,\rho-\mu}(\tau); & \mu\leq\rho\leq\eta-\mu,\\ \tau\boldsymbol{p}_{\eta-\mu,\rho-\mu}(\tau); & \eta-\mu<\rho\leq\eta\end{cases} \tag{2}$$

and $\mathbf{p}_{\eta,\rho}(\tau)$ is the well-known Bernstein basis polynomials [7-8]. For the special cases $\mu=0$ and $\mu=1$, Stancu operators defined by Eq.1 give the classical Bernstein operators.

Recently, many academics have focused on Stancu operator approximation. The researchers in [9-11] showed Stancu operator approximation properties in multiple domains, including the complex plane and distinct forms. The complex form of Schurer-type Stancu operators is defined in [13], and their complex approximation properties are investigated by

authors. In this study, we introduce and examine the real-valued form of operators whose complex form has been examined in [13].

Motivated by the beforementioned studies, we introduce the real variable case of the Schurer form of Stancu operators as follows,

$$L_{\eta,\mu,\gamma}^{\alpha,\beta}(\phi,\tau)=\sum_{\rho=0}^{\eta+\gamma-\mu}\binom{\eta+\gamma-\mu}{\rho}\tau^{\rho}(1-\tau)^{\eta+\gamma-\mu-\rho}\left[(1-\tau)\phi\left(\frac{\rho+\alpha}{\eta+\beta}\right)+\tau\phi\left(\frac{\rho+\mu+\alpha}{\eta+\beta}\right)\right] \tag{3}$$

where α,β are real parameters with $0\leq\alpha\leq\beta$, μ is a non -negative integer, $\eta\in N$ such that $\eta+\gamma>2\mu,\gamma\in N\cup\{0\}$ and examined the approximation properties of them. Here, for the situation $\gamma=0$, these operators become the original Stancu operators represented with the equation (1), and for $\mu=0$, they become Schurer-type Stancu operators.

In this study, we first investigate this new real-valued generalization of the Schurer-type Stancu operators and their properties related to approximation. By applying the renowned Korovkin theorem, we achieve a uniform approximation result and consider the modulus of continuity rate of convergence given. Next, we establish the theorems of Grüss-Voronovskaja. Then, we create related GBS operators of two real variables and examine their approximation properties. Finally, we provide numerical examples to demonstrate the process of approximation using these new operators.

2. Supplementary Findings

To achieve the primary findings, we provide the following information. These findings in this section were written using the results found for the complex variable in [13]. Thus, the results are presented without proof.

Lemma 2.1. Considering the operators (3), we have the following moments,

$$L_{\eta,\mu,\gamma}^{\alpha,\beta}(e_0,\tau)=1,$$

$$L_{\eta,\mu,\gamma}^{\alpha,\beta}(e_1,\tau)=\frac{(\eta+\gamma)\tau+\alpha}{\eta+\beta},$$

$$L_{\eta,\mu,\gamma}^{\alpha,\beta}(e_2,\tau)=\frac{1}{(\eta+\beta)^2}\{(\eta+\gamma-\mu)(\eta+\gamma+\mu-1)\tau^2+[(\eta+\gamma-\mu)(2\alpha+1)+\mu(\mu+2\alpha)]\tau+\alpha^2\},$$

$$L_{\eta,\mu,\gamma}^{\alpha,\beta}(e_3,\tau) = \frac{1}{(\eta+\beta)^3}\{(\eta+\gamma-\mu)(\eta+\gamma+\mu-1)(\eta+\gamma+2\mu-2)\tau^3 + 3(\eta+\gamma-\mu)\,[(\eta+\gamma-\mu-1)(\alpha+1)+\mu(\mu+2\alpha+1)]\tau^2 + [(\eta+\gamma-\mu)(1+3\alpha+3\alpha^2)+\mu(\mu^2+3\alpha\mu+3\alpha^2)]\tau + \alpha^3\},$$

$$L_{\eta,\mu,\gamma}^{\alpha,\beta}(e_4,\tau) = \frac{1}{(\eta+\beta)^4}\{(\eta+\gamma-\mu)(\eta+\gamma+\mu-1)(\eta+\gamma-\mu-2)(\eta+\gamma+3\mu-3)\tau^4 + 2(\eta+\gamma-\mu)(\eta+\gamma-\mu-1)[(\eta+\gamma-\mu-2)(3+2\alpha)+3\mu(2+2\alpha+\mu)]\tau^3 + (\eta+\gamma-\mu)[(\eta+\gamma-\mu-1)(7+12\alpha+6\alpha^2)+4\mu^3+\mu^2(6+12\alpha)+4\mu(1+3\alpha+3\alpha^2)]\tau^2 + [(\eta+\gamma-\mu)(1+2\alpha)(1+2\alpha+2\alpha^2)+\mu^4+4\alpha\mu^3+6\alpha^2\mu^2+4+2\alpha^3\mu]\tau + \alpha^4\}.$$

Lemma 2.2. The central moments corresponding to the operators (3) are displayed below:

$$L_{\eta,\mu,\gamma}^{\alpha,\beta}(\xi-\tau,\tau) = \frac{(\gamma-\beta)\tau+\alpha}{\eta+\beta} := \Phi_{\eta,\mu,\gamma}^{\alpha,\beta,1},$$

$$L_{\eta,\mu,\gamma}^{\alpha,\beta}((\xi-\tau)^2,\tau) = \frac{1}{(\eta+\beta)^2}\{[-(\eta+\gamma)+(\gamma+\beta)^2-\mu(\mu-1)]\tau^2 + [\eta+\gamma+2\alpha(\gamma-\beta)+\mu(\mu-1)]\tau+\alpha^2\} := \Phi_{\eta,\mu,\gamma}^{\alpha,\beta,2},$$

$$L_{\eta,\mu,\gamma}^{\alpha,\beta}((\xi-\tau)^4,\tau) = \frac{1}{(\eta+\beta)^4}\{[3\eta^2+\eta(12\gamma\beta+6\mu^2-6\mu-6-8\beta-6\beta^2)+\gamma^4+\gamma^3(-6-4\beta)+\gamma^2(-6\mu^2+6\mu+11+12\beta+6\beta^2)+\gamma(8\mu^3+6\mu^2+12\beta\mu^2-14\mu-12\beta\mu-6-8\beta-6\beta^2-4\beta^3)\&-3\mu^4-\mu^3(6+8\beta)+\mu^2(3-6\beta^2)+\mu(6+8\beta+6\beta^2)+\beta^4]\tau^4 + [-6\eta^2+\eta(6\gamma^2-12\gamma(2+\alpha+\beta)-12\mu^2+12\mu+12+8\alpha+12\beta+12\alpha\beta+6\beta^2)+\gamma^3(6+4\alpha)+\gamma^2(6\mu^2-6\mu-18-12\alpha-12\beta-12\alpha\beta)+\gamma(-12\mu^3-12\mu^2(1+\alpha+\beta)+12\mu(2+\alpha+\beta)+12+8\alpha+12\beta+12\alpha\beta+12\alpha\beta^2+6\beta^2)+6\mu^4+4\mu^3(3+2\alpha+3\beta)-6\mu^2(1-2\alpha\beta-\beta^2)-2\mu(6+4\alpha+6\beta+6\alpha\beta+3\beta^2)-4\alpha\beta^3]\tau^3 + [3\eta^2+\eta(\gamma(10+12\alpha)+6\mu^2-6\mu-6\alpha^2-12\alpha-7-12\alpha\beta-4\beta)+\gamma^2(7+12\alpha+6\alpha^2)+\gamma(4\mu^3+\mu^2(6+12\alpha)+\mu(-10-12\alpha)-7-12\alpha-6\alpha^2-4\beta-12\alpha\beta-12\alpha^2\beta)-4\mu^4-2\mu^3(3+6\alpha+2\beta)+3\mu^2(1-4\alpha\beta-2\alpha^2)+\mu(7+12\alpha+6\alpha^2+4\beta+12\alpha\beta)+16\alpha^2\beta^2]\tau^2 + [(\eta-\mu)(1+4\alpha+6\alpha^2)+\gamma(1+2\alpha)(1+2\alpha+2\alpha^2)+\mu^4+4\alpha\mu^3+6\alpha^2\mu^2+4\alpha^3\mu]\tau+\alpha^4\}.$$

Lemma 2.3. From the previous lemma we immediately get the following results.

$$\lim_{\eta\to\infty} L_{\eta,\mu,\gamma}^{\alpha,\beta}(\xi-\tau,\tau) = (\gamma-\beta)\tau+\alpha,$$

$$\lim_{\eta\to\infty} L_{\eta,\mu,\gamma}^{\alpha,\beta}((\xi-\tau)^2,\tau) = \tau(1-\tau),$$

$$\lim_{\eta\to\infty} L_{\eta,\mu,\gamma}^{\alpha,\beta}((\xi-\tau)^4,\tau) = 0.$$

3. Main Results for Univariate Operators

As a result of the previous lemmas, the following Korovkin type theorem is easily reached.

Theorem 3.1. If ϕ belongs to the set of continuous functions defined on the interval $[0,1+\gamma]$, $\lim_{\eta\to\infty} L^{\alpha,\beta}_{\eta,\mu,\gamma}(\phi,\tau) = \phi(\tau)$, uniformly on $[0,1]$.

Now, we want to provide an upper limit for the approximation error using the $K-$functional. Let us start by reviewing certain definitions and notations.

The definition of the modulus of continuity for a function ϕ in the space $C[0,1+\gamma]$ with a given value of $\delta > 0$ is as follows:

$$\omega(\phi,\delta) = \sup_{|\xi|<\delta}\ \sup_{\tau,\tau+\xi\in[0,1+\gamma]} |\phi(\tau+\xi)-\phi(\tau)|$$

The Petree's $K-$functional is formally defined as follows:

$$\rho(\phi,\delta) = \inf_{\zeta\in C^2[0,1+\gamma]}\{\|\phi-\zeta\|+\delta\|\zeta''\|\},(\delta>0),$$

where $C^2[0,1+\gamma] = \{\zeta\in C[0,1+\gamma]: \zeta',\zeta''\in C[0,1+\gamma]\}$. Then, for a positive constant M, we have the following inequality [12, p.1]

$$\rho(\phi,\delta) \le M\omega_2\left(\phi,\sqrt{\delta}\right) \tag{4}$$

where modulus of smoothness of the second order for a function ϕ belonging to the space $C[0,1+\gamma]$ is defined as

$$\omega_2\left(\phi,\sqrt{\delta}\right) = \sup_{0<\zeta\le\delta}\ \sup_{\tau,\tau+2\zeta\in[0,1+\gamma]} |\phi(\tau+2\zeta)-2\phi(\tau+\zeta)+\phi(\tau)|.$$

The upper bound for the error $\phi(\tau)-L^{\alpha,\beta}_{\eta,\mu,\gamma}(\phi,\tau)$ can be bounded by the modulus of continuity, as previously described.

Theorem 3.2. If $\phi\in C[0,1+\gamma]$, then

$$\left|L^{\alpha,\beta}_{\eta,\mu,\gamma}(\phi,\tau)-\phi(\tau)\right| \le 2\omega\left(\phi,\sqrt{\delta}\right)$$

where ω denotes the usual modulus of continuity.

Proof. By considering the inequality

$$|\phi(t)-\phi(\tau)| \leq \omega(\phi,\delta)\left(1+\frac{(\xi-\tau)^2}{\delta^2}\right) \tag{5}$$

and applying the operators these operators (3) we have

$$\begin{aligned}\left|L^{\alpha,\beta}_{\eta,\mu,\gamma}(\phi,\tau)-\phi(\tau)\right| &\leq L^{\alpha,\beta}_{\eta,\mu,\gamma}(|\phi(t)-\phi(\tau)|,\tau)\\ &\leq \omega(\phi,\delta)\left(1+\frac{1}{\delta^2}L^{\alpha,\beta}_{\eta,\mu,\gamma}((\xi-\tau)^2,\tau)\right)\end{aligned}$$

if we choose $\delta=\sqrt{\Phi^{\alpha,\beta,2}_{\eta,\mu,\gamma}}$ we reach the desired result.

Theorem 3.3. Let $\gamma \in N \cup \{0\}$ be fixed. For any value of τ inside the interval $[0,1]$ and every function ϕ belonging to the set of continuous functions defined on the interval $[0,1+\gamma]$,the inequality below,

$$\begin{aligned}\left|L^{\alpha,\beta}_{\eta,\mu,\gamma}(\phi;\tau)-\phi(\tau)\right| &\leq 4\rho\left(\phi,\frac{1}{4}\left(\left(\Phi^{\alpha,\beta,2}_{\eta,\mu,\gamma}\right)+{\Phi^{\alpha,\beta,1}_{\eta,\mu,\gamma}}^2\right)\right)+\omega\left(\phi;\Phi^{\alpha,\beta,1}_{\eta,\mu,\gamma}\right)\\ &\leq M\omega_2\left(\phi,\frac{1}{2}\sqrt{\Phi^{\alpha,\beta,2}_{\eta,\mu,\gamma}+{\Phi^{\alpha,\beta,1}_{\eta,\mu,\gamma}}^2}\,\&\right)+\omega\left(\phi;\Phi^{\alpha,\beta,1}_{\eta,\mu,\gamma}\right)\end{aligned}$$

holds.

Proof. We denote $\epsilon^{\alpha,\beta}_{\eta,\mu,\gamma}(\tau)=L^{\alpha,\beta}_{\eta,\mu,\gamma}(t;\tau)=\frac{(\eta+\beta)\tau+\alpha}{\eta+\beta}$ and define the auxiliary operator,

$$\widetilde{L^{\alpha,\beta}_{\eta,\mu,\gamma}}(\phi;\tau)=L^{\alpha,\beta}_{\eta,\mu,\gamma}(\phi;\tau)+\phi(\tau)-\phi\left(\epsilon^{\alpha,\beta}_{\eta,\mu,\gamma}(\tau)\right). \tag{6}$$

By using Lemma 2.1. we can easily reach that,

$$\widetilde{L^{\alpha,\beta}_{\eta,\mu,\gamma}}(1;\tau)=1$$
$$\widetilde{L^{\alpha,\beta}_{\eta,\mu,\gamma}}(\xi;\tau)=\tau$$

Consider a function ϕ that belongs to the class $C^2[0,1+\gamma]$. For any values of τ and ξ that are inside the interval $[0,1+\gamma]$ we have,

and applying $\widetilde{L^{\alpha,\beta}_{\eta,\mu,\gamma}}$ we get

$$\widetilde{L^{\alpha,\beta}_{\eta,\mu,\gamma}}(\zeta(\xi)-\zeta(\tau);\tau)=\zeta'(\tau)\widetilde{L^{\alpha,\beta}_{\eta,\mu,\gamma}}(\xi-\tau;\tau)+\widetilde{L^{\alpha,\beta}_{\eta,\mu,\gamma}}\left(\int_{\tau}^{\xi}(\xi-\upsilon)\zeta''(\upsilon)d\upsilon\,;\tau\right)$$
$$=L^{\alpha,\beta}_{\eta,\mu,\gamma}\left(\int_{\tau}^{\xi}(\xi-\upsilon)\zeta''(\upsilon)d\upsilon\,;\tau\right)-\int_{\tau}^{\epsilon^{\alpha,\beta}_{\eta,\mu,\gamma}(\tau)}\left(\epsilon^{\alpha,\beta}_{\eta,\mu,\gamma}(\tau)-\upsilon\right)\zeta''(\upsilon)d\upsilon.$$

If we continue with absolute values of both sides of last equation

$$\begin{aligned}&\left|\widetilde{L^{\alpha,\beta}_{\eta,\mu,\gamma}}(\zeta(\xi)-\zeta(\tau);\tau)\right|\\&\quad\le L^{\alpha,\beta}_{\eta,\mu,\gamma}\left(\left|\int_{\tau}^{\xi}(\xi-\upsilon)\zeta''(\upsilon)d\upsilon\right|;\tau\right)-\left|\int_{\tau}^{\epsilon^{\alpha,\beta}_{\eta,\mu,\gamma}(\tau)}\left(\epsilon^{\alpha,\beta}_{\eta,\mu,\gamma}(\tau)-\upsilon\right)\zeta''(\upsilon)d\upsilon\right|\\&\quad\le\frac{\|\zeta''\|}{2}L^{\alpha,\beta}_{\eta,\mu,\gamma}((\xi-\tau)^2;\tau)+\frac{\|\zeta''\|}{2}\left(\tau-\epsilon^{\alpha,\beta}_{\eta,\mu,\gamma}(\tau)\right)^2\\&\quad=\frac{\|\zeta''\|}{2}\left[\Phi^{\alpha,\beta,2}_{\eta,\mu,\gamma}(\tau)+\left(\frac{(\beta-\gamma)\tau+\alpha}{\eta+\beta}\right)^2\right].\end{aligned}\tag{7}$$

In the view of Eq. (6) we obtain

$$\left|\widetilde{L^{\alpha,\beta}_{\eta,\mu,\gamma}}(\phi;\tau)\right|=\left|L^{\alpha,\beta}_{\eta,\mu,\gamma}(\phi;\tau)\right|+|\phi(\tau)|+\left|\phi\left(\epsilon^{\alpha,\beta}_{\eta,\mu,\gamma}(\tau)\right)\right|\le 3\|\phi\|\tag{8}$$

Now, for $\phi\in C[0,1+\gamma]$ and $\zeta\in C^2[0,1+\gamma]$, using (7) and (8) we have,

$$\begin{aligned}\left|L^{\alpha,\beta}_{\eta,\mu,\gamma}(\phi;\tau)-\phi(\tau)\right|&=\left|\widetilde{L^{\alpha,\beta}_{\eta,\mu,\gamma}}(\phi;\tau)-\phi(\tau)+\phi\left(\epsilon^{\alpha,\beta}_{\eta,\mu,\gamma}(\tau)\right)-\phi(\tau)\right|\\&\le\left|\widetilde{L^{\alpha,\beta}_{\eta,\mu,\gamma}}(\phi-\zeta;\tau)\right|+\left|\widetilde{L^{\alpha,\beta}_{\eta,\mu,\gamma}}(\zeta;\tau)-\zeta(\tau)\right|+|\zeta(\tau)-\phi(\tau)|\\&\quad+\left|\phi\left(\epsilon^{\alpha,\beta}_{\eta,\mu,\gamma}(\tau)\right)-\phi(\tau)\right|\\&\le 4|\phi-\zeta|+\frac{\|\zeta''\|}{2}\left[\Phi^{\alpha,\beta,2}_{\eta,\mu,\gamma}(\tau)+\left(\frac{(\beta-\gamma)\tau+\alpha}{\eta+\beta}\right)^2\right]+\omega\left(\phi,\tau-\epsilon^{\alpha,\beta}_{\eta,\mu,\gamma}(\tau)\right).\end{aligned}$$

Choosing $\delta=\sqrt{\Phi^{\alpha,\beta,1}_{\eta,\mu,\gamma}}$, we obtain the desired inequality.

The Voronovskaja's-type theorem is given in the study [13] as Theorem 2.1. Therefore, the theorem is presented without proof.

Theorem 3.4. ([13]) Let ϕ be a function in the set of continuous functions defined on the interval $[0,1+\gamma]$. Suppose that function ϕ has a second-order derivative at a point τ on the interval

$[0,1+\gamma]$. Then, by considering the behavior of ϕ around τ and ensuring that the expression accounts for limits approaching from both sides of τ, we have the following conclusion:

$$\lim_{\eta\to\infty}\eta\left[L^{\alpha,\beta}_{\eta,\mu,\gamma}(\phi,\tau)-\phi(\tau)\right]=[(\gamma-\beta)\tau+\alpha]\phi'(\tau)+\frac{1}{2}\tau(1-\tau)\phi''(\tau),$$

where $0\le\alpha\le\beta$.

In the subsequent discussion, we will provide a Grüss-Voronovskaya type theorem using the methodology outlined in (*cf*, [14]).

Theorem 3.5. Let $\phi,\zeta\in C[0,1+\gamma]$, for each $\tau\in[0,1]$ we have,

$$\lim_{\eta\to\infty}(\eta+\beta)\left[L^{\alpha,\beta}_{\eta,\mu,\gamma}(\phi\zeta,\tau)-L^{\alpha,\beta}_{\eta,\mu,\gamma}(\phi,\tau)L^{\alpha,\beta}_{\eta,\mu,\gamma}(\zeta,\tau)\right]=\tau(1-\tau)\phi'(\tau)\zeta'(\tau).$$

Proof. Since

$$(\phi\zeta)(\tau)=\phi(\tau)\zeta(\tau)$$

$$(\phi\zeta)'(\tau)=\phi'(\tau)\zeta(\tau)+\phi(\tau)\zeta'(\tau)$$

and

$$(\phi\zeta)''(\tau)=\phi''(\tau)\zeta(\tau)+2\phi'(\tau)\zeta'(\tau)+\phi(\tau)\zeta''(\tau).$$

$$\begin{aligned}
&L^{\alpha,\beta}_{\eta,\mu,\gamma}(\phi\zeta;\tau)-L^{\alpha,\beta}_{\eta,\mu,\gamma}(\phi;\tau)L^{\alpha,\beta}_{\eta,\mu,\gamma}(\zeta;\tau)\\
&=\left[L^{\alpha,\beta}_{\eta,\mu,\gamma}(\phi\zeta;\tau)-\phi(\tau)\zeta(\tau)+(\phi\zeta)'(\tau)L^{\alpha,\beta}_{\eta,\mu,\gamma}(\xi-\tau;\tau)+\frac{(\phi\zeta)''(\tau)}{2}L^{\alpha,\beta}_{\eta,\mu,\gamma}((\xi-\tau)^2;\tau)\right]\\
&\quad-\zeta(\tau)\left[L^{\alpha,\beta}_{\eta,\mu,\gamma}(\phi;\tau)-\phi(\tau)+\phi'(\tau)L^{\alpha,\beta}_{\eta,\mu,\gamma}(\xi-\tau;\tau)+\frac{\phi''(\tau)}{2}L^{\alpha,\beta}_{\eta,\mu,\gamma}((\xi-\tau)^2;\tau)\right]\\
&\quad-L^{\alpha,\beta}_{\eta,\mu,\gamma}(\phi;\tau)\left[L^{\alpha,\beta}_{\eta,\mu,\gamma}(\zeta;\tau)-\zeta(\tau)+\zeta'(\tau)L^{\alpha,\beta}_{\eta,\mu,\gamma}(\xi-\tau;\tau)+\frac{\zeta''(\tau)}{2}L^{\alpha,\beta}_{\eta,\mu,\gamma}((\xi-\tau)^2;\tau)\right]\\
&\quad+\frac{1}{2}L^{\alpha,\beta}_{\eta,\mu,\gamma}((\xi-\tau)^2;\tau)\left[\phi(\tau)\zeta''(\tau)+2\phi'(\tau)\zeta'(\tau)+\zeta''(\tau)L^{\alpha,\beta}_{\eta,\mu,\gamma}(\phi;\tau)\right]\\
&\quad+\zeta'(\tau)L^{\alpha,\beta}_{\eta,\mu,\gamma}(\xi-\tau;\tau)\left[\phi(\tau)-L^{\alpha,\beta}_{\eta,\mu,\gamma}(\phi;\tau)\right]
\end{aligned}$$

By utilizing Lemma 2.2, we obtain

$$\lim_{\eta\to\infty}(\eta+\beta)\left[L^{\alpha,\beta}_{\eta,\mu,\gamma}(\phi\zeta;\tau)-L^{\alpha,\beta}_{\eta,\mu,\gamma}(\phi;\tau)L^{\alpha,\beta}_{\eta,\mu,\gamma}(\zeta;\tau)\right]$$

$$=\lim_{\eta\to\infty}(\eta+\beta)\left[L^{\alpha,\beta}_{\eta,\mu,\gamma}(\phi\zeta;\tau)-\phi(\tau)\zeta(\tau)\right]-(\phi\zeta)'(\tau)\gamma\tau-\frac{(\phi\zeta)''(\tau)}{2}\tau(1-\tau)$$

$$-\zeta(\tau)\lim_{\eta\to\infty}(\eta+\beta)\left[L^{\alpha,\beta}_{\eta,\mu,\gamma}(\phi;\tau)-\phi(\tau)\right]-\phi'(\tau)\gamma\tau-\frac{\phi''(\tau)}{2}\tau(1-\tau)$$

$$-\lim_{\eta\to\infty}L^{\alpha,\beta}_{\eta,\mu,\gamma}(\phi;\tau)\left[\lim_{\eta\to\infty}(\eta+\beta)\left[L^{\alpha,\beta}_{\eta,\mu,\gamma}(\zeta;\tau)-\zeta(\tau)\right]-\zeta'(\tau)\gamma\tau-\tfrac{\zeta''(\tau)}{2}\tau(1-\tau)\right]$$

$$+\frac{\tau(1-\tau)}{2}\zeta''(\tau)\lim_{\eta\to\infty}\eta\left[\zeta(\tau)-L^{\alpha,\beta}_{\eta,\mu,\gamma}(\phi;\tau)\right]+2\phi'(\tau)\zeta'(\tau)$$

$$+\zeta'(\tau)\gamma\tau\lim_{\eta\to\infty}(\eta+\beta)\left[\phi(\tau)-L^{\alpha,\beta}_{\eta,\mu,\gamma}(\phi;\tau)\right].$$

Considering Theorems 3.1 and 3.4 completes the proof.

4. Approximation Properties in the Space of Bögel Continuous Functions

Yang et. al. examined the multivariate context of the Stancu operators on a simplex and demonstrated that these operators preserve the Lipschitz property of the original function [15]. The operators in question are examined in their two-variable form in reference [16]. In their work [16], the authors presented Voronovskaja-type and Grüss-Voronovskaja-type theorems using the standard modulus of continuity for bivariate Stancu operators, within the context of quantitative mean.

In the bivariate scenario, the ideas that are commonly used in the univariate case are naturally extended. Let $I_{\mu q}\coloneqq I_{\mu}\times I_{q}$ and $I_{\mu}=[0,1+\mu], I_{\nu}=[0,1+\nu]$ and $I^{2}=I\times I, I=[0,1]$. The bivariate Stancu-Schurer operators define as follows,

$$L^{\alpha,\beta,\vartheta,\varsigma}_{\eta,m,\mu,\nu,\gamma,s}(\phi)(\tau,y)=\sum_{\rho=0}^{\eta+\mu-\gamma}\sum_{j=0}^{m+\nu-s}w_{\eta+\mu,\rho,\gamma}(\tau)w_{m+\nu,j,s}(y)\,\phi\left(\frac{\rho}{\eta},\frac{j}{m}\right)$$

where $\phi\in C(I_{\mu q}), w_{\eta+\mu,\rho,\gamma}(\tau)$ and $w_{m+\nu,j,s}(y)$ are similar in the definition (2), $p_{\eta-\gamma,\rho}(\tau), p_{m-s,l}(y)$ are similar to the previous Equation (2), γ, s are non-negative integers, $\eta, m\in N$ such that $\eta+\mu>2\gamma, m+\nu>2s$, and $\mu,\nu\in N_0$. Throughout this paper, $e_{\rho,j}(\tau,y)=\tau^{\rho}y^{j}, j\in N_0$ and $\rho+j\leq 2$.

In this part, we will provide a generalization of operator (3) specifically for the B-continuous functions. To accomplish this, we will create a GBS operator that is linked to the bivariate type operators and examine some of its features related to smoothness.

Karl Bögel developed the ideas of B-continuous and B-differentiable functions in his work, as referenced in sources [17-19]. The Korovkin theorem, which is widely recognized in approximation theory, was established by Badea et al. in their works [20] and [21]. This theorem specifically focuses on B-continuous functions. The authors in [20] established a Korovkin-type theorem for approximating B-continuous functions by employing the Boolean sum technique.

The investigation in [22, 23] focused on the approximation features of the bivariate Bernstein-type operators and their associated generalized Boolean sum operators. In recent years, numerous researchers have made substantial contributions to this area. Please consult the mentioned articles for further information [24-29].

Now, we shall provide fundamental concepts and notations that will be utilized in this research. For more information, please refer to references [17, 18].

Let I and J represent closed intervals in the real numbers and let D be the Cartesian product of I and J. A function $\phi: D \to \mathbb{R}$ is called a B-continuous (Bögel continuous) at a point $(\tau_0, y_0) \in D$ if $\lim_{(\tau,y)\to(\tau_0,y_0)} \Delta_{\tau y}\phi[\tau_0, y_0; \tau, y] = 0$, for any $(\tau, y) \in D$, with $\Delta_{\tau y}\phi[\tau_0, y_0; \tau, y] = \phi(\tau, y) - \phi(\tau, y_0) - \phi(\tau_0, y) + \phi(\tau_0, y_0)$.

The notation $C_b(Q)$ represents the set of all B-continuous functions on $Q = I \times J$ while $C_B(Q)$ represents the set of all ordinary continuous and bounded functions on Q. The GBS operator associated with the operator $L^{\alpha,\beta,\vartheta,\varsigma}_{\eta,m,\mu,\nu,\gamma,s}(\phi; \tau, y)$ is defined as follows:

$$GL^{\alpha,\beta,\vartheta,\varsigma}_{\eta,m,\mu,\nu,\gamma,s}(\phi; \tau, y) := \sum_{\rho=0}^{\eta+\mu-\gamma} \sum_{j=0}^{m+q-s} w_{n+\mu,\rho,\gamma}(\tau) w_{m+\nu,j,s}(y) \times \left[\phi\left(\frac{\rho+\alpha}{\eta+\beta}, y\right) + \phi\left(\tau, \frac{j+\vartheta}{m+\varsigma}\right) - \phi\left(\frac{\rho+\alpha}{\eta+\beta}, \frac{j+\vartheta}{m+\varsigma}\right)\right]. \quad (9)$$

The operator $GL^{\alpha,\beta,\vartheta,\delta}_{n,m,\mu,q,\gamma,s}$ is well-defined on the space $C_b(Q)$ and acts on itself. Additionally, $\phi \in C_b(Q)$. $L^{\alpha,\beta,\vartheta,\varsigma}_{\eta,m,\mu,\nu,\gamma,s}(\phi; \tau, y)$ is an evident linear positive operator that reproduces linear functions.

We calculate the rate at which the sequences of operators (10) converge to ϕ in the space of B-continuous functions on Q, using the modulus of continuity in the Bögel sense. Let us start

by reviewing the definition of the Bögel (mixed) modulus of smoothness for a function $\phi \in C_b(Q)$. The Bögel modulus of smoothness of a function f belonging to the space $C_b(Q)$ is defined as

$$\omega_B(\phi;\delta_1,\delta_2) = \sup\{|\Delta_{(\tau,y)}\phi[t,s;\tau,y]|: |\tau - t| < \delta_1, |y-s| < \delta_2\},$$

for all $(\tau,y),(t,s) \in Q$ and for any $(\delta_1,\delta_2) \in (0,\infty)\times(0,\infty)$ with $\omega_B: [0,\infty)\times[0,\infty) \to R$, [30]. This modulus has similar properties to the usual modulus of continuity. For example, if $\phi \in C_b(Q)$ then ϕ is uniform B-continuous on Q and

$$\lim_{\eta,m\to\infty} \omega_B(\phi;\delta_\eta,\delta_m) = 0.$$

Theorem 4.1. For every $\phi \in C_b(Q)$, in each $(\tau,y) \in Q$, the operators (9) satisfy the following inequality,

$$\left|GL^{\alpha,\beta,\vartheta,\varsigma}_{\eta,m,\mu,\nu,\gamma,s}(\phi;\tau,y) - \phi(\tau,y)\right| \le 4\omega_B(\phi;\delta_\eta,\delta_m) \tag{10}$$

where $\delta_\eta = \sqrt{3\frac{b_\eta}{\eta}\tau + \left(\frac{b_\eta}{\eta}\right)^2}$, $\delta m = \sqrt{3\frac{c_m}{m}y + \left(\frac{c_m}{m}\right)^2}$.

Proof. From the definition of $\omega_B(f;\delta_\eta,\delta_m)$ and by the elementary inequality

$$\omega_B(\phi;\lambda_\eta\delta_\eta,\lambda_m\delta_m) \le (1+\lambda_\eta)(1+\lambda_m)\omega_B(\phi;\delta_\eta,\delta_m); \lambda_\eta,\lambda_m > 0$$

we get,

$$\begin{aligned}|\Delta_{(\tau,y)}\phi[t,s;\tau,y]| &\le \omega_B(\phi;|\tau-t|,|y-s|)\\ &\le \left(1+\frac{|\tau-t|}{\delta_\eta}\right)\left(1+\frac{|y-s|}{\delta_m}\right)\omega_B(\phi;\delta_\eta,\delta_m)\end{aligned} \tag{11}$$

for every $(\tau,y),(t,s) \in Q$ and for any $\delta_\eta,\delta_m > 0$. Using the definition of $\Delta_{(\tau,y)}f[t,s;\tau,y]$, we may write,

$$\phi(\tau,s) + \phi(t,y) - \phi(t;s) = \phi(\tau;y) - \Delta_{(\tau,y)}\phi[t;s;\tau;y].$$

When we apply the $GL^{\alpha,\beta,\vartheta,\varsigma}_{\eta,m,\mu,\nu,\gamma,s}(\phi;\tau,y)$ operator to this equality we get

$$GL^{\alpha,\beta,\vartheta,\varsigma}_{\eta,m,\mu,\nu,\gamma,s}(\phi;\tau,y)=\phi(\tau;y)L^{\alpha,\beta,\vartheta,\varsigma}_{\eta,m,\mu,\nu,\gamma,s}(e_{0,0};\tau,y)-$$
$$L^{\alpha,\beta,\vartheta,\varsigma}_{\eta,m,\mu,\nu,\gamma,s}\left(\Delta_{(\tau,y)}\phi[t;s;\tau;y];\tau,y\right).$$

Since $L^{\alpha,\beta,\vartheta,\varsigma}_{\eta,m,\mu,\nu,\gamma,s}(e_{0,0};\tau,y)=1$, considering inequality (11), using the linearity of the $D_{n,m}$ operator and using Cauchy-Schwarz inequality we have,

$$\left|GL^{\alpha,\beta,\vartheta,\varsigma}_{\eta,m,\mu,\nu,\gamma,s}(\phi;\tau,y)-\phi(\tau,y)\right|\le L^{\alpha,\beta,\vartheta,\varsigma}_{\eta,m,\mu,\nu,\gamma,s}\left(\left|\Delta_{(\tau,y)}\phi[t;s;\tau;y]\right|;\tau,y\right)$$
$$\le\left(L^{\alpha,\beta,\vartheta,\varsigma}_{\eta,m,\mu,\nu,\gamma,s}(e_{0,0};\tau,y)+\delta_\eta^{-1}\sqrt{L^{\alpha,\beta,\vartheta,\varsigma}_{\eta,m,\mu,\nu,\gamma,s}\left(\left(e_{1,0}-\tau\right)^2;\tau,y\right)}\right.$$
$$+\delta_m^{-1}\sqrt{L^{\alpha,\beta,\vartheta,\varsigma}_{\eta,m,\mu,\nu,\gamma,s}\left(\left(e_{0,1}-y\right)^2;\tau,y\right)}$$
$$\left.+\delta_\eta^{-1}\delta_m^{-1}\sqrt{L^{\alpha,\beta,\vartheta,\varsigma}_{\eta,m,\mu,\nu,\gamma,s}\left(\left(e_{1,0}-\tau\right)^2;\tau,y\right)L^{\alpha,\beta,\vartheta,\varsigma}_{\eta,m,\mu,\nu,\gamma,s}\left(\left(e_{0,1}-y\right)^2;\tau,y\right)}\right)\omega_B(\phi;\delta_\eta,\delta_m).$$

From Lemma 2, we can write,

$$L^{\alpha,\beta,\vartheta,\varsigma}_{\eta,m,\mu,\nu,\gamma,s}((t-\tau)^2;\tau,y)=\frac{1}{(\eta+\beta)^2}\{[-(\eta+\mu)+(\mu+\beta)^2-\gamma(\gamma-1)]\tau^2$$
$$+[\eta+\mu+2\alpha(\mu-\beta)+\gamma(\gamma-1)]\tau+\alpha^2\}\le\frac{\mu(\mu+4\beta)}{\eta+\beta}=\Phi^{\alpha,\beta,*}_{\eta,\gamma,\mu},$$

and

$$L^{\alpha,\beta,\vartheta,\varsigma}_{\eta,m,\mu,\nu,\gamma,s}((l-y)^2;\tau,y)\le\frac{\nu(\nu+4\varsigma)}{m+\varsigma}=\Phi^{\gamma,\varsigma,*}_{m,s,\nu}.$$

We obtain,

$$\left|GL^{\alpha,\beta,\vartheta,\delta}_{\eta,m,\mu,\nu,r,s}(\phi;\tau,y)-\phi(\tau,y)\right|\le\left(1+\delta_\eta^{-1}\sqrt{\frac{\mu(\mu+4\beta)}{\eta+\beta}}\right.$$
$$\left.+\delta_m^{-1}\sqrt{\frac{\nu(\nu+4\varsigma)}{m+\varsigma}}+\delta_\eta^{-1}\delta_m^{-1}\sqrt{\frac{\mu(\mu+4\beta)}{\eta+\beta}\frac{\nu(\nu+4\varsigma)}{m+\varsigma}}\right)\omega_B(\phi;\delta_\eta,\delta_m)$$

which gives the assertion of Theorem the desired inequality (9) by choosing $\delta_\eta=\sqrt{\Phi^{\alpha,\beta,*}_{\eta,\gamma,\mu}}$ and $\delta_m=\sqrt{\Phi^{\vartheta,\varsigma,*}_{m,s,\nu}}$.

Now, we study the degree of approximation for the operators $GL^{\alpha,\beta,\gamma,\delta}_{\eta,m,\mu,q,r,s}(\phi;\tau,y)$ by means of the Lipschitz class for B-continuous functions. For $f \in C_b(Q)$, we define the Lipschitz class $Lip_M(\lambda,\upsilon)$ with $\lambda,\upsilon \in (0,1]$ as follows:

$$Lip_M(\lambda,\mu) = \left\{\phi \in C_b(Q): \left|\Delta_{(\tau,y)}\phi[t,s;\tau,y]\right| \leq M|t-\tau|^{\lambda}|s-y|^{\upsilon}\right\}$$

for $(t,s),(\tau,y) \in Q$, $M > 0$.

Theorem 4.2. Let$\phi \in Lip_M(\lambda,\mu)$, then we have,

$$\left|GL^{\alpha,\beta,\vartheta,\varsigma}_{\eta,m,\mu,\nu,\gamma,s}(\phi;\tau,y) - \phi(\tau,y)\right| \leq M\delta_{\eta}^{\lambda/2}\delta_{m}^{\upsilon/2},$$

where δ_{η},δ_{m} are as given in the proof of the previous theorem and $\lambda,\upsilon \in (0,1]$, $(\tau,y) \in Q$.

Proof. By the definition of $GL^{\alpha,\beta,\vartheta,\varsigma}_{\eta,m,\mu,\nu,\gamma,s}$ operator and by linearity of the $L^{\alpha,\beta,\vartheta,\varsigma}_{\eta,m,\mu,\nu,\gamma,s}$ operator, we may write,

$$GL^{\alpha,\beta,\vartheta,\varsigma}_{\eta,m,\mu,\nu,\gamma,s}(\phi;\tau,y) = L^{\alpha,\beta,\vartheta,\varsigma}_{\eta,m,\mu,\nu,\gamma,s}(\phi(\tau,s)+\phi(t,y)-\phi(t;s);\tau,y)$$

$$= L^{\alpha,\beta,\vartheta,\varsigma}_{\eta,m,\mu,\nu,\gamma,s}\left(\phi(\tau;y)-\Delta_{(\tau,y)}\phi[t;s;\tau;y];\tau,y\right) = \phi(\tau;y)L^{\alpha,\beta,\vartheta,\varsigma}_{\eta,m,\mu,\nu,\gamma,s}\left(e_{0,0};\tau,y\right)$$

$$-L^{\alpha,\beta,\vartheta,\varsigma}_{\eta,m,\mu,\nu,\gamma,s}\left(\Delta_{(\tau,y)}\phi[t;s;\tau;y];\tau,y\right).$$

And, by using the hypothesis, we have,

$$\left|GL^{\alpha,\beta,\vartheta,\varsigma}_{\eta,m,\mu,\nu,\gamma,s}(\phi;\tau,y) - \phi(\tau,y)\right| \leq L^{\alpha,\beta,\vartheta,\varsigma}_{\eta,m,\mu,\nu,\gamma,s}\left(\left|\Delta_{(\tau,y)}\phi[t;s;\tau;y]\right|;x,y\right)$$

$$\leq ML^{\alpha,\beta,\vartheta,\varsigma}_{\eta,m,\mu,\nu,\gamma,s}\left(|t-\tau|^{\lambda}|s-y|^{\upsilon};\tau,y\right)$$

$$= ML^{\alpha,\beta,\vartheta,\varsigma}_{\eta,m,\mu,\nu,\gamma,s}\left(|t-\tau|^{\lambda};\tau,y\right)L^{\alpha,\beta,\vartheta,\varsigma}_{\eta,m,\mu,\nu,\gamma,s}(|s-y|^{\upsilon};\tau,y).$$

Applying the Hölder's inequality with $p_1 = 2/\lambda, q_1 = 2/(2-\lambda)$ and $p_2 = 2/\upsilon, q_1 = 2/(2-\upsilon)$, we get

$$\left|GL^{\alpha,\beta,\vartheta,\varsigma}_{\eta,m,\mu,\nu,\gamma,s}(\phi;\tau,y) - \phi(\tau,y)\right| \leq MD_n(|t-\tau|^2;\tau)^{\frac{\lambda}{2}}D_n(|s-y|^2;y)^{\frac{\upsilon}{2}} \leq M\delta_{\eta}^{\frac{\lambda}{2}}\delta_{m}^{\frac{\upsilon}{2}}.$$

5. Graphical Examples

Here, we examine the theoretical findings from the preceding parts via the use of graphical illustrations and a numerical demonstration.

Example 5.1. For the changing values of η as $\eta = 20$(red),$\eta = 50$(green), $\eta = 100$(blue), the convergence of $L^{\alpha,\beta}_{\eta,\mu,\gamma}(\phi,\tau)$ to $\phi(\tau) = \sin(2\pi\tau)$ (black) is illustrated as the first example in the Figure 1.

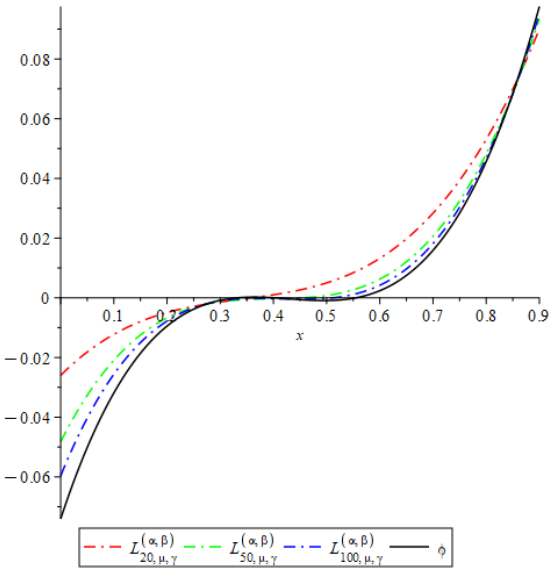

Figure 1: The convergence of $L^{\alpha,\beta}_{\eta,\mu,\gamma}(\phi,\tau)$ to $\phi(\tau) = \sin(2\pi\tau)$ for $\eta = 20,50,100$.

Example 5.2. For the changing values of η as $\eta = 20$(red), $\eta = 50$(green), $\eta = 100$(blue), the convergence of $L^{\alpha,\beta}_{\eta,\mu,\gamma}(\phi,\tau)$ to $\phi(\tau) = \left(\tau - \frac{1}{3}\right)\sin(\pi\tau)$ (black) is illustrated in the coming figure.

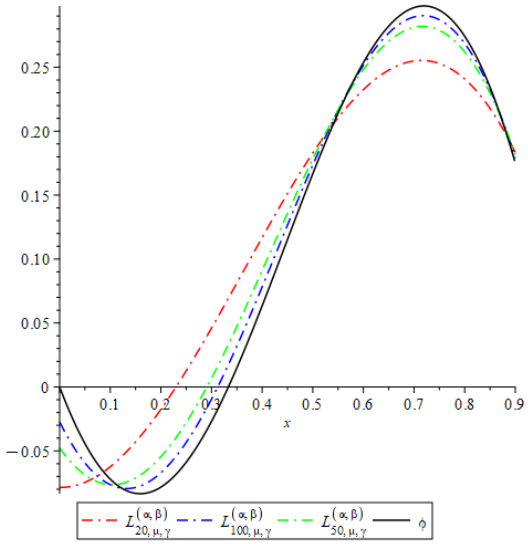

Figure 2: The convergence of $L^{\alpha,\beta}_{\eta,\mu,\gamma}(\phi,\tau)$ to $\phi(\tau)=\left(\tau-\frac{1}{3}\right)\sin(\pi\tau)$ (black) is illustrated for $\eta=20,50,100$.

Example 5.3. For the changing values of η as $\eta=20$(red), $\eta=50$(green), $\eta=100$(blue), the convergence of $L^{\alpha,\beta}_{\eta,\mu,\gamma}(\phi,\tau)$ to $\phi(\tau)=\cos(2\pi\tau)+2\sin(\pi\tau)$ (black) is illustrated in the figure showing that the expression leans toward both sides as η increases.

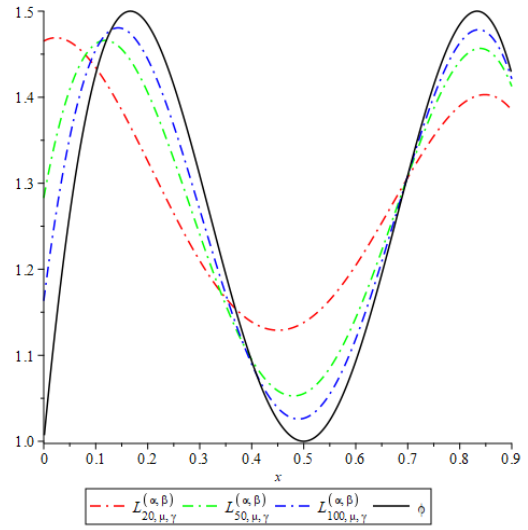

Figure 3: The convergence of $L^{\alpha,\beta}_{\eta,\mu,\gamma}(\phi,\tau)$ to $\phi(\tau)=\cos(2\pi\tau)+2\sin(\pi\tau)$ (black) for $\eta=20,50,100$.

In the next table, the error estimation of the $L^{\alpha,\beta}_{\eta,\mu,\gamma}(\phi,\tau)$ operators are given in comparison with the $L^{\alpha,\beta}_{\eta,\mu,\gamma}(\phi,\tau)$ operators. The absolute value of the difference of both operators with the $\phi(\tau)=\tan(\tau^2+2\tau+10)$ function is given according to the increasing η values and the value of τ. Accordingly, as η values increase in multiples of 10, the approximation of the $L^{\alpha,\beta}_{\eta,\mu,\gamma}(\phi,\tau)$ operators to the $\phi(\tau)$ function is better than the $L^{\alpha,\beta}_{\eta,\mu,\gamma}(\phi,\tau)$ operators.

Table 1: Error estimation for operators $L_{\eta,\mu,\gamma}^{\alpha,\beta}(\phi,\tau)$.

$\tau = 0.5$		
η	$\left\|L_{\eta,\mu,\gamma}^{\alpha,\beta}(\phi,\tau)-\phi(\tau)\right\|$	$\left\|L_{\eta,\mu,\gamma}^{\alpha,\beta}(\phi,\tau)-\phi(\tau)\right\|$
10	4.918308847	4.030402557
10^2	0.022928159	0.091543553
10^3	0.120741290	0.095097202
10^4	0.010993630	0.008609165
10^5	0.001090463	0.000853504

Finally, here we visualized the approach of the new type operators $L_{\eta,\mu,\gamma}^{\alpha,\beta}(\phi,\tau)$ for the changing values of τ where $\alpha = 3, \beta = 5, \gamma = 1$ values are taken.

Example 5.4. Visualization of the convergence of $L_{\eta,\mu,\gamma}^{\alpha,\beta}(\phi,\tau)$ with varying values of τ for the value $\eta = 80$, to $\phi(\tau) = \frac{\tau^2-1}{(\tau-1)^2}$ (black) is illustrated in the figure. The μ values here are chosen as 1,5,10,15 respectively and the colors in which each value is represented can be seen in the figures' legend.

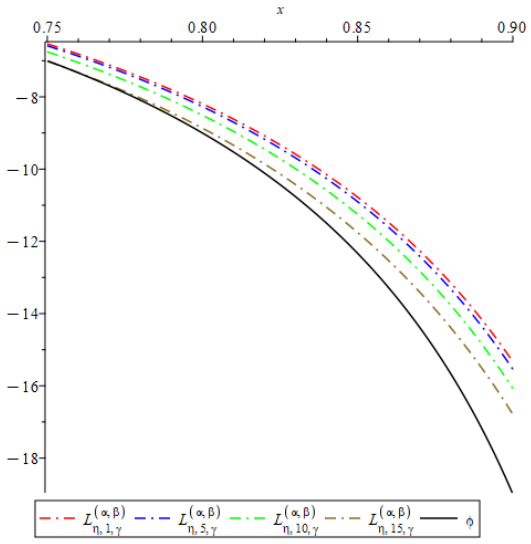

Figure 4: The convergence of $L_{\eta,\mu,\gamma}^{\alpha,\beta}(\phi,\tau)$operators to $\phi(\tau) = (\tau^2-1)/(\tau-1)^2$ (black) for changing μ values.

Now we give some graphics comparing the approximation of the bivariate and GBS operators of corresponding operators.

Example 5.5. Visualization of the convergence of $GL_{\eta,m,\mu,\nu,\gamma,s}^{\alpha,\beta,\vartheta,\varsigma}$ to function $\phi(\tau,y) = sin(4\pi\tau) + sin(\pi y)$. Here ϕ function is blue colored and GBS operators are yellow $for\ \eta, m =$

2 and red for changing $\eta, m = 5$ values. A better approximation is observed as η, m values increase.

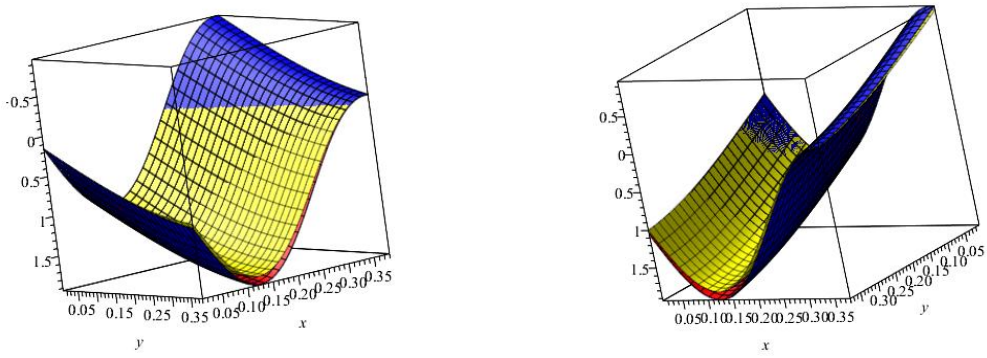

Figure 5: The convergence of $GL^{\alpha,\beta,\vartheta,\varsigma}_{\eta,m,\mu,\nu,\gamma,s}$ operators to $\phi(\tau, y) = 2\tau^2 + 3y^2$ (blue) for changing η, m values.

Example 5.6. Visualization of the convergence of $GL^{\alpha,\beta,\vartheta,\varsigma}_{\eta,m,\mu,\nu,\gamma,s}$ to function $\phi(\tau, y) = 2\tau^2 + 3y^2$. Here function is blue colored and GBS operators are yellow one, so as red is present the bivariate operators. It is clear that GBS operators have a better approach.

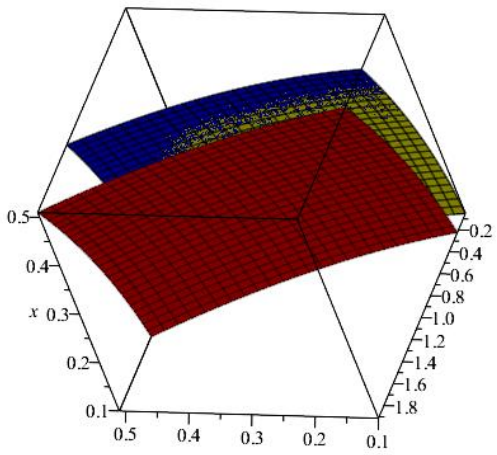

Figure 6: The convergence of $GL^{\alpha,\beta,\vartheta,\varsigma}_{\eta,m,\mu,\nu,\gamma,s}$ operators and bivariate operators to $\phi(\tau, y) = 2\tau^2 + 3y^2$ (blue) for GBS and bivariate operators.

Acknowledgements

We would like to express our sincere gratitude to the editors and reviewers for their valuable contributions and constructive feedback. Their efforts have significantly improved the quality of our manuscript.

References

[1] Bernstein, S. N., *Demonstration du th'eoreme de Weierstrass fondee sur le calcul des probabilities*, Communications of the Kharkov Mathematical Society, 13, 2, 1912.

[2] Schurer, F., *Linear positive operators in approximation theory*, Applied Mathematics Institute Technische Universiteit Delft: report, 1962.

[3] Bărbosu, D., *Schurer-Stancu type operators*, Studia Universitatis Babeş-Bolyai Mathematica, XLVIII, 3(8), 31-35, 2003.

[4] Bodur, M., Manav, N., Tasdelen, F., *Approximation Properties of $\lambda-$Bernstein - Kantorovich-Stancu Operators*, Mathematica Slovaca, 72, 1, 2022.

[5] Çetin, N., Acu, A. M., *Approximation by α–Bernstein–Schurer–Stancu Operators*, Journal of Mathematical Inequalities, 15:2, 2021.

[6] Vedi, T., Özarslan, M. A., *Chlodowsky-type q-Bernstein-Stancu-Kantorovich operators*, Journal of Inequalities and Applications, 1, 2015.

[7] Stancu, D. D., *Quadrature formulas constructed by using certain linear positive operators*, Numerical Integration (Proceedings of the Conference, Oberwolfach, 1981), ISNM 241-251, Birkhauser Verlag, Basel, 57, 1982.

[8] Stancu, D. D., *Approximation of functions by means of a new generalized Bernstein operator*, Calcolo, 20: 211–229, 1983.

[9] Bostancı, T., Başcanbaz-Tunca, G., *On Stancu operators depending on a non -negative integer,* Filomat, 36, 18, 2022.

[10] Çetin, N., Bascanbaz-Tunca, G., *Approximation by a new complex generalized Bernstein operators*, Universitatii din Oradea Fascicola Matematica, 26, 2, 2019.

[11] Yun, L., Xiang, X., *On shape-preserving properties and simultaneous approximation of Stancu operator,* Analysis in Theory and Applications, 24, 2008.

[12] Devore, R. A., Lorentz, G. G., *Constructive Approximation*, Grunddlehren der Mathematischen Wissenschaften, Band 303 (Springer-Verlag, Berlin, Heidelberg, New York, and London), 1993.

[13] Çetin, N., & Mutlu, N. M., *Complex Generalized Stancu-Schurer Operators*, Mathematica Slovaca, 74(5), 1215-1232, 2024.

[14] Gal, S. G., Gonska, H., *Grüss and Grüss-Voronovskaya-type estimates for some Bernstein -type polynomials of real and complex variables*, Jaen Journal on Approximation, 7, 1, 2015.

[15] Yang, R., Xiong, J., Cao, F., *Multivariate Stancu operators defined on a simplex*, Applied Mathematics and Computation, 138, 189-198, 2003.

[16] Başcanbaz-Tunca, G., Erençin A., Olgun, A., *Quantitative estimates for bivariate Stancu operators*, Mathematical Methods in the Applied Sciences, 42 (16), 5241-5250, 2019.

[17] Bögel, K., *Mehrdimensionale Differentiation von Funktionen mehrerer reeller Veränderlichen*, Journal fur die Reine und Angewandte Mathematik, 170, 197-217, 1934.

[18] Bögel, K., *Über mehrdimensionale Differentiation, Integration und beschränkte Variation*, Journal fur die Reine und Angewandte Mathematik, 173, 5-30, 1935.

[19] Bögel, K., *Über die mehrdimensionale differentiation,* Jahresber Deutsch Math-Verein, 65, 45-71, 1962.

[20] Badea, C., Cottin, C., *Korovkin-type theorems for Generalised Boolean Sum operators*, Colloquia Mathematica Societatis Janos Bolyai, Approximation Theory, Kecskemét (Hungary), 58, 51-67, 1990.

[21] Badea, C., Badea, I., Cottin, C., Gonska, H., *Notes on the degree of approximation of B-continuous and B-differentiable functions*, Approximation Theory and Its Applications, 4, 95-108, 1988.

[22] Barbosu, D., *Some generalized bivariate Berstein operators*, Mathematical Notes (Miskolc), 1, 1, 3-10, 2000.

[23] Barbosu, D., *Bivariate Operators of Schurer-Stancu Type*, Analele stiintifice ale Universitatii Ovidius Constanta, 11, 1, 1-8, 2003.

[24] Miclauş, D., *On the GBS Bernstein–Stancu's type operators*, Creative Mathematics and Informatics, 22, 73-80, 2013.

[25] Pop, O. T., Farcas, M. D., *Approximation of B-continuous and B-differentiable functions by GBS operators of Bernstein bivariate polynomials*, Journal of Inequalities in Pure and Applied Mathematics, 7(3), 92, 2006.

[26] Farcaş, M. D., *About approximation of B-continuous functions of three variables by GBS operators of Bernstein type on a tetrahedron*, Acta Universitatis Apulensis, Mathematics-Informatics, 16, 93-102, 2008.

[27] Farcaş, M. D., *About approximation of B-continuous and B-differential functions of three variables by GBS operators of Bernstein–Schurer type*, Buletinul ştiinţific al Universităţii "Politehnica" din Timişoara. Seria matematică-fizică, 52, 66, 13-22, 2007.

[28] Sidharth, M., Ispir, N., Agrawal, P. N., *GBS operators of Bernstein–Schurer–Kantorovich type based on q-integers,* Applied Mathematics and Computation, 269, 558-568, 2015.

[29] Bărbosu, D., Bărbosu, M., *On the sequence of GBS operators of Stancu-type*, Buletinul științific al Universitatii Baia Mare, Seria B, Fascicola matematică-informatică, 1-6, 2002.

[30] Badea, I., *Modulus of continuity in Bögel sense and some applications for approximation by a Bernstein-type operator*, Studia Universitatis Babes-Bolyai, Series Mathematica-Mechanica (Romanian), 18, 2, 69-78, 1973.

Adıyaman University Journal of Science
https://dergipark.org.tr/en/pub/adyujsci
DergiPark AKADEMİK
ISSN 2147-1630
e-ISSN 2146-586X

Congruence of Curves in Weyl-Otsuki Spaces

Beran PİRİNÇÇİ[1,*]

[1]*İstanbul University, Faculty of Science, Department of Mathematics, 34134, İstanbul, Türkiye*
beranp@istanbul.edu.tr, ORCID: 0000-0002-4692-9590

Received: 31.05.2024 **Accepted:** 21.09.2024 **Published:** 31.12.2024

Abstract

In this paper, we study the congruence of curves in Weyl-Otsuki spaces using Ricci's coefficients of that congruence in the orthogonal case. We first prove that Ricci's coefficients λ_{abc} determine the regular general connection of an Otsuki space. Then, we give the condition for these coefficients in Weyl-Otsuki spaces to be skew-symmetric in the first two indices as in Riemannian spaces. We obtain the necessary and sufficient conditions for the curves of congruence to be geodesic, normal, and irrotational. Finally, we prove that if a congruence satisfies the equation, $"T^h_{kj} - 2'T^h_{i[J}U^i_{n|}U_{n|k]} + \varphi_{[k}\delta^h_{j]} = 0$, and any two of the conditions to be geodesic, normal, and irrotational, then it also satisfies the other third one.

Keywords: Weyl-Otsuki spaces; General connections; Ricci's coefficients; Congruence of curves; Geodesic curves.

* Corresponding Author DOI: 10.37094/adyujsci.1493094

Weyl-Otsuki Uzaylarında Kongrüans Eğrileri

Öz

Bu makalede Weyl-Otsuki uzaylarında kongrüans eğrilerini bu eğrilerin ortogonal olması durumda Ricci katsayılarını kullanarak inceledik. İlk olarak, λ_{abc} Ricci katsayılarının bir Otsuki uzayının regüler genel koneksiyonunu belirlediğini gösterdik. Ardından Riemann uzaylarda olduğu gibi Weyl-Otsuki uzaylarında bu katsayıların ilk iki indisine göre ters-simetrik olma koşulunu verdik. Kongrüans eğrilerinin, sırasıyla, jeodezik, normal ve irrotasyonel olması için gerek ve yeter koşulları elde ettik. Son olarak bir kongrüans eğrisinin $"T^l_{ji} - 2'T^l_{k[i}V^k_{n|}V_{n|j]} + \gamma_{[j}\delta^l_{i]} = 0$ denklemi ile birlikte jeodezik, normal ve irrotasyonel olma koşullarından herhangi ikisini sağlaması durumunda diğer üçüncü koşulu da sağladığını kanıtladık.

Anahtar Kelimeler: Weyl-Otsuki uzayları; Genel koneksiyonlar; Ricci katsayıları; Kongrüans eğrileri; Jeodezik eğriler.

1. Introduction

The theory of Otsuki spaces is based on the notion of regular general connection, introduced by T. Otsuki [1]. He gave the theoretical foundation for general connections and showed that they are the generalizations of the classical connections, for instance, the affine, projective, and conformal connections [2, 3]. The general connections were first noticed by A. Moor and were linked with Weyl spaces [4]. These spaces are then called Weyl-Otsuki spaces. Then D.F. Nadj obtained curvatures [5] and the Frenet formulas [6] of the Weyl-Otsuki spaces and also studied Riemann-Otsuki spaces, which are the special cases of the Weyl-Otsuki spaces [7-9]. The general connections were also introduced into vector bundles by N. Abe [10, 11], into general relativity by H. Nagayama [12, 13], and the theory of black holes by T. Otsuki [14-16].

The coefficients of an affine connection on an orthonormal basis are called Ricci's coefficients. Since these coefficients can determine an affine connection, they have great importance in studying some geometric properties of a Riemannian space, such as the parallelism of the unit tangent vector field of an orthogonal ennuple and the conditions for the curves of an orthogonal ennuple to be normal or to be irrotational. Moreover, since Ricci's coefficients with respect to an affine connection are skew-symmetric with its first two indices, they provide an easier investigation of the above geometric properties for Riemannian spaces. But this is not the

case for Weyl-Otsuki spaces. The purpose of the paper is to get some conditions on Weyl-Otsuki spaces, which will be called co-recurrence conditions, for a proper investigation of the above geometric properties of these spaces.

2. Preliminaries

In this section, we will introduce the notion of regular general connection and its properties. Then we will define the co-recurrence condition on Weyl-Otsuki spaces to obtain the geometric properties of these spaces.

Definition 1. A ***regular general connection***[1] of an n-dimensional space M_n is defined as any cross-section Γ of the vector bundle $T(M_n)\otimes \mathcal{D}^2(M_n)$ over M_n, where $T(M_n)$ and $\mathcal{D}^2(M_n)$ are tangent bundle of order 1 and cotangent bundle of order 2 of M_n respectively, [1]. In a coordinate neighborhood, Γ is written as

$$\Gamma = \partial u_k \otimes \left(P_i^k d^2 u^i + \Gamma_{ij}^k du^i \otimes du^j \right),$$

where $P = \left(P_i^k \right)$ is an isomorphism of $T(M_n)$.

If P is the identity transformation, then Γ becomes a classical affine connection. So, general connections[2] are the generalizations of the classical connections, for instance, the affine, projective, and conformal connections.

It follows from Definition 1 that there exist a $(1,1)$-tensor $Q = \left(Q_i^k \right)$ such that $P^{-1} = Q$, since $\det\left(P_i^k \right) \neq 0$. Therefore Γ and P determine two affine connections $'\Gamma$ and $''\Gamma$ which are called ***contravariant and covariant part of*** Γ**,** respectively, in the following way:

$$'\Gamma_{ij}^k = Q_l^k \Gamma_{ij}^l \quad \text{and} \quad ''\Gamma_{ij}^k = \left(\Gamma_{lj}^k - \partial_j P_l^k \right) Q_i^l .$$

Using the above equations, we can define the ***basic covariant differential*** of a (p,q)-tensor $U = \left(U_{i_1 \ldots i_r}^{j_1 \ldots j_s} \right)$ with respect to a regular general connection Γ by

[1] It was called Otsuki connection by Nadj [7].

[2] If P is only a homomorphism, then Γ is called a general connection.

$$\begin{aligned}
&\nabla U^{j_1\cdots j_s}_{i_1\ldots i_r} = \nabla_k U^{j_1\cdots j_s}_{i_1\ldots i_r} du^k, \\
&\nabla_k U^{j_1\cdots j_s}_{i_1\ldots i_r} = \partial_k U^{j_1\cdots j_s}_{i_1\ldots i_r} + \sum_{p=1}^{s} {}'\Gamma^{j_p}_{hk} U^{j_1\cdots j_{p-1} h j_{p+1}\cdots j_s}_{i_1\ldots i_r} - \sum_{q=1}^{r} {}''\Gamma^{h}_{i_q k} U^{j_1\cdots j_s}_{i_1\ldots i_{q-1} h i_{q+1}\ldots i_r}.
\end{aligned} \tag{1}$$

Using (1), one can easily see that the basic covariant differentiation of the tensor product of any two tensors obeys the classical rule;

$$\nabla_k \left(U^{j_1\ldots j_s}_{i_1\ldots i_r} V^{j_{s+1}\cdots j_{s+p}}_{i_{r+1}\ldots i_{r+q}} \right) = \left(\nabla_k U^{j_1\ldots j_s}_{i_1\ldots i_r} \right) V^{j_{s+1}\cdots j_{s+p}}_{i_{r+1}\ldots i_{r+q}} + U^{j_1\ldots j_s}_{i_1\ldots i_r} \left(\nabla_k V^{j_{s+1}\cdots j_{s+p}}_{i_{r+1}\ldots i_{r+q}} \right).. \tag{2}$$

It is well-known that the covariant differentiations and the contractions are commutative operators in classical differential geometry. This is due to the fact that the covariant derivative of the identity transformation I is constant. Hence, if we use (1) for the identity transformation

$$\nabla_j \delta^k_i = {}'\Gamma^k_{ij} - {}''\Gamma^k_{ij}, \tag{3}$$

Then, we have the relations between basic covariant differentiation and contractions as follows:

$$\delta^i_j \left(\nabla_k U^{j_1\ldots j_s j}_{i_1\ldots i_r i} \right) = \nabla_k \left(U^{j_1\ldots j_s j}_{i_1\ldots i_r i} \delta^i_j \right) + U^{j_1\ldots j_s j}_{i_1\ldots i_r i} \nabla_k \delta^i_j. \tag{4}$$

Now, we will give the curvature and the torsion tensors for the affine connections $'\Gamma$ and $''\Gamma$. Let ${}'R^k_{ilj}$, ${}''R^k_{ilj}$ and ${}'T^k_{ij}$, ${}''T^k_{ij}$ be the components of the curvature and the torsion tensors of $'\Gamma$ and $''\Gamma$, respectively. Then, we have

$$\begin{aligned}
{}'R^k_{ilj} &= \partial_l {}'\Gamma^k_{ij} - \partial_j {}'\Gamma^k_{il} + {}'\Gamma^k_{hl} {}'\Gamma^h_{ij} - {}'\Gamma^k_{hj} {}'\Gamma^h_{il} \\
{}''R^k_{ilk} &= \partial_l {}''\Gamma^k_{ij} - \partial_j {}''\Gamma^k_{il} + {}''\Gamma^k_{hl} {}''\Gamma^h_{ij} - {}''\Gamma^k_{hj} {}''\Gamma^h_{il}
\end{aligned} \tag{5}$$

and

$${}'T^k_{ij} = {}'\Gamma^k_{ij} - {}'\Gamma^k_{ji}, \qquad {}''T^k_{ij} = {}''\Gamma^k_{ij} - {}''\Gamma^k_{ji}. \tag{6}$$

Using the equations (1)-(6), we obtain the following ***Ricci formulas:***

$$\begin{aligned}
2\nabla_{[k} \nabla_{l]} U^{j_1\cdots j_s}_{i_1\ldots i_r} &= \nabla_k \nabla_l U^{j_1\cdots j_s}_{i_1\ldots i_r} - \nabla_l \nabla_k U^{j_1\cdots j_s}_{i_1\ldots i_r} \\
&= \sum_{p=1}^{s} {}'R^{j_p}_{hkl} U^{j_1\ldots h\ldots j_s}_{i_1\ldots i_r} - \sum_{q=1}^{r} {}''R^{h}_{i_q kl} U^{j_1\ldots j_s}_{i_1\ldots h\ldots i_r} - {}''T^h_{lk} \nabla_h U^{j_1\ldots j_s}_{i_1\ldots i_r}
\end{aligned} \tag{7}$$

A. Moor [4] introduced the concept of Weyl-Otsuki space by associating the theory of Otsuki space with the Weyl metric as follows:

Definition 2. Let M_n be an n-dimensional space with a regular general connection Γ and a Riemannian metric $g=\left(g_{ij}\right)$. Then M_n is called a ***Weyl-Otsuki space*** if the covariant differential of the metric tensor with respect to Γ holds the ***recurrence equation***,

$$\nabla_k g_{ij}=\varphi_k g_{ij}, \tag{8}$$

for a covariant vector field $\varphi=\left(\varphi_k\right)$. In this case, g is also called ***recurrent metric tensor***.

Remark 1. We will denote the Weyl-Otsuki space with regular general connection Γ, Riemannian metric g and covariant vector field $\varphi=\left(\varphi_k\right)$ by a quadruple $\left(M_n,\Gamma,g,\varphi\right)$.

Unlike an affine connection, the ***co-recurrence equation*** $\nabla_k g^{ij}=-\varphi_k g^{ij}$ does not hold for a regular general connection. Now, we will give the condition that the metric tensor satisfies the co-recurrence equation for regular general connections. In virtue of (2), (4) and (8), we obtain

$$\nabla_j \delta_i^k=\nabla_j\left(g^{kl}g_{li}\right)=g_{li}\nabla_j g^{kl}+\varphi_j\delta_i^k-g^{kh}g_{li}\nabla_j\delta_h^l$$

or equivalently

$$\nabla_j g^{kl}=-\varphi_j g^{kl}+g^{ki}\nabla_j\delta_i^l+g^{li}\nabla_j\delta_i^k.$$

Hence, we have the following lemma:

Proposition 1. Let $\left(M_n,\Gamma,g,\varphi\right)$ be a Weyl-Otsuki space. Then the co-recurrence equation

$$\nabla_k g^{ij}=-\varphi_k g^{ij}, \tag{9}$$

holds in a Weyl-Otsuki space if and only if

$$g^{ih}\nabla_k\delta_h^j+g^{jh}\nabla_k\delta_h^i=0.$$

3. Congruence of Curves in Weyl-Otsuki Spaces

In this section, we will show that Ricci's coefficients determine the connection in Weyl-Otsuki spaces as well as in Riemann spaces. We will use Ricci's coefficients to examine the condition for congruence of curves to be geodesic. Moreover, if the co-recurrence equation is satisfied, we will provide the properties of these coefficients in Weyl-Otsuki spaces.

Definition 3. Let $U=\left(U^1,\ldots,U^n\right)$ be a vector field on a Weyl-Otsuki space $\left(M_n,\Gamma,g,\varphi\right)$. The system of differential equations $\frac{dx^1}{U^1}=\ldots=\frac{dx^n}{U^n}$ admits $n-1$ independent solutions $\psi^i\left(x^1,\ldots,x^n\right)=c^i$, $\left(i=1,\ldots,n-1\right)$, where c's are constants [17]. If we substitute any point $p\in M_n$ in the last equations, the constants c are determined so that these $n-1$ equations define a curve through p. Since one can define such a curve through each point, U determines a family of curves, one of which passes through each point of that space. This family of curves is called a ***congruence*** of curves in a Weyl-Otsuki space[3]. An ***orthogonal ennuple*** in a Weyl-Otsuki space consists of n mutually orthogonal congruences of curves[4].

Let $U_{a|}$[5], $\left(a=1,...,n\right)$, be the unit tangents to the n congruences of an orthogonal ennuple. The contravariant and covariant components of $U_{a|}$ will be denoted by $U^i_{a|}$ and $U_{a|i}$ respectively. Since the n congruences are mutually orthogonal, we have the relations

$$g_{ij}U^i_{a|}U^j_{b|}=\delta_{ab} \qquad \text{or} \qquad U^i_{a|}U_{b|i}=\delta_{ab}. \tag{10}$$

Since $U^i_{a|}$ is the cofactor of $U_{a|i}$ in the determinant $\left|U_{a|i}\right|$ divided by the value of that determinant, we have

$$\sum_a U^i_{a|}U_{a|j}=\delta^i_j. \tag{11}$$

Definition 4. Let $U_{a|}$, $\left(a=1,...,n\right)$, be the unit tangents to the congruences of an orthogonal ennuple in a Weyl-Otsuki space $\left(M_n,\Gamma,g,\varphi\right)$ [17]. The derived vector of $U_{a|}$ in the direction of $U_{c|}$ has components $\left(\nabla_k U^j_{a|}\right)U^k_{c|}$; and the projection of this vector on $U_{b|}$ is a scalar invariant, denoted by η_{abc}, so that

$$\eta_{abc}=\left(\nabla_k U^j_{a|}\right)U_{b|j}U^k_{c|}. \tag{12}$$

[3] In the other words a congruence is the set of integral curves determined by a vector field.

[4] These definitions are the generalizations of the definitions in Riemannian spaces, [17].

[5] The subscript a, followed by a bar distinguishing one congruence from another, and having no significance of covariance.

The invariants η_{abc} are called ***Ricci's coefficients.***

Lemma 1. Let $U_{a|}$, $(a=1,...,n)$, be the unit tangents to the congruences of an orthogonal ennuple in a Weyl-Otsuki space (M_n,Γ,g,φ) Then the Ricci's coefficients η_{abc} determine a classical affine connection $'\Gamma$.

Proof. In virtue of (11) and (12) we have

$$\nabla_k U^j_{a|} = \sum_{b,c} \eta_{abc} U^j_{b|} U_{c|k} \ . \tag{13}$$

Multiplying this equation by $U^k_{c|}$, and using (10), we get

$$U^k_{c|} \nabla_k U^j_{a|} = \sum_b \eta_{abc} U^j_{b|} \ . \tag{14}$$

Now, if we multiply the equation (13) by $U_{a|i}$, and use (1), then we obtain

$$\sum_a \left(\nabla_k U^j_{a|}\right) U_{a|i} = \sum_a \left(\partial_k U^j_{a|} + {}'\Gamma^j_{lk} U^l_{a|}\right) U_{a|i} = \sum_{a,b,c} \eta_{abc} U_{a|i} U^j_{b|} U_{c|k} \ ,$$

by summing with respect to a. From the last equation we have

$${}'\Gamma^j_{ik} = -\sum_a U_{a|i} \partial_k U^j_{a|} + \sum_{a,b,c} \eta_{abc} U_{a|i} U^j_{b|} U_{c|k} \ , \tag{15}$$

which yields us the result. ■

Moreover, for a given isomorphism P of $T(M_n)$, a regular general connection Γ can be determined by $\Gamma^j_{ki} = P^j_l \, {}'\Gamma^l_{ki}$. Hence, using (15) we have the following theorem:

Theorem 1. Let $U_{a|}$, $(a=1,...,n)$, be the unit tangents to the congruences of an orthogonal ennuple in a Weyl-Otsuki space (M_n,Γ,g,φ). Then, for any isomorphism P of $T_p(M_n)$, the Ricci's coefficients η_{abc} determine a regular general connection Γ.

We note that in Riemannian spaces, Ricci's coefficients η_{abc} are skew-symmetric in the indices a and b but this is not the case in Weyl-Otsuki spaces unless the co-recurrence condition holds. In fact, using (2), (4), and (9), we obtain

$$\begin{aligned}\nabla_k U^j_{a|} &= \nabla_k \left(U_{a|l} g^{jl} \right) = g^{jl} \nabla_k U_{a|l} + U_{a|l} \nabla_k g^{jl} - U_{a|l} g^{ji} \nabla_k \delta^l_i \\ &= g^{jl} \nabla_k U_{a|l} - \varphi_k g^{jl} U_{a|l} - U_{a|l} g^{ji} \nabla_k \delta^l_i .\end{aligned}$$

Substituting the last equation in (12), we have

$$\begin{aligned}\eta_{abc} &= \left(g^{jl} \nabla_k U_{a|l} - \varphi_k g^{jl} U_{a|l} - U_{a|l} g^{ji} \nabla_k \delta^l_i \right) U_{b|j} U^k_{c|} \\ &= \left(U^l_{b|} \nabla_k U_{a|l} - \varphi_k \delta_{ab} - U_{a|l} U^i_{b|} \nabla_k \delta^l_i \right) U^k_{c|},\end{aligned}$$

or equivalently

$$U^l_{b|} \nabla_k U_{a|l} = \sum_c \eta_{abc} U_{c|k} + \varphi_k \delta_{ab} + U_{a|l} U^i_{b|} \nabla_k \delta^l_i . \tag{16}$$

On the other hand, using (2) and (4), we have

$$\nabla_k \delta_{ab} = \nabla_k \left(U^j_{a|} U_{b|j} \right) = U_{b|j} \nabla_k U^j_{a|} + U^j_{a|} \nabla_k U_{b|j} - U^i_{a|} U_{b|j} \nabla_k \delta^j_i = 0.$$

Multiplying the last equation by $U^k_{c|}$, we get

$$\begin{aligned}0 &= U^k_{c|} U_{b|j} \nabla_k U^j_{a|} + U^k_{c|} U^j_{a|} \nabla_k U_{b|j} - U^k_{c|} U^i_{a|} U_{b|j} \nabla_k \delta^j_i \\ &= \eta_{abc} + U^k_{c|} \left(\sum_d \eta_{bad} U_{d|k} + \varphi_k \delta_{ab} + U_{b|l} U^i_{a|} \nabla_k \delta^l_i \right) - U^k_{c|} U^i_{a|} U_{b|j} \nabla_k \delta^j_i \\ &= \eta_{abc} + \eta_{bac} + \varphi_k \delta_{ab} U^k_{c|}\end{aligned}$$

from (12) and (16). Hence, we obtain

$$\eta_{abc} + \eta_{bac} = -\varphi_k \delta_{ab} U^k_{c|}, \tag{17}$$

and the following result:

Proposition 2. Let $U_{a|}$, $(a = 1,...,n)$, be the unit tangents to the congruences of an orthogonal ennuple in a Weyl-Otsuki space $(M_n, \Gamma, g, \varphi)$. If the co-recurrence equation is

satisfied, then Ricci's coefficients η_{abc} are skew-symmetric in the indices a and b with $a \neq b$, i.e.,

$$\eta_{abc} = -\eta_{bac}\,,\ (a \neq b). \tag{18}$$

Now, we can give another version of Ricci formulas using Ricci's coefficients for Weyl-Otsuki spaces. Let $U_{a|}$, $(a = 1,...,n)$, be the unit tangents to the congruences of an orthogonal ennuple in a Weyl-Otsuki space $(M_n, \Gamma, g, \varphi)$. Taking the basic covariant differentiation of (13) with respect to u^k, and using (12), (2), (4), (8), we have

$$\begin{aligned}
\nabla_i \nabla_k U^j_{a|} &= \nabla_i \left(\sum_{e,f} \eta_{aef} U^j_{e|} U_{f|k} \right) = \sum_{e,f} \left(U^j_{e|} U_{f|k} \partial_i \eta_{aef} + \eta_{aef} U_{f|k} \nabla_i U^j_{e|} + \eta_{aef} U^j_{e|} \nabla_i U_{f|k} \right) \\
&= \sum_{e,f} U^j_{e|} U_{f|k} \partial_i \eta_{aef} + \sum_{e,f} \eta_{aef} U_{f|k} \left(\sum_{r,s} \eta_{ers} U^j_{r|} U_{s|i} \right) + \sum_{e,f} \eta_{aef} U^j_{e|} \nabla_i \left(U^l_{f|} g_{lk} \right) \\
&= \sum_{e,f} U^j_{e|} U_{f|k} \partial_i \eta_{aef} + \sum_{e,f} \eta_{aef} U_{f|k} \left(\sum_{r,s} \eta_{ers} U^j_{r|} U_{s|i} \right) \\
&\quad + \sum_{e,f} \eta_{aef} U^j_{e|} \left(g_{lk} \nabla_i U^l_{f|} + U^l_{f|} \nabla_i g_{lk} - U^h_{f|} g_{lk} \nabla_i \delta^l_h \right) \\
&= \sum_{e,f} U^j_{e|} U_{f|k} \partial_i \eta_{aef} + \sum_{e,f} \eta_{aef} U_{f|k} \left(\sum_{r,s} \eta_{ers} U^j_{r|} U_{s|i} \right) \\
&\quad + \sum_{e,f} \eta_{aef} U^j_{e|} \left(g_{lk} \sum_{r,s} \eta_{frs} U^l_{r|} U_{s|i} + U^l_{f|} \varphi_i g_{lk} - U^h_{f|} g_{lk} \nabla_i \delta^l_h \right) \\
&= \sum_{e,f} U^j_{e|} U_{f|k} \partial_i \eta_{aef} + \sum_{e,f} \eta_{aef} U_{f|k} \left(\sum_{r,s} \eta_{ers} U^j_{r|} U_{s|i} \right) \\
&\quad + \sum_{e,f} \eta_{aef} U^j_{e|} \left(\sum_{r,s} \eta_{frs} U_{r|k} U_{s|i} + \varphi_i U_{f|k} - U^h_{f|} g_{lk} \nabla_i \delta^l_h \right).
\end{aligned}$$

If we compute $\nabla_k \nabla_i U^j_{a|}$ and subtract it from the above equation, we obtain

$$\begin{aligned}\nabla_i\nabla_k U^j_{a|}-\nabla_k\nabla_i U^j_{a|} &= \sum_{e,f} U^j_{e|}U_{f|k}\partial_i\eta_{aef}+\sum_{e,f}\eta_{aef}U_{f|k}\left(\sum_{r,s}\eta_{ers}U^j_{r|}U_{s|i}\right)\\ &+\sum_{e,f}\eta_{aef}U^j_{e|}\left(\sum_{r,s}\eta_{frs}U_{r|k}U_{s|i}+\varphi_i U_{f|k}-U^h_{f|}g_{lk}\nabla_i\delta^l_h\right)\\ &-\sum_{e,f}U^j_{e|}U_{f|i}\partial_k\eta_{aef}-\sum_{e,f}\eta_{aef}U_{f|i}\left(\sum_{r,s}\eta_{ers}U^j_{r|}U_{s|k}\right)\\ &-\sum_{e,f}\eta_{aef}U^j_{e|}\left(\sum_{r,s}\eta_{frs}U_{r|i}U_{s|k}+\varphi_k U_{f|i}-U^h_{f|}g_{li}\nabla_k\delta^l_h\right)\\ &=2\sum_{e,f}U^j_{e|}U_{f|[k}\partial_{i]}\eta_{aef}+2\sum_{e,f,r,s}\eta_{aef}\eta_{ers}U^j_{r|}U_{f|[k}U_{s|i]}\\ &+2\sum_{e,f}\eta_{aef}U^j_{e|}\left(\sum_{r,s}\eta_{frs}U_{r|[k}U_{s|i]}+U_{f|[k}\varphi_{i]}-U^h_{f|}g_{l[k}\nabla_{i]}\delta^l_h\right).\end{aligned}$$

Multiplying the last equation by $U_{b|j}U^k_{c|}U^i_{d|}$ and summing with respect to i,j,k we get

$$\begin{aligned}\left(\nabla_i\nabla_k U^j_{a|}-\nabla_k\nabla_i U^j_{a|}\right)U_{b|j}U^k_{c|}U^i_{d|} &= 2U_{b|j}U^k_{c|}U^i_{d|}\sum_{e,f}U^j_{e|}U_{f|[k}\partial_{i]}\eta_{aef}\\ &+2U_{b|j}U^k_{c|}U^i_{d|}\sum_{e,f,r,s}\eta_{aef}\eta_{ers}U^j_{r|}U_{f|[k}U_{s|i]}\\ &+2U_{b|j}U^k_{c|}U^i_{d|}\sum_{e,f}\eta_{aef}U^j_{e|}\left(\sum_{r,s}\eta_{frs}U_{r|[k}U_{s|i]}\right.\\ &\left.+U_{f|[k}\varphi_{i]}-U^h_{f|}g_{l[k}\nabla_{i]}\delta^l_h\right)\\ &=2U^i_{[d|}\partial_i\eta_{abc]}+2\sum_e\eta_{ae[c}\eta_{ebd]}+2\sum_f\eta_{abf}\eta_{f[cd]}\\ &+2\eta_{ab[c}\varphi_i U^i_{d]|}-2\sum_f\eta_{abf}U^h_{f|}U_{[c|l}U^i_{d]|}\nabla_{i]}\delta^l_h.\end{aligned}$$

Consequently, if we write the Ricci formulas (7) in this equation, then we have

$$\begin{aligned}\frac{1}{2}\left('R^j_{hik}U^h_{a|}-"T^h_{ki}\nabla_h U^j_{a|}\right)U_{b|j}U^k_{c|}U^i_{d|} &= U^i_{[d|}\partial_i\eta_{abc]}+\sum_e\eta_{ae[c}\eta_{ebd]}+\sum_f\eta_{abf}\eta_{f[cd]}\\ &+2\eta_{ab[c}\varphi_i U^i_{d]|}-\sum_f\eta_{abf}U^h_{f|}U_{[c|l}U^i_{d]|}\nabla_{i]}\delta^l_h.\end{aligned}$$

Now, we will give the condition for congruence of curves to be geodesic in Weyl-Otsuki spaces. Let s_a be the arc-length parameter of one of the curves $u=u(s_a)$ of the ennuple whose unit tangent is $U_{a|}=du/ds_a$. Then, using (14), we have

$$\frac{\nabla U_{a|}^{j}}{ds_a}=\left(\nabla_k U_{a|}^{j}\right)\frac{du^k}{ds_a}=U_{a|}^{k}\nabla_k U_{a|}^{j}=\sum_b \eta_{aba}U_{b|}^{j}\,.$$

Hence we obtain the following result:

Theorem 2. Let $U_{a|}$, $(a=1,...,n)$, be the unit tangents to the congruences of an orthogonal ennuple in a Weyl-Otsuki space (M_n,Γ,g,φ). Then, the curves of the congruence are geodesics if and only if $\eta_{aba}=0$, $(b=1,...,n)$.

4. Normal Orthogonal Ennuples

In this section, we will express the condition of an orthogonal ennuple in a Weyl-Otsuki space in which the co-recurrence equation is satisfied to be normal regarding Ricci's coefficients.

Definition 5. [17] An orthogonal ennuple that intersects orthogonally with a family of hypersurfaces, $\phi=const.$ is called a ***normal orthogonal ennuple***.

Let $U_{a|}$ be the unit tangent to the congruences of an orthogonal ennuple in a Weyl-Otsuki space in which the co-recurrence equation is satisfied, and $\phi=const.$ be a family of hypersurfaces. Then this ennuple is normal when the gradient of ϕ at each point has the direction of the vector $U_{a|}$. This condition is expressed as

$$\frac{\partial_1\phi}{U_{a|1}}=\frac{\partial_2\phi}{U_{a|2}}=...=\frac{\partial_n\phi}{U_{a|n}}\,.$$

But the necessary and sufficient condition for the existence of such a function ϕ is

$$U_{a|j}\left(\partial_i U_{a|k}-\partial_k U_{a|i}\right)+U_{a|k}\left(\partial_j U_{a|i}-\partial_i U_{a|j}\right)+U_{a|i}\left(\partial_k U_{a|j}-\partial_j U_{a|k}\right)=0\,.$$

Now, let a congruence of an orthogonal ennuple with unit tangent $U_{n|}$ be normal. Using (1) in the last equation, we have

$$\begin{aligned}&U_{n|j}\left(\nabla_i U_{n|k}+"\Gamma_{ki}^{h}U_{n|h}-\nabla_k U_{n|i}-"\Gamma_{ik}^{h}U_{n|h}\right)\\&+U_{n|k}\left(\nabla_j U_{n|i}+"\Gamma_{ij}^{h}U_{n|h}-\nabla_i U_{n|j}-"\Gamma_{ji}^{h}U_{n|h}\right)\\&+U_{n|i}\left(\nabla_k U_{n|j}+"\Gamma_{jk}^{h}U_{n|h}-\nabla_j U_{n|k}-"\Gamma_{kj}^{h}U_{n|h}\right)=0.\end{aligned}$$

If we multiply this equation by $U^j_{a|}U^i_{b|}$, $(a,b=1,2,...,n-1)$, in virtue of (16), (3), and (6), we get

$$\begin{aligned}
0 &= U^j_{a|}U^i_{b|}U_{n|k}\left(\nabla_j U_{n|i} + "\Gamma^h_{ij}U_{n|h} - \nabla_i U_{n|j} - "\Gamma^h_{ji}U_{n|h}\right)\\
&= U_{n|k}\left(\eta_{nba} + \varphi_j\delta_{nb}U^j_{a|} + U_{n|h}U^i_{b|}U^j_{a|}\nabla_j\delta^h_i + "\Gamma^h_{ij}U_{n|h}U^j_{a|}U^i_{b|}\right.\\
&\qquad \left. -\eta_{nab} - \varphi_i\delta_{na}U^i_{b|} - U_{n|h}U^j_{a|}U^i_{b|}\nabla_i\delta^h_j - U^j_{a|}U^i_{b|}"\Gamma^h_{ji}U_{n|h}\right)\\
&= U_{n|k}\left(\eta_{nba} + U_{n|h}U^i_{b|}U^j_{a|}\nabla_j\delta^h_i + "\Gamma^h_{ij}U_{n|h}U^j_{a|}U^i_{b|}\right.\\
&\qquad \left. -\eta_{nab} - U_{n|h}U^j_{a|}U^i_{b|}\nabla_i\delta^h_j - U^j_{a|}U^i_{b|}"\Gamma^h_{ji}U_{n|h}\right)\\
&= U_{n|k}\left(\eta_{nba} - \eta_{nab} + 'T^h_{ij}U^j_{a|}U^i_{b|}U_{n|h}\right).
\end{aligned}$$

Hence, we have the following result:

Theorem 4. In a Weyl-Otsuki space in which the condition (9) holds, the necessary and sufficient condition that the congruences $U_{n|}$ of an orthogonal ennuple be normal is that

$$\eta_{nab} - \eta_{nba} = 'T^h_{ij}U^j_{a|}U^i_{b|}U_{n|h}, \qquad (a,b=1,2,...,n-1). \tag{19}$$

If all the congruences of an orthogonal ennuple are normal, all the invariants η_{abc} with three distinct indices must be zero. Using the equation (18) in (19), we have

$$\begin{aligned}
\eta_{abc} &= \eta_{acb} + 'T^h_{ij}U^j_{b|}U^i_{c|}U_{a|h} = -\eta_{cab} + 'T^h_{ij}U^j_{b|}U^i_{c|}U_{a|h}\\
&= -\eta_{cba} - 'T^h_{ij}U^j_{a|}U^i_{b|}U_{c|h} + 'T^h_{ij}U^j_{b|}U^i_{c|}U_{a|h}\\
&= \eta_{bca} + 'T^h_{ij}\left(U^j_{b|}U^i_{c|}U_{a|h} - U^j_{a|}U^i_{b|}U_{c|h}\right)\\
&= \eta_{bac} + 'T^h_{ij}U^j_{c|}U^i_{a|}U_{b|h} + 'T^h_{ij}\left(U^j_{b|}U^i_{c|}U_{a|h} - U^j_{a|}U^i_{b|}U_{c|h}\right)\\
&= -\eta_{abc} + 'T^h_{ij}\left(U^j_{b|}U^i_{c|}U_{a|h} + U^j_{c|}U^i_{a|}U_{b|h} - U^j_{a|}U^i_{b|}U_{c|h}\right).
\end{aligned}$$

Consequently, we obtain the following result:

Theorem 5. In a Weyl-Otsuki space in which the condition (9) holds, the necessary and sufficient condition that all the congruences of an orthogonal ennuple be normal is that

$$\eta_{abc} = \frac{1}{2}'T^h_{ij}\left(U^j_{b|}U^i_{c|}U_{a|h} + U^j_{c|}U^i_{a|}U_{b|h} - U^j_{a|}U^i_{b|}U_{c|h}\right),$$
$$(a,b,c=1,2,...,n;\ a,b,c \text{ unequal}).$$

5. Curl of an Orthogonal Ennuple

In this section, we will give the condition for an orthogonal ennuple to be irrotational in Weyl-Otsuki spaces in terms of Ricci's coefficients. We will also express the relationship between the geodesic, normal, and irrotational conditions of an orthogonal ennuple in Weyl-Otsuki spaces in which the co-recurrence equation is satisfied.

Definition 6. [17] The curl of the unit tangent to an orthogonal ennuple is briefly called ***the curl of the orthogonal ennuple***. If the curl of an orthogonal ennuple vanishes identically, the ennuple will be described as ***irrotational***.

Consider the n th congruence of an orthogonal ennuple whose unit tangent vector is $U_{n|}$ in a Weyl-Otsuki space in which the condition (9) holds. Putting $a = n$ in (16), multiplying it by $U_{b|i}$ and summing with respect to b, we obtain

$$\nabla_k U_{n|i} = \sum_{b,c} \eta_{nbc} U_{b|i} U_{c|k} + \varphi_k U_{n|i} + U_{n|l} \nabla_k \delta_i^l . \tag{20}$$

Since the curl of the unit tangent to the n th congruence of an orthogonal ennuple is the tensor, whose components are $\nabla_k U_{n|j} - \nabla_j U_{n|k}$, then from (20), these components have the values

$$\nabla_k U_{n|j} - \nabla_j U_{n|k} = \sum_{b,c} \left(\eta_{nbc} - \eta_{ncb} \right) U_{b|j} U_{c|k} + 2 \left(\nabla_{[k} \delta_{j]}^l + \varphi_{[k} \delta_{j]}^l \right) U_{n|l} .$$

This double sum may be separated into two sums as follows. In the first, let b and c take the values $1, 2, ..., n-1$; and, in the second, let either or both take the value n. Then we have

$$\begin{aligned} \nabla_k U_{n|j} - \nabla_j U_{n|k} = & \sum_{b,c=1}^{n-1} \left(\eta_{nbc} - \eta_{ncb} \right) U_{b|j} U_{c|k} + \sum_{b=1}^{n-1} \left(\eta_{nbn} - \eta_{nnb} \right) U_{b|j} U_{n|k} \\ & + \sum_{c=1}^{n-1} \left(\eta_{nnc} - \eta_{ncn} \right) U_{n|j} U_{c|k} + 2 \left(\nabla_{[k} \delta_{j]}^l + \varphi_{[k} \delta_{j]}^l \right) U_{n|l} . \end{aligned} \tag{21}$$

Now, we will give the relationship between the geodesic, normal, and irrotational conditions of an orthogonal ennuple in Weyl-Otsuki spaces where the co-recurrence equation is satisfied.

Theorem 6. Let $U_{n|}$ be the unit tangent to the n th congruence of an orthogonal ennuple in a Weyl-Otsuki space $\left(M_n,\Gamma,g,\varphi\right)$ in which the condition (9) holds. If this congruence satisfies

$$"T_{kj}^{h}-2'T_{i[j}^{h}U_{n|}^{i}U_{n|k]}+\varphi_{[k}\delta_{j]}^{h}=0, \tag{22}$$

and any two of the following conditions, then it will also satisfy the other third one;

i) that it be a normal congruence, **ii)** that it be a geodesic congruence, **iii)** that it be irrotational.

Proof. Case 1. Suppose that the n th congruence is both normal and geodesic. Using (19), we can write the first term on the right-hand side of (21) as

$$\begin{aligned}\sum_{b,c=1}^{n-1}\left(\eta_{nbc}-\eta_{ncb}\right)U_{b|j}U_{c|k}&=\sum_{b,c=1}^{n-1}{'T_{il}^{h}U_{b|}^{l}U_{c|}^{i}U_{n|h}U_{b|j}U_{c|k}}\\&={'T_{il}^{h}\left(\delta_{j}^{l}-U_{n|}^{l}U_{n|j}\right)\left(\delta_{k}^{i}-U_{n|}^{i}U_{n|k}\right)U_{n|h}}\\&={'T_{il}^{h}\left(\delta_{j}^{l}\delta_{k}^{i}-\delta_{j}^{l}U_{n|}^{i}U_{n|k}-\delta_{k}^{i}U_{n|}^{l}U_{n|j}+U_{n|}^{l}U_{n|j}U_{n|}^{i}U_{n|k}\right)U_{n|h}}\\&=\left({'T_{kj}^{h}-'T_{ij}^{h}U_{n|}^{i}U_{n|k}-'T_{kl}^{h}U_{n|}^{l}U_{n|j}+'T_{il}^{h}U_{n|}^{l}U_{n|j}U_{n|}^{i}U_{n|k}}\right)U_{n|h}\\&=\left({'T_{kj}^{h}-'T_{ij}^{h}U_{n|}^{i}U_{n|k}+'T_{ik}^{h}U_{n|}^{i}U_{n|j}}\right)U_{n|h}\\&=\left({'T_{kj}^{h}-2'T_{i[j}^{h}U_{n|}^{i}U_{n|k]}}\right)U_{n|h}.\end{aligned} \tag{23}$$

Since the congruence is also a geodesic curve, then we have

$$\eta_{nbn}=\eta_{ncn}=0,$$

from Theorem 2. So (21) can be written as

$$\begin{aligned}\nabla_{k}U_{n|j}-\nabla_{j}U_{n|k}&=\left({'T_{kj}^{h}-2'T_{i[j}^{h}U_{n|}^{i}U_{n|k]}}\right)U_{n|h}-\sum_{b=1}^{n-1}\eta_{nnb}U_{b|j}U_{n|k}\\&\quad+\sum_{c=1}^{n-1}\eta_{nnc}U_{n|j}U_{c|k}+2\left(\nabla_{[k}\delta_{j]}^{l}+\varphi_{[k}\delta_{j]}^{l}\right)U_{n|l}\\&=\left({"T_{kj}^{h}-2'T_{i[j}^{h}U_{n|}^{i}U_{n|k]}+2\varphi_{[k}\delta_{j]}^{l}}\right)U_{n|h}\\&\quad+\sum_{b=1}^{n-1}\eta_{nnb}\left(U_{n|j}U_{b|k}-U_{b|j}U_{n|k}\right).\end{aligned}$$

If we use (17) for the last term on the right-hand side of the above equation, then we have

$$\begin{aligned}\sum_{b=1}^{n-1}\eta_{nnb}\left(U_{n|j}U_{b|k}-U_{b|j}U_{n|k}\right)&=-\frac{1}{2}\varphi_i\sum_{b=1}^{n-1}U^i_{b|}\left(U_{n|j}U_{b|k}-U_{b|j}U_{n|k}\right)\\&=-\frac{1}{2}\varphi_iU_{n|j}\left(\delta^i_k-U^i_{n|}U_{n|k}\right)+\frac{1}{2}\varphi_iU_{n|k}\left(\delta^i_j-U^i_{n|}U_{n|j}\right)\\&=\varphi_{[j}U_{n|k]}.\end{aligned}\quad(24)$$

So we obtain

$$\nabla_kU_{n|j}-\nabla_jU_{n|k}=\left("T^h_{kj}-2'T^h_{i[j}U^i_{n|}U_{n|k]}+\varphi_{[k}\delta^l_{j]}\right)U_{n|h}.$$

Hence, a normal and geodesic congruence that satisfies equation (22) is irrotational.

Case 2. Let the n th congruence be both normal and irrotational. At first, if we substitute (23) in (21) and use (17), (24) as in case 1, then we get

$$\nabla_kU_{n|j}-\nabla_jU_{n|k}=\left("T^h_{kj}-2'T^h_{i[j}U^i_{n|}U_{n|k]}+\varphi_{[k}\delta^l_{j]}\right)U_{n|h}+\sum_{b=1}^{n-1}\eta_{nbn}\left(U_{b|j}U_{n|k}-U_{n|j}U_{b|k}\right).$$

Now, since the congruence is irrotational and satisfies (22), then the last equation yields

$$\sum_{b=1}^{n-1}\eta_{nbn}\left(U_{b|j}U_{n|k}-U_{n|j}U_{b|k}\right)=0.$$

Then, this congruence is geodesic by Theorem 2.

Case 3. Let the n th congruence be both geodesic and irrotational. By the definition of irrotational curve and Theorem 2, (21) takes the form

$$\sum_{b,c=1}^{n-1}\left(\eta_{nbc}-\eta_{ncb}\right)U_{b|j}U_{c|k}+\sum_{b=1}^{n-1}\eta_{nnb}\left(U_{n|j}U_{b|k}-U_{b|j}U_{n|k}\right)+2\left(\nabla_{[k}\delta^l_{j]}+\varphi_{[k}\delta^l_{j]}\right)U_{n|l}=0.$$

If we use (3), (6) and (24) in the last equation, then we have

$$\sum_{b,c=1}^{n-1}\left(\eta_{nbc}-\eta_{ncb}\right)U_{b|j}U_{c|k}+\left('T^l_{jk}-"T^l_{jk}+\varphi_{[k}\delta^l_{j]}\right)U_{n|l}=0.$$

Since the congruence satisfies (22), we obtain

$$\sum_{b,c=1}^{n-1}\left(\eta_{nbc}-\eta_{ncb}\right)U_{b|j}U_{c|k}+\left('T^{l}_{jk}+2'T^{l}_{i[j}U^{i}_{n|}U_{n|k]}\right)U_{n|l}=0.$$

Finally, by multiplying the last equation by $V^{i}_{b|}V^{j}_{c|}$ we get

$$\begin{aligned}\eta_{nbc}-\eta_{ncb}&=-\left('T^{l}_{jk}+2'T^{l}_{i[j}U^{i}_{n|}U_{n|k]}\right)U_{n|l}U^{j}_{b|}U^{k}_{c|}\\&=-\left('T^{l}_{jk}U^{j}_{b|}U^{k}_{c|}+2'T^{l}_{i[j}U^{i}_{n|}U_{c|k]}U^{j}_{b|}\right)U_{n|l}\\&='T^{l}_{ji}U^{j}_{b|}U^{i}_{c|}U_{n|l}.\end{aligned}$$

Hence, this congruence is normal by Theorem 4. ■

Acknowledgements

In consideration of the memory of my doctoral supervisor Prof. Dr. Leyla Zeren Akgün.

References

[1] Otsuki, T., *Tangent bundles of order 2 and general connections*, Mathematical Journal of Okayama University, 8, 143-179, 1958.

[2] Otsuki, T., *On general connections I*, Mathematical Journal of Okayama University, 9, 99-164, 1960.

[3] Otsuki, T., *On general connections II*, Mathematical Journal of Okayama University, 10, 113-124, 1961.

[4] Moor, A., *Otsukische Übertragung mit rekurrentem masstensor*, Acta Scientiarum Mathematicarum, 40, 129-142, 1978.

[5] Nadj, D.F., *On curvatures of the Weyl-Otsuki spaces*, Publicationes Mathematicae Debrecen, 28, 59-73, 1981.

[6] Nadj, D.F., *Die Frenetformeln des Weyl-Otsukischen raumes*, Publicationes Mathematicae Debrecen, 36 (1-4), 221-228, 1989.

[7] Nadj, D.F., *On subspaces of Riemann-Otsuki space*, Publications de l'Institut Mathématique Nouvelle Série, 30 (44), 53-58, 1981.

[8] Nadj, D.F., *Autoparallel curves of Riemann-Otsuki spaces*, Zbornik radova PMF Novi Sad, 13, 227-243, 1983.

[9] Nadj, D.F., *The Gauss, Codazzi and Kühne equations of Riemann-Otsuki spaces*, Acta Mathematica Hungarica , 44 (3-4), 255-260, 1984.

[10] Abe, N., *General connections on vector bundles*, Kodai Mathematical Journal, 8, 322-329, 1985.

[11] Abe, N., *Geometry of certain first order differential operators and its applications to general connections*, Kodai Mathematical Journal, 11, 205-223, 1988.

[12] Nagayama, H., *A theory of general relativity by general connections I*, TRU Mathematics, 20, 173-187, 1984.

[13] Nagayama, H., *A theory of general relativity by general connections II*, TRU Mathematics, 21, 287-317, 1985.

[14] Otsuki, T., *A construction of spaces with general connections which have points swallowing geodesics*, Mathematical Journal of Okayama University, 24, 157-165, 1982.

[15] Otsuki, T., *A certain space-time metric and smooth general connections*, Kodai Mathematical Journal, 8, 307-316, 1985.

[16] Otsuki, T., *Singular point sets of a general connection and black holes*, Mathematical Journal of Okayama University, 30, 199-211, 1988.

[17] Weatherburn, C.E., *An introduction to Riemannian geometry and the tensor calculus*, Cambridge University Press, New York, Macmillan, 1st ed., 191p, 1938.

Adıyaman University Journal of Science
https://dergipark.org.tr/en/pub/adyujsci
DergiPark AKADEMİK
ISSN 2147-1630
e-ISSN 2146-586X

Tumor Detection by Classification of Brain MRI Images Using the Vision Transformers

Uğur DEMİROĞLU[1,*]

[1]*Kahramanmaraş İstiklal University, Faculty of Engineering, Architecture and Design, Department of Software Engineering, Kahramanmaraş, Türkiye*
ugur.demiroglu@istiklal.edu.tr, ORCID: 0000-0002-0000-8411

Received: 23.10.2024 **Accepted:** 19.12.2024 **Published:** 31.12.2024

Abstract

The interplay between applied mathematics and artificial intelligence is pivotal for advancing both fields. AI fundamentally relies on statistical and mathematical techniques to derive models from data, thus enabling computers to improve their performance over time. Classification of brain MRI images for tumor detection has improved significantly with the advent of machine learning and deep learning techniques. Classical classifiers such as Support Vector Machines (SVM), Tree, and k-Nearest Neighbors (k-NN) have been widely used in conjunction with feature extraction methods to improve the accuracy of tumor detection in MRI scans. Recent studies have shown that classical classifiers can effectively analyze features extracted from MRI images, which can lead to improved diagnostic capabilities. Feature extraction is a critical step in the classification process. Classification of brain MRI images using Vision Transformers (ViTs) represents a significant advancement in medical imaging and tumor detection. ViTs leverage the transformer architecture, which is highly successful in natural language processing, to effectively process visual data. This approach allows for capturing long-range dependencies within images and enhances the ability of the model to distinguish complex patterns associated with brain

* Corresponding Author DOI: 10.37094/adyujsci.1572289

tumors. Recent studies have demonstrated the effectiveness of ViTs in various classification tasks, including medical imaging. In our study, the classification accuracy of the dataset from the ViTs network was 78.26%. In order to increase tumor detection performance, features of the ViTs network were extracted and given to classical classifiers, and 81.9% accuracy was achieved in Tree classifier. As a result, classification of brain MRI images using ViTs represents a new approach with the strengths of deep learning and traditional machine learning methods, namely feature extraction and classification in classical classifiers.

Keywords: Brain MRI; Tumor detection; Classification; Vision transformers; Applied mathematics.

Vision Transformers Kullanılarak Beyin MRI Görüntülerinin Sınıflandırılmasıyla Tümör Tespiti

Öz

Uygulamalı matematik ve yapay zeka arasındaki etkileşim, her iki alanın da ilerlemesi için çok önemlidir. Yapay zeka, verilerden modeller türetmek için temelde istatistiksel ve matematiksel tekniklere güvenir ve böylece bilgisayarların zamanla performanslarını iyileştirmelerini sağlar. Beyin MRI görüntülerinin tümör tespiti için sınıflandırılması, makine öğrenimi ve derin öğrenme tekniklerinin ortaya çıkmasıyla önemli ölçüde iyileşmiştir. Destek Vektör Makineleri (SVM), Ağaç ve k-En Yakın Komşular (k-NN) gibi klasik sınıflandırıcılar, MRI taramalarında tümör tespitinin doğruluğunu artırmak için özellik çıkarma yöntemleriyle birlikte yaygın olarak kullanılmıştır. Son çalışmalar, klasik sınıflandırıcıların MRI görüntülerinden çıkarılan özellikleri etkili bir şekilde analiz edebileceğini ve bunun da gelişmiş tanı yeteneklerine yol açabileceğini göstermiştir. Özellik çıkarma, sınıflandırma sürecinde kritik bir adımdır. Görme Dönüştürücüleri (ViT) kullanılarak beyin MRI görüntülerinin sınıflandırılması, tıbbi görüntüleme ve tümör tespitinde önemli bir ilerlemeyi temsil etmektedir. ViT, görsel verileri etkili bir şekilde işlemek için doğal dil işlemede oldukça başarılı olan dönüştürücü mimarisinden yararlanır. Bu yaklaşım, görüntüler içindeki uzun menzilli bağımlılıkları yakalamaya olanak tanır ve modelin beyin tümörleriyle ilişkili karmaşık örüntüleri ayırt etme yeteneğini artırır. Son çalışmalar, tıbbi görüntüleme dahil olmak üzere çeşitli sınıflandırma görevlerinde ViT'in etkinliğini göstermiştir. Çalışmamızda, ViT ağından gelen veri setinin sınıflandırma doğruluğu %78,26 idi. Tümör tespit performansını artırmak için ViT ağının özellikleri çıkarılıp klasik sınıflandırıcılara verildi ve Ağaç sınıflandırıcısında %81,9 doğruluk

elde edildi. Sonuç olarak, Görme Dönüştürücüleri kullanılarak beyin MRI görüntülerinin sınıflandırılması, klasik sınıflandırıcılarda özellik çıkarma ve sınıflandırma olmak üzere derin öğrenme ve geleneksel makine öğrenme yöntemlerinin güçlü yönlerine sahip yeni bir yaklaşımı temsil etmektedir.

Anahtar Kelimeler: Beyin MRI; Tümör tespiti; Sınıflandırma; Görüntü transformatörleri, Uygulamalı matematik.

1. Introduction

Brain tumors are abnormal growths that develop inside the brain or its surrounding tissues. These tumors can be benign (non-cancerous) or malignant (cancerous), with symptoms varying greatly depending on their location, size, and form [1]. Common symptoms include migraines, seizures, vision problems, balance challenges, personality or behavioral changes, and trouble speaking or swallowing. Imaging examinations, such as magnetic resonance imaging (MRI) or computed tomography (CT) scans, are commonly used to diagnose tumors. A biopsy, which includes removing a sample of tumor tissue for examination under a microscope, is frequently required to diagnose the type of tumor. Treatment choices for brain tumors are determined by the tumor's features, such as type, size, location, and the patient's overall health. Surgery is commonly used to remove benign and certain malignant tumors, whereas radiation treatment and chemotherapy are used to kill cancer cells. Targeted therapy, which utilizes medications to specifically target cancer cells, is also becoming more essential in the treatment of brain tumors. Some brain tumors are curable, but others are more difficult to treat. The prognosis of brain tumors varies greatly depending on these characteristics. Ongoing research aims to produce more effective and targeted medicines for brain tumors, with the ultimate goal of improving patient outcomes. Even if the tumor is treatable, early diagnosis of the disease is life-saving. Thus, developments on this issue are significantly important.

As mentioned in the previous paragraph, MRI and CT have been frequently used to diagnose tumors. MRI is a non-invasive diagnostic technique that uses a powerful magnet and radio waves to create detailed images of the body's internal structures. Unlike X-rays or CT scans, MRI does not use ionizing radiation. Instead, it aligns the hydrogen atoms in the body with the magnetic field and then disturbs them using radio waves. As the atoms realign, they emit signals that are detected by the MRI machine. These signals are processed by a computer to create images that can show organs, bones, muscles, and blood vessels in great detail. MRI is particularly useful for examining soft tissues and is often used to diagnose conditions such as brain tumors, spinal cord injuries, and joint problems. Specifically, the study in this paper focuses on MRI to detect

brain tumors. Brain MRI is a technique to obtain detailed images of the brain and surrounding structures [2]. The patient lies inside a cylindrical magnet, and radiofrequency pulses are applied to the brain, causing the hydrogen atoms in the body to temporarily shift their alignment. As these atoms realign, they emit signals that are detected by the MRI machine. These signals are processed by a computer to create images that can show the brain's anatomy, blood flow, and metabolism. The advantage of Brain MRI lies in its ability to provide high-resolution images without the use of ionizing radiation, making it a safer option compared to CT scans or X-rays. MRI can also be used to detect subtle changes in brain tissue, making it valuable for diagnosing conditions such as tumors, strokes, and multiple sclerosis. Additionally, MRI can be used to assess brain function and monitor treatment response. Although it has a higher cost compared to other imaging techniques, the longer scan time, and the potential for discomfort or claustrophobia in some patients, MRI remains one of the most reliable imaging techniques.

Classification techniques for medical images play a crucial role in the field of healthcare by enabling accurate and efficient diagnosis and treatment. These techniques involve the use of algorithms to categorize medical images into different classes based on their visual characteristics. For instance, they can be used to differentiate between benign and malignant tumors, identify various types of diseases, or analyze the progression of a disease over time. By automating the classification process, medical professionals can save time and enhance diagnostic accuracy, leading to improved patient outcomes. Furthermore, classification techniques can be used to assist in treatment planning and monitoring, ensuring that patients receive appropriate care. This paper implements the ViTs method for classification [3]. ViTs have significantly impacted the field of computer vision, particularly in image classification. Unlike traditional convolutional neural networks (CNNs), ViTs utilize transformers, a sequence-to-sequence modeling architecture originally developed for natural language processing. ViTs divide images into patches, flatten them into vectors, and then feed them into a transformer encoder. This approach allows ViTs to handle images of various sizes and resolutions efficiently. Additionally, ViTs have demonstrated competitive performance with CNNs, especially on large-scale datasets. Their scalability, flexibility, and strong theoretical foundation make them a promising choice for various computer vision tasks, including medical image analysis and remote sensing. More information about the method can be found in the further sections.

Based on the above information, computerized techniques have significant importance in early diagnosis of tumors. This idea has attracted the attention of researchers and has led to valuable studies on the subject. For instance, Elbedoui et al. studied deep learning approaches for dermoscopic image-based skin cancer diagnosis in [4]. They concentrated on utilizing deep

learning methodologies for the detection of skin cancer through dermoscopic images, demonstrating the efficacy of neural networks in identifying malignant patterns. Mejri et al. implemented the Visual Geometry Group and ResNet-50 in their study in [5]. In the study, they employed Visual Geometry Group (VGG) networks and ResNet-50, two powerful convolutional neural network (CNN) architectures, to proficiently categorize skin cancer photos. The ViT formed the basis of the study by Hameed et al. [6]. In this study, Hameed et al. investigated the Vision Transformer (ViT) for skin cancer classification, highlighting its capacity to grasp intricate connections among picture components. Similarly, the ViT is combined with MobileNetV2 for skin cancer classification in [7]. The integration of ViT with MobileNetV2 exemplifies a hybrid strategy that optimizes performance while ensuring computational economy, rendering it appropriate for use in resource-limited settings. Specialized in brain tumor detection, Karthik et al. used a fusion of advanced methodologies for this purpose in [8]. The study utilized a combination of modern technologies in brain tumor detection to improve diagnosis accuracy. Subba and Sunaniya implemented an attention based GoogLeNet-style CNN to optimize brain tumor classification in [9]. They developed an attention-based GoogLeNet-style CNN that enhances categorization by concentrating on the most pertinent areas of the picture. A study of Sathya et al. employed Xception CNN through high-precision MRI analysis for brain tumor diagnosis in [10]. The Xception model was selected for its depthwise separable convolutions, which improve computing efficiency and precision. The methodology prioritizes the mitigation of demographic biases through the integration of various data and the establishment of bias detection systems. The ConvNext architecture is used to classify brain tumor grade in [11]. The study, utilized the ConvNext architecture to identify brain tumor grades, hence satisfying the essential requirement for accurate tumor grading in treatment planning. A ViT named as ViT-BT has been designed for classifying brain tumors in [12] and a mobile ViT model is presented in [13]. Similar to these studies, more studies can be found related to classification of medical images and also ViT based classification problems. In these studies, the Vision Transformer was specifically modified for brain tumor categorization, resulting in the creation of a dedicated ViT-BT model to enhance its efficacy for this purpose. A mobile-compatible ViT model was developed, integrating the sophisticated feature extraction abilities of transformers with lightweight, efficient processing for use in portable or resource-constrained environments. These publications together highlight the progression of deep learning in medical imaging, namely the transition from conventional CNNs to sophisticated architectures such as ViTs and their hybrid forms. They emphasize the use of attention processes and streamlined models, which improve accuracy while maintaining application in various clinical and real-world settings.

This paper introduces an innovative method for brain tumor diagnosis by combining ViTs with conventional machine learning classifiers. This research utilizes ViTs for feature extraction, distinguishing it from traditional approaches that depend exclusively on classical classifiers or CNNs, as ViT adeptly captures long-range correlations in pictures. It subsequently improves classification accuracy by integrating ViT-derived features with conventional classifiers like Decision Trees. The research demonstrated a significant increase in accuracy, increasing from 78.26% with ViT alone to 81.9% with a Tree classifier, illustrating the collaboration between sophisticated deep learning and traditional techniques. This hybrid method represents a substantial improvement in medical imaging, delivering a more reliable and precise diagnostic instrument for brain tumor identification. This study's originality stems from its revolutionary integration of ViTs with traditional machine learning classifiers to enhance the precision of brain tumor identification in MRI images. ViTs, originally developed for natural language processing, have lately been repurposed for computer vision applications, including medical imaging. Nonetheless, its independent use in tumor diagnosis frequently encounters difficulties in attaining maximum accuracy due to the restricted quantity and intricacy of medical datasets. This study mitigates these limitations by employing ViT for its robust capacity to capture long-range dependencies and complex visual patterns, while also extracting features from the ViT model to input into traditional classifiers such as Decision Trees, Naïve Bayes, and k-Nearest Neighbors. This dual-stage technique is innovative since it combines the representational capabilities of deep learning with the interpretability and simplicity of conventional machine learning models. The study indicates that ViT attains a baseline accuracy of 78.26%, while the incorporation of ViT-derived features with a Tree classifier enhances performance to 81.9%, resulting in a 3.64% improvement. This technique leverages the advantages of both paradigms—ViT for sophisticated feature extraction and traditional classifiers for effective and precise decision-making. By integrating these techniques, the study establishes a comprehensive and scalable framework for enhancing diagnostic precision, establishing a new standard for hybrid models in medical imaging. This concept improves tumor detection efficacy and demonstrates the possibility of combining contemporary and classic methods to address intricate challenges in healthcare.

This paper is organized in the following way. The materials and methods used in the study are presented in Section 2. Section 3 gives the case study with illustrations and the last section has the concluding remarks.

2. Materials and Methods

2.1. The Dataset

A malignant brain tumor is a potentially fatal disorder. Glioblastoma is the most common type of brain cancer in adults and has the worst prognosis, with a median survival of less than a year. The presence of a specific genetic sequence in the tumor known as MGMT promoter methylation is a good prognostic indicator and a strong predictor of treatment response. Currently, genetic analysis of cancer needs surgery to get a tissue sample. It may take many weeks to discover the genetic characterization of the tumor. Depending on the findings and the type of initial therapy chosen, more surgery may be required. If an accurate approach for predicting cancer genetics only by imaging (i.e., radiogenomics) could be developed, it could reduce the number of surgeries and modify the type of therapy required.

The dataset used is "Brain MRI Scan Images" and was downloaded from the Kaggle website [14]. The scanned images are divided into 2 subclasses to be used in tumor detection. These images are images exported from the RSNA-MICCAI Brain Tumor Competition. The dataset size is 7MB and consists of 2 subfolders as negative and positive. While there are 98 negative images, there are 129 positive images, a total of 227 Brain MRI images. The images are in 96 DPI resolution, 24-bit depth, the images are at least 200 pixels in width and height and jpg image format. The image format is jpg Positive/Negative MGMT status, used to label the tumor types. The dataset used in the study has a public license and is frequently used in the fields of medicine, cancer, computer vision free of charge and provides uninterrupted access and download. Two sample images from the dataset are shown in Fig. 1.

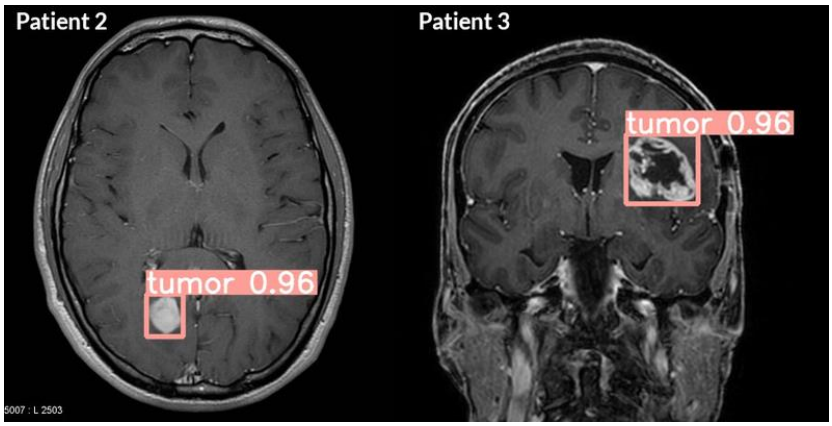

Figure 1: Sample images from the dataset.

2.2. The Vision Transformers

In 2022, the ViT emerged as a competitive alternative to CNNs, which are currently state-of-the-art in computer vision and thus widely used for various image recognition tasks. ViT models outperform the latest CNN technology by nearly four times in terms of computational efficiency and accuracy. Unlike traditional CNNs, which eliminate the need for manually crafted features, the ViT distinguishes itself by leveraging a self-attention mechanism to gather global contextual information from the entire image. This innovative approach involves dividing an input image into fixed-size patches, subjecting each patch to linear embeddings that transform them into high-dimensional vectors, and then processing these vectors through a transformer encoder. This methodology empowers ViT with the ability to skillfully capture complex long-range dependencies and subtle relationships between different regions of the image.

In this study, a pre-trained ViT neural network will be used for the classification of brain MRI images. The model utilizes a transformer architecture to encode image inputs into feature vectors. The network consists of two main components: the backbone and the head. The backbone is responsible for the encoding step, where it takes input images and extracts feature vectors. The head is responsible for making predictions by mapping the encoded feature vectors to prediction scores. By employing transfer learning, the model can be fine-tuned for better performance on specific tasks. The block diagram of the ViT network is illustrated in Fig. 2 [15].

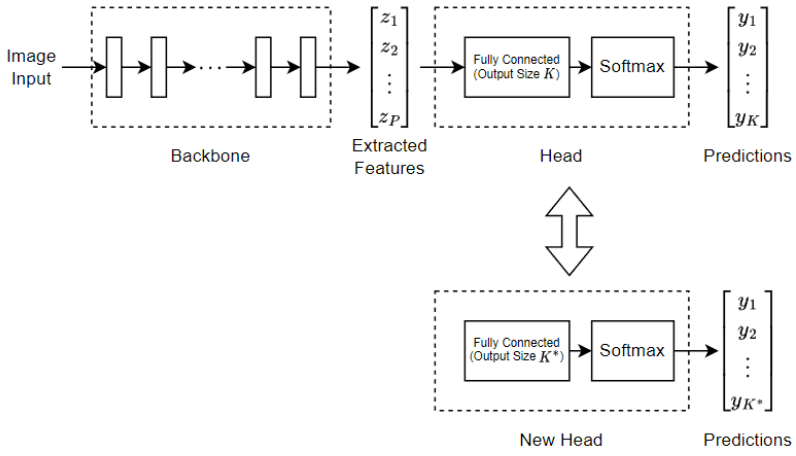

Figure 2: The block diagram of the ViT network.

This diagram outlines the architecture of a ViT network that makes predictions for K classes and illustrates how the network is structured to enable transfer learning for a new dataset with K classes. ViTs represent a revolutionary architecture in computer vision, using the ideas of the Transformer model—originally designed for natural language processing (NLP)—to interpret visual information. ViTs analyze pictures by segmenting them into fixed-size patches, typically

16x16 pixels, and using each patch as a token, similar to words in natural language processing tasks. The patches are flattened and linearly inserted into a fixed-dimensional space, with positional encodings used to preserve spatial information. The Transformer encoder, central to ViTs, employs self-attention processes to represent global interactions across patches, enabling the network to successfully capture long-range dependencies and contextual characteristics. In contrast to CNNs, which depend on localized operations, ViTs are proficient at collecting global context, especially when trained on extensive datasets. Nonetheless, their quadratic complexity in self-attention renders them computationally demanding for high-resolution photos. To address this, versions like as Swin Transformers implement hierarchical structures and localized self-attention, enhancing computing efficiency. Hybrid models integrate the advantages of CNNs and ViTs by employing convolutional layers for preliminary feature extraction before transmitting data to Transformer layers. Mobile ViTs tackle the issue of resource use, facilitating implementation on edge devices. Notwithstanding their benefits, ViTs are data-intensive, sometimes necessitating considerable pretraining on large datasets like ImageNet or JFT-300M to achieve optimal performance. In the absence of such resources, their performance may be inferior to that of CNNs, which are intrinsically more efficient with smaller datasets. Nevertheless, ViTs exhibit exceptional scalability and adaptability, rendering them suitable for a range of vision applications, such as image classification, object identification, medical image analysis, and video comprehension. Their applicability is expanding, with research aimed at enhancing computing efficiency and versatility.

It would be comprehensive to include information about how the components of the ViTs model contribute to the model performance. The Backbone in a deep learning model refers to the feature extraction component. This module processes input data, such as an image, and extracts both low- and high-level features that are subsequently used by other parts of the model. In ViTs, the backbone is built on the Transformer architecture. Unlike traditional convolutional neural networks (CNNs), ViTs divide visual input into patches and process each patch as a vector. These vectors are then analyzed using the Transformer model's attention mechanism, making it a unique method for feature extraction. In detail:

- **Input Images and Patches**: ViT segments an image into fixed-size patches. For example, an image of size 224x224 can be divided into 16x16 patches, with each patch converted into a vector.
- **Patch Embeddings**: Each patch is transformed into a vector and serves as input for the Transformer model.

- **Transformer Encoder**: These patch vectors are processed by the encoder in ViT, which leverages the attention mechanism to understand the context of each patch, thereby extracting higher-level features.

In summary, the backbone provides the foundational structure for extracting meaningful features from visual data. The Head module represents the inference component of the model. It transforms the features extracted by the backbone into a final output. In ViT, the head module typically performs the following steps:

- **Pooling and Classification**: Features from the backbone are aggregated and formatted for final classification, often using global average pooling or a Multi-Layer Perceptron (MLP).
- **Result Generation**: The output is tailored for specific tasks, such as classification, regression, or other objectives. For instance, in image classification, the head module predicts the class of the input image.

ViT commonly uses a single "class token" in its head module, which combines the representations of all patches for classification. This process is carried out using the attention mechanism typical of Transformer architectures.

Functions of the Backbone and Head Modules

- **Backbone**: Extracts and transforms features from the image into meaningful high-level representations.
- **Head**: Utilizes these features to perform specific tasks, such as classification.

In summary:

- The **Backbone** processes visual data and extracts features in a format that the model can understand.
- The **Head** uses these features to produce the final output, such as a class prediction.

Together, these two components form the core structure of Google's Vision Transformer, playing a crucial role in processing visual data and generating accurate predictions. In traditional artificial intelligence models, performance augmentation techniques are often employed in the literature by extracting features from the model post-training, prior to the classification layer, and utilizing alternative classifiers instead of the network's classifier. This study utilized the

characteristics from the head layer of the ViT network post-training, employing classical classifiers for classification.

The ViTs represents a notable advancement in deep learning and image processing, presenting distinct benefits while encountering certain limits. In contrast to conventional CNNs, ViT obviates the necessity for convolutional layers by employing the Transformer architecture, hence offering a more adaptable and generalizable framework for visual applications. By modifying the Transformer, first created for natural language processing, for visual input, ViT acquires a more profound comprehension of contextual relationships inside pictures. The attention mechanism proficiently captures long-range dependencies, accurately representing the links between distant components in a picture. Moreover, ViT provides versatility in data preprocessing and network architecture, enabling the modification of patch dimensions and attention techniques. It excels on extensive datasets, such as ImageNet, frequently attaining elevated accuracy rates. Nonetheless, ViT possesses some restrictions. Its dependence on attention processes and a substantial number of parameters renders it computationally demanding, necessitating robust hardware such as GPUs or TPUs and extended training durations. The large number of parameters leads to prolonged and more resource-demanding training. Another difficulty is its inferior performance on tiny datasets, as CNNs frequently surpass ViT. To get optimal outcomes with constrained data, ViT generally necessitates methodologies such as pre-trained models or data augmentation. In our work utilizing a dataset of 227 brain MRI images, we employed transfer learning to address these problems. This method increased the model's accuracy to 81.9%, illustrating the efficacy of transfer learning in augmenting ViT's performance with limited datasets. In conclusion, although ViT presents revolutionary advancements in image processing, its efficacy is contingent upon the accessibility of computing resources and extensive datasets. However, methods like transfer learning can alleviate its shortcomings, rendering it an effective instrument for visual analytic tasks.

3. Results

80% of the dataset is used for training, while 20% is strictly reserved for test data that is not involved in the training process. The scanned images in the dataset are scaled and normalized to a uniform size of 384x384x3 and treated as colored images during both the training and testing phases. The training parameters are determined as Mini Batch Size = 16, Max Epochs = 5, Iterations Per Epoch = 11 and Validation Frequency = 3. This study utilized hyperparameter values commonly seen in the literature. The MiniBatchSize was set at 16, and the MaxEpochs was established at 5. These options are typically used due to their efficacy in training machine learning models. The IterationsPerEpoch value was computed as the estimated ratio of the entire

dataset size utilized for training divided by the MiniBatchSize. The ValidationFrequency values were determined by dividing the IterationsPerEpoch by the MaxEpochs, resulting in a framework where validation steps are evenly distributed throughout the training phase. The model's performance was consistently assessed throughout and following the training process. The selection of these hyperparameters seeks to enhance the efficiency of the training process as well as the validation and generalization performance of the model.

The training of the network utilized Stochastic Gradient Descent with Momentum (SGDM) as the optimizer, employing a stochastic solver. Parallel computing was leveraged on a graphics card, with 16 parallel workers running simultaneously to accelerate the training process. The remaining training parameters are InitialLearnRate = 1e-4, Shuffle = every-epoch and ExecutionEnvironment = parallel. The specifications of the computer used in the experiment are listed in Table 1.

Table 1: Specifications of the computer used in the experiment.

Processor	12th Gen Intel(R) Core(TM) i9-12900F 2.40 GHz
Cores, Processors	16, 24
Installed RAM	64.0 GB (63.7 GB usable)
GPU	NVIDIA RTX A4000
DirectX version	12 (FL 12.1)
GPU Memory	47.9 GB (16.0 GB Dedicated, 31.9 GB Shared)
SSD Capacity	477 GB

The training process was completed in 26 minutes and 3 seconds. Training accuracy was achieved as 0.7826. Fig. 3 gives the confusion matrix obtained.

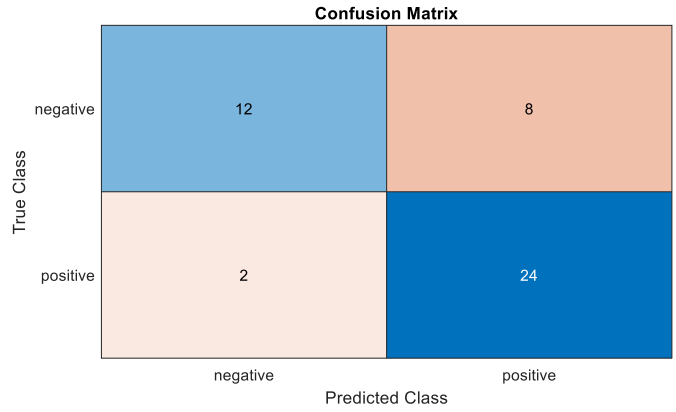

Figure 3: The confusion matrix.

Upon examining the Confusion Matrix, it is observed that out of 46 test samples, 20 are negative and 26 are positive images. Among the negative images, 12 were correctly predicted, while 8 were misclassified. Similarly, out of 26 positive images, 24 were accurately predicted.

The progress of training iterations, the duration of each iteration, mini-batch performance, test performance, and errors are presented in Table 2.

Table 2: Training iterations.

Epoch	Iteration	Time Elapsed (hh:mm:ss)	Mini-batch Accuracy	Validation Accuracy	Mini-batch Loss	Validation Loss
1	1	00:00:36	31.25%	47.83%	2.6602	1.1102
1	3	00:01:36	43.75%	56.52%	2.1689	1.1805
1	6	00:03:07	75.00%	56.52%	0.7524	0.9590
1	9	00:04:32	50.00%	63.04%	2.2467	1.0096
2	12	00:06:00	50.00%	63.04%	1.3735	0.6843
2	15	00:07:23	37.50%	58.70%	2.3455	0.9527
2	18	00:08:45	81.25%	76.09%	0.3105	0.5432
2	21	00:10:15	75.00%	58.70%	1.1402	1.4605
3	24	00:11:40	87.50%	71.74%	0.4229	0.6494
3	27	00:13:02	62.50%	60.87%	1.8355	0.9578
3	30	00:14:25	68.75%	89.13%	1.8386	0.4378
3	33	00:15:51	62.50%	89.13%	0.9929	0.4451
4	36	00:17:12	81.25%	65.22%	0.5713	0.8979
4	39	00:18:34	87.50%	80.43%	0.6988	0.4610
4	42	00:19:59	56.25%	89.13%	1.3256	0.4217
5	45	00:21:21	81.25%	60.87%	0.6538	1.0530
5	48	00:22:45	75.00%	71.74%	0.5961	0.5908
5	50	00:23:38	62.50%		2.0322	
5	51	00:24:08	93.75%	80.43%	0.1706	0.4489
5	54	00:25:31	93.75%	73.91%	0.1351	0.6625
5	55	00:26:01	68.75%	78.26%	0.6194	0.5166

It would be useful to enlighten the meanings of the above training parameters. An Epoch signifies a full traversal of the whole training dataset. This is a quantitative measure of the number of instances the model has encountered the complete dataset throughout the training process. During each epoch, the dataset is partitioned into smaller segments known as mini-batches, and the model is modified iteratively for each mini-batch. These updates are termed Iterations, and the quantity of iterations per epoch is contingent upon the batch size and the dataset size. The Time Elapsed (hh:mm:ss) captures the total duration since the commencement of training, facilitating the assessment of training efficiency and progress over time. It is very beneficial for predicting the completion time of the instruction. Mini-batch Accuracy evaluates the model's performance on the current mini-batch during training, offering a rapid yet localized assessment of its predictive capability. Validation Accuracy assesses the model's performance on a distinct validation set post-epoch, indicating its capacity to generalize to novel data. Loss values are also essential. Mini-batch Loss measures the model's mistake on the current mini-batch during training, informing the necessary adjustments to the model's weights. The validation loss, computed post-epoch, reflects the model's performance on the validation dataset. If the validation loss ceases to decline or starts to rise while the training loss continues to fall, it may indicate

overfitting. Monitoring these variables collectively offers an extensive perspective on the training process, facilitating the prompt identification of problems such as overfitting, underfitting, or ineffective training.

The training and the error visualities are given in Fig. 4. As seen in the figure, the test accuracy of the training process using the ViT network reached 78.26%. Before passing through the classification layer, the dataset's training features were extracted and classified using classical classifiers such as Tree, Discriminant Analysis, SVM, KNN, and others.

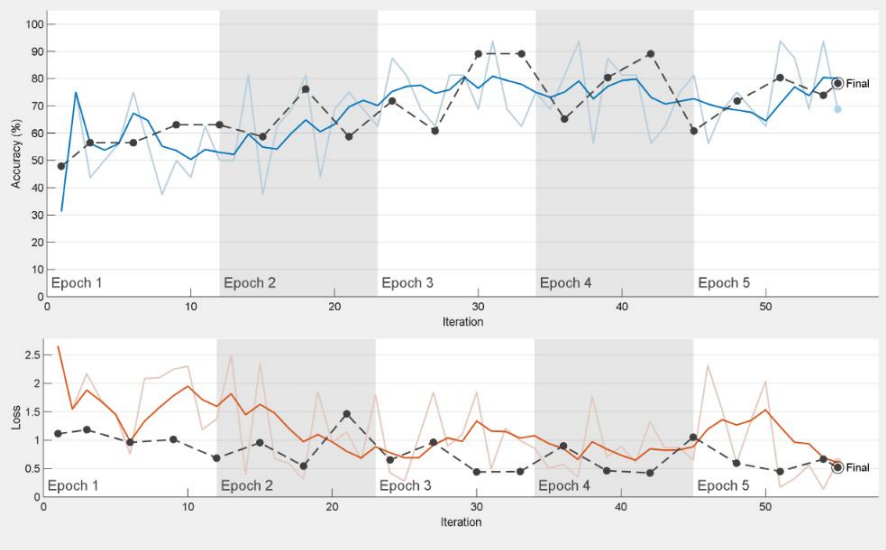

Figure 4: The training and the error graphs.

The classification results are shown in Table 3. Upon reviewing the results, the accuracy increased to 81.9%, representing a 3.64% improvement compared to the standard training performance.

Table 3: Top 12 accuracies of classical classifiers.

No	Models	Sub Models	Accuracy (%)
1	Tree	Coarse Tree	81.9%
2	Quadratic Discriminant	Quadratic Discriminant	81.9%
3	Navie Bayes	Gaussian Naïve Bayes	81.9%
4	Navie Bayes	Kernek Navie Bayes	81.9%
5	KNN	Medium KNN	81.5%
6	Ensemble	Subspace Discriminant	81.5%
7	Binary GLM Logistic Regression	Binary GLM Logistic Regression	81.1%
8	Efficient Linear SVM	Efficient Linear SVM	81.1%
9	SVM	Linear SVM	81.1%
10	SVM	Medium Gaussian SVM	81.1%
11	Linear Discriminant	Linear Discriminant	80.6%
12	SVM	Quadric SVM	80.6%

Similarly, when examining the confusion matrix for the classical classifier that achieved the highest performance given in Fig. 6, it is observed that out of 227 training and test samples—the entire dataset—98 are negative and 129 are positive images. Among the negative images, 76 were correctly predicted, while 22 were misclassified. Similarly, out of 129 positive images, 110 were accurately predicted.

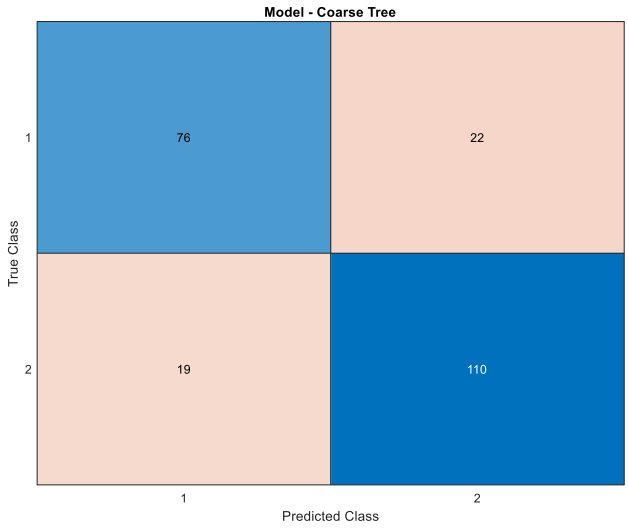

Figure 5: Coarse tree confusion matrix.

Figure 6 shows the prediction distribution of the classical classifier that achieved the highest performance. This distribution illustrates how the model predicted across different classes, highlighting the frequency of correct and incorrect predictions for both the positive and negative samples. The visualization provides insights into the classifier's overall accuracy and the balance between true positives, false positives, true negatives, and false negatives.

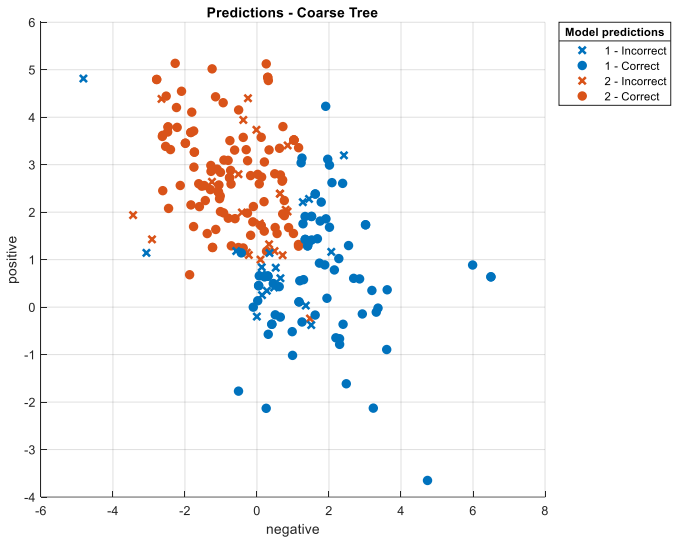

Figure 6: Coarse tree predictions.

Hence, the success of the proposed method is shown.

4. Conclusion

The field of medical imaging has witnessed substantial progress in brain tumor detection, primarily driven by advancements in machine learning and deep learning algorithms. Traditional classifiers like Support Vector Machines, Decision Trees, and k-Nearest Neighbors, when combined with effective feature extraction techniques, have demonstrated promising results in identifying tumors from MRI scans. Recent research has consistently highlighted the efficacy of these classical classifiers in analyzing extracted features from MRI images, leading to enhanced diagnostic capabilities. Feature extraction, a pivotal step in the classification process, plays a crucial role in optimizing the performance of these models.

ViT, a groundbreaking development in medical imaging and tumor detection, has emerged as a powerful tool. Leveraging the transformer architecture, which has proven highly effective in natural language processing, ViT enables the efficient processing of visual data. This approach facilitates the capture of long-range dependencies within images, empowering the model to discern intricate patterns associated with brain tumors. Numerous studies have validated the effectiveness of ViT in various classification tasks, including medical imaging. In our research, the ViT network achieved a classification accuracy of 78.26% on the given dataset. To further enhance tumor detection performance, we extracted features from the ViT network and fed them to classical classifiers. Notably, the Decision Tree classifier exhibited an impressive accuracy of 81.9% when utilizing these extracted features.

In conclusion, the classification of brain MRI images using ViT presents a novel approach that seamlessly integrates the strengths of deep learning and traditional machine learning methods. By combining the powerful feature extraction capabilities of deep learning models with the effective classification techniques of classical classifiers, this approach offers a promising avenue for improving the accuracy and reliability of brain tumor detection.

References

[1] Amin, J., Sharif, M., Haldorai, A., Yasmin, M., Nayak, R. S., *Brain tumor detection and classification using machine learning: a comprehensive survey*, Complex & intelligent systems, 8(4), 3161-3183, 2022.

[2] Ali, H., Biswas, M. R., Mohsen, F., Shah, U., Alamgir, A., Mousa, O., Shah, Z., *The role of generative adversarial networks in brain MRI: a scoping review*, Insights into imaging, 13(1), 98, 2022.

[3] Khan, A., Rauf, Z., Sohail, A., Khan, A. R., Asif, H., Asif, A., Farooq, U., *A survey of the vision transformers and their CNN-transformer based variants*, Artificial Intelligence Review, 56 (Suppl 3), 2917-2970, 2023.

[4] Elbedoui, K., Mzoughi, H., Slima, M. B., *Deep Learning Approaches for Dermoscopic Image-Based Skin Cancer Diagnosis*, In 2024 IEEE 7th International Conference on Advanced Technologies, Signal and Image Processing (ATSIP) 1, 1-7, 2024.

[5] Mejri, S., Oueslati, A. E., *Dermoscopic Images Classification Using Pretrained VGG-16 and ResNet-50 Models*, IEEE 7th International Conference on Advanced Technologies, Signal and Image Processing, 1, 342-347, 2024.

[6] Hameed, M., Zameer, A., Raja, M. A. Z., *A Comprehensive Systematic Review: Advancements in Skin Cancer Classification and Segmentation Using the ISIC Dataset*, Computer Modeling in Engineering & Sciences, 140(3), 2024

[7] Kumar, M. R., Priyanga, S., Anusha, J. S., Chatiyode, V., Santiago, J., Revathi, P., *Synergistic Skin Cancer Classification: Vision Transformer alongside MobileNetV2*, 4th International Conference on Intelligent Technologies, 1-7, 2024.

[8] Karthik, A., Sahoo, S. K., Kumar, A., Patel, N., Chinnaraj, P., Maguluri, L. P., Rajaram, A., *Unified approach for accurate brain tumor Multi-Classification and segmentation through fusion of advanced methodologies*, Biomedical Signal Processing and Control, 100, 106872, 2025.

[9] Subba, A. B., Sunaniya, A. K., *Computationally optimized brain tumor classification using attention based GoogLeNet-style CNN*, Expert Systems with Applications, 125443, 2024.

[10] Sathya, R., TR, M., Bhatia Khan, S., Malibari, A. A., Asiri, F., *Employing Xception Convolutional Neural Network through High-Precision MRI Analysis for Brain Tumor Diagnosis,* Frontiers in Medicine, 11, 1487713, 2024.

[11] Mehmood, Y., Bajwa, U. I., *Brain tumor grade classification using the ConvNext architecture,* Digital Health, 10, 20552076241284920, 2024.

[12] Ali Al-Hamza, K., *ViT-BT: Improving MRI Brain Tumor Classification Using Vision Transformer with Transfer Learning*. Available at SSRN, http://dx.doi.org/10.2139/ssrn.4959261, 2024.

[13] Odusami, M., Damasevicius, R., Milieskaite-Belousoviene, E., Maskeliunas, R., *Multimodal Neuroimaging Fusion for Alzheimer's Disease: An Image Colorization Approach with Mobile Vision Transformer*, International Journal of Imaging Systems and Technology, 34(5), e23158, 2024.

[14] https://www.kaggle.com/datasets/volodymyrpivoshenko/brain-mri-scan-images-tumor-detection, Last Accesed in 10.10.2024.

[15] https://www.mathworks.com/help/deeplearning/ug/train-vision-transformer-network-for-image -classification.html, Last Accessed in 10.10.2024.

Adıyaman University Journal of Science
https://dergipark.org.tr/en/pub/adyujsci
DergiPark AKADEMİK
ISSN 2147-1630
e-ISSN 2146-586X

On Solution of Complex Equations with the Homotopy Perturbation Method

Murat DÜZ[1,*], Şeyda ÇAMLICA[2]

[1]*Karabük Üniversitesi, Faculty of Sciences, Department of Mathematics,78050, Karabük, Turkey*
mduz@karabuk.edu.tr, ORCID:0000-0003-2387-4045
[1]*Karabük Üniversitesi, Faculty of Sciences, Department of Mathematics,78050, Karabük, Turkey*
sydcmlc@hotmail.com, ORCID:0000-0002-0419-17780

Received: 16.05.2024 **Accepted:** 27.11.2024 **Published:** 31.12.2024

Abstract

In this study, complex differential equations are solved using the homotopy perturbation method (HPM). Firstly, we separated the real and imaginary parts of the equation. Thus, from one unknown equation is obtained two unknown equation systems. Later, we applied HPM real and imaginary to parts of the equation. So, we have obtained real and imaginary parts of the solution.

Keywords: Homotopy perturbation method; Complex equations; Equation system.

Homotopi Pertürbasyon Metodu ile Kompleks Denklemlerin Çözümü Üzerine

Öz

Bu çalışmada kompleks denklemler homotopi pertürbasyon metodu(HPM) kullanılarak çözüldü. İlk önce denklemi reel ve imajiner kısımlarına ayırdık. Böylece bir bilinmeyenli

* Corresponding Author DOI: 10.37094/adyujsci.1484685

denklemden iki bilnmeyenli denklem sistemi elde edildi. Daha sonra HPM'yi denklemin reel ve imajiner kısımlarına uyguladık. Böylece çözümün reel ve imajiner kısımlarını elde ettik.

Anahtar Kelimeler: Homotopi pertürbasyon metodu; Kompleks denklemler; Denklem sistemi.

1. Introduction

General solutions of some equations in real space can't be found. For example,

$$U_{xx} + U_{yy} = 0 \tag{1}$$

Laplace equation hasn't got the general solution in R^2. But

$$U_{z\bar{z}} = 0 \tag{2}$$

which is equivalent to (1) Laplace equation has got the general solution in complex space, and the solution of (2) is

$$U = f(z) + g(\bar{z}) \tag{3}$$

The most basic works in the theory of complex differential equations are "Theory of Pseudo Analytic Functions" which is written by L. Bers [1] and "Generalized Analytic Functions" which is written by I, N. Vekua [2]. There are studies related to the solution of complex differential equations. For example, complex differential equations of Lane Emden type have been solved by the differential transformation method [3]. In addition, there are studies related to approximate solutions of linear complex differential equations [4-5].

In this study, we solved the first-order constant coeffients complex differential equations with HPM. Such equations have previously been solved by integral transformations such as laplace, fourier, elzaki, and a relation for the solution has been obtained [6-8]. In addition, such equations were solved using the variational iteration method and an iteration relation was obtained [9]. In addition, linear complex differential equations with variable coefficients from the first order were solved by the adomian decomposition method and an iteration relation was obtained [10].

Many methods can be used to solve linear equations, but some of them can't be applied to the solutions of the most nonlinear equations. This situation has led us to approximate methods of finding solutions for nonlinear equations. Various numerical and analytical approach methods have been developed for such equations. Some of them are the Variational Iteration Method,

Adomain Decomposition Method, Homotopy Perturbation Method, and Differential Transform Method. HPM is a mathematical method used to solve linear and nonlinear equations. The HPM, first proposed by Dr. Ji Huan He, has successfully been applied to solve many types of linear and nonlinear functional equations. This method, which is a combination of homotopy in topology and classic perturbation techniques, provides us with a convenient way to obtain analytic or approximate solutions for a wide variety of problems arising in different fields. This method which is used in the solution of many linear and nonlinear ordinary and partial differential equations used in the fields of engineering, physics, applied mathematics, and quantum mechanics [11-17]. In addition, this method is also used in the field of environmental events and health [18-20]. In article [21], it has been shown that the Taylor series expansion is the same as the HPM with particular choices of the auxiliary parameters.

This paper has been organized as follows. In Section 2.1, we have mentioned the homotopy perturbation method. In Section 2.2, we have given a theorem associated with the solution of complex equations by using HPM. Moreover, we have provided some examples of the validity of the method.

2. Materials and Methods

2.1. Homotopy Perturbation Method

To illustrate the basic ideas of the method, we consider the following nonlinear differential equation

$$Au + f(r) = 0, \quad r \in \Omega \tag{4}$$

with boundary conditions

$$B\left(u, \frac{\partial u}{\partial n}\right) = 0,$$

where A is a general differential operator, B is a boundary operator, $f(r)$ is a known analytic function. The operator A can, generally speaking, be divided into two parts L and N, where L is linear, while N is nonlinear. Therefore, Eq. (4) can be rewritten as follows:

$$Lu + Nu - f(r) = 0 \tag{5}$$

The linear term is decomposed into $L + R$, where L is the highest order differential operator and R is the remainder of the linear operator. Thus the equation can be written

$$Ly + Ry + Ny = g(x) \tag{6}$$

where Ny represents the nonlinear terms. The equation type which we have investigated is linear, since there is not nonlinear term $Ny = 0$. Therefore, Eq. (6) can be written as:

$$Ly + Ry = g(x). \tag{7}$$

Let we apply HPM to the Eq. (7).

$$Ly = g(x) - p.Ry \tag{8}$$

where p is artificial parameter. The artificial parameter method assumes that the approximation of Eq. (8) can be expressed as a series of the power of p, i.e.

$$y = y_0 + py_1 + p^2y_2 + \cdots \tag{9}$$

When $p \to 1$, Equality (9) corresponds to the approximate solution of Eq. (7).

2.2. Solution of Complex Equations with HPM

In this section, we will study the solution of complex equations from the first order with HPM. Firstly, let us give complex derivatives equality from kind real derivatives.

Definition 1: Let $w = w(z, \bar{z})$ be a complex function. Here $z = x + iy$, $w(z, \bar{z}) = u(x, y) + iv(x, y)$. First order derivatives according to z and $\bar{z}$ of $w(z, \bar{z})$ are defined as follows:

$$\frac{\partial w}{\partial z} = \frac{1}{2}\left(\frac{\partial w}{\partial x} - i\frac{\partial w}{\partial y}\right), \frac{\partial w}{\partial \bar{z}} = \frac{1}{2}\left(\frac{\partial w}{\partial x} + i\frac{\partial w}{\partial y}\right) \tag{10}$$

Theorem 1: Let A, B, C are real constants, $F(z, \bar{z})$ is a polynomial of $z, \bar{z}$ and $w = u + iv$ is a complex function. Then the solution of

$$A\frac{\partial w}{\partial z} + B\frac{\partial w}{\partial \bar{z}} + Cw = F(z, \bar{z}) \tag{11}$$

$$w(x, 0) = f(x) \tag{12}$$

is given as:

$$w(z,\bar{z}) = u(x,y) + iv(x,y) = \sum_{n=0}^{\infty} \left(u_n(x,y) + iv_n(x,y)\right)$$

$$u_{n+1} = \int \left(\frac{(A+B)\frac{\partial v_n}{\partial x} + 2Cv_n}{A-B} \right) dy$$

$$v_{n+1} = \int \left(\frac{(A+B)\frac{\partial u_n}{\partial x} + 2Cu_n}{B-A} \right) dy$$

$$u_0 = f(x), v_0 = 0$$

Proof: We can obtain the following equality in (11) using (10) equality.

$$A\frac{1}{2}\left(\frac{\partial w}{\partial x} - i\frac{\partial w}{\partial y}\right) + B\frac{1}{2}\left(\frac{\partial w}{\partial x} + i\frac{\partial w}{\partial y}\right) + Cw = F(z,\bar{z}). \tag{13}$$

If we write $w = u + iv$ in (13), then following equality is obtained.

$$A\left[\frac{\partial u}{\partial x} + i\frac{\partial v}{\partial x} - i\left(\frac{\partial u}{\partial y} + i\frac{\partial v}{\partial y}\right)\right] + B\left[\frac{\partial u}{\partial x} + i\frac{\partial v}{\partial x} + i\left(\frac{\partial u}{\partial y} + i\frac{\partial v}{\partial y}\right)\right] + 2C(u+iv)$$
$$= 2F_1(x,y) + 2iF_2(x,y)$$

If we seperate (13) as real and imaginer parts, then following equation system is obtained

$$(A+B)\frac{\partial u}{\partial x} + (A-B)\frac{\partial v}{\partial y} + 2Cu = 2F_1(x,y)$$

$$(A+B)\frac{\partial v}{\partial x} + (B-A)\frac{\partial u}{\partial y} + 2Cv = 2F_2(x,y)$$

$$\frac{\partial v}{\partial y} = \frac{2F_1(x,y) - (A+B)\frac{\partial u}{\partial x} - 2Cu}{A-B}$$

$$\frac{\partial u}{\partial y} = \frac{2F_2(x,y) - (A+B)\frac{\partial v}{\partial x} - 2Cv}{B-A}$$

Now let's apply the homotopy perturbation technique.

$$\frac{\partial v}{\partial y} = \frac{2F_1(x,y)}{A-B} - p\frac{(A+B)\frac{\partial u}{\partial x} + 2Cu}{A-B}$$

$$\frac{\partial u}{\partial y} = \frac{2F_2(x,y)}{B-A} - p\frac{(A+B)\frac{\partial v}{\partial x} + 2Cv}{B-A}$$

where $u = u_0 + pu_1 + p^2u_2 + \cdots$ and $v = v_0 + pv_1 + p^2v_2 + \cdots$

In these equalities, we equal to coeffients of the same powers of p then we get the following equalities.

$$u_0 = \int \frac{2F_2(x,y)}{B-A}dy + f(x)$$

$$v_0 = \int \frac{2F_1(x,y)}{A-B}dy$$

$$\frac{\partial v_{n+1}}{\partial y} = \frac{(A+B)\frac{\partial u_n}{\partial x} + 2Cu_n}{B-A}$$

$$\frac{\partial u_{n+1}}{\partial y} = \frac{(A+B)\frac{\partial v_n}{\partial x} + 2Cv_n}{A-B}$$

$$\frac{\partial u_1}{\partial y} = p\left[\frac{(A+B)\frac{\partial v_0}{\partial x} + 2Cv_0}{A-B}\right]$$

$$\frac{\partial v_1}{\partial y} = p\left[\frac{(A+B)\frac{\partial u_0}{\partial x} + 2Cu_0}{B-A}\right]$$

$$\frac{\partial u_2}{\partial y} = p\left[\frac{(A+B)\frac{\partial v_1}{\partial x} + 2Cv_1}{A-B}\right]$$

$$\frac{\partial v_2}{\partial y} = p\left[\frac{(A+B)\frac{\partial u_1}{\partial x} + 2Cu_1}{B-A}\right]$$

⋮

$$\frac{\partial u}{\partial y}=\frac{2F_2(x,y)}{B-A}+p\left[\frac{(A+B)\frac{\partial v_0}{\partial x}+2Cv_0}{A-B}\right]+p\left[\frac{(A+B)\frac{\partial v_1}{\partial x}+2Cv_1}{A-B}\right]+\cdots$$

$$=\frac{2F_2(x,y)}{B-A}+p\sum_{n=0}^{\infty}\frac{(A+B)\frac{\partial v_n}{\partial x}+2Cv_n}{A-B}$$

$$\frac{\partial v}{\partial y}=\frac{2F_1(x,y)}{A-B}+p\left[\frac{(A+B)\frac{\partial u_0}{\partial x}+2Cu_0}{B-A}\right]+p\left[\frac{(A+B)\frac{\partial u_1}{\partial x}+2Cu_1}{B-A}\right]+\cdots$$

$$=\frac{2F_1(x,y)}{A-B}+p\sum_{n=0}^{\infty}\frac{(A+B)\frac{\partial u_n}{\partial x}+2Cu_n}{B-A}$$

$$u(x,y)=\int\left[\frac{2F_2(x,y)}{B-A}+p\sum_{n=0}^{\infty}\frac{(A+B)\frac{\partial v_n}{\partial x}+2Cv_n}{A-B}\right]dy+f(x)$$

$$v(x,y)=\int\left[\frac{2F_1(x,y)}{A-B}+p\sum_{n=0}^{\infty}\frac{(A+B)\frac{\partial u_n}{\partial x}+2Cu_n}{B-A}\right]dy$$

Example 1: [10] Solve the following problem

$$4\frac{\partial w}{\partial z}+\frac{\partial w}{\partial \bar{z}}=0$$

with the condition $w(x,0)=-\frac{1}{3x}$.

Solution: Clearly the coefficients of equation which are as follows

$$A=4,B=1,C=0,F=0$$

$$u_0=-\frac{1}{3x},v_0=0$$

$$u_1=0,\frac{\partial v_1}{\partial y}=-\frac{5}{3}p\frac{1}{3x^2},v_1=-\frac{5yp}{9x^2}$$

$$v_2=0,\frac{\partial u_2}{\partial y}=\frac{5}{3}p\left(\frac{10yp}{9x^3}\right),u_2=\frac{25y^2p^2}{27x^3}$$

$$u_3 = 0, v_3 = \frac{125p^3y^3}{81x^4}$$

$$\vdots$$

$$v_{2n} = 0, u_{2n} = \frac{(-1)^{n-1}(5yp)^{2n}}{(3x)^{2n+1}}, v_{2n+1} = \frac{(-1)^{n-1}(5yp)^{2n+1}}{(3x)^{2n+1}}$$

$$w(z,\bar{z}) = \lim_{p\to 1}\sum_{n=0}^{\infty}(u_n + iv_n) = \lim_{p\to 1}(u_0 + iv_0 + u_1 + iv_1 + u_2 + iv_2 + \cdots)$$

$$= -\frac{1}{3x} - \frac{5iy}{9x^2} + \frac{25y^2}{27x^3} + \frac{125iy^3}{81x^4} + \cdots = \frac{-\frac{1}{3x}}{1 - \frac{5iy}{3x}} = \frac{1}{5iy - 3x} = \frac{1}{z - 4\bar{z}}$$

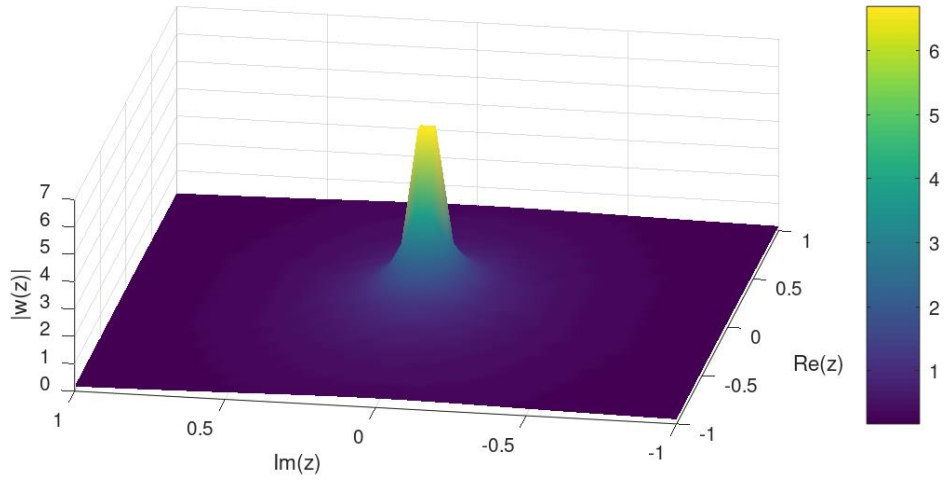

Figure 1: Graph of the absolute value of $w(z,\bar{z}) = \frac{1}{z-4\bar{z}}$ when the real and imaginary parts of z are in the range [-1,1].

Example 2: [6] Solve the following problem

$$2\frac{\partial w}{\partial z} - \frac{\partial w}{\partial \bar{z}} = 4z + 1$$

with the condition

$$w(x,0) = x^2 + 5x.$$

Solution:

The coefficients of equation which are $A = 2, B = -1, C = 0$ and $F(z,\bar{z}) = 4z + 1 = 4x + 1 + 4iy$

$$u_0 = x^2 + 5x + \int \frac{8y}{-3} dy = x^2 + 5x - \frac{4y^2}{3}, v_0 = \int \frac{8x+2}{3} dy = \frac{8xy+2y}{3}$$

$$u_1 = p\frac{4y^2}{9}, v_1 = -\frac{1}{3}p(2xy + 5y)$$

$$u_2 = -\frac{1}{9}p^2y^2, v_2 = 0$$

$$u_n = v_n = 0 \ (n \geq 3)$$

$$w(z,\bar{z}) = \lim_{p\to 1} \sum_{n=0}^{\infty} (u_n + iv_n) = \lim_{p\to 1} (u_0 + iv_0 + u_1 + iv_1 + u_2 + iv_2 + \cdots)$$

$$= x^2 + 5x - \frac{4y^2}{3} + i\frac{8xy+2y}{3} + \frac{4y^2}{9} - \frac{1}{3}i(2xy + 5y) - \frac{1}{9}y^2$$

$$= x^2 - y^2 + 2ixy + 3(x - iy) + 2(x + iy) = z^2 + 3\bar{z} + 2z.$$

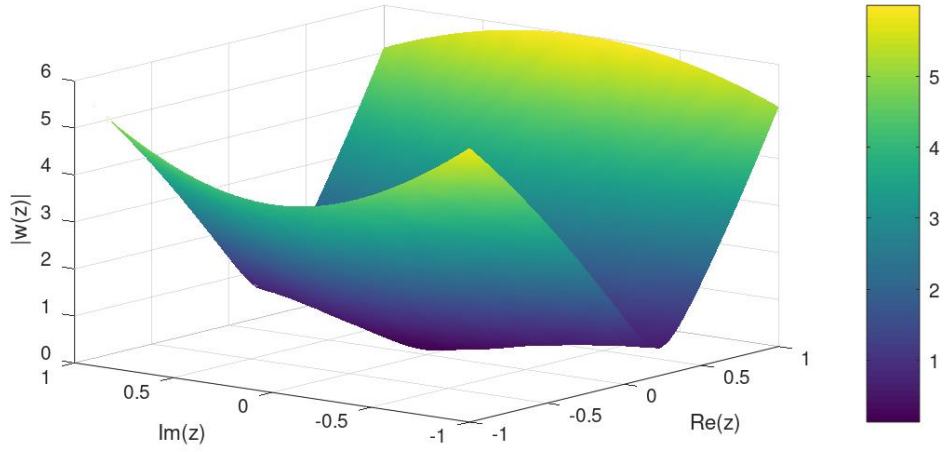

Figure 2: Graph of the absolute value of $w(z,\bar{z}) = z^2 + 3\bar{z} + 2z$ when the real and imaginary parts of z are in the range [-1,1].

3. Results and Discussion

In this study, we have studied solutions of first order with constant coefficients complex partial differential equations by using HPM. We know that such equations can be solved by the lagrange system used for semi-linear equations from the first order. Our aim is that an alternative approach solution is obtained for such equations by using HPM. We applied the iteration relation on two samples. In the first example, an infinite geometric series was obtained, and the solution

was reached. In the second example, it was seen that all terms after the fourth iteration were zero and thus a solution in the form of polynomials. The results obtained are consistent with the literature.

4. Conclusion

In this study, it is thought that the iteration relationship obtained for the solution of first-order complex equations with constant coefficients can also be obtained for higher-order equations with constant and variable coefficients. We know that HPM is applied for nonlinear equations. We think that this study can also be applied to non-linear complex equations.

References

[1] Bers, L., *Theory of Pseudo-Analytic Functions*. New York University Institute for Mathematics and Mechanics, 1st ed., 187 p., 1953.

[2] Vekua, I. N., *Verallgemeinerte Analytische Funktionen*. Berlin, Akademie Verlag, 1st edition, 538p, 1959.

[3] Merdan, M., Merdan, M., Şahin, R., *Investigation of Behavior on Solutions of Lane–Emden Complex Differential Equations by a Random Differential Transformation Method*, Complexity, 2023, 1-12, 713454, 2023.

[4] Sezer, M., Tanay, B., Gülsu, M.A., *Polynomial approach for solving high-order linear complex differential equations with variable coefficients*, Erciyes Üniversitesi Fen Bilimleri Enstitüsü Dergisi, 25(1-2), 374 – 389, 2009.

[5] Gülsu, M., Sezer, M., *Approximate solution to linear complex differential equation by a new approximate approach*, Applied Mathematics and Computation, 185, 636-645, 2007.

[6] Düz, M., *On an application of Laplace transforms*, New Trends in Mathematical Sciences, 5, 193-198, 2017.

[7] Düz, M., *Application of Elzaki transform to first order constant coefficients complex equations*, Bulletin of International Mathematical Virtual Institute, 7, 387-393, 2017.

[8] Düz, M., *Solution of complex differential equations by using Fourier Transform*, International Journal of Applied Mathematics, 31(1), 23-32, 2018.

[9] Kayabaşı, H., Murat Düz, M., Issa, A., *Solution of complex differential equations by using variational iteration method*, The Aligarh Bulletin of Mathematics, 43(1), 57 – 63, 2024.

[10] Düz, M., *Solutions of complex equations with adomian decomposition method*, TWMS Journal of Applied and Engineering Mathematics, 7, 66-73, 2017.

[11] He, J., *Homotopy perturbation method: a new nonlinear analytical technique*, Applied Mathematics and Computation, 135, 73–79, 2003.

[12] He, J., *Homotopy perturbation technique*, Computer Methods in Applied Mechanics and Engineering, 178(3-4), 257-262, 1999.

[13] He, J., *A coupling method of a homotopy technique and a perturbation technique for non linear problems*, International Journal of Non-Linear Mechanics, 35(1), 37-43, 2000.

[14] Abbasbandy, S., *Homotopy perturbation method for quadratic Riccati differential equation and comparison with Adomian's decomposition method*, Applied Mathematics and Computation, 172(1), 485-490, 2006.

[15] Abbasbandy, S., *Numerical solutions of the integral equations: Homotopy perturbation method and Adomian's decomposition method*, Applied Mathematics and Computation, 173(1), 493-500, 2006.

[16] Babolian, E., Azizi, A., Saeidia, J., *Some notes on using the homotopy perturbation method for solving time-dependent differential equations*, Mathematical and Computer Modelling, 50(1-2), 213-224, 2009.

[17] Türkyılmazoglu, M., *An analytic shooting-like approach for the solution of nonlinear boundary value problems*, Mathematical and Computer Modelling, 53(9-10), 1748-1755, 2011.

[18] Merdan, M., *Homotopy perturbation method for solving modelling the pollution of a system of lakes*, Süleyman Demirel University Faculty of Arts and Science Journal of Science, 4 (1) 99-111, 2009.

[19] Merdan., M., *A multistage homotopy perturbation method for solving human T-cell lymphotropic virus I (HTLV-I) infection of CD4+ T-cells model,* Mathematical and Computational Applications, 14(2), 85-96, 2009.

[20] Merdan, M., *Homotopy perturbation method for solving a model for HIV infection of CD4+ T cells*, İstanbul Commerce University Journal of Science, 6(12), 39-52, 2007.

[21] Türkyılmazoglu., M., *Is homotopy perturbation method the traditional Taylor series expansion*, Hacettepe Journal of Mathematics and Statistics, 44(3), 651 – 657, 2015.